

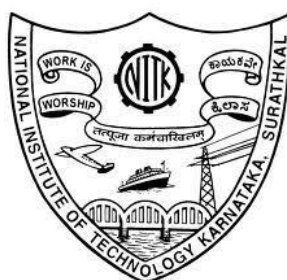
**SYNTHESIS, STRUCTURE, PROPERTIES
AND APPLICATIONS OF ELECTROSPUN
POLY(VINYLIDENE FLUORIDE)-
FUNCTIONAL NANOFILLER COMPOSITES**

Thesis

Submitted in partial fulfilment of the requirements for the degree of
DOCTOR OF PHILOSOPHY

By

MOHAMMED KHALIFA




DEPARTMENT OF METALLURGICAL AND MATERIALS
ENGINEERING
NATIONAL INSTITUTE OF TECHNOLOGY KARNATAKA,
SURATHKAL, MANGALURU – 575 025

OCTOBER, 2019

DECLARATION

By the Ph.D Research Scholar

I hereby *declare* that the Research Thesis titled “**Synthesis, structure, properties and applications of poly(vinylidene fluoride)-functional nanofiller composites**”, which is being submitted to the **National Institute of Technology Karnataka, Surathkal** in partial fulfilment of the requirements for the award of the Degree of **Doctor of Philosophy in Metallurgical and Materials Engineering** is a *bonafide report of the research work carried out by me*. The material contained in this Research Thesis has not been submitted to any University or Institution for the award of any degree.



09.10.2019

Mohammed Khalifa

Register number: 148042MT14F09

Department of Metallurgical and Materials Engineering

National Institute of Technology Karnataka, Surathkal

Place: NITK-Surathkal

Date: 09-10-2019

CERTIFICATE

This is to *certify* that the Research Thesis titled “**Synthesis, structure, properties and applications of poly(vinylidene fluoride)-functional nanofiller composites**”, submitted by **Mohammed Khalifa** (Register No: **148042MT14F09**) as the record of the research work carried out by him, is *accepted as the Research Thesis submission* in partial fulfilment of the requirements for the award of degree of **Doctor of Philosophy**.



Prof. S. Anandhan

Research guide & Chairman DRPC

Chairman - DRPC
Dept. of Metallurgical and Materials Engineering
National Institute of Technology Karnataka, Surathkal
Post Srinivasnagar, Mangaluru - 575 025
Karnataka, India

Dedicated to my parents, Late. Gaibumardan Khalifa and Late. Saleema Khalifa.

ACKNOWLEDGMENT

I most sincerely like to express heartfelt gratitude to my mentor Prof. S. Anandhan, Professor & Head, Department of Metallurgical and Materials Engineering for his invaluable guidance and tremendous support during the research work. I do not know if it is possible to convey in words the sense of thankfulness. Having him as my mentor, teacher and supervisor over the past four years has been one of the best things to happen in my life. He always inspired me to achieve at a level higher than I thought possible. His tremendous support and encouragement during the thesis process was invaluable. Because of him, I discover a passion for learning and exploring new ideas that weren't even on my radar four years ago. I am forever thankful.

I would like to express my deep and sincere appreciation to my research progress assessment committee members, Prof. Rajmohan., Department of Chemical Engineering, and Dr. Ravishankar. S, Department of Metallurgical and Materials Engineering for their overwhelming support, and also making my research work more constructive with their thoughtful comments and suggestions.

I profusely thank Dr. Rizwan-ur Rahman, Prof. Jagannath Nayak, Prof. K.N Prabhu, Prof. Udaya Bhat K, Dr. Subray Hegde, Department of Metallurgical and Materials Engineering, NITK Surathkal for their valuable suggestions and encouragement in different stages of my research work. I also thank the entire faculty of Department of Metallurgical and Materials Engineering for their direct/indirect support throughout my research work.

I also owe my gratitude to Dr. Arunjunairaj Mahendran, Dr. Guenter Wuzella and Dr. Herfried Lammer (Kompetenzzentrum Holz GmbH, Linz, Austria), Dr. Venimadhav Adyam, Associate Professor, Cryogenic Engineering Center, IIT Kharagpur, Prof. Sudipto Ghosh, Professor, Department of Metallurgical and Materials Engineering, IIT Kharagpur for providing the most needed support and their kind assistance in various characterization techniques.

I would also like to thank Mr. S Janakiraman, Research Scholar, Department of Metallurgical and Materials Engineering, IIT Kharagpur, Mr. Prakash Pawar, Research Scholar, Department of Metallurgical and Materials Engineering, NITK Surathkal for their support in various stages of my research work. I wish to thank Mr. Prashanth Huilgol, Mr. Palaksha, Mr. Sangamesh Rajole, Ms. Rashmi, Mr. Vinayak, Mr. Dhanush and Mr. Prajwal, NITK Surathkal for their assistance in various characterization techniques. I also would like to thank innovation center, Manipal university, SAIF research center, Cochin, Mangalore university for their kind assistance in carrying out various characterization techniques.

It is my most cherished duty to heartily thank Mrs. Sharmila Dinesh for helping me throughout my stay at NITK during my research work with an eternal smile and ever-increasing enthusiasm. I also thank the technicians and non-teaching staff (Mrs. Vinaya D. Shettigar, Mr. Sundara Shettigar, Mr. Yashvanth K. S, Mr. Satish P., Mr. Lokesh, Mr. Sachin and Mr. Dinesha S.) of Department of Metallurgical and Materials Engineering, NITK Surathkal, for helping me throughout my experimental work in the laboratories.

It is a privilege and great pleasure to thank Dr. Akshata Patil and Mr. Govind Ekbote for continuous support and encouragement. I am indeed pleased and happy to extend my heartfelt thanks to all my colleagues, Dr. T. Senthil, Dr. Gibin George, Dr. Sachin Kumar, Ms. Shamitha C., Mr. Sawan Shetty and Mr. Nitin Reddy for helping me by providing the technical support and cooperation during the entire research work.

I take this opportunity to thank my friends for their support, love and affection, Mr. Bhemappa Halavar, Mr. Uday Patil, Mr. Manjunath. M, Mr. Sunil Meti, Mr. Komal Krishna, Dr. Arun Augustin, Mr. Deewan, Mr. Suhail Bakshi, Mr. Pavan Sandur, Mr. Prabhu C., Mr. Aranganathan, Mr. Abdul Razak Buradi, Mr. Altaf Bagawan, Mr. Wajid, Mr. Mubassir Shaikh, Mr. Mahesh Patil, Dr. Zakir, Mr. Vinay Singh Thakur, Mr. Ganesh I., Ms. Azra Nasreen Taj and Vinod. S. are only a few among them.

It is my privilege and great pleasure to thank Prof. Vadiraj Katti, Prof. S.B Koulagi, Prof. Vijaykumar Nagathan, Prof.. S. Chappar, Prof.. R.S Kattimani, Dr. Basavaraj Angadi, Prof. L. N Karadi (B.L.D.E C. E. T, Bijapur) and Mrs. Sadiya Siddique, Mrs. Sajida Fatima, Mr. Vasudev Murty (R.T.P.S Highschool, Shaktinagar) and all my teachers for shaping my mind, developing the confidence and being so encouraging about my work.

I am humbled when I think of extending my thanks to my family members. Words cannot express how grateful I am to my father Late. Gaibumardan Khalifa, mother Late. Saleema Khalifa for all the sacrifices they made on my behalf. Their prayers and wishes gave me the strength to sustain this far. I would also like to thank my brothers and sisters for their continuous encouragement and support for pursuing higher studies. I also would like to thank my brothers in law and sisters in law. Finally, I thank all my friends, colleagues for their kind assistance, comments and suggestions and indirectly for completing my research work.

-MOHAMMED KHALIFA

Abstract

Electrospun poly(vinylidene fluoride) (PVDF) based nanocomposites were synthesized for various applications. Incorporation of nanofillers [halloysite nanotubes (HNT), polyaniline (PANi), graphitic-carbon nitride nanosheets (g-C₃N₄)] not only reduced the diameter of the PVDF nanofibers, but also improved the morphology of nanofibers. Fourier transform infrared spectroscopy, wide-angle X-ray diffraction and differential scanning calorimetry techniques were used to characterize the crystallinity, polymorphism and polymer-filler interaction in the electrospun PVDF nanocomposites. HNT and g-C₃N₄ acted as nucleating agents and helped in the formation of the β -phase of PVDF. The primary objective was to explore the potential of electrospun PVD/HNT nanocomposite, PVDF/g-C₃N₄ nanocomposite, PVDF/HNT/PANi blend nanocomposite and PVDF/g-C₃N₄/PANi blend nanocomposite for piezoelectric force sensor, energy harvesting, battery separator and gas sensing applications. The inclusion of nanofillers and electrospinning synergistically improved the mechanical and piezoelectric properties. However, the degree of crystallinity decreased due to the hindrance to the polymer chain mobility. PVDF/HNT nanocomposite exhibited piezoelectric voltage and current output of 0.95 V and 32 nA, respectively. Addition of PANi to PVDF/HNT nanofibers significantly improved the electrical conductivity and piezoelectric properties. Electrospun PVDF/HNT nanocomposite was used in lithium-ion batteries (LIB) due to its relevant characteristics as gel polymer electrolytes (GPE). The GPE showed high ionic conductivity, electrolyte uptake and improved charge-discharge performance. The GPE outperformed commercial Celgard[®]2400 and pristine PVDF nanofibers in every aspect investigated. The highest β -phase content of 97% was attained by electrospun PVDF/PANi/g-C₃N₄ blend nanocomposite (PPBF). The PPBF was used for energy harvesting from human locomotion and nitrogen dioxide (NO₂) gas sensing. Flexible PPBF based nanogenerator exhibited excellent piezoelectric performance and was capable of generating a voltage and current output of ~30 V and 3.72 μ A, respectively, which could play a prominent role in energy harvesting application. Further, the PPBF based gas sensor showed excellent response to NO₂ gas along with high sensitivity, selectivity, durability and reproducibility. The PVDF based nanocomposite non-wovens developed in this study are potentially useful as a force sensor, energy harvesting nanogenerator, GPE and gas sensor. Flexibility, low cost, non-toxicity, eco-friendliness and industry scalability are added attractive characteristics of these electrospun PVDF nanocomposites.

Keywords: *Electrospinning; poly(vinylidene fluoride); energy harvesting; gas sensor; gel polymer electrolyte; nanocomposite*

CONTENTS

List of figures	i
List of tables	vi
Nomenclature	vii
CHAPTER: 1 INTRODUCTION AND LITERATURE SURVEY	1
1.1. INTRODUCTION	1
1.1.1. Piezoelectricity	2
1.1.2. Poly(vinylidene fluoride)	5
1.1.3. Electrospinning	7
1.1.4. Gel polymer electrolytes	11
1.1.5. Chemi-resistive gas sensors	13
1.2. REVIEW OF LITERATURE	14
1.2.1. Review on piezoelectricity of PVDF	14
1.2.2. Review on PVDF as GPE	16
1.2.3. Review on PVDF nanofibers for gas sensing	18
1.3. Problem identification	23
1.4. SCOPE AND OBJECTIVES OF PRESENT WORK	23
1.4.1. Scope	23
1.4.2. Objectives	24
1.4.3. Layout of the thesis	25
CHAPTER: 2 MATERIALS AND METHODS	27
2.1. Materials used	29
2.2. Methodology	29
2.2.1. Synthesis of PANi.	29
2.2.2. Synthesis of g-C ₃ N ₄ nanosheets	30
2.2.3. Electrospinning of electrospun HNT/PVDF nanocomposite	30
2.2.4. Electrospinning of PANi/HNT/PVDF Blend nanocomposites	30
2.2.5. Fabrication of PANi/PVDF films	31
2.2.6. Synthesis of electrospun PVDF/ g-C ₃ N ₄ nanocomposites	31
2.2.7. Synthesis of electrospun of PVDF/GPC nanocomposite	32
2.3. Measurement and characterization	32

2.4.	Setups and methodology used for the applications of electrospun PVDF nanocomposites	35
2.4.1.	Piezoelectric evaluation setup	35
2.4.2.	Coin cell fabrication	36
2.4.3.	Gas sensing evaluation setup	37
CHAPTER: 3 PROBING THE SYNERGISM OF HALLOYSITE NANOTUBES AND ELECTROSPINNING ON CRYSTALLINITY, POLYMORPHISM AND PIEZOELECTRIC PERFORMANCE OF POLY(VINYLDENE FLUORIDE)		39
3.1.	Results and discussion	41
3.1.1.	SEM results	42
3.1.2.	FTIR Spectroscopy and WAXD analysis	43
3.1.3.	DSC analysis	45
3.1.4.	TGA analysis	46
3.1.5.	TEM analysis	47
3.1.6.	Polymer-filler Interaction mechanism in PHNF webs	48
3.1.7.	Piezoelectric Performance of PHNF webs	49
3.2.	Conclusions	49
CHAPTER: 4 PVDF/HALLOYSITE NANOCOMPOSITE-BASED NON-WOVENS AS GEL POLYMER ELECTROLYTE FOR HIGH SAFETY LITHIUM ION BATTERY		51
4.1.	Results and discussion	53
4.1.1.	SEM, FESEM and AFM results	54
4.1.2.	Ionic transference number	55
4.1.3.	Electrochemical stability of PHNF webs	56
4.1.4.	Thermal shrinkage test	57
4.1.5.	Mechanical properties of E-PVDF and PHNF webs	58
4.1.6.	AC ionic conductivity of PHNF webs	59
4.1.7.	Cycle performance of Li/PHNF/LiCoO ₂ cell	61
4.2.	Conclusions	63

CHAPTER 5: DURABLE, EFFICIENT AND FLEXIBLE PIEZOELECTRIC	65
NANOGENERATOR FROM ELECTROSPUN PANi/HNT/PVDF BLEND	
NANOCOMPOSITE	
5.1. Results and Discussion	67
5.1.1. Synthesis of PANi	68
5.1.2. Morphological studies	68
5.1.3. FTIR analysis	69
5.1.4. WAXD analysis	70
5.1.5. TEM analysis	70
5.1.6. Piezoelectric performance of BNCNF nanogenerator	71
5.2. Conclusions	76
CHAPTER 6: SYNERGISM OF GRAPHITIC-CARBON NITRIDE AND	77
ELECTROSPINNING ON THE PHYSICO-CHEMICAL	
CHARACTERISTICS AND PIEZOELECTRIC PROPERTIES OF	
FLEXIBLE POLY(VINYLDENE FLUORIDE) BASED	
NANOGENERATOR	
6.1. Results and Discussion	79
6.1.1. Morphological studies	80
6.1.2. FTIR and WAXD analysis	81
6.1.3. DSC analysis and tensile properties	82
6.1.4. TGA and DTG analysis	84
6.1.5. Piezoelectric performance of PGN-X	85
6.2. Conclusions	90
CHAPTER 7: EFFECTUAL AUGMENTATION OF PIEZOELECTRIC	91
ENERGY CONVERSION OF ELECTROSPUN POLY(VINYLDENE	
FLUORIDE)/POLYANILINE/GRAPHITIC-CARBON NITRIDE BLEND	
NANOCOMPOSITES	
7.1. Results and Discussion	93
7.1.1. Morphological studies of PANi/g-C ₃ N ₄ nanocomposites	94
7.1.2. FTIR analysis of GPC	95
7.1.3. SEM micrographs of electrospun PVDF nanocomposites	96
7.1.4. Polymorphism and Crystallinity analysis	97
7.1.5. Mechanical properties	100

7.1.6.	Piezoelectric evaluation of PPBF	101
7.2.	Conclusions	110
CHAPTER 8: DURABLE, SENSITIVE AND FLEXIBLE ELECTROSPUN POLY(VINYLDENE FLUORIDE)/POLYANILINE/GRAPHITIC CARBON NITRIDE NANOCOMPOSITE-BASED GAS SENSOR FOR NO₂ SENSING		111
8.1.	Results and Discussion	113
8.1.1.	UV-Vis spectroscopy	114
8.1.2.	SEM Micrographs	115
8.1.3.	FTIR and WAXD analysis	116
8.1.4.	Gas sensing evaluation	117
8.2.	Conclusions	121
CHAPTER 9: SUMMARY & CONCLUSIONS		125
	Scope for further work	129
	Appendix	130
	References	145
	Bio-data	175
	List of publications	177

LIST OF FIGURES

Figure No.	Captions	Page. No
1.1	Orientation of dipoles in monocrystalline and polycrystalline materials.	3
1.2	Schematic representation of different types of piezoelectric polymers.	4
1.3	Phases of PVDF.	6
1.4	Interconversions of PVDF phases through different routes.	7
1.5	a) Schematic representation of electrospinning Process b) Digital photograph of electrospinning equipment.	8
1.6	A schematic representing components of LIB.	11
2.1	schematic of the setup used in the piezoelectric evaluation.	36
2.2	Schematic diagram of the package assembly of the Li/PHNF/LiCoO ₂ in a coin cell.	37
2.3	Schematic of indigenously build gas sensing set-up used for the evaluation of the performance of PPBF sensor.	37
3.1	SEM images (magnification 5,000× and scale bar = 5 μm) of electrospun PHNF webs with HNT loading of a) E-PVDF b) 2.5% c) 5 % d)7.5 % e) 10 % and f) 20 %.	41
3.2	FTIR spectra of unstretched PVDF film, E-PVDF and PHNF webs.	42
3.3	a) WAXD patterns of unstretched PVDF film, E-PVDF and PHNF webs b) DSC traces of electrospun PVDF and PHNF webs.	44
3.4	a) TGA curves of E-PVDF and PHNF webs b) DTG curves of E-PVDF and PHNF webs.	45
3.5	TEM images of a) Pristine HNT and b) 10% HNT/PVDF webs; and c) SAED patterns of 10% HNT/PVDF webs.	46
3.6	a) FTIR spectra of E-PVDF, pristine HNT and PHNF webs b) Plausible interaction mechanism between HNT and PVDF in the PHNF webs.	47
3.7	Piezoelectric responses of E-PVDF and PHNF webs at different loads.	49
4.1	a) TEM image of HNT; b) Schematic representation of HNT chemical structure.	54
4.2	a) SEM image of E-PVDF b) SEM image of PHNF c) FESEM image of PHNF without electrolyte d) FESEM image of PHNF with electrolyte e) AFM image of PHNF f) SEM image of Celgard [®] 2400.	55

4.3	a) DC polarization curves of PVDF and PHNF based separators b) Linear sweep voltammograms of SS/Celgard [®] 2400/Li, SS/E-PVDF/Li and SS/PHNF/Li at 10mVs ⁻¹ .	57
4.4	a) and b) TEM micrographs of PHNF; c) Interactions between PHNF and LiPF ₆ .	57
4.5	Digital photographs of the thermal shrinkage test of Celgard [®] 2400 E-PVDF and PHNF webs before and after the heat treatment (the arrows indicate regions of shrinkage).	58
4.6	a) Stress-strain curves of E-PVDF and PHNF webs b) Load-displacement curves of puncture test for E-PVDF and PHNF webs.	59
4.7	a) Impedance spectra of PVDF and PHNF based gel electrolytes b) Electrochemical impedance spectra of Li/LiCoO ₂ cells containing PVDF, and PHNF electrolyte membranes.	60
4.8	a) Initial charge/discharge profiles of Li/E-PVDF/LiCoO ₂ , Li/PHNF/LiCoO ₂ and Li/Celgard [®] 2400/LiCoO ₂ cell b) Charge-discharge performance and coulombic efficiency of Li/PHNF/LiCoO ₂ cell.	61
4.9	a) Charge-discharge performance and coulombic efficiency of Li/Celgard [®] 2400/LiCoO ₂ cell b) Discharge capacity of Li/Celgard [®] 2400/LiCoO ₂ , Li/PVDF/LiCoO ₂ and Li/PHNF/LiCoO ₂ at different current rates.	62
5.1	a) WAXD pattern of PANi nanorods; b) ATR mode FTIR spectrum of PANi nanorods.	68
5.2	SEM micrographs of electrospun nanofiber mats: (a) E-PVDF; (b) PPNF; (c) PHNF; (d) BNCNF.	69
5.3	a) FTIR spectra b) WAXD patterns of pristine PVDF film, E-PVDF, PPNF, PHNF and BNCNF.	70
5.4	a) TEM micrograph of BNCNF; and b) SAED pattern of BNCNF.	71
5.5	Schematic showing the formation of network of PANi in: a) PVDF/PANi film; and b) BNCNF.	71
5.6	a) Schematic and b) digital photograph of indigenous setup for the evaluation of piezoelectric performance; c) Piezoelectric performance of BNCNF nanogenerator under different pressure.	73

5.7	Piezoelectric performance of BNCNF nanogenerator under a) one finger tapping b). two-finger tapping.	73
5.8	Voltage output of BNCNF nanogenerator patch a) attached to a human arm (Inset: Digital photograph of BNCNF patch attached to human arm) b) Variation of piezoelectric performance of BNCNF nanogenerator with time.	74
5.9	a) Current and voltage output with respect to the load resistance under two finger tapping b) Power density of BNCNF nanogenerator with respect to the load resistance under one and two fingers tapping	75
6.1	HRSEM image of in-situ synthesized g-C ₃ N ₄ along with elemental composition.	80
6.2	SEM micrographs of a) E-PVDF b) PGN-0.25 c) PGN-0.5 d) PGN-0.75 e) PGN-1.0 f) PGN-2.0	80
6.3	TEM micrograph of a) in-situ synthesized g-C ₃ N ₄ nanosheets b) PGN-0.75.	81
6.4	E-PVDF and PGN-X at different loadings of g-C ₃ N ₄ nanosheets a) FTIR spectra of. b) WAXD patterns.	81
6.5	E-PVDF and PGN-X at different loadings of g-C ₃ N ₄ a) DSC curves b) Stress-strain curves.	83
6.6	a) TGA curves of of E-PVDF and PGN-X for different loadings of g-C ₃ N ₄ b) DTG curves of E-PVDF and PGN-X for different loadings of g-C ₃ N ₄ .	84
6.7	a) & b) Piezoelectric performance of E-PVDF and PGN-X for different loadings of g-C ₃ N ₄ under one finger tapping mode.	85
6.8	a) & b) Piezoelectric performance of E-PVDF and PGN-X for different loadings of g-C ₃ N ₄ under two finger tapping mode.	86
6.9	Piezoelectric performance of PGN-0.75 under a) thumb imparting b) palm (slapping).	86
6.10	Voltage output response of PGN-0.75 under a) forward bias connection b) reverse bias connection.	87
6.11	a) Voltage output of PGN-0.75 nanogenerator under bending mode b) Power density of PGN-0.75 nanogenerator with respect to the load resistance under two fingers tapping.	87

6.12	Current output of E-PVDF and PGN-X (X = 0.25, 0.5, 0.75, 1.0 & 2.0).	88
6.13	a) SEM micrograph of PGN-0.75 after 10000 cycles b) FTIR spectrum of PGN-0.75 after 10000 cycles and 30 days.	88
6.14	Charging voltage across a capacitor in PGN-0.75 nanogenerator.	89
6.15	(a) Charging voltage across a capacitor in PGN-0.75 nanogenerator (b) Dependence of g-C ₃ N ₄ nanosheet loading on the piezoelectric coefficient and piezoelectric voltage coefficient.	89
7.1	HRSEM image of a) GPC-5.0 b) GPC-7.5 c) GPC-10 with chemical composition (d-f). Elemental mapping of major elements in GPC-7.5 sample.	94
7.2	FTIR spectra of PANi nanorods and GPC for different loadings.	95
7.3	SEM micrographs of a) E-PVDF b) PPBF-5.0 c) PPBF-7.5 d) PPBF-10.	96
7.4	E-PVDF, PVDF/PANi blend and PPBF-X at different loadings of GPC a) FTIR spectra b) WAXD patterns of E-PVDF and PPBF-X at different loadings of GPC.	97
7.5	Plausible interaction mechanism between g-C ₃ N ₄ nanosheets, PANi nanorods, DMF and PVDF chains for the formation of TTT conformation.	99
7.6	E-PVDF and PPBF-X at different loadings of g-C ₃ N ₄ loading a) DSC curves b) Stress-strain curves.	99
7.7	Piezoelectric evaluation of E-PVDF and PPBF-X nanogenerators under periodic human finger (one) tapping mode.	101
7.8	Piezoelectric performance of PPBF-7.5 nanogenerator a) Forward connection b) Reverse connection.	102
7.9	Piezoelectric voltage output of PPBF-7.5 nanogenerator under two finger tapping mode a) PPBF-7.5 (Inset: light up of LED lights) b) Voltage and current output of E-PVDF and PPBF-X nanogenerators.	102
7.10	TEM micrograph of PPBF-7.5 with schematic showing the formation of PANi nanorod network within PVDF fiber.	103

7.11	Piezoelectric performance of PPBF-7.5 nanogenerator a) Thumb imparting b) Bending c) Wrist movement d) Blowing (mouth).	104
7.12	Piezoelectric voltage output of PPBF-7.5 nanogenerator a) Human arm motion b) Toe imparting (Inset: Lighting-up of LED lights (15 nos) c) Palm (impact) mode (Inset: Lighting-up of LED lights (14 nos) d) Heel pressing (Inset: Lighting -up of LED lights (18 nos).	104
7.13	Piezoelectric voltage output of PPBF-7.5 under a) Bending and straightening of fingers b) Cantilever free vibration c) Blowing with hair dryer at different velocity d) Durability of nanogenerator under blowing condition (>10000 cycles).	105
7.14	a) Piezoelectric voltage output of PPBF-7.5 under punching mode b) capacitor charging performance of PPBF-7.5 nanogenerator (Inset: schematic of the circuit used for the evaluation) c) Voltage and current output as a function of load resistance (Inset: schematic circuit used for the evaluation) d) Power density of PPBF-7.5 nanogenerator as a function of load resistance.	108
7.15	Piezoelectric coefficient and voltage coefficient of E-PVDF and PPBF-X nanogenerators.	109
7.16	Response of the PPBF-7.5 nanogenerator tested over 15 weeks under finger tapping mode.	110
8.1	a) UV–Visible spectra of g-C ₃ N ₄ , PANi and GPC b) Band gap of PANi and GPC.	114
8.2	a) SEM micrograph of SPF b) SEM micrograph of SCNF c) SEM micrograph of E-PVDF d) SEM micrograph of PPBF.	115
8.3	a) FTIR spectra of SPF, SCNF, E-PVDF and PPBF b) WAXD patterns of SPF, SCNF, E-PVDF and PPBF.	116
8.4	Digital photograph and schematic of gas sensor used in this study a) SCNF- based gas sensor b) PPBF-based gas sensor.	117
8.5	Response and recovery curves of SCNF and PPBF against NO ₂ gas at a different concentration b). Effect of g-C ₃ N ₄ nanosheet loading on the response of PPBF sensor against NO ₂ gas at different concentrations.	117

8.6	a) Sensitivity of SCNF and PPBF against NO ₂ gas at a different concentration of gas b) selectivity (with error bar) of PPBF-based gas sensor.	118
8.7	Plausible sensing mechanism of PPBF-based gas sensor for NO ₂ sensing.	119
8.8	a) The response of SCNF and PPBF-based gas sensor exposed to NO ₂ gas for over 100 cycle b) Long-term stability of SCNF and PPBF-based gas sensor.	120
8.9	PPBF sensor response against NO ₂ at different humidity conditions.	122

LIST OF TABLES

Table No	Caption	Page. No
1.1	PVDF for piezoelectric energy harvesting application.	19
1.2	PVDF for Gel polymer electrolytes in LIB	21
3.1.	WAXD and FTIR results of PHNF webs.	44
3.2	DSC results of PHNF webs.	45
6.1	Melting temperatures, crystallization temperature and crystallinity of E-PVDF and PGN-X at different loadings of g-C ₃ N ₄ .	84
7.1	% β -phase, Melting temperature, degree of crystallinity and Tensile strength of E-PVDF and PPBF -X samples.	100

NOMENCLATURE

PVDF	Poly(vinylidene fluoride)
KDP	Potassium dihydrogen phosphate
BaTiO ₃	Barium titanate
HNT	Halloysite nanotube
g-C ₃ N ₄	graphitic-carbon nitride
PANi	Polyaniline
GPC	g-C ₃ N ₄ /PANi nanocomposite
PZT	Lead zirconate titanate
PbTiO ₃	Lead titanate
PbZrO ₃	Lead zirconate
SrTiO ₃	Strontium titanate
E-PVDF	Electrospun PVDF nanofibers
PHNF	Electrospun PVDF/HNT Nanocomposite
PPNF	Electrospun PVDF/PANi Nanocomposite
BNCNF	Electrospun PVDF/HNT/PANi blend Nanocomposite
PPBF	Electrospun PVDF/GPC blend Nanocomposite
SCNF	PVDF/GPC blend nanocomposite film
PGN	Electrospun PVDF/g-C ₃ N ₄ nanocomposite
SPF	Solution cast PVDF film
DMF	Dimethylformamide
DMSO	Dimethyl sulfoxide
APS	Ammonium persulfate
HCl	Hydrochloric acid
NO ₂	Nitrogen dioxide
NH ₃	Ammonia gas
WAXD	wide angle x-ray diffraction
FTIR	Fourier transform infrared spectroscopy
DSC	Differential scanning calorimetry
FESEM	Field-emission scanning electron microscopy
UTM	Universal testing machine
AFD	Average fiber diameter

SEM	Scanning electron microscope
TGA	Thermogravimetric analysis
DTG	Differential thermogravimetric
TEM	Transmission electron microscope
EDX	Energy-dispersive X-ray
HRSEM	High-resolution scanning electron microscopy
AFM	Atomic force microscopy
SD	Standard deviation
UV-Vis-NIR	Ultraviolet visible near infrared
TCD	Tip to collector distance
w/v %	Weight by volume percent
mL/h	Milliliter per hour
μF	micro Faraday
μA	Microamps
$\mu\text{W}/\text{Cm}^2$	Microwatt per square centimeter
μm	Micrometer
kV	kilovolts
rpm	revolutions per minute
R_a	Resistance in air
R_g	Resistance in the gas atmosphere
S	Sensitivity
nm	Nanometer
h	hour
μJ	Microjoules
X_c	Degree of crystallinity
Ω	Ohms
\bar{M}	Average molecular weight
ΔH_m	apparent enthalpy of fusion
T_m	Melting point

CHAPTER 1

INTRODUCTION AND LITERATURE SURVEY

CHAPTER 1

INTRODUCTION AND LITERATURE SURVEY

This chapter gives a brief introduction to poly(vinylidene fluoride) (PVDF) based nanocomposites and their processing routes. An overview of energy harvesting, piezoelectricity, PVDF, electrospinning process and advancements in PVDF nanofibers has been presented. A brief literature review on PVDF for various applications such as energy harvesting, gel polymer electrolyte and gas sensing is also presented. Finally, the motivation for this study, problem identification along with scope and objectives of the present study are discussed.

1.1. INTRODUCTION

In recent years, energy harvesting has been receiving significant attention from various sectors mainly due to its potential impact in enabling self-powered devices. Energy harvesting is the conversion of energy from the environment and surroundings into other useful forms of energy. In a time when everyone is utilizing resources at a rapid rate, unearthing alternate energy sources will pave a great way to produce sustainable energy, which could be a solution to the energy crisis. In recent decades, various energy scavenging technologies have been developed that use the unexploited energy (by-product from industries) or natural energy (wind, water, etc.) for the generation of electricity. Most often electricity is generated from energy coming out of industries, including either mechanical energy in the form of vibration, stress, friction, etc, and thermal energy in the form of heat coming out of furnaces, engines, etc. Moreover, natural sources such as solar energy, electromagnetic energy, wind energy, hydro energy and human locomotion that could be of significant potential in medical devices, transportation, portable electronics, automation industries, military, and self-powered devices.

With the advancement of smart materials, the energy required to run devices has dropped dramatically, often milliwatts in run mode and nanowatts in standby mode. As a result, low power wireless devices have gained attention with histrionic implementation. The development of low power consumption of integrated circuits, chips, sensors provides a broader path and motivation in the field of energy harvesting and enabling sensors and actuators, a platform where they can function automatically without any interruptions and significantly extend its life. Also, the sensors can be able to function in any remote place and transmit necessary information such as humidity, temperature, velocity, etc. (Mateu and Moll 2005). Generally, conventional devices often receive power from a battery source. Frequent recharging or replacement of battery results in an increase of overall cost and size. The combination of low power microcontrollers and energy harvesting led

to the rise of a wide range of applications that were not possible earlier. Currently, market for energy harvesting is enormous and has been increasing remarkably. According to experts, energy harvesting market will be more than 5 billion dollars by 2020, which means approximately 300 million sensors will be in the market that entirely run on energy harvesting systems. There are various sources through, which energy is being harvested. However, most widely used sources are solar, wind, thermoelectricity, pyroelectricity and piezoelectricity.

1.1.1. Piezoelectricity

Piezoelectric materials are the broader class of ferroelectric materials. The piezoelectric effect is the ability of certain materials to produce electrical charges upon the application of mechanical strain. The development in the field of piezoelectricity was observed during the world war-1 wherein piezoelectric materials were used to develop the ultrasonic technology. Rochelle salt was used as the piezoelectric material for the detection of submarines, which exhibits ferroelectricity and high electromechanical coupling. Later, potassium dihydrogen phosphate (KDP) was discovered in 1935 by predicting the origin of the piezoelectricity due to the presence of hydrogen bonds in the crystals. Various piezoelectric materials such as ammonium dihydrogen phosphate, barium titanate (BaTiO_3), lead zirconate titanate (PZT) etc were discovered. Gray and Shepard discovered that electrically-poled BaTiO_3 exhibited piezoelectricity, which facilitated the development of transducers. BaTiO_3 has a high electromechanical coupling coefficient and piezoelectric coefficient; most importantly it is insoluble in water. Following BaTiO_3 , the perovskite oxides such as lead titanate (PbTiO_3), lead zirconate (PbZrO_3), and strontium titanate (SrTiO_3) were developed.

The piezoelectric effect occurs due to orientation of electric dipoles. Upon application of an electric field, dipoles orient themselves along the direction of the applied electric field, creating polarization. The effect is closely associated with the moment of dipoles in the material in which they display a local charge separation based on the structure of the crystal lattice (Minazara et al. 2008). When the electric field is removed, the material cannot return to its initial state, but an ordered structure allows to exhibit the piezoelectric effect in the material.

In monocrystalline materials, the polar axis of dipoles are arranged in one direction, but in polycrystalline materials, dipoles are arranged randomly (Fig. 1.1). There are two modes in piezoelectric materials: longitudinal and transverse modes. In the longitudinal mode, the polarization direction is parallel to the direction of mechanical stress, while in the transverse mode, the direction of polarization is perpendicular to the direction of the stress. In most of the cases, when a voltage is applied in the transverse mode, the piezoelectric material gets compressed along

the z-axis, the voltage produced will be positive and when the material is compressed along the x-axis, the voltage generated is negative. Reports suggest that the piezoelectric conversion efficiency in longitudinal mode is better than in the transverse mode. (Murayama et al. 1976; Osone et al. 2008; Delnavaz and Voix 2014).

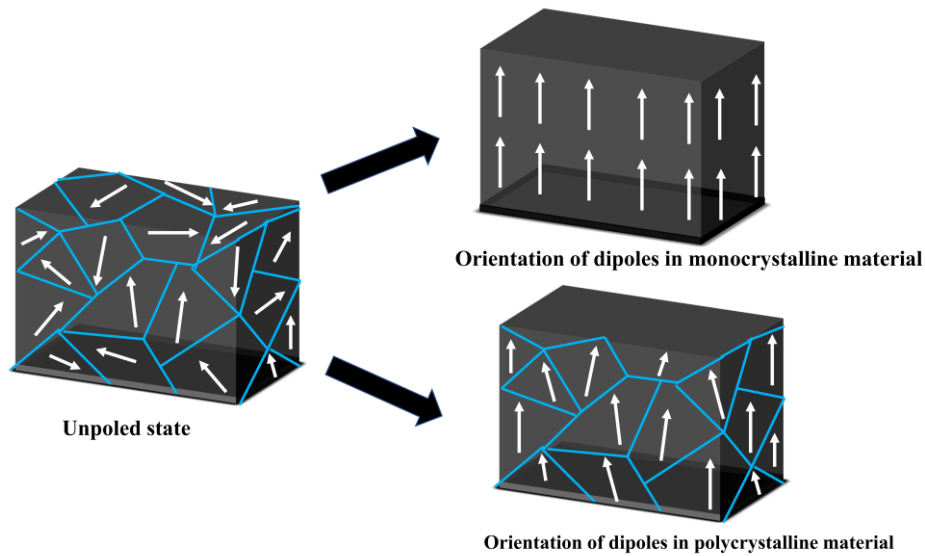


Fig. 1.1 Orientation of dipoles in monocrystalline and polycrystalline materials.

The piezoelectric energy harvesting technology based on vibrations, wind or mechanical motions has received considerable attention. To date, piezoceramics are the most widely exploited piezoelectric materials in sensors, actuators, capacitors, transducers etc. However, piezoceramics have serious issues such as high toxicity, fragility, expensive and lower tensile strength. In addition, small variations in the composition of piezoceramics could lead to significant changes in their physical properties (Jain et al. 2015; You et al. 2017). Another, major issue with piezoceramic is aging, where the material slowly tends to return to its original unpolarized state with time. There has been considerable research carried out to control the aging characteristics of piezoceramics. However, complicated process and may change the physical properties of the material, especially, the dielectric losses. Also, low mechanical strength of piezoceramics makes it difficult to fabricate them in the form of complex shapes (Ulrich et al. 2000).

Selection of piezoelectric materials is essential as there are more than 200 piezoelectric materials available and each of them has different characteristics. Piezoceramics display very high piezoelectric conversion efficiency, but are brittle. Piezoelectric polymers have been receiving much attention for energy harvesting application because of their flexibility, lightweight and non-toxicity characteristics. Piezoelectric polymers undergo higher strain values, but their piezoelectric coefficients are comparatively lesser than that of piezoceramics. Hence, owing to the persistent

quest, the current research is focused on either improving the flexibility of piezoceramics or enhancing the piezoelectric response of the polymers (Hooker 1998; Kao 2004).

Generally, piezoelectric polymers are classified into three groups: Bulk, composite and voided charged polymers (Fig 1.2). Bulk polymers possess piezoelectric characteristics based on their molecular structure and arrangement. For piezoelectric characteristics, the polymer should comprise of molecular dipoles, which are required to orient in a preferred state. The second type is piezoelectric polymer composites wherein piezoceramic particles are incorporated into the polymer matrix. The integrated particles offer the piezoelectricity, while polymer provide the necessary flexibility and mechanical strength.

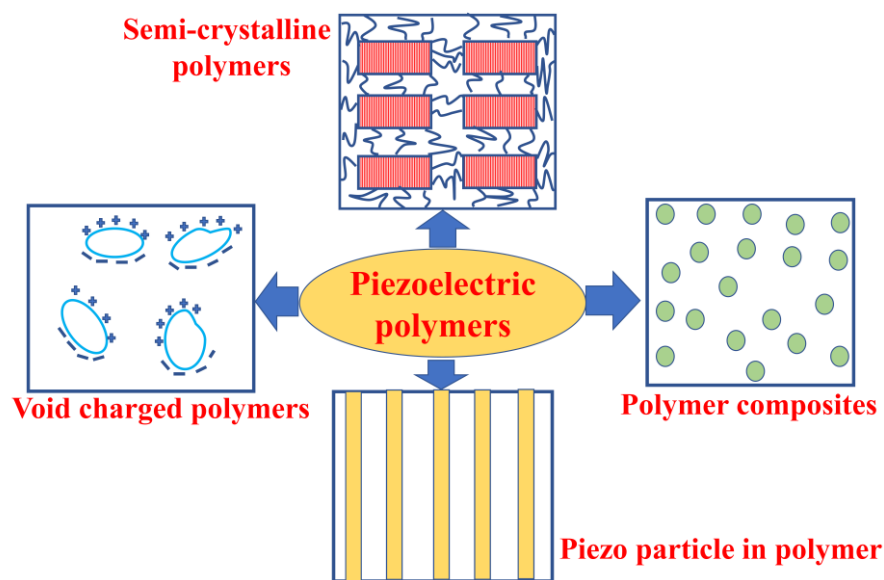


Fig. 1.2 schematic representation of different types of piezoelectric polymers.

Another type of piezoelectric polymer is voided charged polymer (e.g. cellular polypropylene) in which the presence of gas voids introduces the surface charges in such a way that it forms internal dipoles. The piezoelectric coefficient in these systems depends on various factors such as density, void size and shape, and void pressure (Murayama and Obara 1983; Arlt and Wegener 2010).

The properties of piezoelectric polymers are distinct from those of piezoceramics and are capable of performing effectively where other materials cannot perform. Contrary to the piezoelectric strain constant (d_{31}), piezoelectric stress constant (g_{31}) of polymers are much better than piezoceramics, which makes them suitable for sensors and actuators. Sensors made of polymers are much lighter, robust and can be molded into any complex shape and size. Further, the low dielectric constant, excellent mechanical properties with high sensitivity makes them a strong contender for device configurations.

1.1.2. Poly(vinylidene fluoride)

Poly(vinylidene fluoride) (PVDF) is a semi-crystalline polymer, which has a simple chemical structure with $-(\text{CH}_2-\text{CF}_2)-$ monomers that mostly occur in head to tail configuration and crystallizes in spherulites form. The crystalline phase offers the necessary mechanical strength and thermal stability, while the amorphous phase provides flexibility to the structure. In addition, PVDF exhibits excellent chemical stability and corrosion resistance. PVDF is synthesized through free radical polymerization and exhibits five different phases, namely α , β , γ , ϵ and δ related to its chain configuration. For α and δ phases, it has a chain conformation of TGTG' (trans-gauche-trans-gauche), for β -phase it has all-trans conformation (TTT) and T3GT3G' conformation for γ and ϵ phases (Fig.1.3). PVDF and its copolymers are suitable for making sensors and actuators due to their strong electrical dipole moment, which is due to the presence of fluorine atoms that are electronegative α and ϵ are non-polar phases due to their antiparallel packing of the dipoles. β and γ phases are considered to be the most electroactive ones that display piezoelectric response. In α -phase, the TGTG' conformation is not electroactive because the dipoles nullify the net polarization effect. In α -phase, the chains are neither in helical nor zig-zag configuration, but a combination of both. The sequence of G (gauche bonds) or TG represents the complete helical structure and the presence of G' in the conformation would mean that the backbone tilted from the plane. Repeated G or G' bond conformation would have a right or left helix, but with the TGTG' conformation the backbone has chain changes its direction with alternating G and G' bonds. α -phase is the most chemically stable phase because the van der Waals forces acting between the backbone and other molecules have intermolecular stability, whereas the β -phase is based on intramolecular stability that is relatively lower than that of α -phase. The β -phase of PVDF has all-trans conformation with a planar zig-zag structure in which all the hydrogen and fluorine atoms are in the opposite sides of the chain structure. In β -phase the stability is stalled because the fluorine atoms are closer to each other and their van der Waals radii almost overlap with each other. Further, the helical structure requires much lower energy than that of planar zig-zag structure results in the formation of the α -phase from the melt (Doll and Lando 1968; Lovinger et al. 1987; Martins et al. 2014).

Various strategies or techniques have been adopted to develop the electroactive phases (β and γ) in PVDF. The presence of electroactive phases is the reason for the piezoelectric, pyroelectric and ferroelectric properties of PVDF. The electroactive phases in PVDF obtained by uniaxial stretching, high pressure, ultra-fast cooling, drawing, high electric poling, annealing or by the addition of nucleating agents such as carbon nanotube, graphene, clay etc. A schematic representation of interrelations and conversions of phases is shown in Fig. 1.4.

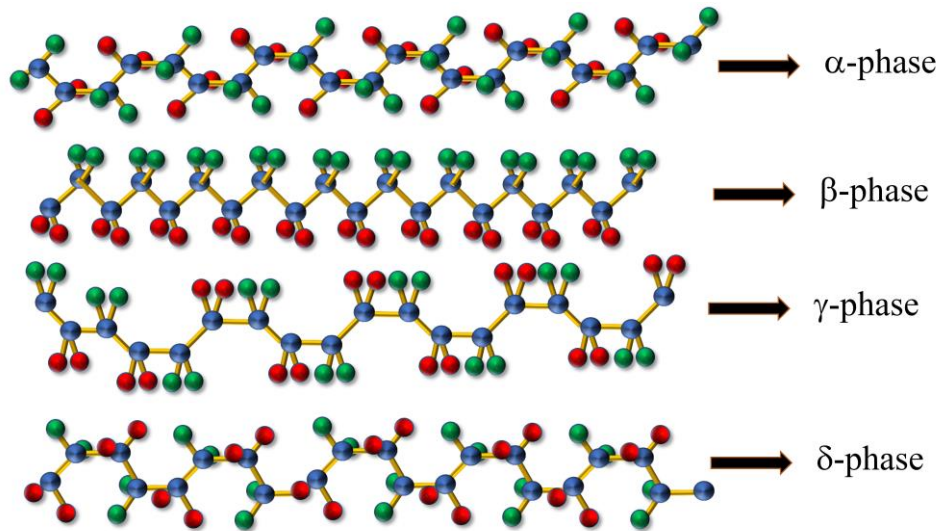


Fig 1.3. Different phases of PVDF.

Kawai et al. were the first to discover the piezoelectric effect in uniaxially stretched PVDF film and several reports later elucidated the mechanism (Kawai 1969; Kepler 1995). The uniaxial stretching of the PVDF film result in the stress effects that transform the spherulite into a microfibrillar structure upon necking. As a result, the dipoles orient themselves normal to the direction of the applied stress and the electroactive phase is observed. Also, the temperature during the stretching process significantly affects the orientation of the dipoles and electroactive phases (Crecorio and Cestari 1994). The β -phase can also be induced by proper quenching and annealing of samples at high temperature. Solution cast PVDF film develops electroactive phases when annealed up to a temperature of 100 °C for 5 hrs (Kaur et al. 2017). The annealing temperature significantly affects the crystallinity, crystallite size, mechanical and electrical properties of PVDF (Nakamura et al. 2003). A higher percentage of electroactive phase was observed when the films were cast from the solution at 90 °C, while the PVDF films cast at 50 °C do not possess any electroactive phases (Satapathy et al. 2011). The compression and injection molding of PVDF may also lead to the formation of the β -phase (Aggarwal et al. 2016; Wan and Bowen 2017). In another study, the PVDF film prepared by compression molding at 220 °C and cooled under a pressure of 170 bar would induce the β -phase of PVDF up to 29% (Salimi and Yousefi 2003a). There are several reports, which describe the processing methods and techniques adopted such as compression molding (Vacche et al. 2012), injection molding (Chang et al. 2010), spin coating (Ramasundaram et al. 2009), electrospinning (Fuh et al. 2012), electrospaying (Yanilmaz et al. 2014), melt spinning (He et al. 2014), Langmuir Blodgett deposition (Martins et al. 2014), solution

cast (Ma et al. 2008), immersion precipitation process (Mago et al. 2008) etc., to induce the electroactive phase in PVDF.

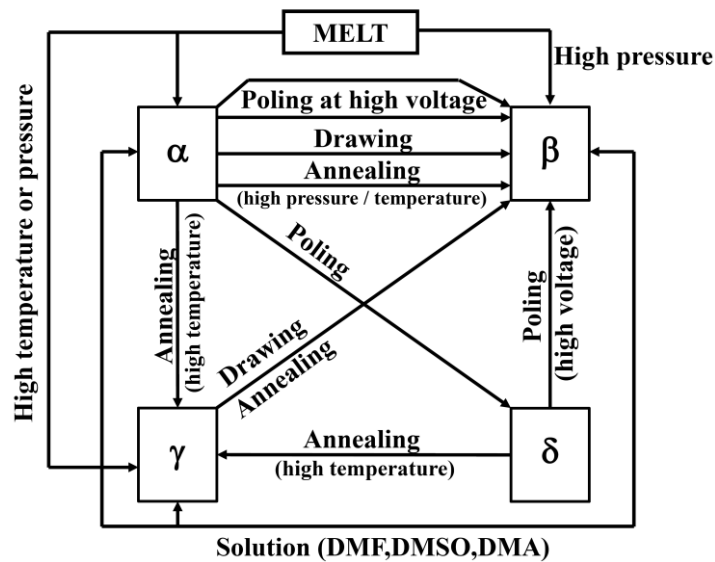


Fig.1.4. Interconversions of PVDF phases through different routes.

1.1.3. Electrospinning

Electrospinning is a process of spinning fibers of diameter ranging from few nanometers to micrometers using electrostatic forces. The technique was first patented on the fabrication of yarns by Formhals in early 1930s (Formhals 1934). Electrospinning has gained much attention in the last two decades because of its capability of producing fibers in nanometer range (nanofiber) (Mirjalili and Zohoori 2016). The term fiber or fibre is extracted from Latin word “fibra” which means a slandered, elongated and thread-like structure. In nanotechnology, fibers with a diameter below 100 nm are generally termed as nanofibers. However, textile industry standards and commercial sectors have allowed broader flexibility up to 500-1000 nm. The uniqueness of electrospun fibers is due to their fiber connectivity, high surface area and nanoscale interstitial space.

In electrospinning, a polymer solution is subjected to electrostatic potential, that causes the elongation of solution droplet to form a fiber, unlike conventional drawing method in which the polymer melt is forced mechanically to pass through a die. Materials such as polymers and polymer composite nanofibers can be produced directly by electrospinning. Other materials such as ceramics and carbon nanotubes require post-processing of the electrospun fibers. Electrospinning has three primary components viz; feed pump, voltage supply unit and a collector unit (grounded) as shown in the Fig.1.5. The controlled rate of solution fed with the help of syringe pump. When the voltage is applied to the solution, the pendant droplet converts into fine fiber jet commonly termed as Taylor cone. During the flight, due to the interaction between the solution jet, electric

field and repulsive force, the jet under goes a whipping instability that leads to stretching of fibers. During the flight, the solvent evaporates to leave behind fine fibers, which collect onto the grounded collector(Hu et al. 2014; Sun et al. 2016).

The characteristics of electrospun nanofibers depend on a number of parameters. These parameters commonly divided into three categories: solution parameters (solution concentration, solution viscosity, solution surface tension, and solution conductivity), process parameters (feed rate, applied voltage, and tip to collector distance), and ambient parameters (ambient temperature and relative humidity). Solution concentration is one of the significant factors that define the morphology of the electrospun nanofibers. Finer nanofibers can be produced with the lower concentration of polymer in the solution. However, the lower concentration may lead to the formation of bead and defects. The formation of beads can be prevented by increasing the polymer concentration above its critical entanglements. Further the solution concentration directly affects the viscosity of the solution. With an increase in solution concentration, the viscosity of the solution increases due to higher polymer chain entanglements that result in thicker fiber formation (Beachley and Wen 2009; Zhu et al. 2017).

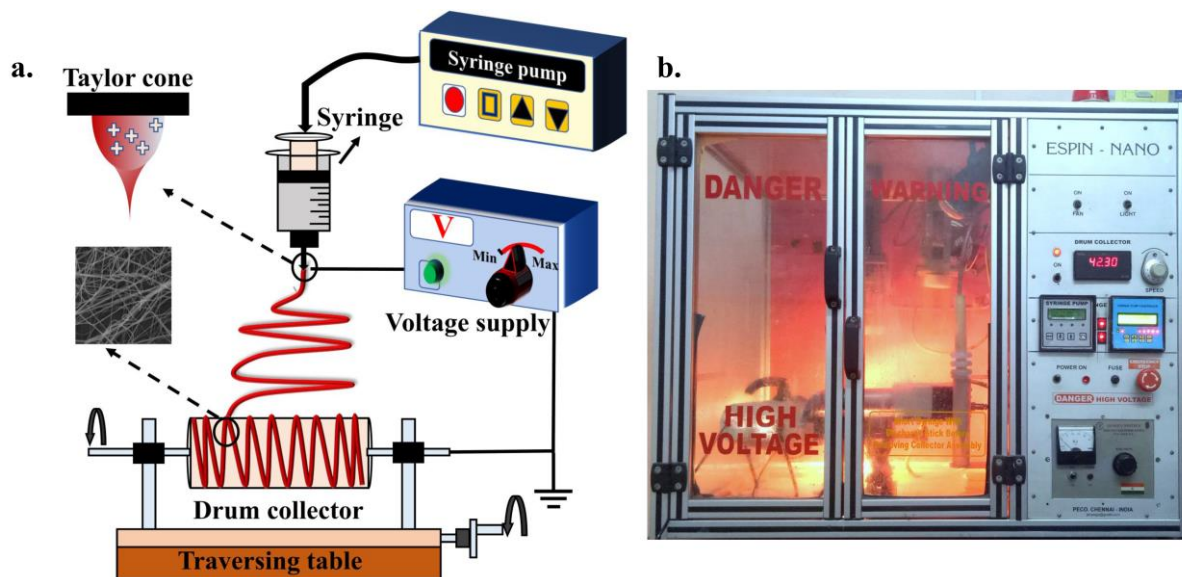


Fig 1.5. a). Schematic representation of electrospinning Process b). Digital photograph of electrospinning equipment.

The viscosity is also affected by the molecular weight of the polymer that represents the length of the polymer chain. The length of the polymer chain determines the entanglements in the polymer solution. Also, higher viscosity makes it difficult for the pump to push the solution out of the spinneret (Nurwaha et al. 2013; Abbasipour et al. 2017).

The electric charges present in the polymer solution must be sufficient to overcome the surface tension of the solution. When the droplet is stretched to form a fiber, the surface tension of the solution may tend to break the droplets, which may lead to the electrospaying rather than electrospinning (Beachley and Wen 2009; Edmondson 2013). Hence, selection of solvent is crucial; solvents such as dimethylformamide (DMF), dimethyl sulfoxide (DMSO) are preferred because of their high dielectric constants (Subbiah et al. 2005; Yang et al. 2006).

Distance between the spinneret tip and collector (TCD) affects the diameter and morphology of nanofibers. Optimum TCD is necessary for appropriate stretching of fibers and allow sufficient time for the solvent to evaporate completely. If the distance is too close, the solvent may not evaporate and result in thicker fibers. Higher TCD deteriorates the electric field and results in weak of electrostatic forces. (Haghi 2009; Motamedi et al. 2017). In addition, the voltage applied during electrospinning process has a strong influence on the diameter and morphology of nanofibers. The fiber is formed only when the voltage potential exceeds the threshold voltage. (Doshi and Reneker 1993). The feed rate of the polymer solution is another process parameter that affects the jet velocity and transfer rate. The diameter and porosity of the fibers can be tuned by optimizing the feed rate of the polymer solution (Thompson et al. 2007).

Humidity and temperature during the process affect the fiber structure and morphology. At a relative humidity higher than 60%, it is often seen that the evaporation of solvent is incomplete and the fibers entangle on the collector surface, while the temperature affects the evaporation rate and viscosity of the solution. Improper evaporation of solvent may lead to the fusing of fibers and influences the jet thinning and phase separation (Supaphol et al. 2005; Okutan et al. 2014). The collector should possess sufficient conductivity for collection of fibers. Therefore, conductive foils (aluminium) or carbon clothes are grounded that creates electrostatic field effect. Also, the fiber diameter, orientation, morphology and porosity of fibers are dependent on the type of collector. Rotating drum or circular disks yield aligned and uniform fibers while, static collectors yield randomly oriented fibers (Vonch et al. 2007; Li and Wang 2013; Nurwaha et al. 2013).

Recently, electrospun nanofibers received significant attention in the field of scaffolds, sensors, actuators, battery, biomedical, wound healing, catalyst, filtration membrane, energy harvesting, supercapacitors etc. Electrospun nanofibers can be used as tissue scaffolds that help in growth of cells and their proliferation. Cells seeded inside nanofibers can be implanted to a patient's body for the restoration of injured tissues. Nanofibers are incorporated with drug components could be used as capsule that carries the drug through the digestive system. Due to the high surface area of nanofibers, bacteria, dust, moisture can be filtered at the nanoscale. Further, modified nanofibers can be used to kill germs and bacteria (Hu and Tan 2017).

Nanofibers for the detection of harmful gases are also becoming a reality because of their durability, high surface area and flexibility. Also, electrospun nanofibers can be seen as an ideal reinforcing material, because of their ability to transfer stresses (Paul 2005; Haghgi 2009; Thenmozhi et al. 2017). Electrospun nanofibers in the field of lithium and sodium ion batteries have attracted attention of researchers because of their high surface area, porosity, high ionic conductivity, and cycle performance. Components such as anode, cathode and a separator made of electrospinning process have been explored widely. Recently, electrospun nanofibers have shown their potential in many more applications such as solar cells, protective filters, agricultural and energy sectors, etc (Sun et al. 2016).

PVDF is considered to be the most versatile polymer due to its high piezoelectric coefficient, mechanical and thermal stability and has widely been used in strain sensing, pressure sensing, energy harvesting and health monitoring application. Aforesaid, β -phase of PVDF is responsible for the piezoelectric effect and there are various routes to obtain the same. Among them, electrospinning is considered to be the best technique for the improvement of the β -phase of PVDF. Electrospun PVDF nanofibers do not require post-processing such as uniaxial stretching, annealing or poling, which is necessary for most of the methods. In fact, the average piezoelectric conversion efficiency of electrospun nanofibers is as high as 12.5-21.8% which is much higher than the conversion efficiency of PVDF films (~1.3%) (Ohigashi 1985; Richardson 1989; Chang et al. 2009b).

Unlike other techniques, electrospinning is one step process in which simultaneous electrical poling and stretching help in developing piezoelectricity in PVDF (Martins et al. 2014). PVDF nanofibers based piezoelectric sensors are envisaged to have the potential in real-time applications such as robots, aircraft, self-powered electronic devices and energy harvesting. PVDF nanofibers are capable of harvesting and storing energy, which could be used to run small electronic devices to power themselves indefinitely without the aid of external power sources. Also, mechanical energy gathered from human body motions can be used in self-powered pacemakers.

Most importantly, the production of electrospun PVDF nanofibers can be carried out at an industrial scale. There are three electrospinning techniques (solution spinning, melt spinning and emulsion spinning) that are commonly used in the production of nanofibers at a large scale. Melt spinning is usually preferred over the other methods because of the solvent-free synthesis process (Chang et al. 2012; Persano et al. 2013; Shi et al. 2015; Cardoso et al. 2018).

Uniform, long, continuous, aligned, defect-free and small fiber diameter is ideal for high piezoelectric performance of PVDF. However, to achieve all these characteristics simultaneously

is very difficult. Aligned and defect free nanofibers can be obtained at a higher solution concentration of PVDF, but thicker fibers are obtained that is detrimental for the piezoelectric performance. The diameter of PVDF nanofibers can be controlled by increasing the TCD, voltage and rotating drum speed (Shao et al. 2015a; Thakur et al. 2017).

1.1.4. Gel polymer electrolytes

A battery is a device that converts chemical energy into electricity by producing electrons through electrochemical reactions. Since the first lithium-ion batteries (LIB's) became commercially available, LIB's caught attention and became one of the primary power sources for electronic devices. Among different varieties of batteries, LIB is one of the most dynamic entrants due to high-power density, long cycle life and finds their usage at a larger scale ranging from a nano-electronic device to hybrid vehicles. A LIB consists of four major components, anode, cathode, separator and electrolyte (Fig.1.6). The anode and cathode store the lithium. A separator is placed between the anode and the cathode that prevents the electrodes from physical contact and enables ion transport. The electrolyte carries the ions from the positive terminal to negative terminals and vice versa through the separator. The movement of the lithium ions from one component to the other creates electrons in the anode that produces a charge at the current collector (positive) then through the load it flows towards the negative current collector. When the battery is in use the anode releases ions to the cathode, making the electrons to move from one side to the other. While charging, the ions are released by the cathode and flow towards the anode (Deng 2015; Jiang and Zhang 2015).

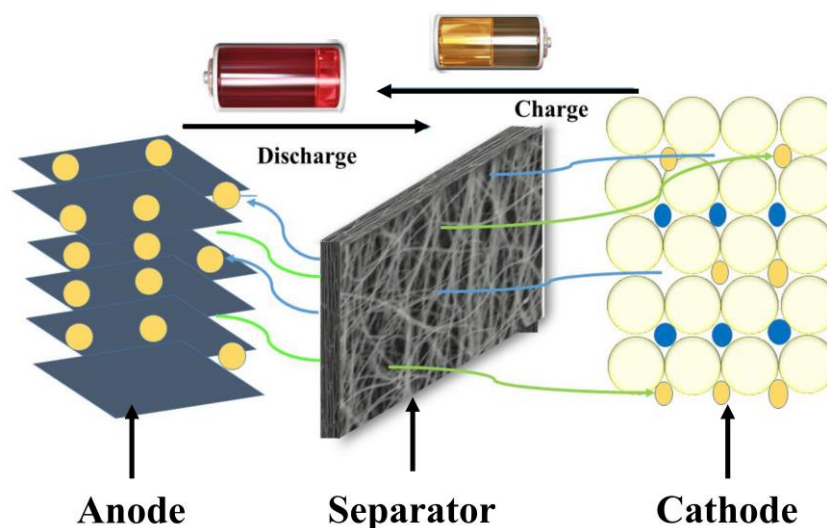


Fig. 1.6. A schematic representing components of LIB.

In the recent decade, a tremendous development is seen in the battery technology by optimizing the performance of individual components or by new battery chemistries. However, still no battery has been fabricated that gives an ideal and optimum performance under all the environments. The main advantage of LIB is that it can store a large amount of energy in a lighter and smaller space. However, the main limitation of LIB's is their lower efficiency and longer time to charge than other batteries. Much research is focused on nanotechnology to make the LIB is a highly efficient, lighter and more reliable (Wu et al. 2015b).

The separator is an essential component in a battery. Aforesaid, it prevents the battery from short circuit and enables the flow of ions from one terminal to the other. A separator is made of thin polymer membranes that are chemically, electrochemically and mechanically stable. In the 1970s the innovative idea of Wright and Armand on polymer electrolytes have made the LIB as one of the potential sources of electricity. Polymer electrolytes prevent battery from leakage of electrolyte and enable high energy and power density with safety features. Structurally, the separator should possess high surface area and porosity to absorb the electrolyte. However, separator adds up to the electrical resistance and size of the battery. Hence, the selection of the separator and its dimensions are very critical to the performance of the battery. Higher thickness of the separator improves the safety features of the battery, however; the movement of ions is hindered. Thin separator with high porosity provides better ionic conductivity and power density, but there are chances of explosion of the battery due to short circuit. Another problem associated with battery is overheating and structural failure. Additional features such as wettability, thermal shrinkage, dimensional stability, mechanical stability, pore size, cost, permeability need to be taken care. Currently, much attention is dedicated to nanostructured materials synthesized by different routes and methods such as chemical vapor deposition, wet chemical synthesis, sol-gel template, molten salt technique, electrospinning etc. Among them, electrospinning is seen to be the most versatile one as it takes care of the most of the features of the separator (Costa et al. 2013b). Commercially used separator in LIB's is made up of polypropylene or polyethylene microporous membranes, which has limitations such as lower porosity, poor thermal stability and inevitably lower efficiency. Separators made of electrospun nanofibers are advantageous because of their high porosity, thermal stability, ionic conductivity and mechanical strength.

Separators made of PVDF nanofibers are seen to benefit the electrochemical performance of the battery. At higher temperature, PVDF fibers tend to soften and form an interconnected web structure, which could significantly improve the physical properties. However, PVDF nanofibers exhibit inferior thermal stability, lower strength and hydrophobic nature and it is a difficult task to optimize all the properties and characteristics simultaneously. Hence, PVDF nanofibers are

prepared in the form of nanocomposites, blends, etc to optimize most of the properties in a separator (Stephan 2006; Zhang 2007; Kumar and Dek 2010; Long et al. 2016).

1.1.5. Chemi-resistive gas sensors

A chemi-resistive gas sensor is a device that changes its electrical properties when it comes in contact with gas molecules. The performance of a gas sensor is dependent on sensitivity, durability, reproducibility, stability, detection limits, and response and recovery times. Various materials such as zinc oxide (ZnO), carbon nanotubes (CNT), graphene, tin oxide (SnO₂), nickel oxide (NiO), etc. have been studied for the detection of gas molecules (Wang et al. 2004, 2009; Qureshi et al. 2009; Senthil and Anandhan 2014; Yang et al. 2016a). Metal oxide-based gas sensors are of relatively low cost and highly sensitive. However, these materials show poor sensitivity and long recovery periods at room temperature, which limits applicability. For improved performance, metal oxide-based gas sensors are operated at high temperatures, which in turn increases the operating cost and poses maintenance issues. To overcome these issues various strategies have been exploited by choosing a proper selection of materials, fabrication techniques and optimized geometry of the gas sensor (Varghese et al. 2015; Yang et al. 2016b).

Two dimensional (2D) layered materials have tremendous potential in sensing because of their unique chemical and physical properties. 2D layered structures are relatively lighter in weight, possess high surface area with superior surface activities and can be used at room temperature (Yang et al. 2016b). Various 2D layered structures have been explored as gas sensing material such as molybdenum disulfide (MoS₂) (Shokri and Salami 2016), graphene (Novikov et al. 2016), black phosphorus (Donarelli et al. 2016), boron nitride (BN) (Sajjad and Feng 2014), tin disulfide (SnS₂) (Ou et al. 2015). Graphene is an extensively studied material for gas sensing application, however, reports suggest that graphene has poor gas sensitivity and recovery characteristics, which limits its use in gas sensors (Zhang et al. 2017).

One dimensional structured material in the form of nanofibers, nanorods, nanotubes, nanoribbons, etc., have been reported as a gas sensing material that possesses high sensitivity. Among them, nanofibers with higher aspect ratio exhibit a high performance by providing high surface area and porosity. Nanofibers consisting of polyelectrolytes, conducting polymer, metal oxide fillers, and semiconductors have been used in gas sensing based on resistive, acoustic, photoelectric and optic techniques. The reports suggest that nanofiber-based sensor offers higher sensitivity, quicker response and faster recovery. So far, many attempts have been carried out to detect gases such as ammonia, nitrogen dioxide, carbon dioxide, carbon monoxide, ethanol vapors, toluene vapors etc., (Ding et al. 2009a, 2010; Arafat et al. 2012). Various conducting polymers

such as polyaniline (PANi), polypyrrene, polythiophene etc., have been used for gas sensing. PANi is considered to be the most attractive conducting polymer in gas sensing application. PANi based electrospun nanocomposite fibers have synthesized for gas sensing that showed better performance and stability that could replace thin film sensors (Ji et al. 2008; Low et al. 2014; Rozemarie et al. 2017). In addition, scaling up for mass production is possible through electrospinning making them an essential tool for gas sensing application.

1.2. REVIEW OF LITERATURE

1.2.1. Review on piezoelectricity of PVDF

PVDF is of particular interest, because of its flexibility, ferroelectricity, piezoelectricity and pyroelectricity. In 1969, Kawai discovered the presence of a piezoelectric effect in PVDF film and found its piezoelectric coefficient to be higher than that of other polymers. The influence of uniaxial stretching and poling on the piezoelectric properties of PVDF films were investigated. The films were stretched seven times to their original length to exhibit high piezoelectric effect (Fukada and Sakurai 1970). In 1975, Oshiki and Fukada investigated the piezoelectric stress and electrostriction coefficients for poled PVDF films. With the cyclic alteration in D.C electric bias field, the piezoelectric coefficient showed hysteresis. PVDF dipoles orient along the direction of electric poling and thus producing a polarization allied with the residual stresses (Oshiki and Fukada 1975). Stretching ratio of PVDF films directly affects the β -phase formation. With an increase in stretching ratio the β -phase of PVDF increases up to the stretching ratio of 4.0-4.5%; with further increase in the stretching ratio, a decline in the same was observed. Also, the β -phase increases with an increase in temperature of the film up to 80-90 °C during the stretching of PVDF (Crecorio and Cestari 1994; Salimi and Yousefi 2003b).

Since then a tremendous development is seen in understanding and improving the piezoelectricity, pyroelectricity and ferroelectricity of PVDF. The electroactive phases of PVDF can also be improved by the addition of suitable nanofiller that act as a nucleating agent (Fukada and Furukawa 1981; Murayama and Obara 1983; Yang and Thomas 1984). Upon the addition of reduced graphene oxide (rGO), the spherulite size of PVDF decreased attributing to the increase of heterogeneous nucleation sites. Uniaxially stretched PVDF/rGO films (400%) exhibited higher voltage output (293%) compared to pure PVDF films (Alamusi et al. 2012). Seoul et.al (2003), Gupta and Wilkes (2003), Choi et.al (2003) were among the first to present PVDF nanofibers with piezoelectric, pyroelectric and ferroelectric properties (Choi et al. 2003; Gupta and Wilkes 2003; Seoul et al. 2003).

The effect of solution concentration, type of solvent, viscosity and solution conductivity on the morphology of PVDF nanofibers were investigated. The solvent and PVDF concentration were the essential factors that significantly affect the morphology of PVDF nanofibers, which in turn affected the β -phase formation (Zhao et al. 2005). Yee et al. (2007) investigated the polymorphism and molecular orientation of PVDF nanofibers. The synergistic use of electrospinning and DMF/acetone mixture resulted in the induction of β -phase of PVDF while, α and γ -phase were induced in spin-coated samples. Crystallites were seen to be oriented along the fiber axis when the fibers were oriented (Yee et al. 2007). Electrospun PVDF nanofiber non-woven webs displayed excellent stability and flexibility with an energy conversion efficiency of $\sim 13.5\%$ (Fang et al. 2011). Well-aligned fibers exhibit better piezoelectric response than randomly arranged nanofibers, which is attributed to the alignment of dipoles along the fiber axis (Tao et al. 2013; Zampetti et al. 2014; Lee et al. 2016; Gee et al. 2018; Jiyong et al. 2018). A robust and interconnected PVDF nanofibers were fabricated using near-field electrospinning technique showed β -phase content over 80% and piezoelectric voltage and current up to 2.55 V and 2.9 μA (Shao et al. 2015a). Repeated stretching of electrospun PVDF nanogenerator generated a voltage and current output of 1.5 V and 400 nA, respectively and demonstrated its applicability by generating voltage against human respiration, voice recognition and muscle movement (Liu et al. 2017).

Electrospun PVDF/MWCNT nanofiber membrane showed significant improvement in the β -phase content of PVDF ($>90\%$) and enhanced the piezoelectric properties of PVDF (Ahn et al. 2013a). Addition of nano-clay significantly increased the spinnability of PVDF fibers, which is attributed to presence of surface charges clay on surface. In addition, the synergistic effect of electrospinning and nano clay improved the β -phase of PVDF (Yu and Cebce 2009a). The oxygen atom of clay and CH_2 group of PVDF forms a dipole-dipole interaction and the hydrogen bonding between fluorine atom of PVDF and hydroxyl group of clay helps in the formation of long polar chains (Wang and Huang 2014a). The presence of PANi and BaTiO_3 in the PVDF matrix significantly improved the piezo sensitivity at a very low poling voltage. The poling of hybrid composites enhanced the piezoelectric coefficient (d_{33}) from ~ 3.5 to ~ 50 pC/N (Patil et al. 2007).

It is imperative to choose appropriate fillers and processing technique for improving the piezoelectric properties of PVDF nanofibers. Incorporation of BaTiO_3 particles in PVDF nanofibers showed reduced power output compared to pure electrospun PVDF nanofibers due to decreased ductility (Nunes-Pereira et al. 2013). In another study, the presence of BaTiO_3 in PVDF films prepared by hot extrusion technique, showed a high piezoelectric response (Kakimoto et al.

2013). Also, high energy ball milling of PVDF/BaTiO₃ nanocomposite showed high voltage output and better reproducibility upon imparting pressure by tapping mode (Olmos et al. 2013). A hybrid piezoelectric nanogenerator consisting of PVDF and ZnO nanowire layers was fabricated for a wearable device. Both inner core ZnO nanowires and PVDF (outer shell) served as the piezoelectric material. By attaching the nanogenerator to different parts of the human body, the nanogenerator produced 0.1V, 10 nA.cm⁻² and 16 μW.cm⁻³ of voltage, current density and power density, respectively (Lee et al. 2012).

Unpoled PVDF/rGO nanocomposite film prepared by solution cast process favors the formation of γ -phase in PVDF. In an open circuit, maximum voltage and current up to 5.1 V and 0.25 μA were generated, respectively under periodic tapping. The improvement in piezoelectric performance may be attributed to the strong interaction between CH₂ and CF₂ groups of PVDF and delocalized π -electrons and oxygen atoms of rGO (Mandal 2015). A sound absorbing material based on the electrospun PVDF/CNT nanocomposite membrane was fabricated for energy conversion. The high surface area of electrospun nanofibers provides a large number of active sites to interact with sound waves to convert them into useful electrical potential (Wu and Chou 2016a). PVDF nanofibers doped with cobaltous chloride hexahydrate (CoCl₂·6H₂O) and ferrous chloride tetrahydrate (FeCl₂·4H₂O) salts showed significant improvement in the piezoelectric properties of PVDF nanogenerator. A maximum voltage output of ~12.5 V and a current output of ~300 nA were generated with FeCl₃·6H₂O doped PVDF nanofiber (Yu et al. 2017). Addition of tri-p-tolylamine (electron transfer) and 2-(4-tert-butylphenyl)-5-(4-biphenyl)-1,3,4-oxadiazole (hole transfer) to PVDF nanofiber improved the piezoelectric properties (2.1 V and 2.6 μA) (Shao et al. 2017). Electrospun hybrid PVDF/BaTiO₃/graphene nanogenerator displayed high piezoelectric response with good flexibility and durability. PVDF nanofibers composed of 15 wt% of BaTiO₃ and 0.15 wt% of graphene generated maximum voltage output of 11 V and power output up to 4.1 μW in an open circuit voltage under a frequency of 2Hz (Shi et al. 2018).

1.2.2. Review on PVDF as GPE

Gel polymer electrolytes (GPE) consisting of PVDF and its copolymer have been studied widely because of their high chemical and mechanical stability. In addition, the dimensional and thermal stability of PVDF averts the battery from internal short circuits. However, PVDF based GPE show low ionic conductivity because of its high crystallinity that hinders the mobility of lithium (Li⁺) ions. Batteries based on PVDF GPE display low capacity and poor charge rate values. On the other

hand, electrospinning of PVDF nanofiber GPE offer high porosity, interconnected network, large surface area and higher electrolyte uptake, that could be useful in improving the ionic conductivity. Electrospun PVDF membrane with $\text{LiPF}_6/\text{EC}/\text{DMC}$ electrolyte offered high porosity and interconnected structure, which led to the electrolyte being tightly held within the pores of PVDF that resulted in high electrolyte uptake, with improved physical and electrochemical properties (Choi et al. 2003, 2004; Kim et al. 2004).

A separator based on PVDF/polyethylene (PE) non-wovens provided high safety and mechanical strength necessary for high-performance GPE. PVDF nanofibers improved the ionic conductivity and electrochemical performance, while PE offered high mechanical and thermal stability. The separator was seen to be stable and maintained 86% of capacity after 100 cycles with the electrochemical stability of 4.5 V (Lee Min et al. 2005). Electrospun PVDF/polyacrylonitrile (PAN) blend exhibited electrolyte uptake of 300% and was electrochemically stable up to 5.1 V. Addition of PAN in PVDF nanofibers led to the higher ionic conductivity with reduced interfacial resistance. Pouch cell was fabricated with Li/PVDF- PAN/ LiCoO_2 and subjected to cycle tests. At a charge/discharge rate of 0.1 C, the specific capacity of 120 mAh^{-1} was achieved (Gopalan et al. 2008). The electrochemical performance of aligned and randomly arranged PVDF nanofibers was investigated. Randomly arranged nanofibers showed increased ionic conductivity ($4 \times 10^{-6} \text{ S.cm}^{-1}$) and electrochemical stability up to 5 V versus Li/Li^+ , while aligned fibers showed poor response. (Costa et al. 2013a).

Electrospun PVDF nanofibers were incorporated with SiO_2 nanoparticles to overcome the deficiencies of PVDF. The mechanical properties were improved significantly with the addition of SiO_2 particles. Also, the degree crystallinity of PVDF reduced considerably, which was attributed to the surface charges of SiO_2 contributing to the increase in the amorphous phase of PVDF as a result of β -nucleating activity. The increment in electrolyte uptake and a reduction in the degree of crystallinity synergistically enhanced the ionic conductivity of GPE (Kim et al. 2011; Zhang et al. 2014). Electrospun PVDF/PVC blend nanofibers offered high electrolyte uptake and ionic conductivity. The cycle performance of Li/PVDF-PVC/ LiFePO_4 cell was carried out at room temperature. The initial cycle showed a specific capacity of 145 mAhg^{-1} , which is relative ~85% of the theoretical efficiency (Zhong et al. 2012). Sandwiched structure of PVDF/poly(m-phenylene isophthalamide) (PMIA)/PVDF nanofibrous membrane displayed high mechanical and thermal stability. Furthermore, the Li/PVDF-PMIA-PVDF/ LiCoO_2 coin cell showed higher retention of capacity even after repeated cycling (Zhai et al. 2014).

Grafting of poly(methyl methacrylate) (PMMA) onto the surface of PVDF/SiO₂ nanofibers increased electrolyte uptake. Also, the membrane offered high ionic conductivity up to 2.3 mS.cm⁻¹ and tensile strength of 8.2 MPa. The coin cell assembled with Li/GPE/LiFePO₄ delivered a capacity of 156 mAhg⁻¹ and retained 97% of the initial capacity after 90 cycles (Yang et al. 2015). Use of nanofillers such as SiO₂, Al₂O₃ and nano clay with PVDF nanofibers contribute towards the high performance of GPE in LIB. First, use of nanofillers improve the morphology and reduce the fiber diameter that eventually improves the porosity and electrolyte uptake. Second, the reduced degree of crystallinity of PVDF improve the mobility of Li⁺ ions. Third, the hydrogen bonding between the hydroxyl group of clay and fluorine atom of LiPF₆ electrolyte help in the hindering of [PF₆]⁻ anions. In addition, the tensile properties and thermal stability of PVDF membrane improved significantly (Ma et al. 2016; Zhu et al. 2016; Bhute et al. 2017).

1.2.3. Review on PVDF nanofibers for gas sensing

PVDF offers good porosity, chemical and thermal stability, which are essential for gas sensing performance. PVDF/ Li-Ti *co*-doped NiO nanocomposites were fabricated by citrate gel technique to evaluate the gas sensing characteristics against ammonia (NH₃) gas. The sensor was sensitive to the concentration of gas molecules and working temperature. However the response of sensor decrease with increase in the temperature of the sensing environment (Qureshi et al. 2009). PVDF/carbon black (CB) composite film was synthesized to evaluate the gas sensing performance against acetone and tetrahydrofuran (THF) vapors. The composite was spray coated onto the surface of copper electrodes. The composite film was heat treated to improve its electrical properties. The sensor was selectively responding to acetone and THF vapors with quicker response and reproducibility. The response of the sensor increased when the composite film was heat-treated at 80 °C (Liu and Luo 2006).

Electrospun nanofibers could be useful in gas sensing because of their high surface area, porosity and active surfaces that are readily available for interacting with gas molecules. Various reports describe the use of electrospun nanofibers for gas sensing. The response of electrospun based gas sensors was evaluated against gases such as ethanol, acetone, THF, NH₃, NO₂ etc. PMMA/PANi blend nanofibers were synthesized by electrospinning technique for NH₃ gas sensing. The nanofibers responded quickly when exposed to NH₃ gas molecules at different concentrations (Jia et al. 2016). There are several reports on PVDF as energy harvester, GPE and gas sensor; but since the discussion on them will be beyond the scope of this thesis, a summary of some select applications is listed in Table 2. along with the technique and the fillers used in the process for the improvement of piezoelectric and electrochemical properties.

Table. 1.1. PVDF for piezoelectric energy harvesting application.

Filler/polymer	Technique	% β -phase	Voltage output (V)	Remarks	Reference
Nickel nanowires	Swift high irradiation/Electrodeposition			Piezoelectric efficiency up to 4.9%	(Melilli et al. 2018)
CaCl ₂	Electrospinning		0.89	CaCl ₂ salt showed better response than NaCl, KCl, FeCl ₃ , NiCl ₂ , CuCl ₂ and MgCl ₂	(Prasad et al. 2017)
	Electrospinning	~75-80	0.4	Voltage applied during spinning affected the β -phase content	(Sengupta et al. 2017b)
PVDF-TrFE	Spin coating (multilayers)		1.5	Power generated= 0.1 nW	(Toprak and Tigli 2018)
ZnO	Solution casting	~80	24.5	Self-charging characteristics	(Thakur et al. 2017)
Formamidinium lead halide perovskite nanoparticles	Solution casting		30	Energy conversion efficiency = 0.55%	(Ding et al. 2017)
MWCNT/graphene/MnO ₂ hybrid	Solution casting			Piezoelectric coefficient = 17-33 pC/N	(Yang et al. 2018b)
gallium ferrite nanoparticles	Solution casting		~4	Current output = 4 nA	(Mishra et al. 2018)
Graphene	Solvent-mediated	65		Piezoelectric coefficient = 5.2 pm/V	(Fortunato et al. 2017)
ZnO	Solution casting	76.1	1.81	Power density = 0.21 μ W/cm ⁻²	(Singh et al. 2018)

BaTiO ₃	3D printing	64	4	Piezoelectric coefficient = 18 pC/N	(Bodkhe et al. 2017)
barium nitrate, titanium dioxide, zirconium oxide	Hot press	~50		Piezoelectric coefficient = -45 pC/N	(Hemeda et al. 2017)
PVDF-HFP/Ni doped ZnO	Solution casting	51.1	1.3	Piezoelectric coefficient = -20 pC/N	(Parangusan et al. 2017)
Graphene	Solution cast & chemical vapor deposition		7.6	81.3 W/m ³ (Multi layers)	(Park et al. 2017)
MWCNT/Clay	Hot press	84.5		Piezoelectric coefficient = 0	(Yousefi 2011)
CNT	Electrospinning	70		Piezoelectric coefficient = 18.8 pC/N	(Wu and Chou 2016b)
	Solution casting		1.1	Power = 123 nW	(Tang and Li 2013)
Silver nanowires	Electrospinning	~55		Sensitivity = 30 pC/N	(Li et al. 2014)
MWCNT	Electrospinning	90		Remanent Polarization = 60.8 mC/m ²	(Ahn et al. 2013b)
Laponite	Solution casting	$\gamma = 98\%$	~6	Power density = 6.3 mW/cm ⁻²	(Rahman et al. 2017)
OMMT	Compression molding	81.7		Piezoelectric coefficient = 3.1 pC/N	(Yang et al. 2011)
MWCNT	Electrospinning		0.150	Tensile strength = ~48 MPa	(Liu et al. 2015)
Iron oxide	Solution casting	72.5		Piezoelectric coefficient = 37 pC/N	(Ouyang et al. 2015)
GO/Cu-Go/Au	Solution casting	$\gamma = 95$		Dielectric constant = 50	(Fakhri et al. 2016)

Table. 1.2. PVDF for Gel polymer electrolytes in LIB.

Material	Cathode type	Method	Electrolyte uptake (%)	Ionic conductivity (mS.cm⁻¹)	Tensile strength (MPa)	Initial capacity (mAh.g⁻¹)	Ref.
PVDF/ Glass fiber	LiNi _{1/3} Co _{1/3} Mn _{1/3} O ₂	Paper making process	59	1.2	13.1		(Huang and Hitt 2013)
PVDF	LiMn ₂ O ₄	Electrospinning	~145		14.3		(Hwang et al. 2011a)
PVDF/PMMA	LiFePO ₄	Electrospinning	377	1.9	~8		(Ding et al. 2009b)
PVDF-PEMA		Solution cast			0.15		(Sivakumar et al. 2007)
PVDF/ Al ₂ O ₃	LiMn ₂ O ₄	Electrospinning & dip coating	152.4		2.4	~114	(Wu et al. 2017)
PVDF/ Glass fiber	LiFePO ₄	Solution cast and coating	132	1.1	14.3	~118	(Zhu et al. 2013)
PVDF	LiCoO ₂	Electrospinning	~400	1	7.5	~135	(Choi et al. 2007)
PVDF/ Microfiber	LiFePO ₄	Coating	~120	0.65	9.1	~141	(Hao et al. 2014)
PVDF		Electrospinning	260	1.7			(Li et al. 2011)
PVDF/Polyurethane/PS	LiFePO ₄	Electrospinning	280	5.4	12.8	~170	(Tang et al. 2015)
PVDF/Polyimide	LiCoO ₂	Electrospinning	427	1.3		141	(Park et al. 2016)
polyethylene terephthalate/PVDF	LiMn ₂ O ₄	Electrospinning	124	8.3	34.5	112.5	(Wu et al. 2015a)

PVDF/PMMA	LiClO ₄	Electrospinning	285				(Mahant et al. 2015b)
PVDF/TiO ₂	LiFePO ₄	Electrospinning	367	1.4		143	(Ding et al. 2008)
PP coated PVDF/SiO ₂	LiFePO ₄	Electrospinning & Coating	291	2.6	3.9	163	(Yanilmaz et al. 2013)
Lanthanum oxide/PVDF-HFP		Electrospinning	621	1.4			(Wootthikanokhan et al. 2015)
PVDF-g-PMMAS	LiFePO ₄	Electrospinning		1.4		~133	(Lee and Liu 2017)
PVDF/polyethylene oxide	LiFePO ₄	Electrospinning	527		6.5	150	(La Monaca et al. 2017)
PVDF/PMMA	LiFePO ₄	Electrospinning	290	1.5		150.3	(Mahant et al. 2018)
PVDF/TPU/PAN	LiFePO ₄	Electrospinning	311	6.9		168	(Liu et al. 2017)
PVDF/PAN	LiFePO ₄	Molding	289	2	1.5	148.5	(Wu et al. 2016)
Fly ash/PVDF/PAN		Solution cast	409	2.8	14.5		(Maulana et al. 2016)
PVDF/ZnO	LiFePO ₄	Solution cast	689	9		126	(Endah et al. 2018)

1.3. Problem Identification

Among all the piezoelectric materials, ceramic-based piezoelectric materials are widely used for sensor applications, but they are brittle and stiff and are difficult to attach on the curved surfaces. Piezoelectric polymers have flexibility and can be bound to the complex surfaces covering the large surface area. Poly(vinylidene fluoride) (PVDF) is a specialty polymer known for its ferroelectric and piezoelectric properties. Compared to other polymers, PVDF has the highest piezoelectric and pyroelectric coefficients. However, the response is low compared to the properties of ceramic materials because of its low electroactive phase content. This difficulty can be surmounted by the addition of nucleating agents or piezo-ceramic particles. PVDF films are flexible, lightweight and can be made into different shapes and sizes. It has excellent sensitivity, low density and also mechanically tough. In addition, the compliance of PVDF nanofibers is much greater than that of ceramic-based piezoelectric materials and are better suited for sensing applications. By improving the piezoelectric characteristics, makes PVDF more attractive material for sensor and actuator applications. Also, PVDF with high surface area and porosity could also be useful as gel polymer electrolytes in lithium-ion batteries and gas sensors.

1.4. SCOPE AND OBJECTIVES OF PRESENT WORK

1.4.1. Scope

PVDF has represented itself as a radical alternative to the piezoceramics because of its flexibility and ferroelectric properties. Recent research confirmed the utility of nanofillers such as graphene, carbon nanotubes, clay, etc., enhance the piezoelectric properties of PVDF. Electrospinning is one of the simplest and most effective technique to form electroactive phases of PVDF. Synergistic effect of electrospinning and nanofillers significantly reduces the degree of crystallinity and provides high surface area and porosity, which makes it suitable for a separator in LIB and gas sensing applications. This work aimed to develop high-performance electrospun PVDF based nanocomposites for piezoelectric energy harvesting, force-sensor, separator in battery and gas sensor.

1.4.2. Objectives

- 1) To optimize the electrospinning conditions for poly(vinylidene fluoride) (PVDF).
- 2) Synthesis of electrospun PVDF/ halloysite nanotubes (HNT) nanocomposite.
- 3) Synthesis of electrospun PVDF/HNT/Polyaniline (PANi) blend nanocomposite.
- 4) Synthesis of electrospun PVDF/graphitic-carbon nitride (g-C₃N₄) nanocomposite.
- 5) Synthesis of electrospun PVDF/g-C₃N₄/PANi blend nanocomposite.
- 6) To characterize the above-mentioned nanofibers through wide-angle x-ray diffraction (WAXD), Scanning electron microscopy (SEM), Fourier transform infrared (FTIR) spectroscopy, Thermogravimetric analysis (TGA), Differential scanning calorimetry (DSC) and Transmission electron microscopy (TEM).
- 7) To explore suitable application for electrospun non-wovens of PVDF nanocomposites such as a piezoelectric sensor, gas sensor and batteries.

1.4.3. LAYOUT OF THE THESIS

The dissertation has nine chapters, which discuss the synthesis and characterization of electrospun nanocomposites of PVDF and various chosen functional nanofillers. Also, the results of various studies exploring the application potential of these systems have been discussed in detail.

Chapter 1 gives a brief introduction and literature review on electrospun PVDF nanofibers for various applications.

Chapter 2 gives detailed information on the materials, methodology, experimental setups and briefly discuss the characterization and testing carried out to study the various properties of electrospun PVDF nanofibers.

Chapter 3 discusses the synergism of electrospinning and HNT on the polymorphism, crystallinity, morphology and piezoelectric characteristics of electrospun PVDF/HNT nanocomposites.

Chapter 4 focuses on gel polymer electrolyte (GPE) based on electrospun PVDF/HNT nanocomposite was synthesized and its suitability as a separator in the lithium-ion battery (LIB) was explored.

Chapter 5 details the study on the polymorphism, crystallinity, morphology and piezoelectric performance of electrospun PVDF/HNT/PANi blend nanocomposite for energy harvesting application.

Chapter 6 focuses on the influence of g-C₃N₄ nanosheets on the physical and piezoelectric characteristics of electrospun PVDF nanocomposites for energy harvesting application.

Chapter 7 details the piezoelectric performance of PVDF/PANi/g-C₃N₄ blend nanocomposite for energy harvesting application.

Chapter 8 details the fabrication and NO₂ gas sensing performance of flexible electrospun PVDF/PANi/g-C₃N₄ blend nanocomposite.

Chapter 9 Conclusions from the present study are summarized concisely.

CHAPTER 2
MATERIALS AND METHODS

CHAPTER 2

MATERIALS AND METHODS

This chapter discusses the details of materials used in the study for the synthesis of PVDF nanocomposites and also the evaluation of those nanocomposites for various applications. The preparation of the electrospinning solution, preparation of nanofillers such as polyaniline (PANi) nanorods and graphitic-carbon nitride nanosheets (g-C₃N₄) are discussed followed by a brief description of the characterization techniques used in this study.

2.1. MATERIALS USED

PVDF ($\bar{M}_w = 534,000$) was purchased from Alfa Aesar, Hyderabad, India. Another grade of PVDF (Solef 1015, Italy) ($\bar{M}_w = 575,000$) was purchased from Prakash chemicals, India. Dimethyl sulfoxide (DMSO) and dimethylformamide (DMF) of purity in excess of 99% was purchased from Central drug house, New Delhi, India. HNT was purchased from Sigma-Aldrich, Bangalore, India (product ID: 685445; Diameter: 30–70 nm and length: 1–3 μm). Ammonium peroxydisulfate (APS) of 98% purity was purchased from Merck, Mumbai, India. Aniline and hydrochloric acid were purchased from Molychem, Mumbai, India. Thiourea with 99% purity was obtained from Ranbaxy laboratories, India. Silver paste was purchased from Sigma Aldrich, Bangalore, India.

2.2. METHODOLOGY

In this study, electrospun PVDF nanocomposites were fabricated and characterized. The fibers were then explored for various applications such as piezoelectric force sensor, gel polymer electrolyte, energy harvesting and gas sensing application. Also, nanofillers such as polyaniline (PANi) and graphitic carbon nitride (g-C₃N₄) nanosheets were synthesized in our laboratory.

2.2.1. Synthesis of PANi nanorods

PANi was synthesized by solid-state synthesis. Prior to the synthesis of PANi nanorods, a mortar was precooled in an ice bath below 0°C. 2 mL of HCl (dopant) was put into mortar to which 2 mL of aniline was added slowly. After grinding for about 5 min, the mixture became a thick white paste. Then 4.4 g of APS (oxidant and initiator) was added to the mixture followed by 15 min of grinding. After 15 min of grinding, the mixture became dark green in color. It

was then washed and filtered with demineralized water until the solution became colorless. Finally, the mixture was dried in a vacuum oven at 70°C for 4 h.

g-C₃N₄/PANi nanocomposite (GPC) was prepared by the in-situ polymerization technique. Similar to the synthesis of PANi nanorods, once the mixture of HCl and aniline became a thick white paste, g-C₃N₄ nanosheets were added to the mixture followed by grinding the mixture for about 5-7 min. Then 4.4 g of APS was added to the mixture followed by 15 min of grinding. It was then washed and filtered with demineralized water until the solution became colorless. Finally, the mixture was dried in a vacuum oven at 50°C for 12 h.

2.2.2. Synthesis of g-C₃N₄ nanosheets

Bulk g-C₃N₄ was synthesized by a facile and efficient thermal decomposition technique. In a typical process, a given amount of thiourea was put into a semi-closed alumina crucible. The crucible was then heated to 550 °C in a muffle furnace at 5°/min for 3 h. The resultant powder was then cooled down to room temperature.

2.2.3. Electrospinning of HNT/PVDF Nanocomposite

18 w/v% solution of PVDF in DMSO was prepared. For the synthesis of electrospun PVDF/HNT nanocomposite (PHNF), HNT was added to the polymer solution at different loadings (0, 2.5, 5, 7.5, 10 and 20 wt. % based on the wt. of PVDF). HNT was suspended in DMSO by ultrasonication for one hour. The mixture was then loaded into a 10 mL syringe with (0.5 mm inner diameter) bevel edge needle. The pure PVDF solution and that containing HNT were electrospun under the following optimized conditions: solution flow rate: 0.5 mL/h; relative humidity: 55±3%; temperature: 32±2 °C; voltage: 20 kV; tip to collector distance: 20 cm. Several experiments were done for optimizing the electrospinning parameters to get bead-free and uniform nanofibers with smaller average fiber diameter (Section. I.1). For producing aligned fibers, an aluminum foil-wrapped rotating drum collector (2000 rpm) was used. A vertical electrospinning setup (e-spin Nano, Physics Equipment Co., Chennai, India) was used. For the comparison study, solution cast PVDF film was prepared (Section. I.2).

2.2.4. Electrospinning of PANi/HNT/PVDF blend nanocomposites

To prepare the electrospinning solution, 13 w/v% of PVDF in powder form was dissolved in 85:15 mixture of DMF and acetone. For the preparation of nanofibers from PVDF/PANi blend (PPNF) and PHNF nanocomposites, the dispersions of the respective additives were added to

the PVDF solution. Prior to the addition, PANi and HNT were dried in a vacuum oven at 35 and 75 °C, respectively for 3 h. PANi and HNT were ultrasonicated in DMF for 3 h at 25 °C and these dispersions were added to the PVDF solution and stirred for 4 h. 17.5 wt% of PANi and 10 wt% HNT (on the basis of weight of PVDF) were used for the preparation of PPNF and PHNF, respectively. For the preparation of electrospun PVDF/HNT/PANi hybrid nanocomposites (BNCNF), HNT dispersion was added to PVDF solution followed by that of PANi and the mixture was stirred for 4 h. The mixture was loaded into a 10-mL syringe attached with 18-gauge beveled edge stainless steel needle. The following optimized electrospinning conditions were used to produce electrospun PVDF (E-PVDF), PPNF, PHNF, and BNCNF: solution feed rate: 0.8 mL/h; voltage: 22 kV; rotating drum collector speed: 1,500 rpm; spinneret tip to collector distance: 15 cm; relative humidity: 60%.

2.2.5. Fabrication of PANi/PVDF films

15 w/v % solution of PVDF in DMF: acetone (85:15 v/v) was prepared to which PANi was added. PVDF/PANi blend films were prepared by solution cast process with different PANi loading (5, 10, 15, 17.5, 20 and 25 wt.% based on the weight of PVDF). For, uniform dispersion specific amount PANi was added to DMF and ultrasonicated for 3 h. Once the PVDF was completely dissolved, PANi dispersion was added to it and the mixture was stirred for 4h. This mixture was then poured into a clean petri dish and left to dry for 48 h. The dried film was then kept in a vacuum oven at 50 °C for 6 h to eliminate the traces of solvent. PANi was made into a thin wafer using a hydraulic press for the measurement of its electrical conductivity.

2.2.6. Synthesis of electrospun PVDF/ g-C₃N₄ nanocomposites (PGN)

Electrospinning solution of PVDF was prepared with different loadings of g-C₃N₄ (0.25, 0.5, 0.75, 1.0 and 2.0 wt% based on the weight of PVDF). 12.5 w/v% solution of PVDF in DMF was prepared and stirred at room temperature. To the PVDF solution, the dispersion of g-C₃N₄ in DMF containing the predetermined amount was added and vigorously stirred for 4 h. All the solutions were processed into fibers at a constant feed rate of 0.8 mL/h and a voltage of 20 kV on the syringe needle and rotating drum collector speed was 1400 rpm kept at a distance of 15 cm from the tip of the needle. The fibers were spun at 30 ± 2 °C and 45± 2% relative humidity. In this study, electrospun g-C₃N₄/PVDF nanocomposite fibers were denoted as PGN-X where, X may be 0.25, 0.5, 0.75, 1.0 or 2.0.

2.2.7. Synthesis of electrospun of PVDF/GPC nanocomposite

For the preparation of electrospun PVDF/GPC blend nanocomposite (PPBF) for energy harvesting application, 20 wt% of GPC-5.0, GPC-7.5 or GPC-10 dispersed in DMF, added to completely dissolved PVDF solution and stirred it for 4 h at 30 ± 2 °C. The optimized conditions of E-PVDF are; solution concentration: 13.5 w/v% in DMF; applied voltage: 18 KV; tip to collector distance: 15 cm; feed rate: 0.6 mL/h; relative humidity: $55 \pm 3\%$, drum collector speed: 1500 rpm. The obtained webs were denoted as E-PVDF and PPBF-X, where X may be 5.0, 7.5 and 10 representing the loading of g-C₃N₄ nanosheets in GPC.

On the other hand, 10 wt/v% of PVDF was dissolved in 90:10 mixtures of DMF: acetone and 25 wt% of GPC-X (X may be 10, 20 or 30 wt% of g-C₃N₄ nanosheets) was added to the PVDF solution for gas sensing application.

2.3. MEASUREMENT AND CHARACTERIZATION

Morphological studies: Scanning electron microscopy (SEM) (JEOL, JSM 6380, Japan) was used to study the morphology of samples. A thin layer of gold was sputter coated onto the samples using auto fine sputtering unit (Jeol, JFM1600, Japan). Field emission scanning electron microscopy (FESEM) [Zeiss Merlin, Germany] and atomic force microscopy (AFM) [Agilent 5500, India] were used to investigate the morphology, and interaction of the electrolyte with nanofibers. AFM images were obtained in the tapping mode. The elemental and chemical composition of GPC samples were carried out by energy-dispersive X-ray (EDX) spectrum (Carl Zeiss, South Korea) attached with high-resolution scanning electron microscopy (HRSEM) (Carl Zeiss Co. Ltd, South Korea). The morphology of HNT, PANi nanorods, g-C₃N₄ and PANi/g-C₃N₄ nanocomposite (GPC) was investigated using transmission electron microscopy (TEM) (JEOL, JEM-2010, Japan). Homogenous dispersion of nanoparticles was prepared in ethanol. The dispersion consisted of 5 mg of nanoparticles in 20 mL ethanol and ultrasonicated for 4 h. The temperature during the ultrasonication was maintained below 20 °C. Using, micropipette, the ethanolic solution was coated onto carbon coated copper grid (200 mesh) and dried in a vacuum oven at 50 °C for 12 h. A transmission electron microscope (TEM) (JEOL JEM-2010, Japan) was used to image single nanofiber. Fibers were directly electrospun on a carbon coated 200 mesh copper grid for about 10s and dried in a vacuum oven at 40 °C for 24 h. The main aim of doing the TEM analysis was to observe the orientation of HNTs, PANi nanorods network etc in PVDF nanofibers and to determine the polymorphs of PVDF using selected area electron diffraction (SAED) patterns. Image-J tool (Fiji image-J, National institute of health, USA) was used for the analysis of

measurement of average fiber diameter (AFD). The diameter of an individual fiber was calculated by taking an average of three values measured. To measure the AFD, at least, 50 fiber diameters were obtained and then the standard deviation along with AFD was reported.

Fourier transform infrared (FTIR) spectroscopy: FTIR spectra (Jasco FTIR-4200, Japan) were acquired by KBr pellet method in the wavenumber range of 4000–400 cm^{-1} . In addition, spectra were also acquired by ATR mode in the wavenumber range of 4000–650 cm^{-1} . The spectra were carried out at an average of 32 scans in the at a spectral resolution of 1 cm^{-1} . β -phase content (F_β) of PVDF was calculated using the following equation:

$$F_\beta = \frac{A_\beta}{(1.26 A_\alpha + A_\beta)} \quad (2.1)$$

where, A_α and A_β , respectively correspond to the absorbance at 766 cm^{-1} (α -phase) and 840 cm^{-1} (β -phase), respectively. K_α and K_β are the absorbance coefficients for each phase at their respective wave number ($K_\alpha = 6.1 \times 10^{-4}$ and $K_\beta = 7.7 \times 10^{-4} \text{ cm}^2/\text{mole}$) (Mostafaei and Zolriasatein 2012b).

UV-Vis spectroscopy: The optical properties of PANi nanorods, g- C_3N_4 nanosheets and GPC samples were analyzed using UV-Vis NIR spectroscopy (Cary-5000, USA). The samples were analyzed in diffuse reflectance (DRS) mode in the wavelength range of 200-800 nm.

WAXD analysis: Wide angle X-ray diffraction (WAXD) (JEOL DX-GE-2P X-ray diffractometer, Japan and Rigaku 5th miniflex, USA) measurements were carried out to determine the degree of crystallinity, polymorphism and interactions between PVDF chains and nanofillers. Samples were scanned at a speed of 1° min^{-1} in the 2θ range of 10°– 40°. % crystallinity (X_c) of the nanofiber webs was calculated by the deconvolution method and the following equation was used in the calculation:

$$X_c = \frac{I_c}{I_c + I_a} \quad (2.2)$$

Where, I_c and I_a are the integrated intensities of crystalline and amorphous phase, respectively.

The following equation was used to obtained the interplanar distances (d):

$$d = \frac{\lambda}{2 \sin \theta} \quad (2.3)$$

Thermal analysis: Differential scanning calorimetric (DSC) analysis was carried out to study the crystallinity, melting point and heat of fusion of electrospun PVDF nanocomposite webs. About 5 mg of the samples were kept in hermetically sealed aluminum pans. DSC scans (822e - Mettler Toledo, USA) were done from 0 °C to 200 °C at a heating rate of 10 °C min^{-1} .

Nitrogen gas was purged through the furnace at a flow rate of 50 mL min⁻¹. The degree of crystallinity was calculated from the peak area using the following equation.

$$X_c = \frac{\Delta H_m}{\Delta H_m^*} \times 100 \quad (2.4)$$

Where, X_c = % crystallinity,

ΔH_m is the apparent enthalpy of fusion, J.g⁻¹.

ΔH_m^* = enthalpy of fusion/gram for 100% crystallinity, 104.5 Jg⁻¹.

To understand the thermal decomposition behaviors of the electrospun PVDF nanocomposite webs, thermogravimetric analysis (TGA) was carried out. Analyses were carried out at a heating rate of 10 °C min⁻¹ under nitrogen atmosphere at a flow rate of 50 mL min⁻¹. Around 5 mg of sample was used to perform the TG analysis (TGA Q5000 V3.10 Build 258; TA Instruments, New Castle, Delaware, USA).

Thermal shrinkage test was carried out to study the shrinkage of E-PVDF and PHNF samples for separator application. Samples were heated up to 130 °C for 4 h and 8 h at uniform heating rate.

Mechanical properties: The tensile test of electrospun webs were carried out using universal testing machine (UTM) [Shimadzu, AGX plus 100, Japan]. The test was carried out according to ASTM D882-12. Specimens were prepared in the form of a strip with 100 mm × 20 mm × 0.01 mm size and the test was carried out at 23 °C and 48 ± 3% relative humidity. The extension rate was kept constant at 5 mm/min.

The puncture test of E-PVDF and PHNF webs was performed using a UTM (Shimadzu, AGX plus 100, Japan) according to ASTM F1306. The dimensions of the specimen (7.5 cm × 4.0 cm × 0.0025 cm) were maintained uniform for all the samples. Tests were performed at 24 °C and 46 ± 3% relative humidity. The puncture strength was calculated using the following equation:

$$P_s = \frac{F}{t} \quad (2.5)$$

Where, 'P_s' is the puncture strength, 'F' is the maximum load in (N) and 't' is the thickness of the electrospun web(He et al. 2016).

Porosity and electrolyte uptake test: Using n-butanol uptake method, the % porosity of PVDF nanofiber webs was measured webs using the following equation:

$$\% \text{ porosity} = \frac{M_b / \rho_b}{M_b / \rho_b + M_m / \rho_m} \times 100 \quad (2.6)$$

Where, M_b and M_m are the mass of n-butanol swollen membrane and mass of dry membrane, respectively, ρ_m is the density of PVDF, and ρ_b is the density of n-butanol. To carry out the

test, accurately weighed pieces of E-PVDF and PHNF mats were immersed in n-butanol for 2 h. These mats were then taken out and wiped out with tissue paper to remove excess butanol from the webs. The weights of swollen mats were recorded. Three trials were done for pure PVDF and PHNF mats. In addition, the electrolyte uptakes were calculated by the formula:

$$Uptake (\%) = \frac{M_w - M_d}{M_d} \quad (2.7)$$

Where, M_w and M_d are the masses of swollen electrolyte membrane and dry membrane, respectively.

Electrochemical studies: Dried PHNF mat 0.7 cm radius and 25.6 μm thickness was immersed in 1M LiPF_6 in EC: DEC (1:1 vol.%) for 12 h. Fabrication of GPE was carried out in a glove box filled with argon at 25 °C. The ionic conductivities of GPE separators were measured using electrochemical workstation AC impedance spectroscopy (Hioki, 3532-50 LCR, Japan) at 25 °C. The cell was prepared by sandwiching the GPE between stainless steel electrodes and enclosed with CR2032 coin cell shell. Test was carried out over the frequency range of 50 Hz to 1 MHz at amplitude of 10 mV. Ionic conductivity of separators (σ) was calculated by measuring the bulk resistance using the equation:

$$\sigma = \frac{t}{R_s \times A} \quad (2.8)$$

Where, ' R_s ' is the bulk resistance of separator, 't' is the thickness of the nanofiber membrane and 'A' is the area of separator membrane.

The ionic transference number was determined by a combination of AC impedance and DC polarization techniques (Evans et al. 1987; Bruce et al. 1988). GPE was sandwiched between two lithium electrodes. The initial and steady state interfacial resistance was measured by electrochemical impedance spectroscopy. The initial and steady state currents were measured using a chronoamperometry measurement with a potential difference of 10mV. The lithium ion transference number (T^+) was calculated using the following equation:

$$T^+ = \frac{I_s(\Delta V - I_o R_o)}{I_o(\Delta V - I_s R_s)} \quad (2.9)$$

Where, I_o and I_s are initial and steady state current, respectively. R_o and R_s are initial and steady state interfacial resistance, respectively, ΔV is the DC voltage applied.

Electrochemical stability of separators was analyzed by linear sweep voltammetry (LSV). Lithium metal was used as a counter electrode and stainless steel was used as the working electrode (SS/GPE/Li) at a scanning rate of 10 mV s^{-1} over a potential range of 1 V to 7 V at 30 °C. CR2032 cell was fabricated to evaluate the electrochemical performance of Li/GPE/LiCoO₂ system. The charge-discharge behavior of cell was evaluated using high

precision automatic battery cycler (Arbin BT 2000, USA). The test was performed at a voltage range of 2.7 to 4.2 V at a constant current rate of 0.1 C for 50 cycles. In addition, the current-rate capability was measured at various current densities (0.1C, 0.2C, 0.5C & 1C).

2.4. SETUPS AND METHODOLOGY USED FOR THE APPLICATIONS OF ELECTROSPUN PVDF NANOCOMPOSITES

2.4.1. Piezoelectric evaluation setup

Fig. 2.1 shows the schematic illustration of the indigenous setup used to explore the potential of the electrospun PVDF nanocomposite webs for force sensor, pressure sensor and energy harvesting application. Electrospun nanofiber mat was sandwiched between two interdigitated copper electrodes ($3.0 \times 2.0 \times 0.01$ cm) [supplied by Lifeline circuits Pvt. Ltd., Hosur, India]. The electrodes were then covered with a flexible non-conducting sheet made of polyvinyl chloride. The copper wires were connected to digital oscilloscope [Analog discovery 2 USB, Digilent Inc., Pullman] via circuit board by using single strand wires.

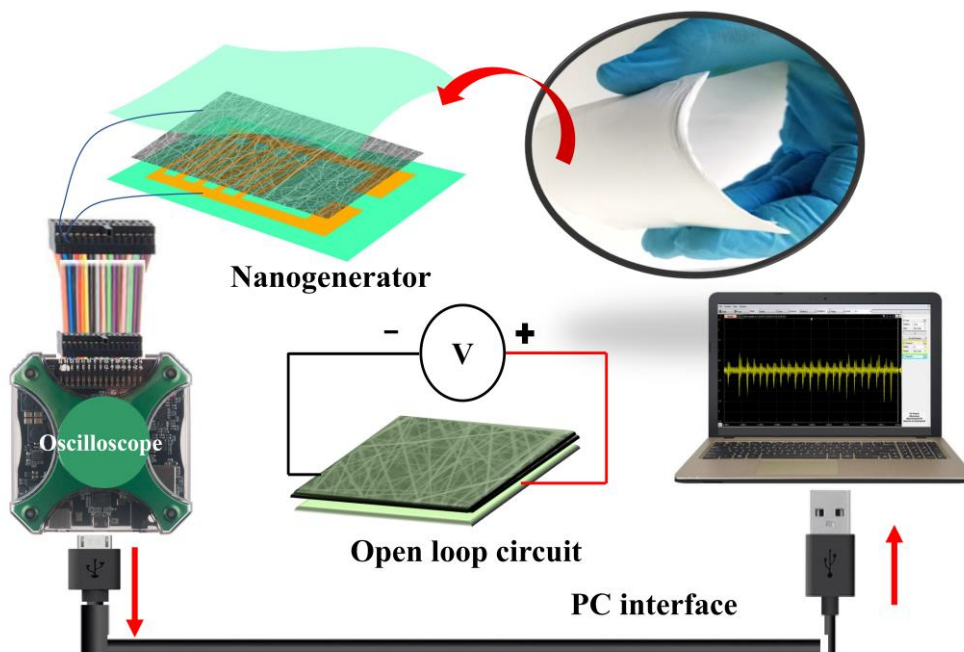


Fig. 2.1 schematic of the setup used in the piezoelectric evaluation.

2.4.2. Coin cell fabrication

Fig. 2.2 shows a schematic of the coin cell assembly of Li/PHNF/LiCoO₂ used to evaluate the charge-discharge performance. Prior to the fabrication, anode, cathode and separator were punched into a disc of 1.5 cm diameter. The assembly was carried out in the glove box. First, the springs were placed into the coin cell (CR2032) cases followed by the stainless-steel spacers. Then, two drops of electrolyte (LiPF₆/EC: DEC) was added on to the cell cup and then

the working electrode placed into the cases. Then, another three drops of electrolyte was added followed by the separator (PVDF, PHNF and Celgard®2400) with another few drops of electrolyte before putting the counter electrode into the casing. Then, two stainless steel spacers and gasket were placed onto the counter electrode and closed with a housing. The cell assembly was pressed using a compact crimping machine.

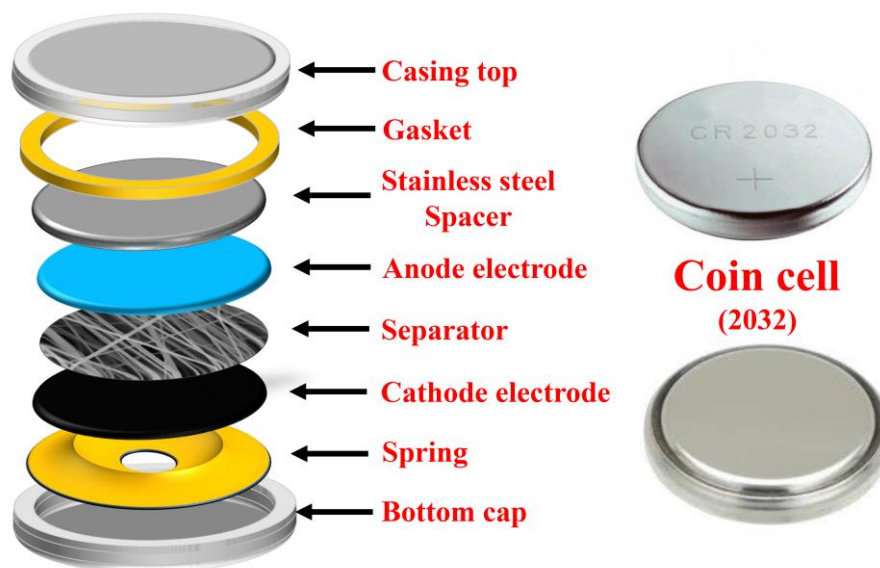


Fig. 2.2. Schematic diagram of the package assembly of the Li/PHNF/LiCoO₂ in a coin cell.

2.4.3. Gas sensing evaluation setup

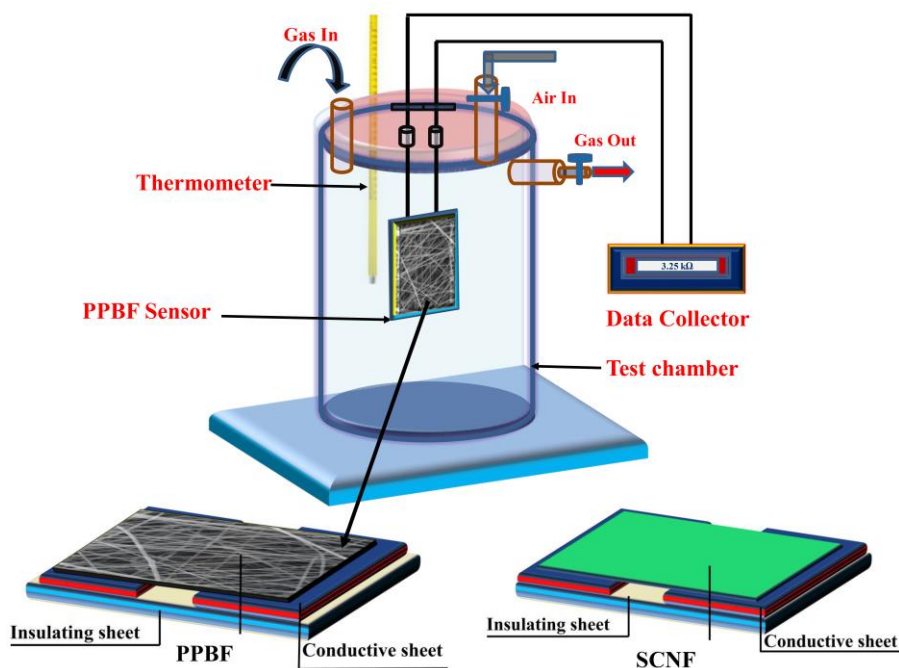


Fig. 2.3. Schematic of indigenously built gas sensing set-up used for the evaluation of the performance of PPBF sensor.

The performance of PPBF and solution cast PVDF/g-C₃N₄/PANi (SCNF) based sensor was studied using an indigenous setup (**Fig. 2.3**). In brief, the PPBF were directly spun onto the ITO coated PET sheet, while SCNF was coated on the ITO coated PET sheet (Sigma Aldrich, India) using doctor blade technique. The thickness of the samples was ~25 μm. Sensor was kept in a glass sealed chamber in which the sensor was exposed to NO₂ gas. Initially, the electrical resistance of sensor was measured in atmospheric air. NO₂ gas at different concentrations (9-108ppm) were injected into the test chamber through the inlet valve. The response of the sensor was determined as a function of the change in electrical resistance and measured using multifunctional digital multimeter (Meco meter. Ltd., Mumbai). After the test, the gases were evacuated to atmosphere through the outlet valve. Tests were carried out at 45 ± 3% relative humidity and 28 ± 3 °C and the response and recovery times were measured for each cycle. The response was taken as R_a/R_g , where, R_a and R_g are the electrical resistance of gas sensor in air and NO₂ atmosphere, respectively. At least three trials were carried out for each concentration. The sensitivity of gas sensor was measured using the equation $S = (R_g - R_a)/R_a$.

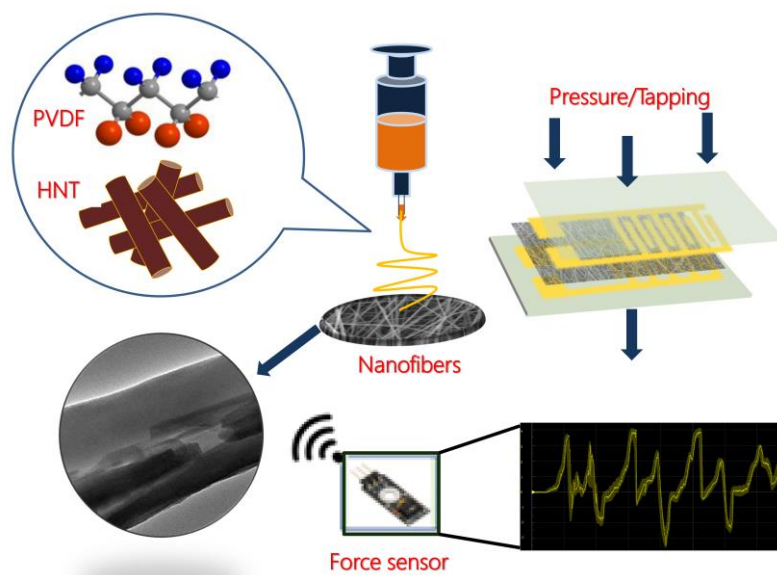
CHAPTER 3

PROBING THE SYNERGISM OF HALLOYSITE NANOTUBES AND ELECTROSPINNING ON CRYSTALLINITY, POLYMORPHISM AND PIEZOELECTRIC PERFORMANCE OF POLY(VINYLIDENE FLUORIDE)

The results of this chapter have been published in RSC advances, 2016; 6 (115), 114052-114060.

CHAPTER 3

PROBING THE SYNERGISM OF HALLOYSITE NANOTUBES AND ELECTROSPINNING ON CRYSTALLINITY, POLYMORPHISM AND PIEZOELECTRIC PERFORMANCE OF POLY(VINYLIDENE FLUORIDE)



This chapter discusses the fabrication of uniaxially aligned nanofibers developed from halloysite nanotubes (HNT)/PVDF nanocomposite (PHNF) using electrospinning technique. Fourier transform infrared spectroscopy, wide angle X-ray diffraction and differential scanning calorimetry techniques were used to characterize the crystallinity, polymorphism and polymer-filler interaction in the nanocomposite fibers. Thermal gravimetric analysis was carried out to study the thermal behavior. A force sensor was indigenously designed to study the piezoelectric responses of the nanocomposite fibers. Incorporation of HNT and use of electrospinning synergistically enhanced the β -phase content and hence the piezoelectric behavior of PVDF.

- In this study, electrospun PVDF fibers were denoted as E-PVDF, while, HNT/PVDF nanocomposite fibers were denoted as PHNF-X where, X may be 2.5, 5, 7.5, 10, 15 or 20 wt% (loading of HNT).

3.1.RESULTS AND DISCUSSION

3.1.1. SEM results

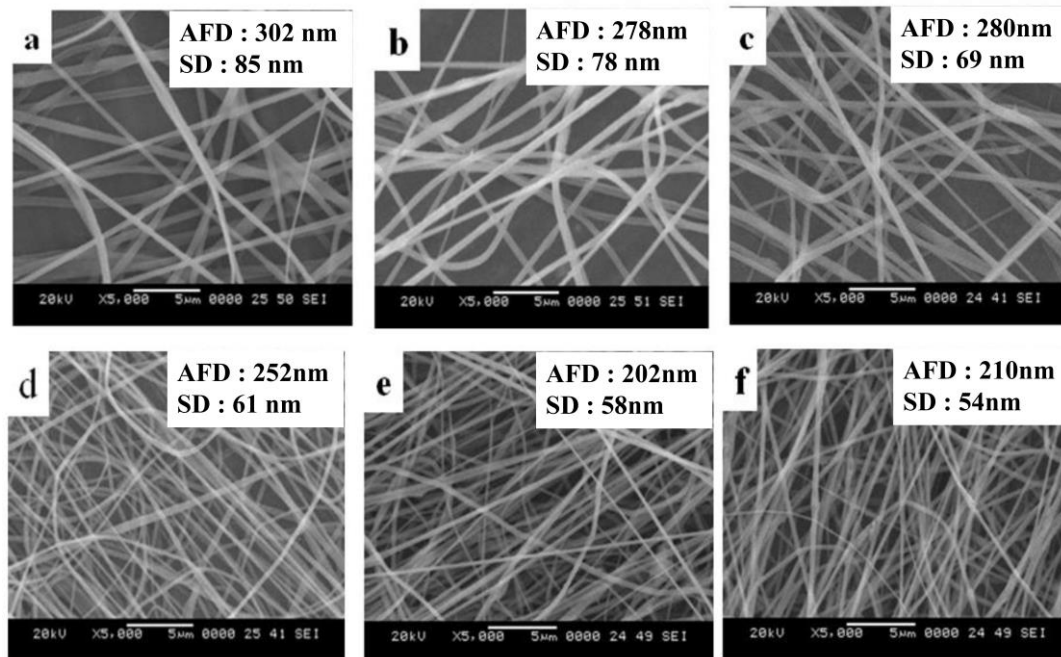


Fig.3.1 SEM images of (a) E-PVDF (b) PHNF-2.5 (c) PHNF-5 (d) PHNF-7.5 (e) PHNF-10 (f) PHNF-20.

Fig. 3.1. (a-f) shows the SEM micrographs of E-PVDF and PHNF-X webs with different HNT loading. In the pristine PVDF webs, the fibers were smooth and randomly distributed. The outer surface of HNT is chemically similar to SiO_2 while its inner cylinder core is related to Al_2O_3 . The charge (zeta potential) behavior of HNT can be roughly described by superposition of mostly negative surface potential of SiO_2 , with a small contribution from the positive Al_2O_3 inner surface. These charged surfaces enhance the electrostatic conductivity of the solution. Thus, incorporation of HNT into PVDF increases charge density on the surface of the solution jet during electrospinning. The accumulated charges overcome cohesive forces resulting in long, homogenous and defect-free nanofibers (Touny et al. 2010; Prashantha 2011; Wang and Huang 2014). Also, these nanofibers were expectantly stretched by the rotation of the high-speed drum collector. Interestingly, many of these nanofibers were not uniformly aligned. It has been reported earlier that DMSO might cause jet instability as its high dielectric constant leads to misalignment of fibers (Yong Lei, Qinglin Wu, Craig M. Clemons, Fei Yao 2007; Janakiraman et al. 2016). The average fiber diameter (AFD), as well as the standard deviation of fiber diameter (SD), decreased with an increase in HNT loading in the fibers. This indicates that HNT could be used as a processing aid for PVDF that can lead to finer electrospun fibers.

3.1.2. FTIR Spectroscopy and WAXD analysis

The combined effects of HNT and electrospinning on the polymorphism of PVDF were probed using FTIR spectroscopy. FTIR spectra of unstretched PVDF film, E-PVDF and PHNF webs are shown in Fig. 3.2. From literature (Bartenev et al. 1975; Bormashenko et al. 2004; Yee et al. 2007; Yu and Cebe 2009a; Deka and Kumar 2011; Yang et al. 2011; Neppalli et al. 2013) the spectral peaks were identified and their respective phases and vibrational modes. In the spectrum of the unstretched film, all the bands are related to TGTG' conformations. Bands at 630, 707, 816, 859, 950, 1017, 1143, 1357 and 1653 cm^{-1} correspond to α -phase. For E-PVDF, there is a remarkable decrease in the intensities of peaks corresponding to the α -phase. Moreover, a number of new bands were observed at 467, 680, 840, 1021, 1194, 1286 and 1402 cm^{-1} . These bands can be attributed to the β -phase, which has TTT conformation.

β -phase content of PVDF increased remarkably by the synergistic effects of HNT and electrospinning. β -phase content increased continuously up to a HNT loading of 10 wt % after which there was a decrease in it. This may be attributed to the excess of HNT loading, which leads to reduced polymer-filler interaction. The highest β -phase content was 81% at 10 wt % of HNT loading (Table 3.1.). C-H bonds in PVDF repeating units are partially positively charged. This could result in ion-dipole interaction with the negatively charged HNT surface, which may lead to an enhancement of β -phase content as in nano-clay/PVDF composites. For the present system, a plausible polymer-filler interaction mechanism has been proposed in section 3.5. In literature, it has been reported that after addition of nano-clay into PVDF, γ -phase was observed (Ramasundaram et al. 2008; Prashantha 2011; Yang et al. 2011; Bai et al. 2012; Neppalli et al. 2013). But, there is no significant amount of γ -phase present in the PHNF webs prepared in this study.

In the WAXD patterns of unstretched PVDF film, E-PVDF and the PHNF webs characteristic peaks for different phases were present (Fig.3.3a). Peaks at 17.7°, 18.4°, 19.9° and 26.6° are characteristic of the α -phase. Peaks at 17.7°, 18.4°, 19.9° and 26.6° correspond to (1 0 0), (0 2 0), (1 1 0) and (0 2 1) planes of PVDF, respectively. For electrospun fibers, these peaks almost diminished and a new peak was observed at 20.36° that corresponds to the (1 1 0)/(2 0 0) crystal plane of β -phase with an interplanar space of 0.43 nm. Broader peaks were seen for nanofibers, which may be due to a decrease in the crystallinity of PVDF. β -phase content increased proportionately with HNT loading up to 10 wt% beyond which there was a decrease in it. At 20 wt% HNT loading, β -phase content decreased and the peak around 20° began to

shift towards left and a new peak at 24.56° appeared; this may be attributed to the reformation of α -crystals due to an overdose of HNT into PVDF.

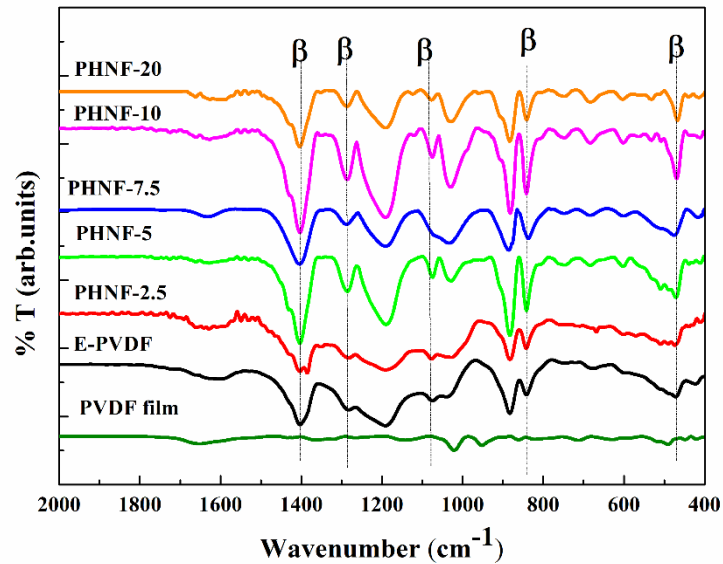


Fig.3.2. FTIR spectra of unstretched PVDF film, E-PVDF and PHNF webs (the vibrational bands used for calculating X_{β} are highlighted).

Table 3.1. WAXD and FTIR results of PHNF webs

HNT loading (wt.%)	2θ (°)	d-space (nm)	X_c (%)	X_{β} (%)
				FTIR method
0	20.36	0.43	38.8	34.6 ± 0.9
2.5	20.53	0.43	37.5	52.0 ± 0.5
5	20.54	0.43	35.4	59.4 ± 1.0
7.5	20.56	0.42	34.2	62.4 ± 1.9
10	20.83	0.42	31.0	81.1 ± 2.4
15	*	*	*	44.0 ± 1.1
20	20.57	0.43	35.1	28.4 ± 0.7

* This sample was prepared to check if the β -phase content and piezoelectric response improve beyond 10 wt% HNT loading. Hence, only FTIR spectroscopy was performed on this sample.

3.1.3. DSC analysis

The DSC traces of PHNF webs are shown in Fig. 3.3b. In DSC curves of E-PVDF two peaks were observed. The first peak at 112.6 °C corresponds to the magnetic transition of PVDF from ferroelectric to paraelectric, which is the curie transition (T_c) (Martins et al. 2014). The second one at 142.1 °C corresponds to the crystalline melting point (T_m) of PVDF. For the PHNF

webs, T_c increased in comparison with E-PVDF. Moreover, the T_c peak overlapped T_m peak. For E-PVDF, the T_m is 142.5 °C, but there is a shift in the T_m for the HNT loaded PVDF nanofibers to a higher temperature.

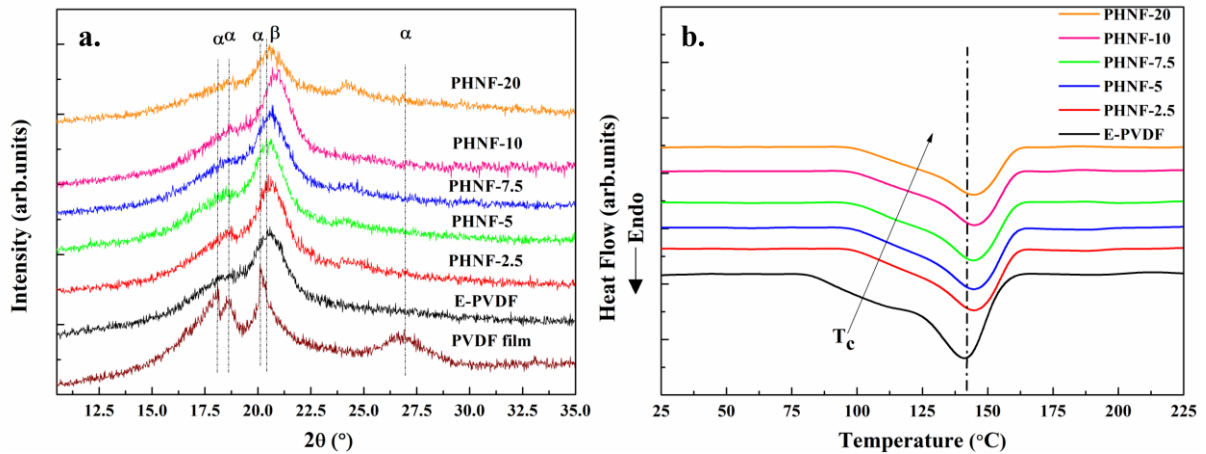


Fig.3.3 (a) WAXD patterns of unstretched PVDF film, E-PVDF and PHNF webs
(b) DSC traces of electrospun PVDF and PHNF webs.

Table. 3.2. DSC results of PHNF webs.

HNT loading (wt.%)	ΔH_m (Jg ⁻¹)	T_m (°C)	X_c (%)
0	41.3	142.0	39.6 ± 0.3
2.5	39.2	145.6	38.5 ± 0.5
5	37.3	146.0	37.5 ± 0.4
7.5	36.1	146.1	37.3 ± 0.3
10	34.4	146.2	36.6 ± 0.6
20	33.1	145.2	39.5 ± 0.2

This is attributable to the rearrangement of PVDF crystals and the resultant increase in β -phase content. The shifting and overlapping of T_c and T_m peaks is associated with a significant change in crystallinity of PVDF. Due to the synergistic effect of electrospinning and nucleation by HNT, the PVDF chains in the PHNF webs get polarized, which induces the formation of the β -phase. The degree of crystallinity of PVDF (X_c) tends to decrease with an increase in the dosage of HNT (Table. 3.2), which is in line with the WAXD results. Clays in general play a dual role in influencing the crystallization process of PVDF, which depends on both their quantity and state of dispersion. Clay not only acts as a nucleating agent, but also is a physical obstacle to the motion of polymer chains (Yu and Cebé 2009a). In the present study, HNTs

acted as a nucleating agent up to 10 wt% HNT loading beyond which there was a decrease in the β -phase content and an increase in the X_c of PVDF. Difference in X_c obtained from DSC and WAXD results is due to ineluctable error, which may happen during the calculation process. In DSC, the error may be due to the baseline correction carried out during evaluation of heat of fusion; in WAXD analysis, it may be linked with the separation of amorphous and crystalline region from the diffraction (George et al. 2017).

3.1.4. TGA results

TGA curves and the corresponding differential thermal curves (DTG) of the nanofiber webs are shown in Fig. 3.4a and Fig. 3.4b, respectively. PVDF was stable up to 400° C and above this temperature it underwent weight loss continuously up to 775 °C. However, a major loss in weight was observed at 467 °C. This weight loss may be attributed to the chain stripping of monomers. PVDF degrades rapidly, which results in the formation of hydrogen fluoride along with the monomers.

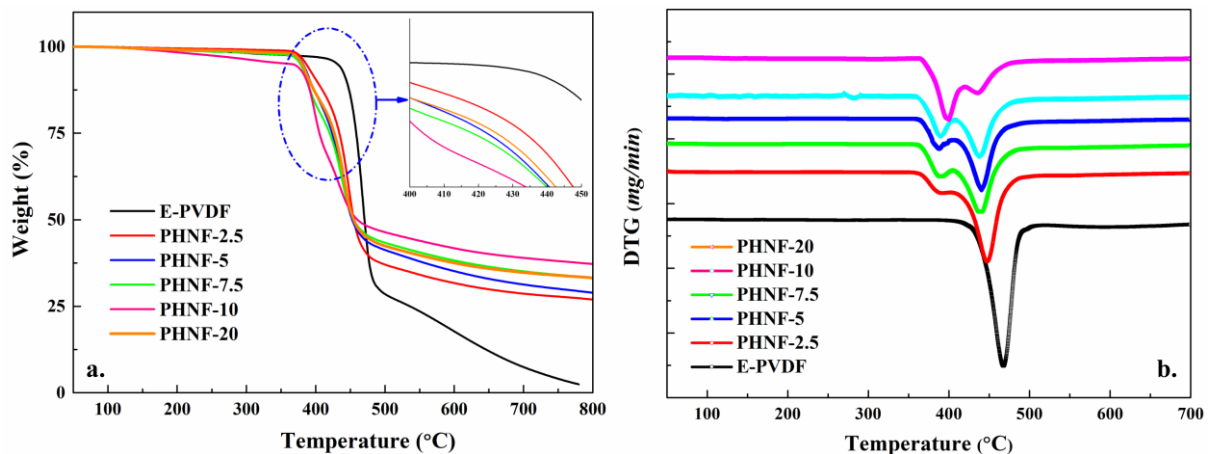


Fig.3.4 a) TGA curves of E-PVDF and PHNF webs **b)** DTG curves of E-PVDF and PHNF webs.

In the PHNF webs, thermal degradation took place in two steps. Weight loss for nanocomposite fiber webs starts at a very low temperature i.e., 130 °C due probably to dehydration of HNTs. Addition of HNT resulted in a decrease in the onset of decomposition temperature of PVDF (inset in Fig.3.4b). When the HNT loaded PVDF is exposed to heat, it generates free radicals from HNT that could accelerate the chain scissoring of the PVDF chain and further separating CH and CF bonds (Gaabour 2015).

3.1.5. TEM analysis

Fig. 3.5a. shows the TEM micrograph of pristine HNT in which its inner and outer walls are clearly visible. Inside a single PHNF, some HNTs are seen that are oriented along the fiber axis; their orientation happens during the formation of nanofibers in electrospinning due to process induced alignment (Fig. 3.5b).

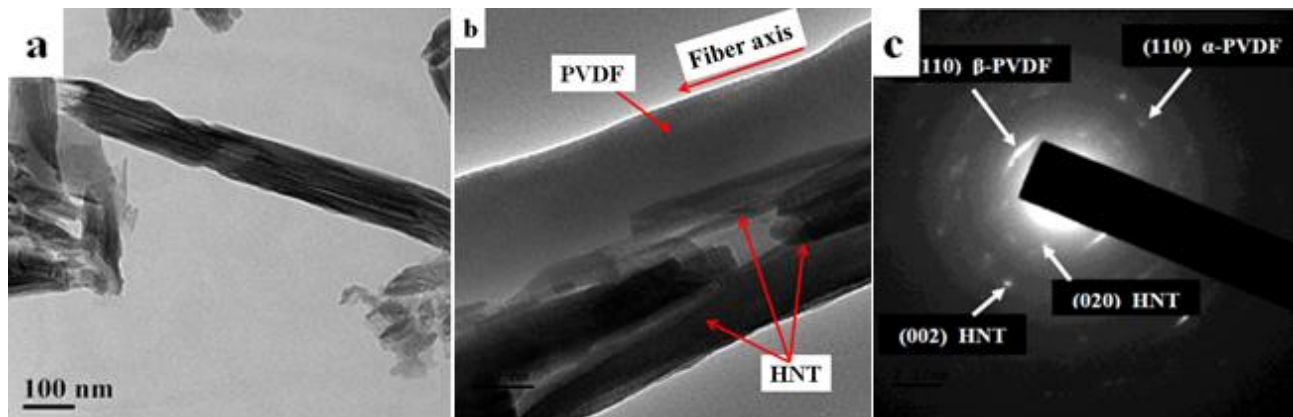


Fig. 3.5. TEM images of (a) Pristine HNT (b) PHNF-10; and (c) SAED patterns of PHNF-10.

The HNT are finely dispersed in the PVDF matrix due to an excellent polymer- filler interaction as discussed in section 3.5. Selected area electron diffraction (SAED) pattern allows determination of crystal plane orientation in the nanofibers (Fig. 3.5c). The dot patterns were indexed and the interplanar distance for (1 1 0)/(2 0 0) crystal planes was found to be 0.43 nm, corresponding to the β -phase of PVDF. Interplanar distances of 0.44 nm and 0.3 nm for (0 2 0) and (0 0 2) planes respectively relate to HNT crystal (Dong et al. 2015); (1 1 0) crystal plane with an interplanar distance of 0.37 nm corresponds to α -phase crystallites of PVDF. These results are in good agreement with WAXD results.

3.1.6. Polymer-filler interaction mechanism in PHNF webs

The surface of HNT is made of Si-O-Si groups and the inner walls are made of Al-OH groups. Thus, a strong interaction between the hydrogen atoms of PVDF chains and negatively charged surface of HNT can be expected. Fig.3.6a. shows the FTIR spectra of pure PVDF, pristine HNT and 10 wt.% HNT-loaded PHNF webs. In pristine HNT spectrum, peaks at 3697 cm^{-1} and 3515 cm^{-1} correspond to the stretching vibration of Al-OH groups in the inner surface. 1028 cm^{-1} and 909 cm^{-1} peaks correspond to Si-O stretching and Al-OH bending vibrations, respectively (George et al. 2017). In the spectrum of PHNF, peak at 1028 cm^{-1} shifted to a lower wave number i.e., 1027 cm^{-1} . Similarly, the peak at 3697 cm^{-1} shifted to 3693 cm^{-1} , which may be attributed to intermolecular hydrogen bonding between the F-atoms of PVDF and OH

groups of HNT. Also, a peak at 909 cm^{-1} that represents OH groups in HNT seems to have moved towards the lower wave number and merged with the neighboring PVDF peak. This may also be due to hydrogen bonding between F-atoms of PVDF and OH groups of HNT, which led to the formation of long TTT conformation (Yu and Cebe 2009a). In pure PVDF, a peak at 487 cm^{-1} corresponds to CH_2 wagging vibration and in pristine HNT, a peak at 466 cm^{-1} corresponds to Si-O bending vibration. In the spectrum of the PHNF web, the Si-O peak overlapped with that of the CH_2 groups of PVDF. Along with this overlapping, the Si-O peak shifted to a lower wave number (i.e., 464 cm^{-1}). This may be attributed to the interaction between CH_2 bonds of PVDF with the negatively charged surface of HNT that induce formation of long TTT conformations. Fig. 3.6b. shows the schematic of a plausible filler-polymer interaction mechanism in the PHNF webs. (Ramasundaram et al. 2008).

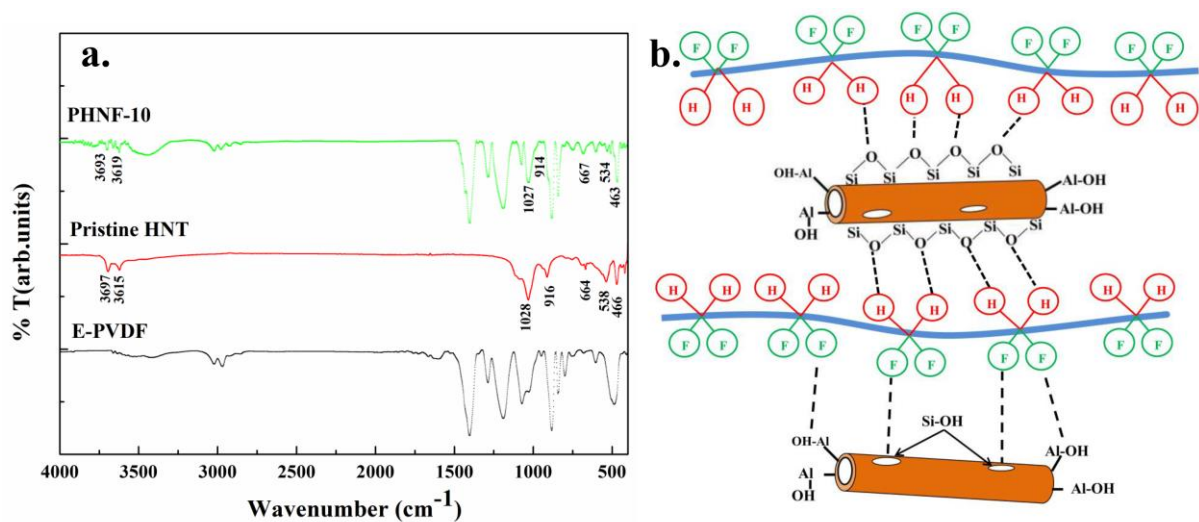


Fig.3.6. (a) FTIR spectra of E-PVDF, pristine HNT and PHNF webs (b) Plausible interaction mechanism between HNT and PVDF in the PHNF webs.

3.1.7. Piezoelectric Performance of PHNF webs

The piezoelectric voltage and current outputs of the PHNF webs for different loads are shown in Fig. 3.7a & b. PVDF generates voltage only when the fibers are compressed and then relaxed from all the loads. Performance of the PHNF webs is directly proportional to the β -phase content. PHNF webs with 10% HNT loading exhibited the highest voltage and current output of 955 mV and 34 nA, respectively under a load of 100 g. For PHNF webs with 15 and 20% HNT loading, the voltage outputs were very low due to their low β -phase content.

Flexible, self-powered materials are highly sought after for various applications, such as energy harvesting, robotic devices, and lab-on-a-chip medical diagnostics. Self-powered materials are based on piezoelectric nanogenerators, which are powered by their enormous

kinetic energy or renewable energy. These materials rely on the presence of piezoelectric potential generated by the material. However, simple flexibility alone does not guarantee their conformal bonding to nonplanar substrates. Therefore it is mandatory to focus on electrospun nanofibers for use in highly stretchable devices due to their high piezoelectric voltage outputs, the PHNF webs developed in the present study could be used in flexible nanogenerator and nano-pressure sensors.

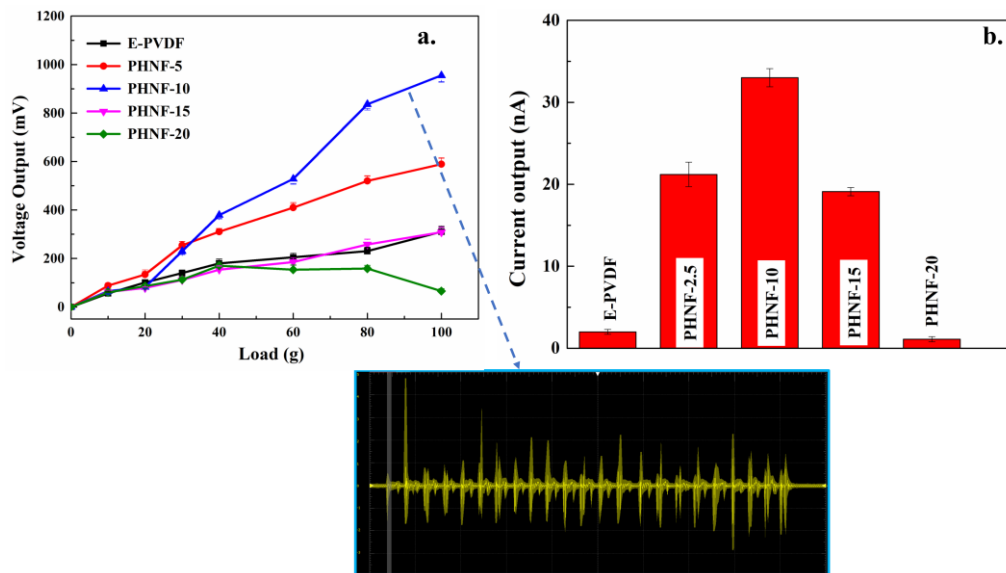


Fig. 3.7. Piezoelectric responses of E-PVDF and PHNF webs at different loads (a) Voltage output (b) Current output.

3.2. CONCLUSIONS

Finer PVDF nanofibers can be produced by electrospinning of PVDF solution containing HNT. Crystallinity of PVDF decreases upon the addition of HNT, while the β - phase content increases simultaneously. The highest β -phase content was observed in the PHNF webs containing 10wt.% of HNT. HNTs are oriented along the axis of the fiber and there is a strong interaction between HNTs and PVDF. The onset temperature of thermal degradation of the PHNF webs decreases compared with that of E-PVDF due to the catalytic action of HNT in chain scissoring. The piezoelectric response of PVDF is also enhanced appreciably due to the synergism of HNT and electrospinning. This study proves that the interplay between the effects brought about by HNT and electrospinning could be used to engineer the crystallinity, polymorphism and piezoelectric behavior of PVDF for advanced applications, such as flexible nanosensors and nanogenerators.

CHAPTER 4

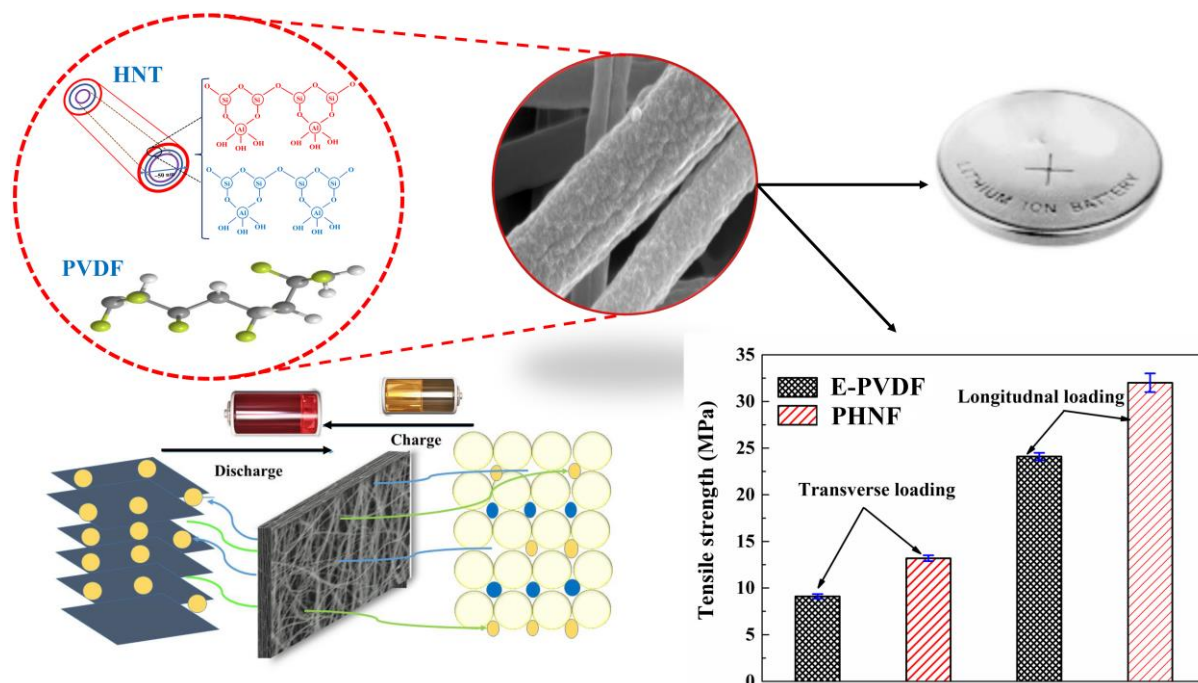
**PVDF/HALLOYSITE NANOCOMPOSITE-BASED NON-WOVENS AS
GEL POLYMER ELECTROLYTE FOR HIGH SAFETY LITHIUM ION
BATTERY**

*The results of this chapter have been published in *Polymer composites*, 2018;*

DOI: [10.1002/pc.25043](https://doi.org/10.1002/pc.25043).

CHAPTER 4

PVDF/HALLOYSITE NANOCOMPOSITE-BASED NON-WOVENS AS GEL POLYMER ELECTROLYTE FOR HIGH SAFETY LITHIUM ION BATTERY



This chapter discusses about the fabrication of gel polymer electrolyte (GPE) based on electrospun poly(vinylidene fluoride) (PVDF)/halloysite nanotube (HNT) nanocomposite non-wovens (PHNF) and its suitability as a separator in lithium-ion battery (LIB) was explored. A detailed analysis on the morphology, degree of crystallinity and polymorphism were carried out using FTIR, WAXD and DSC characterization techniques. The tensile, puncture and thermal shrinkage test was carried out, which are considered to be most essential for the safety features of battery. The coin cell was fabricated (Li/PHNF/LiCoO₂) to study the electrochemical performance. In addition, PVDF nanofibers and commercially available celgard[®]2400 were also investigated to demonstrate the advantages of PVDF/HNT nanocomposite non-wovens as GPE. The cycling performance of Li/PHNF/LiCoO₂ cell was studied for 50 cycles.

4.1. RESULTS AND DISCUSSION

4.1.1. SEM, FESEM and AFM results

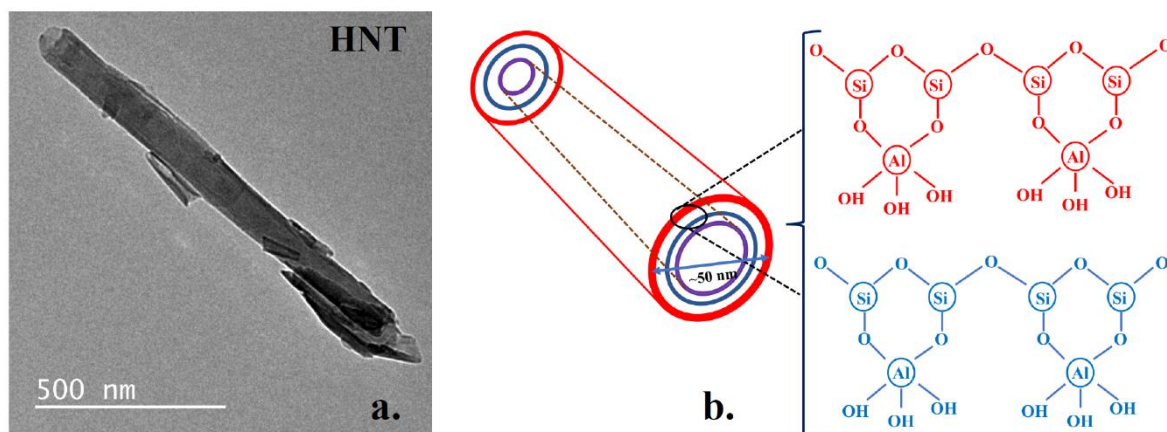


Fig. 4.1 (a) TEM image of HNT (b) Schematic representation of HNT chemical structure.

HNT has a tubular structure, which can be clearly seen from the TEM micrograph (Fig. 4.1a). The surface groups of HNT are schematically illustrated in Fig. 4.1b. The outer and inner surfaces of HNT are chemically similar to SiO_2 and Al_2O_3 , respectively. HNT has a negative surface potential from the outer surface and positive surface potential from the inner surface (Yuan et al. 2015). The charge potentials are helpful in enhancing the electrostatic conductivity of the electrospinning solution. Fig. 4.2(a-b) shows the SEM micrographs of E-PVDF and HNT/PVDF nanocomposite (PHNF). Nanofibers produced are uniform, continuous, bead-free and flexible. These characteristics of nanofibers are advantageous for the electrochemical performance of LIB's. The average fiber diameter (AFD) of E-PVDF and PHNF were found to be 302 and 210 nm, respectively. Besides, the standard deviation (SD) of the fiber diameter also decreased from 85 to 58 nm. The decrease in AFD of PHNF is attributed to the addition of HNT in PVDF solution. Fig. 4.2 c & d show the FESEM micrographs of pure PHNF web and that with electrolyte, respectively. The interlacing of fibers in PHNF webs results in a highly porous structure. Porosity between the fibers is essential for the effective entrapping of electrolyte and the effective transport of ions. AFM images of pure PHNF web with entrapped electrolyte is shown in Fig. 4.2e. AFM image clearly reveals the space between the interconnected nanofibers three dimensionally. This kind of structure is advantageous as it hinders the growth of lithium dendritic structures and offers long life (Zhang 2007). The non-woven fibrous structure offers high electrolyte uptake, porosity and ionic conductivity. Porosity of E-PVDF mats and PHNF are 72% and 85%, respectively. The average electrolyte uptake was found to be 296% and 456% for E-PVDF and PHNF, respectively. This increase in

electrolyte uptake for PHNF is attributed to the decrease in AFD and increased porosity. The SEM image of Celgard[®]2400 made of single layer polypropylene is shown in Fig. 4.2f. The presence of open and straight through porous structure offers high power densities. However, the porosity and ionic conductivity are quite low (Huang 2011a). The % porosity and electrolyte uptake of Celgard[®]2400 were 41% and 122%, respectively.

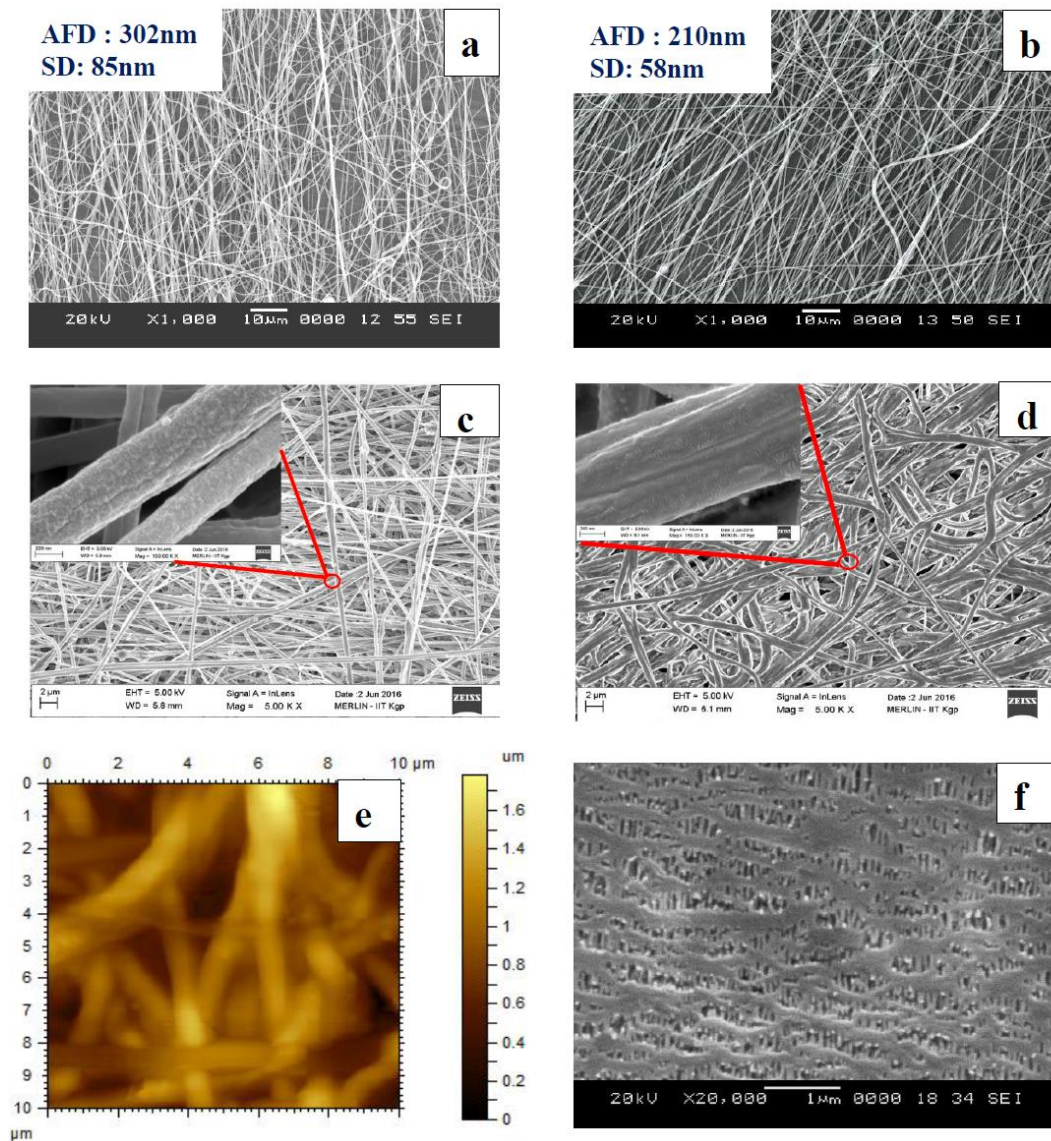


Fig. 4.2 (a) SEM image of E-PVDF (b) SEM image of PHNF (c) FESEM image of PHNF without electrolyte (d) FESEM image of PHNF with electrolyte (e) AFM image of PHNF; (f) SEM image of Celgard[®]2400.

4.1.2. Ionic transference number

Ionic transference number is another important parameter in GPE. Fig. 4.3a shows the current versus time plot for PVDF and PHNF based GPE. The initial (before polarization) and

saturation resistance (after polarization) were taken by intercepting the curves to the x-axis from the EIS curves. The ionic transference number of E-PVDF and PHNF are 0.48 and 0.57, respectively, whereas for Celgard[®]2400 it is 0.33 (Yoon and Kelarakis 2014). The higher transference number of PHNF is a result of its higher porosity, higher specific surface area and lower crystallinity (Zhu et al. 2013). The degree of dissociation of the electrolyte decides the amount of charges passing across the separator due to the fact that only the free Li⁺ ions are capable of carrying the current.

4.1.3. Electrochemical stability of PHNF webs

Selection of GPE's with high voltage stability is the most effective way to increase the capacity of LIB (Croy et al. 2014). Electrochemical stability of polymeric separators in batteries at the operating voltage considered to be important factor for battery performance. The electrochemical stability of the cell with PHNF separator was studied using LSV (Fig. 4.3b). The oxidation peak of PHNF separator is steady up to 5.3 V versus Li/Li⁺ and there is no anodic spike observed between 0 V and 5.3 V. The electrochemical stability of Celgard[®]2400 and E-PVDF separator are 4.5 V and 5 V versus Li/Li⁺, respectively. The enhancement of stability window of PHNF is attributed to the synergistic effect of electrospinning and HNT. In addition, higher electrochemical stability is also caused by the excellent affinity of PVDF towards carbonate groups of EC and DEC. Therefore, the dipole-dipole attraction between F-atoms of PVDF and carbonate molecules enhances the electrochemical stability (Raghavan et al. 2010). Also, the strong electron withdrawing effect of the fluorine atoms of PVDF have higher oxidation potentials, which improve the electrochemical stability (Chiang et al. 2003). The decomposition voltage for PHNF is comparable with that of high voltage LIB systems (Li et al. 2015).

In the TEM micrograph (Fig. 4.4a) HNT's are oriented along the fiber axis of PVDF nanofiber, which is due to the process induced alignment. However, at some regions, HNT's are protruding from the PVDF nanofibers (Fig. 4.4b). Based on this morphology, the mechanism of interaction between HNT's and the electrolyte is proposed as follows: hydrogen bonds can form between the fluorine atoms of LiPF₆ and hydroxyl group of HNT; there is also a possibility of a dipole-dipole attraction between the oxygen atoms of HNT and Li⁺ of LiPF₆. There is hydrogen bonding interaction between fluorine atoms of LiPF₆ with the hydrogen atoms of PVDF. All the aforesaid interactions are schematically depicted in Fig. 4.4c.

Both the aforesaid factors could possibly weaken the bonding between Li⁺ and [PF₆]⁻ leading to a higher population of free Li⁺ ions. These free ions, in turn, are capable of moving through

the gel towards the oppositely charged electrode leading to the performance enhancement of the LIB. Due to the hindering of anions, electrochemical stability and ionic transference increase drastically for the PHNF based electrolyte. The high ionic transference number of GPE could possibly reduce the over potential at high current density (Xue et al. 2015; Long et al. 2016).

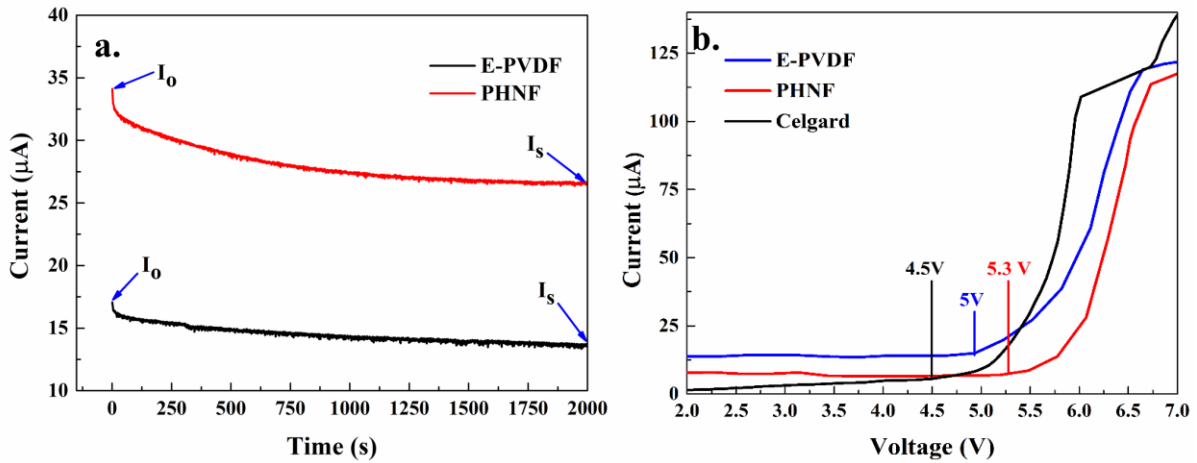


Fig. 4.3. (a) DC polarization curves of PVDF and PHNF based separators (b) Linear sweep voltammograms of SS/Celgard[®]2400/Li, SS/E-PVDF/Li and SS/PHNF/Li at 10 mVs⁻¹.

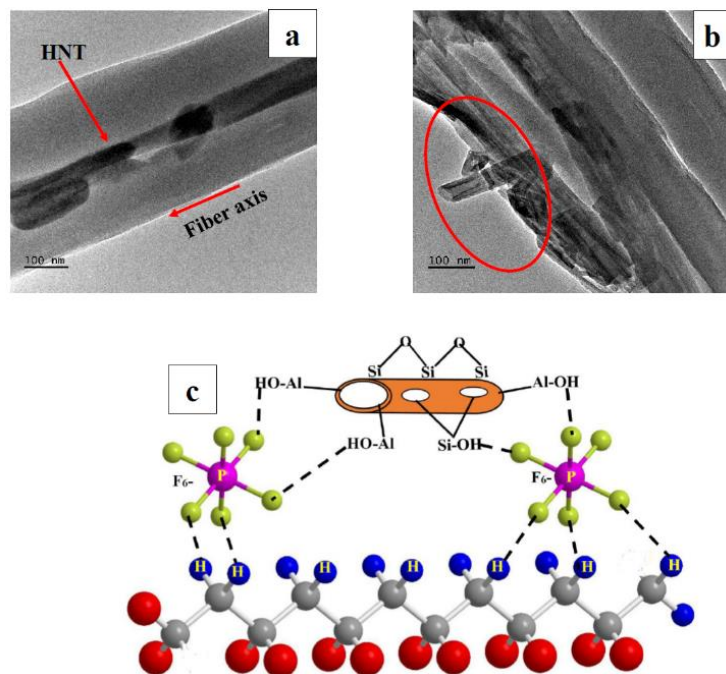


Fig. 4.4. (a) and (b) TEM micrographs of PHNF (c) Interactions between PHNF and LiPF₆.

4.1.4. Thermal shrinkage test

Thermal shrinkage of separators at high temperature is considered to be a critical problem in LIB's. PVDF and PHNF mats were heated at 130°C for 4 h and 8 h in a hot air oven. The

thermal shrinkage of PHNF mats was negligible while, PVDF and Celgard[®]2400 exhibited notable shrinkage (Fig. 4.5). The lesser shrinkage of PHNF mats would considerably reduce the potential risk of short circuits and explosions when it is used as a separator in LIB's. One of the most striking features of Celgard separators is the fuse function, which plays a vital role in avoiding external short circuits. However, due to its low melting temperatures Celgard separators habitually suffer from severe thermal shrinkage. Although, the fuse function blocks the pores thereby converting the separator into insulator around its melting temperature. However, even after shut down, the temperature often continues to increase, which may lead to internal short circuit and explosions. These accidents are often confronted due to overcharging or overheating of batteries.

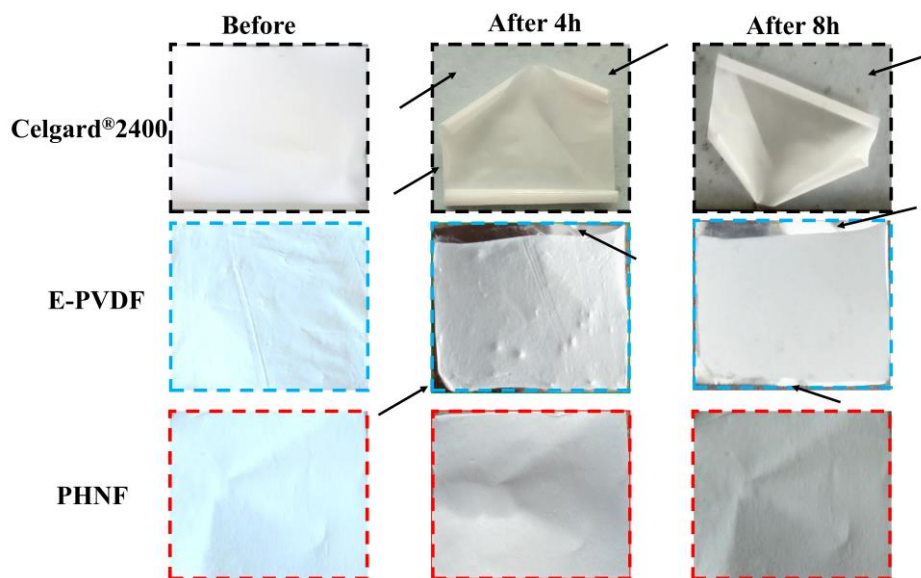


Fig. 4.5 Digital photographs of the thermal shrinkage test of Celgard[®]2400 E-PVDF and PHNF webs before and after the heat treatment (the arrows indicate regions of shrinkage).

4.1.5. Mechanical properties of electrospun PVDF and PHNF webs

Fig. 4.6a shows the stress-strain curves of electrospun PVDF and PHNF webs when loaded in transverse direction to the fiber length. The maximum tensile strength of PVDF was 9.1 MPa with 74% elongation. The PHNF webs had a tensile strength of 14.2 MPa with 89% of elongation, which is considered to be adequate for separators in LIB (commercial requirement, tensile strength - 13 MPa) (Huang 2011a; Prashantha 2011; Huang and Hitt 2013). In addition, the tensile strength of nanofiber webs along the longitudinal direction was also determined. The maximum tensile strength was 32 MPa with 99% of elongation (for PVDF nanofiber mat it was 24.1 MPa with 84% elongation). The tensile strength of PHNF webs was better than that of polyetherimide fibers (21MPa), paper-supported inorganic composite (5.31

MPa), and thermally crosslinked fluorinated polyimide nanofiber membrane (32.7 MPa) reported previously (Kong et al. 2018a, 2018b; Wang et al. 2018b). This may be attributed to

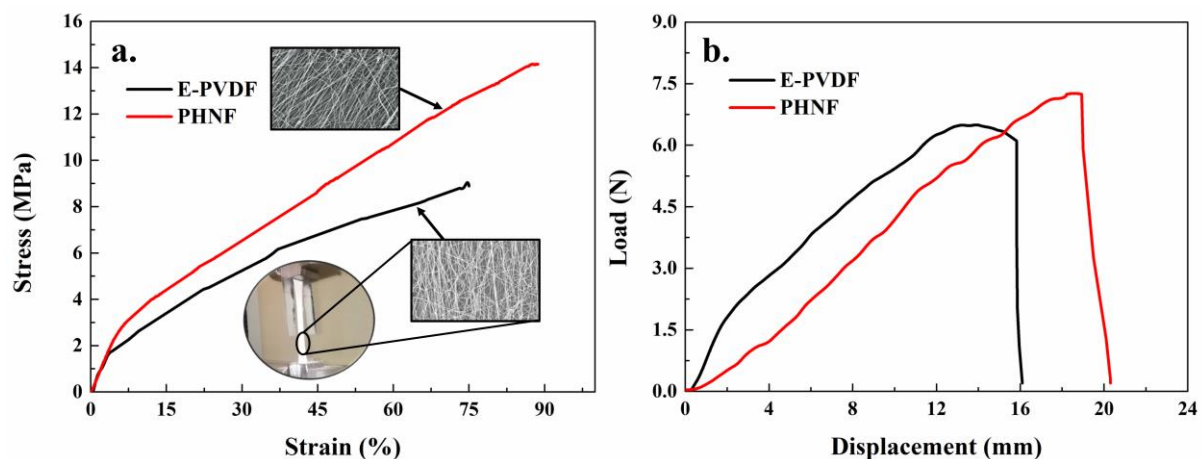


Fig. 4.6 (a) Stress-strain curves of E-PVDF and PHNF webs (b) Load-displacement curves of puncture test for E-PVDF and PHNF webs.

the addition of HNT and improved orientation of PHNF fibers. It is a well-known fact that high elongation at break is very essential for GPE in batteries as it enhances the impact resistance. Higher tensile strength and toughness of PHNF webs not only extend the life of the separator, but also reduce the risk of failure (Tang et al. 2015). Further, it is predicted that higher mechanical strength suppresses the dendritic formation and promotes uniform formation of SEI layer (Monroe and Newman 2003; Khurana et al. 2014).

Puncture strength of separators is considered to be a very important parameter. Due to the repeated charge-discharge cycles, Li^+ ions deposit on anode and grow in the form of ramified structure that punctures the separator and leads to the failure of LIB (Choudhury et al. 2015). The force-displacement curves of electrospun PVDF and PHNF webs are shown in Fig. 4.6b. E-PVDF and PHNF webs withstood a maximum load of 6.5 N and 7.2 N, respectively. Also, PHNF showed high elongation before the perforation. The puncture strength values of E-PVDF and PHNF were 25.4 kN/m and 27.5 kN/m, respectively. Both the separators satisfy the requirement of USABC standard for separators in LIB for puncture strength (300g/25.4 μm) (Huang 2011b).

4.1.6. AC ionic conductivity of PHNF webs

Fig. 4.7a shows the impedance spectra of PVDF and PHNF at room temperature. The bulk resistance was determined by taking the intercept on the x-axis (real axis). The bulk resistance values of Celgard[®]2400, E-PVDF and PHNF are 4.8 Ω , 2.3 Ω and 0.9 Ω , respectively. The absence of semi-circular region at both medium and high frequency in impedance spectra may

be due to the fact that the ions are the current carriers and the conductivity is due solely to the ionic conduction. At low frequency region a steep slope corresponds to the resistance due to the stainless-steel electrodes (Rajendran et al. 2008; Raghavan et al. 2010). Ionic conductivity of PHNF was found to be 1.77 mS cm^{-1} , which is much higher than that of E-PVDF (0.94 mS cm^{-1}) and commercial Celgard[®]2400 (0.35 mS cm^{-1}).

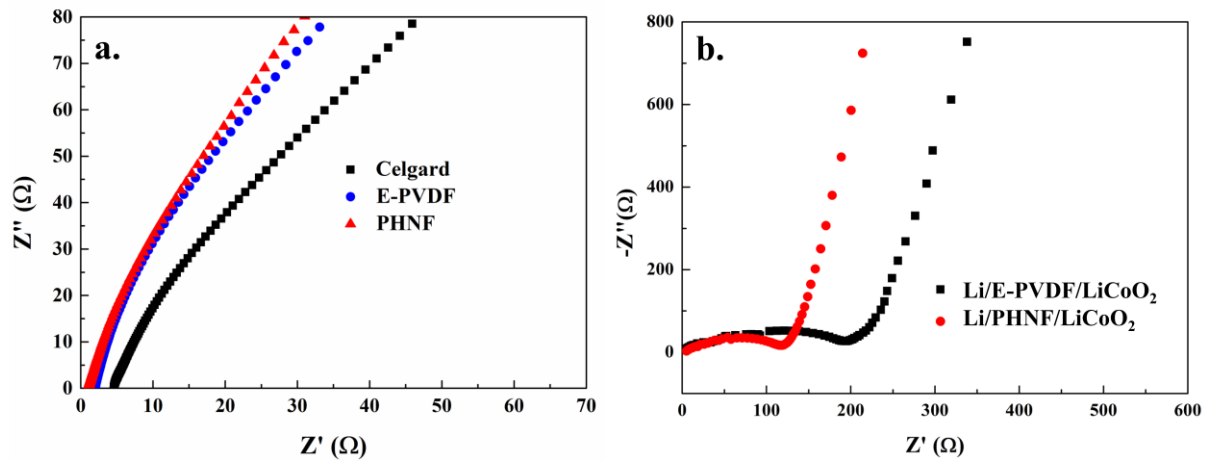


Fig. 4.7 (a) Impedance spectra of PVDF and PHNF based gel electrolytes (b) Electrochemical impedance spectra of Li/LiCoO₂ cells containing PVDF, and PHNF electrolyte membranes.

Higher ionic conductivity and cationic mobility not only improves the cycle performance, but also suppresses the nucleation of dendritic structure. The lower conductivity of PVDF is due to the low β -phase content and higher percentage of crystallinity that tends to resist the transport of lithium ions. The decrement in crystallinity, increased porosity and high electrolyte uptake of PHNF favor the improvement in the ionic conductivity. It is recognized that polymer separator electrolyte consists of amorphous swollen electrolyte phase, liquid phase with the electrolyte and solid fibrous phase. The swollen phase tightly holds and checks the leakage of the electrolyte solution (Gao et al. 2006). In addition, the high porosity of the GPE leads to sorption of more liquid electrolyte and thus it serves as a tunnel for the movement of lithium ions.

It is also imperative to have good interfacial properties between the liquid electrolyte-soaked membranes and the other active electrode materials. Fig. 4.7b shows the electrochemical impedance spectra of Li/LiCoO₂ cells containing E-PVDF, and PHNF nanofibrous electrolyte membranes. The interfacial resistance was taken as the intercept of curve to Z' -axis at higher frequency (Wang and Gao 2016; Zhang et al. 2016a; Kong et al. 2018b). The interfacial resistances are 189 and 114 $\Omega \text{ cm}^{-2}$, respectively for these cells while, for celgard separator it is $\sim 160 \Omega \text{ cm}^{-2}$ (Xu et al. 2017). For the cell with pure PVDF membrane,

the high interfacial resistance of $189 \Omega\text{cm}^{-2}$ is due to the low porosity and ionic conductivity of the separator membrane. The reduced interfacial resistance of PHNF is beneficial for realizing excellent electrochemical properties, especially C-rate performance of Li/LiCoO₂ cells.

The combination of high porosity, tensile strength, puncture strength and ionic conductivity with low thermal shrinkage is seen to be very rare in separators. PHNF separator not only has higher porosity and ionic conductivity, but also is capable of addressing the safety concerns caused by thermal shrinkage, dimensional instability and unexpected environmental changes. In addition, the use of highly scalable electrospinning approach to fabricate a strong and high-performance separator will facilitate practical enactment of PHNF in LIB.

4.1.7. Cycle performance of Li/PHNF/LiCoO₂ cell

Fig. 4.8a shows the cycle performance of the cell for the initial cycle of PVDF, PHNF and Celgard[®]2400 separators assembled with Li/LiCoO₂ system. The cell with PHNF separator delivered a capacity of 138.01 mAhg^{-1} , which is larger than that with the PVDF and Celgard[®]2400 separators. Further, the difference in charge-discharge capacity of the cell with PHNF is smaller compared with those of the PVDF and Celgard[®]2400 separators. The above investigations and cycle performance confirm the improved performance of PVDF by the addition of HNT and its suitability as a separator in LIB's.

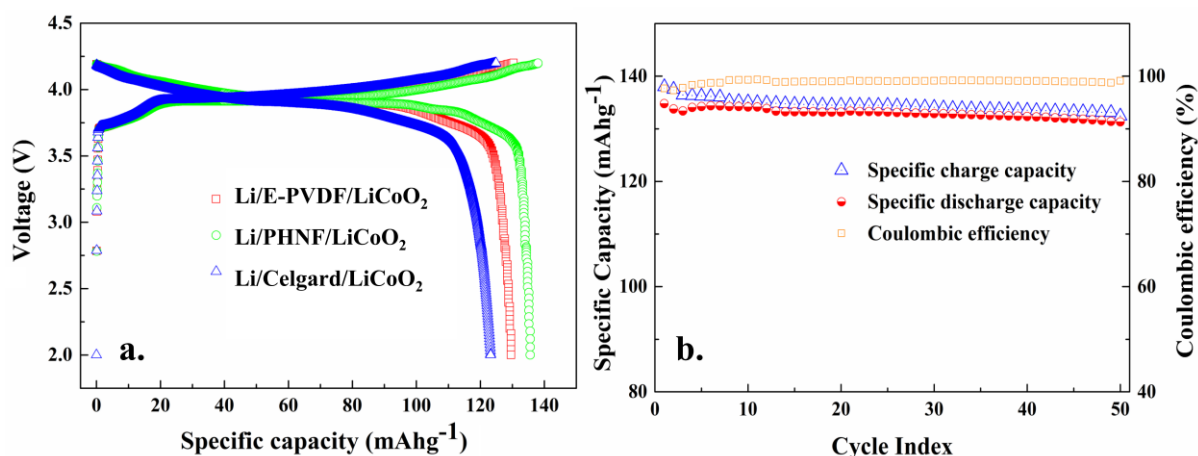


Fig. 4.8 (a) Initial charge/discharge profiles of Li/E-PVDF/LiCoO₂, Li/PHNF/LiCoO₂ and Li/Celgard[®]2400/LiCoO₂ cell (b) Charge-discharge performance and coulombic efficiency of Li/PHNF/LiCoO₂ cell.

Further, to understand the advantages and evaluate the high performance of PHNF non-wovens as a separator in LIB's, the electrochemical performance of Li/Celgard[®]2400/LiCoO₂ and Li/PHNF/LiCoO₂ cell were evaluated for 50 cycles. For the initial cycle of Li/Celgard[®]2400/LiCoO₂, a charge capacity of 127 mAhg^{-1} for the initial cycle corresponds to

87.7% theoretical efficiency of LiCoO_2 . There was a gradual drop in capacity after 10 cycles, but a considerable loss in capacity was observed after 25 cycles. After 50 cycles, the specific capacity was 109.5 mAhg^{-1} , which is $\sim 86\%$ of that of the initial cycle. However, the coulombic efficiency was found to be uniform after 50 cycles (Fig.4.8b). The charge capacity of 138.01 mAhg^{-1} for the initial cycle corresponds to 95.45% theoretical efficiency of LiCoO_2 . The coulombic efficiency is 97% for the initial cycle, which increased to 99% after 7 cycles. After the initial cycle, a slight drop in the voltage resulted in an improved coulombic efficiency. High performance of PHNF may be attributed to its lower crystallinity, improved electrolyte uptake and higher ionic conductivity. After 50 cycles, the specific charge capacity reduced to 132.1 mAhg^{-1} , which is 95% of that of initial cycle. However, The Li/PHNF/LiCoO_2 cell displayed high charge-discharge capacities with very little loss in capacities up to 50 cycles. The charge-discharge capacity versus cycle index along with coulombic efficiency of this cell is shown in Fig. 4.9a. This confirms that the PHNF based separator electrolyte exhibits better cycle performance and could be a promising material as separator in LIB's.

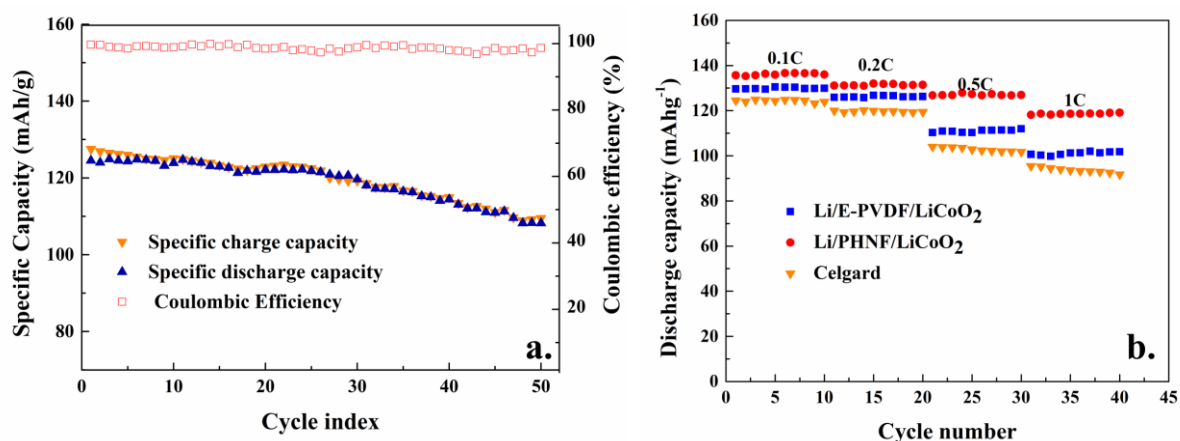


Fig. 4.9 (a) Charge-discharge performance and coulombic efficiency of $\text{Li/Celgard}^{\text{®}}2400/\text{LiCoO}_2$ cell (b) Discharge capacity of $\text{Li/Celgard}^{\text{®}}2400/\text{LiCoO}_2$, Li/E-PVDF/LiCoO_2 and Li/PHNF/LiCoO_2 at different current rates.

Rate capabilities of the cell with $\text{Celgard}^{\text{®}}2400$, PVDF and PHNF based separator were also tested and the results are shown in Fig. 4.9b. Cells were charged and discharged at current densities 0.1 C , 0.2 C , 0.5 C and 1 C for 10 times in order to form a good interface layer on the electrode surface. From 0.1 C to 0.2 C there is a little change in capacity. However, at higher current densities the capacity drops, because, at higher current densities the effect of ion transport on the ohmic polarization will increase significantly, leading to the loss in capacity (Wang et al. 2015). PHNF based separator exhibited high cycle performance with better charge

rate, while a considerable loss in capacity was observed in Celgard[®]2400 and PVDF based separators. The stability of PHNF at higher current densities may be attributed to the better Li-ion transport and the compatibility between HNT and PVDF that improved ionic conductivity of PHNF. In addition, HNT provides positive reactions on the interface stability absorbing impurities in the electrolyte that hinders the reactions between the impurities in the liquid electrolyte with lithium metal (Zhu et al. 2016).

PVDF/HNT based non-wovens have several advantages, such as low cost, eco-friendliness, unpretentious and efficient productivity. It exhibits many interesting characteristics including high porosity, lower crystallinity, higher absorbance of electrolyte, high ionic conductivity, electrochemical stability and thermal stability with exceptional cycle performance and mechanical properties. It is important to notice that the use of PVDF/HNT non-wovens helps in improving all the characteristics simultaneously, which is considered to be very difficult with most of the systems. In addition, these non-wovens can be produced on an industrial scale due to the scalability of electrospinning.

4.2. CONCLUSIONS

The synergistic effect of electrospinning and HNT plays a vital role in producing long, homogenous and smooth fibers. In PHNF, the β -phase of PVDF improved to 81% and the crystallinity of PVDF decreased to 31%. PHNF mats have uniform and interconnected porous structure, which resulted in a high electrolyte uptake. Electrochemical stability and ionic transference of PHNF separator increased compared with that of the commercial and PVDF separator. PHNF separator has low ionic resistance, superior tensile strength and thermal stability. The separator showed high resistance to puncture compared with PVDF based separator. PHNF based separator not only addresses the issue of ionic conductivity and high energy density, but is also safe and cost effective. The Li/PHNF/LiCoO₂ cell showed a high capacity for the initial cycle. The performance of PHNF separator at different current densities was remarkably better than those of Celgard[®]2400 and PVDF separators. Most importantly the separator performed exceptionally well when subjected to repeated charge-discharge cycles. This study not only demonstrates the role of PHNF separator in LIB's, but also proves that it could enhance the performance of LIB's.

CHAPTER 5

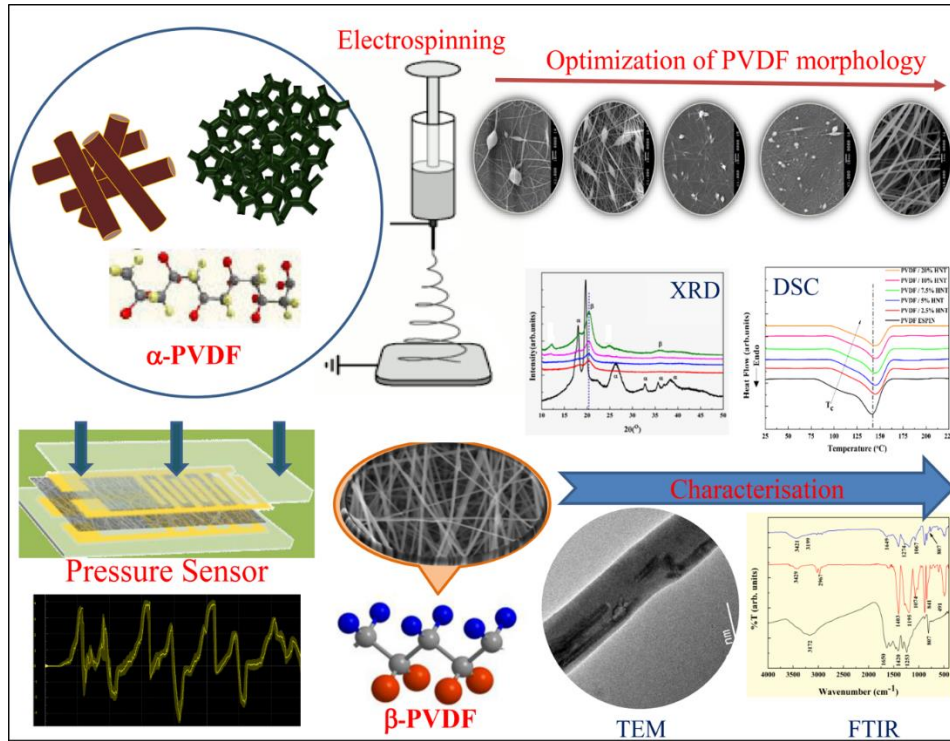
DURABLE, EFFICIENT AND FLEXIBLE PIEZOELECTRIC NANOGENERATOR FROM ELECTROSPUN PANi/HNT/PVDF BLEND NANOCOMPOSITE

The results of this chapter have been published in Polymer composites, 2018;

DOI: [10.1002/pc.24916](https://doi.org/10.1002/pc.24916).

CHAPTER 5

DURABLE, EFFICIENT AND FLEXIBLE PIEZOELECTRIC NANOGENERATOR FROM ELECTROSPUN PANi/HNT/PVDF BLEND NANOCOMPOSITE



This chapter discusses about the fabrication of piezoelectric nanogenerator based on electrospun PANi/HNT/PVDF blend nanocomposite (BNCNF). Polymorphism, crystallinity and morphology of the nanogenerator were explored in detail. HNT and PANi acted as a nucleating agent and conductive filler, respectively in PVDF; their synergism helps to improve the piezoelectric performance of PVDF. The piezoelectric performance of the nanogenerator patch was studied under various external mechanical stresses, such as pressure, tapping, and impact. To demonstrate the applicability of the BNCNF nanogenerator for self-powered devices, a nanogenerator patch was attached to a human elbow.

5.1. RESULTS AND DISCUSSION

5.1.1. Characterization of PANi

WAXD analysis was carried out to ascertain the formation of PANi (Fig. 5.1a). In WAXD, due to the parallel and perpendicular periodicity of PANi chains, broad diffraction peaks were observed between 10 and 30°. Peaks at 22.15° and 25.40° with d-space of 4.08 and 3.6Å, respectively indicate the amorphous nature of PANi. Peaks at 22.15 and 25.4° may be ascribed to the parallel and perpendicular periodicity of polymer chains. Further, low crystallinity may be attributed to the periodicity of benzenoid and quinoid rings in PANi chains (Mostafaei and Zolriasatein 2012a).

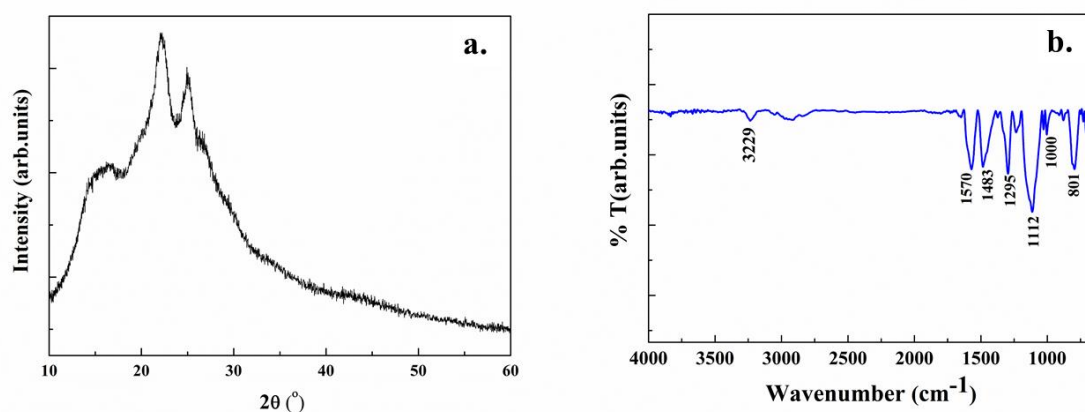


Fig. 5.1 (a) WAXD pattern of PANi nanorods (b) ATR mode FTIR spectrum of PANi nanorods.

FTIR spectrum of PANi prepared by solid state synthesis method is shown in Fig. 5.1b. The bands arising at 801 and 1112 cm^{-1} correspond to the out of plane bending of C-H in benzene rings. Bands at 684 and 700 cm^{-1} , respectively are assigned to the NH_2 wagging and C-H out of plane bending in aromatic rings. Bands arising at 1483 and 1570 cm^{-1} are assigned to the C=N stretching of benzenoid and quinoid rings, respectively. Similarly, the band at 1295 cm^{-1} corresponds to the aromatic stretching of C-N aromatic amine group. Bands observed at 1374 and 3229 cm^{-1} , respectively correspond to the C≡N stretching and N-H stretching (Reddy and Anandhan 2016a). Thus, the WAXD and FTIR results confirm the formation of PANi. TEM micrograph (Fig. 5.2a) of PANi reveals its rod-like morphology with relatively smooth surface and uniform size. AFD of PANi nanorods was 65 nm with SD of 7 nm (Fig. 5.2b).

5.1.2. Morphological studies

Fig. 5.3a–d shows the SEM images of electrospun nanofibers of E-PVDF, PPNF, PHNF, and BNCNF. Electrospinning parameters were optimized to produce smooth, uniform and bead-free nanofibers. E-PVDF produced were non-uniform and randomly arranged. For E-PVDF, AFD was found to be 351 nm with SD of 153 nm. But, PPNF, PHNF and BNCNF were fine, smooth, uniform and the AFD decreased drastically. This is due to the addition of PANi and HNT, which increase the electrical conductivity of the solutions (Martins et al. 2013; Dhakras et al. 2014).

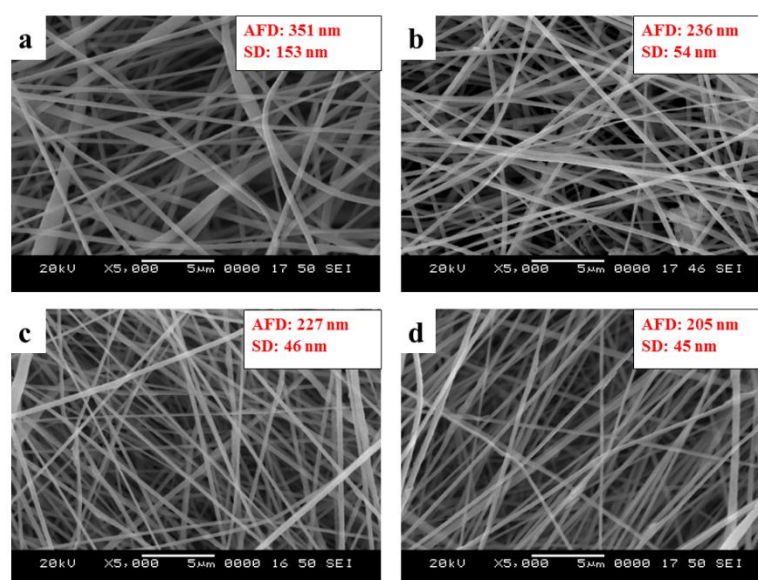


Fig.5.2 SEM micrographs of electrospun nanofiber mats: (a) E-PVDF; (b) PPNF; (c) PHNF; (d) BNCNF.

PANi carries charges, hence when the voltage is applied on the solution droplet, fibers are subjected to high tensile force resulting in decrease of AFD (Pillay et al. 2013). HNT is identical to kaolinite clay, but has tubular morphology. The outer surface of HNT is made of Si-O units and the inner core comprises of Al-O units. Therefore, HNT has negative surface potential and partially positive potential from the inner core of HNT leading to the improved electrospinning solution conductivity (Leporatti 2017). Interestingly, most of the BNCNF nanofibers were uniaxially aligned due to the increased solution conductivity that led to improved stretching of the electrospun jets.

5.1.3. FTIR analysis

Effect of PANi, HNT and electrospinning on the polymorphism of PVDF was investigated using FTIR spectroscopy (Fig. 5.4a). In pristine PVDF film, bands arising at 490, 614, 713, 862, 952, 1019, and 1685 cm^{-1} correspond to the α -phase of PVDF, whereas bands appearing

at 464, 754, 840, 1075, and 1400 cm^{-1} correspond to the β -phase of PVDF. (Kobayashi et al. 1975; Bormashenko et al. 2004; Lopes et al. 2011; Janakiraman et al. 2016). Pristine PVDF film (unstretched) predominantly consists of the α -phase. But, β -phase bands were observed predominantly for the electrospun mats. The β -phase content of PPNF, PHNF and BNCNF increased to 43.2, 78.7, and 84.1%, respectively. In PPNF, β -phase improvement was not significant compared with E-PVDF. Interestingly, PANi does not play any role in enhancing the β -phase of PVDF, but the small increment of β -phase is attributed to the increase in stretching force of fibers due to improved solution conductivity (Mostafaei and Zolriasatein 2012b; Yu et al. 2016). Meanwhile, PHNF fibers showed drastic improvement in β -phase content, which is attributed to the synergistic effect of HNT and electrospinning. HNT has been proven to act as a nucleating agent for PVDF, which is due to the dipole-dipole attraction between the oxygen atoms of HNT and C-H groups of PVDF. Alongside, the hydrogen bonding between hydroxyl groups of HNT and the fluorine atoms of PVDF enhances the formation of β -phase (TTT conformations) in PVDF (Neppalli et al. 2013; Wang and Huang 2014b).

5.1.4. WAXD analysis

WAXD patterns of pristine PVDF film, E-PVDF, PPNF, PHNF, and BNCNF are shown in Fig. 5.4b. For pristine PVDF film, peaks at 18.3, 19.6, 26.2, 35.6, and 38.4°, respectively correspond to the following crystal planes α -phase of PVDF: (0 2 0), (1 1 0), (0 2 1), (2 0 0), and (0 0 2). For electrospun PVDF mats, peaks representing α -phase diminished and a new peak was observed at 20.5° corresponding to the (1 1 0/2 0 0) crystal plane of the β -phase.

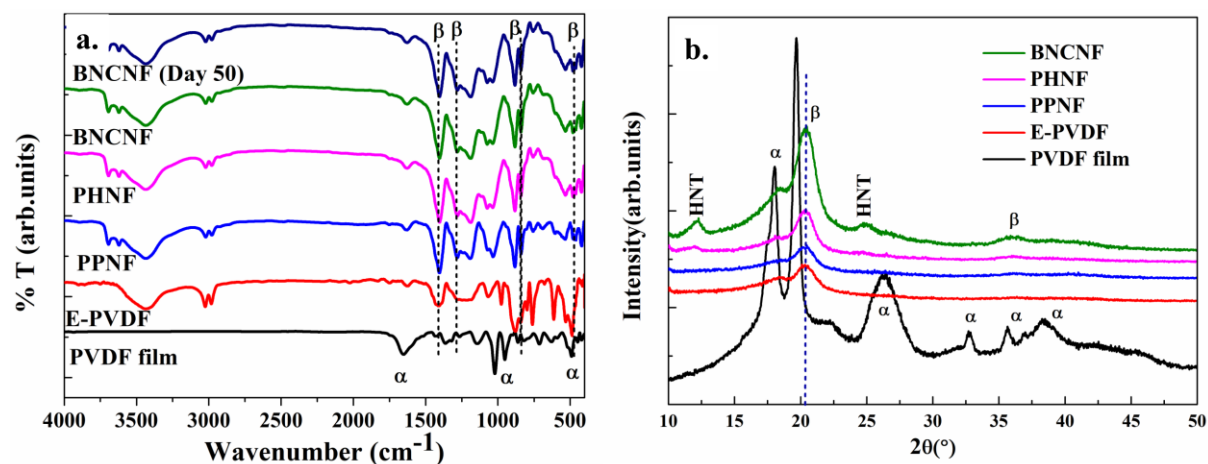


Fig. 5.3 (a) FTIR spectra (b) WAXD patterns of pristine PVDF film, E-PVDF, PPNF, PHNF and BNCNF.

The β -phase content was increased further by the addition of HNT and PANi. In the WAXD patterns of PHNF and BNCNF, peaks observed at 12.5 and 24.8° correspond respectively to

the (1 1 0) and (0 2 0) crystal planes of HNT (Yu and Cebe 2009a; Price et al. 2010; Kizildag et al. 2016).

5.1.5. TEM analysis

TEM micrograph of BNCNF is shown in Fig. 5.5a. Inside a single BNCNF, HNT and PANi are clearly visible. HNT's are oriented along the fiber axis due to the process induced alignment during the electrospinning. SAED pattern (Fig. 5.5b) was used to determine the polymorphism, interplanar distance and crystal planes. The interplanar distance for (1 1 0/2 0) crystal plane was found to be 0.44 nm that corresponds to the β -phase of PVDF. Interplanar distances for (0 0 2) and (0 2 0) crystal planes were found to be respectively 0.3 and 0.4 nm that correspond to HNT crystals. Similarly, (1 1 0) crystal plane with an interplanar distance of 0.37 nm corresponds to the α -phase of PVDF.

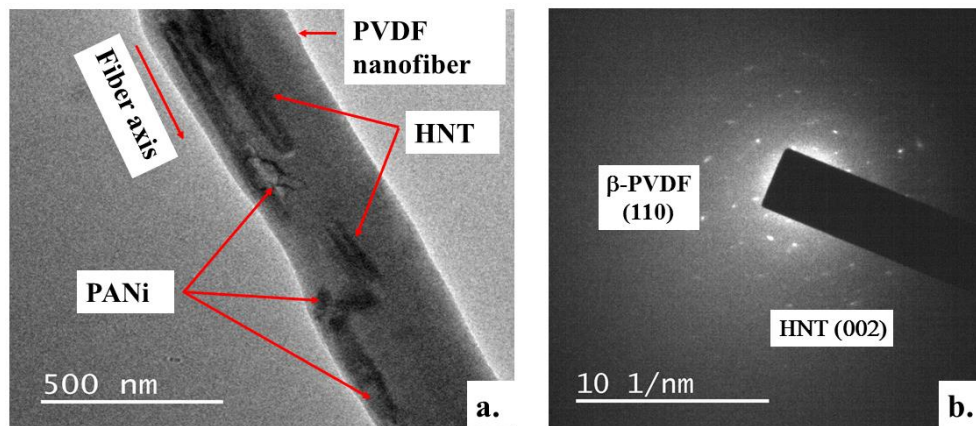


Fig. 5.4 (a) TEM micrograph of BNCNF; and (b) SAED pattern of BNCNF.

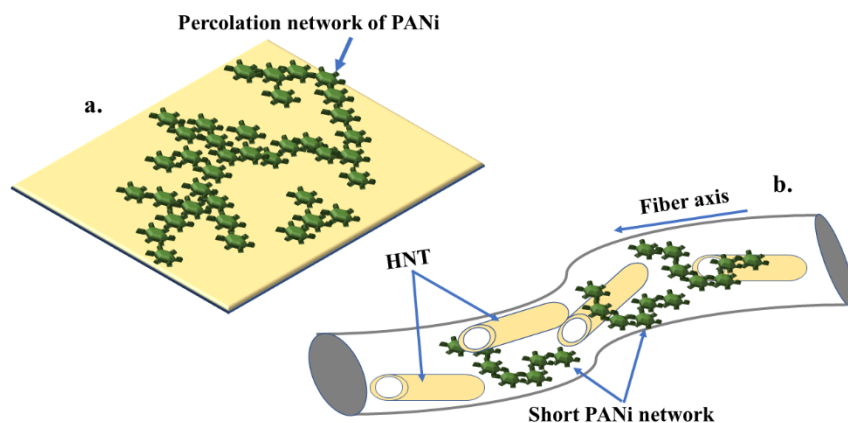


Fig. 5.5 Schematic showing the formation of network of PANi in: (a) PVDF/PANi film; and (b) BNCNF.

Short PANi networks are seen in the TEM micrographs of BNCNF, which may be ascribed to the high stretching of fibers during the electrospinning process. High stretching of nanofibers induces the orientation of HNT along the fiber axis, whereas it hinders the formation of a continuous network of PANi. This resulted in varied electrical conductivity of BNCNF nanofibers at different locations.

Also, the fine dispersion of PANi in PVDF solution leads to weakening of percolation network, which deteriorates its electrical conductivity (Price et al. 2010). Further, during the electrospinning of BNCNF, the solvent evaporates rapidly and hence the formation of percolation network is difficult; whereas in solution casting, there will be sufficient time for the complete evaporation of solvent, which favors the PANi network formation (Fig. 5.6a and 5.6b). Even though the PANi networks are short, there was an increase in the piezoelectric performance of BNCNF because of the mere presence of PANi. E-PVDF fibers were white in color that turned dark green upon the addition of PANi. Above 17.5 wt% of PANi loading, the electrospinning of BNCNF was difficult and the resultant nanofibers were highly disordered with lots of beads. This may be attributed to the agglomeration of PANi at high concentrations (Kizildag et al. 2016). Also, the inhomogeneity of solution led to blocking at the spinneret tip.

5.1.6. Piezoelectric performance of BNCNF nanogenerator

The piezoelectric response and energy harvesting capability of BNCNF were measured using an indigenous setup under different loads (Fig. 5.7a). 10 wt% of HNT and 17.5 wt% of PANi were present along with PVDF in the BNCNF. The highest β -phase content of PVDF was obtained at 10 wt% loading of HNT; whereas, for PANi the percolation threshold was 17.5 wt%. To begin with, the piezoelectric voltage outputs of E-PVDF, PPNF, PHNF, and BNCNF were measured to confirm the role of the β -phase in their piezoelectric performance. The voltage output was recorded under varying pressure (0.11–1.2 MPa) on nanofibers mats of the dimensions $2 \times 2 \times 0.0045$ cm. The piezoelectric voltage output for BNCNF nanogenerator under various pressures is shown in Fig. 5.7b. The lowest voltage output was recorded for E-PVDF followed by PHNF and PPNF. By adding HNT in PVDF, the β -phase content (78%) and the piezoelectric voltage output (0.9V) were improved compared to E-PVDF (β -phase: 31.1% and voltage output: 0.35 V). However, to further improve the piezoelectric conversion efficiency and conductivity of PVDF, PANi nanorods were added to PVDF alongside HNT.

For, BNCNF, the β -phase content was 84%, while the piezoelectric voltage output was approximately 4.2 V. The voltage output from BNCNF is approximately 5 and 10 times higher than that of the PHNF and E-PVDF, respectively.

The piezoelectric performance of BNCNF mats under real life situation was evaluated under tapping by human finger (one- as well as two-finger tapping) on the nanogenerator mat. The setup used in this study is shown in Fig. 5.8a and 5.8b. When the generator was tapped continuously the output voltage was generated. Interestingly, the output voltage produced was stable and consistent under continuous tapping. For one-finger tapping, a voltage output of 3.4 V was generated (Fig. 11a).

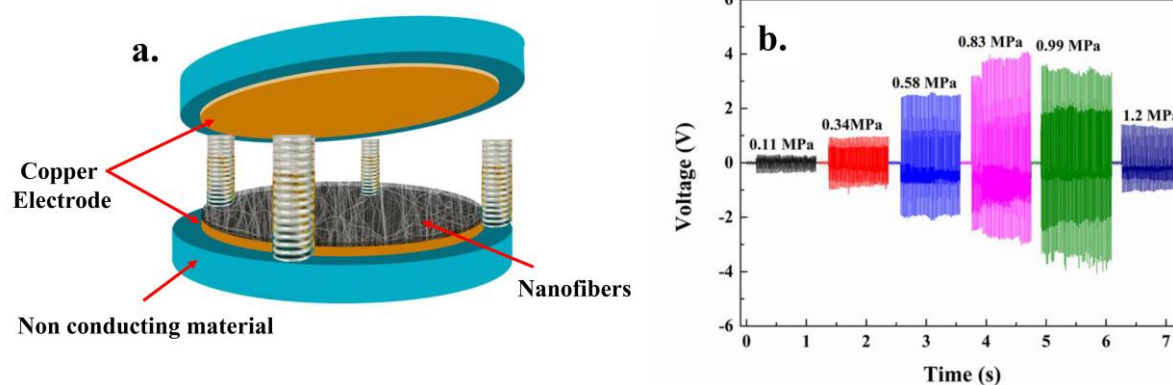


Fig.5.6 (a) Schematic, and b) digital photograph of indigenous setup for the evaluation of piezoelectric performance; (c) Piezoelectric performance of BNCNF nanogenerator under different pressure.

Similarly, voltage output of 6.5 V was generated for two-finger tapping (Fig. 11b), which is 15 times higher than that produced by E-PVDF nanogenerator under the same loading condition. The piezoelectric output voltage consistently showed positive and negative signs, which indicates the imparting and releasing of finger from the nanogenerator. To demonstrate the applicability of the BNCNF nanogenerator for self-powered devices, a nanogenerator patch was attached to a human elbow. To generate an external stress, the arm was bent and straightened. Upon bending and straightening, the nanogenerator patch generated an output voltage up to 1.5 V (Fig. 5.9a). Further, to study the stability and repeatability of BNCNF nanogenerator, it was tapped 2,000 times continuously. Interestingly, the output voltage was stable and consistent even after 2,000 cycles. The durability and repeatability of BNCNF nanogenerator patch, its piezoelectric performance was evaluated at regular intervals over a period of 50 days in tapping mode. The voltage output generated by the nanogenerator was

found to be uniform even after 50 days (which is obviously due to the retention of the β -phase content in BNCNF even after 50 days with little loss (Fig.5.9b).

The piezoelectric response of BNCNF nanogenerator was studied also under impact loads. Standard weights of 7, 14 and 19 g were dropped from a height of 5, 10, and 20 cm. The voltage output was generated for a very short period of time that is, 0.25 s. A maximum voltage output of 7.2V was generated for 14g load and 10cm height.

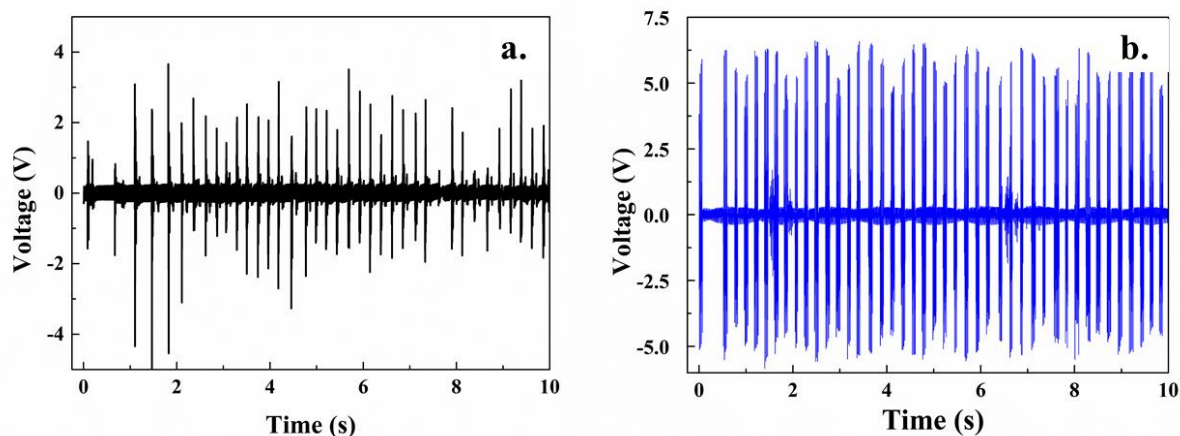


Fig. 5.7 Piezoelectric performance of BNCNF nanogenerator under: (a) one finger tapping (b) two-finger tapping.

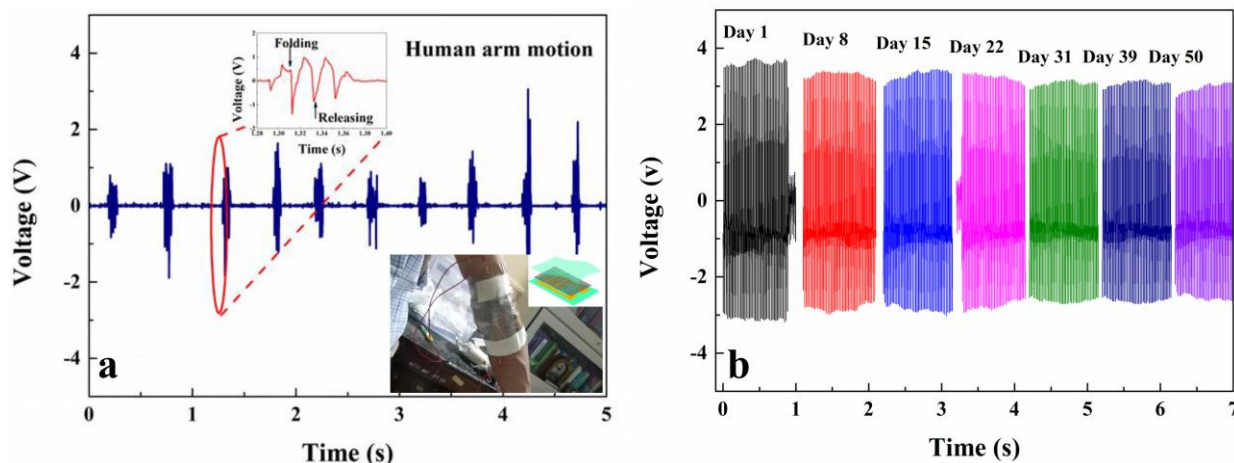


Fig. 5.8 Voltage output of BNCNF nanogenerator patch (a) attached to a human arm (Inset: Digital photograph of BNCNF patch attached to human arm) (b) Variation of piezoelectric performance of BNCNF nanogenerator with time.

The power density, voltage and current output from the nanogenerator were also measured. Fig. 5.10a shows the voltage and current output of BNCNF nanogenerator measured under one-finger and two-finger tapping mode, respectively at different load resistance (0.5-15M Ω). With an increase in load resistance, the current output decreased gradually, while the

voltage output increased. The power density (P) of BNCNF nanogenerator under tapping mode was calculated by

$$P = \frac{V^2}{R_L \cdot A} \quad (5.1)$$

where V is the voltage output, R_L is the load resistance and A is the effective area of the nanogenerator (5.1 cm^2) (Jang et al. 2016; Li et al. 2017). Fig. 5.10b shows the power density of BNCNF nanogenerator under tapping mode. The maximum power output was produced at a load resistance of $3 \text{ M}\Omega$ under two-finger tapping that decreased gradually with increasing load resistance. The flexible BNCNF nanogenerator showed a maximum current and power density of $0.75 \mu\text{A}$ and $0.25 \mu\text{W}/\text{cm}^2$.

From the ongoing discussion it can be seen that the BNCNF nanogenerator exhibited enhanced performance compared to E-PVDF nanogenerator. In addition, BNCNF has a natural advantage of being non-toxic and environmentally compatible. Further, such nanogenerator can be attached to a movable part or objects to harvest energy. The successful creation of BNCNF and evaluation reveals its potential in sensors and self-powered devices. To sum up, cost effective and ecofriendly BNCNF mats can be produced continuously on an industrial scale due to the scalability and simplicity of the electrospinning technique.

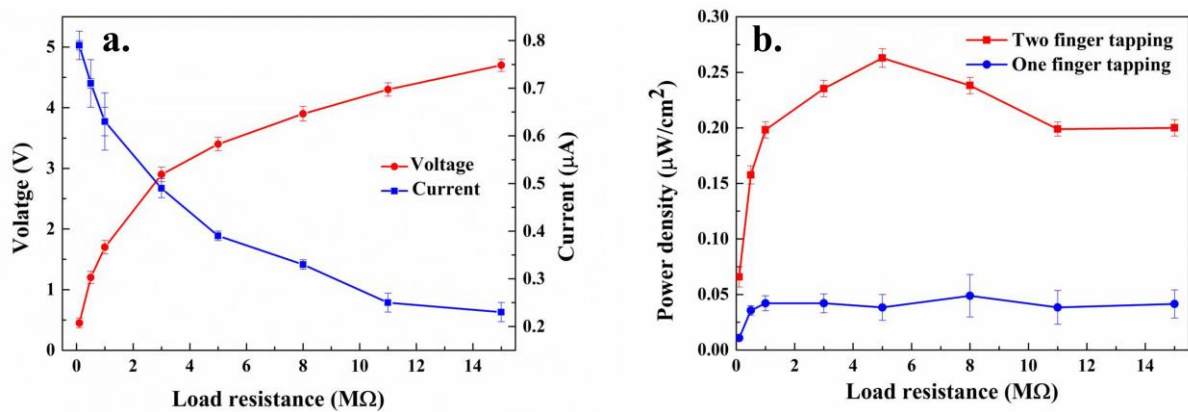


Fig. 5.9. (a) Current and voltage output with respect to the load resistance under two finger tapping (b) Power density of BNCNF nanogenerator with respect to the load resistance under one and two fingers tapping.

5.2. CONCLUSIONS

Flexible nanogenerator based on electrospun fabric of BNCNF was synthesized. The β -phase content was the maximum (84.1%) in BNCNF mats. The newly developed nanogenerator showed high performance and generated voltage up to 7.2V. The maximum current and power density output of BNCNF nanogenerator were respectively 0.75 μ A and 0.25 μ W/cm². This nanogenerator showed a constant voltage output even after 50 days and 2,000 cycles of loading without any significant loss, confirming the durability of this nanogenerator. Overall, the simplicity and scalability of fabrication of this nanogenerator combined with its high performance could make it a suitable candidate for flexible self-powered devices and sensors.

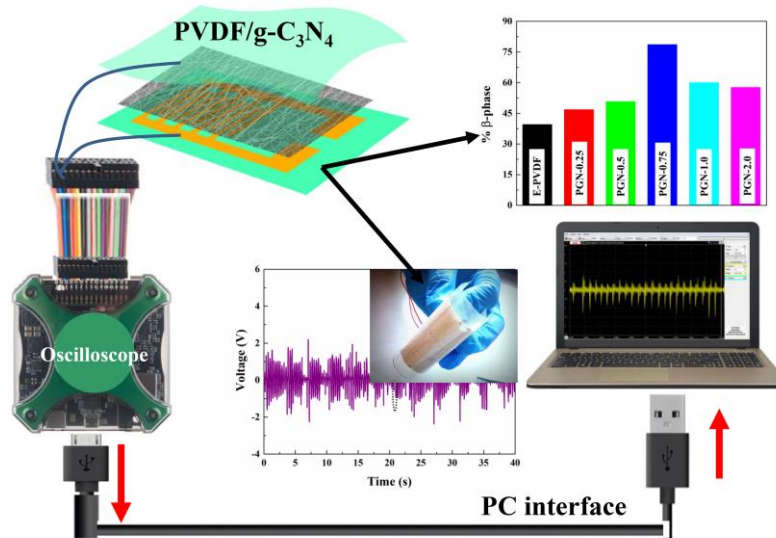
CHAPTER 6

**SYNERGISM OF GRAPHITIC-CARBON NITRIDE AND
ELECTROSPINNING ON THE PHYSICO-CHEMICAL CHARACTERISTICS
AND PIEZOELECTRIC PROPERTIES OF FLEXIBLE POLY(VINYLDENE
FLUORIDE) BASED NANOGENERATOR**

*The results of this chapter have been published in Journal of polymer research, 2018;
26:73.*

CHAPTER 6

SYNERGISM OF GRAPHITIC-CARBON NITRIDE AND ELECTROSPINNING ON THE PHYSICO-CHEMICAL CHARACTERISTICS AND PIEZOELECTRIC PROPERTIES OF FLEXIBLE POLY(VINYLIDENE FLUORIDE) BASED NANOGENERATOR



This chapter emphasizes to investigate the piezoelectric performance of electrospun poly(vinylidene fluoride)/graphitic carbon nitride (PVDF/g-C₃N₄) nanocomposite fibers (PGN-X). The morphological, structural and thermal characteristics were also investigated. The synthesized PGN non-woven mats were flexible and are easily deformable without disrupting the continuity of fibers. Detailed investigation was carried out to study the polymorphism, crystallinity and thermal characteristics of PGN-X. Addition of g-C₃N₄ nanosheets are expected to improve the thermal and mechanical properties. g-C₃N₄ nanosheets were incorporated at different loadings (0.25, 0.5, 0.75, 1.0 & 2.0 wt% based on the weight of PVDF). The samples were tested for piezoelectric performance by imparting human finger forces.

6.1. RESULTS AND DISCUSSION

6.1.1. Morphological studies

Fig. 6.1. shows the SEM images of E-PVDF and PGN-X nanofiber mats at different loadings of g-C₃N₄ nanosheets. Although PVDF nanofibers were obtained in all the cases without any beads and defects, the AFD and SD of the nanofibers decreased upon the addition of g-C₃N₄. There was a notable decrease in AFD observed up to 0.5 wt% of g-C₃N₄ nanosheets loading, thereafter there was a marginal change in the morphology. Uniform, continuous and finer fibers are considered to be ideal for the improvement of electroactive phases and piezoelectric properties of PVDF. The decrease in AFD and improved uniformity of nanofibers may be attributed to the increase of the solution conductivity upon the addition of g-C₃N₄ (Ma et al. 2017).

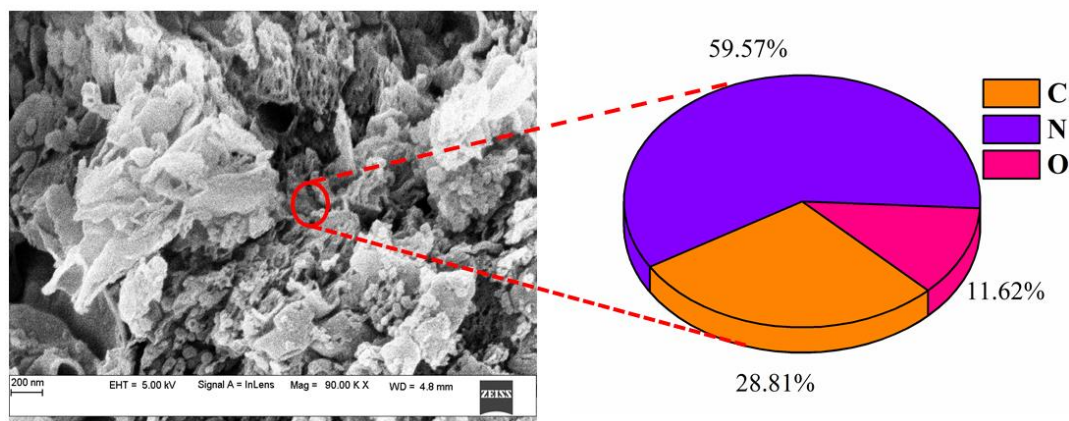


Fig. 6.1. HRSEM image of in-situ synthesized g-C₃N₄ along with elemental composition.

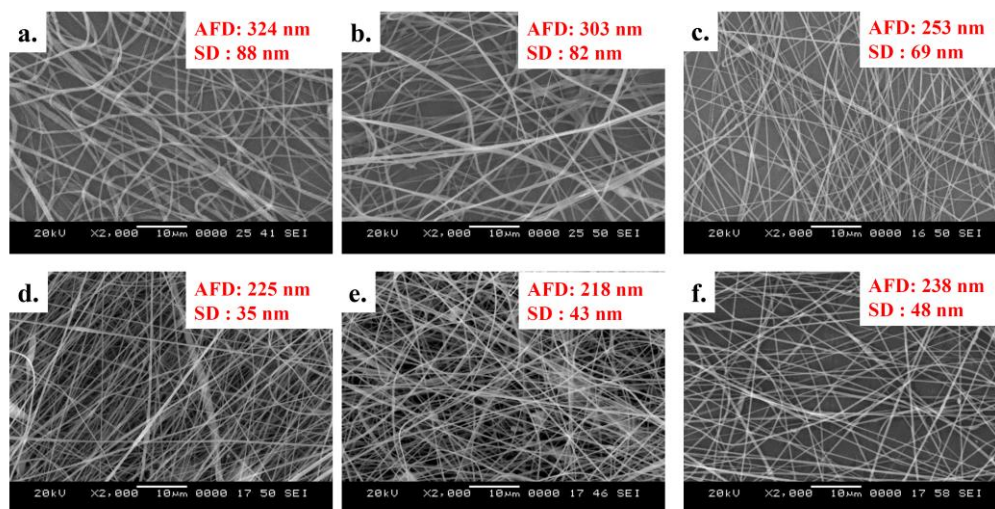


Fig. 6.2. SEM micrographs of (a) E-PVDF (b) PGN-0.25 (c) PGN-0.5 (d) PGN-0.75 (e) PGN-1.0 (f) PGN-2.0.

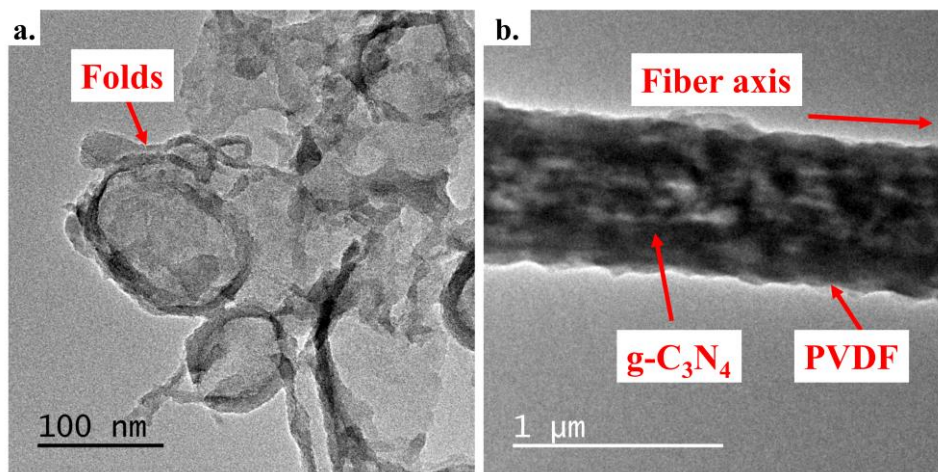


Fig. 6.3 TEM micrograph of (a) in-situ synthesized $g\text{-C}_3\text{N}_4$ nanosheets (b) PGN-0.75.

The presence of a layered structure of $g\text{-C}_3\text{N}_4$ confirmed from TEM micrograph (Fig. 6.3a). Folds can be clearly seen on the edges of the structure, which indicate the layered morphology of $g\text{-C}_3\text{N}_4$. The layered morphology would provide high surface area and improve the interaction with PVDF. Further, the TEM micrograph of PGN-0.75 was carried out (Fig. 6.3b). $g\text{-C}_3\text{N}_4$ nanosheets (dark spots) were seen inside the PVDF nanofiber and dispersed throughout the PVDF nanofiber.

6.1.2. FTIR and WAXD analysis

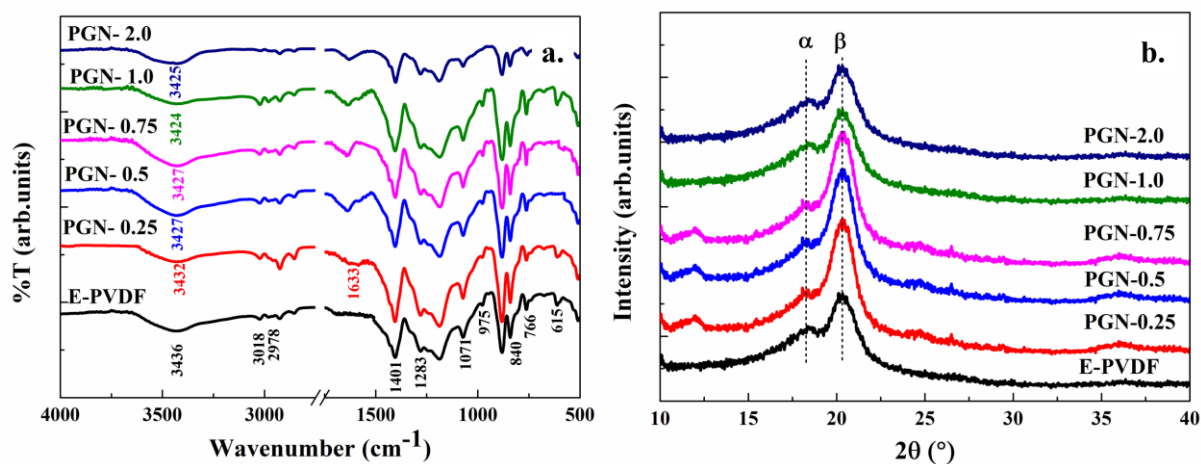


Fig.6.4 E-PVDF and PGN-X at different loadings of $g\text{-C}_3\text{N}_4$ nanosheets (a) FTIR spectra of. (b) WAXD patterns.

Fig. 6.4a shows the FTIR spectra of E-PVDF and PGN-X samples at different loadings of $g\text{-C}_3\text{N}_4$. In the spectrum of E-PVDF, bands arising at 615, 766 and 975 cm^{-1} correspond to the α -phase of PVDF, while bands at 510, 841, 1071, 1283 and 1401 cm^{-1} correspond to the

β -phase of PVDF. Band arising at 510, 615 and 766 cm^{-1} correspond to the CF_2 bending vibration while, the one at 841 cm^{-1} corresponds to the CH_2 rocking vibration. The bands arising at 976 and 1283 cm^{-1} , respectively correspond to the CH and CF out-of-plane deformations. Band arising 3018 and 2978 cm^{-1} correspond to the CH_2 symmetric and asymmetric stretching, respectively (Bormashenko et al. 2004; Cai et al. 2017). Also, a broad band at 3436 cm^{-1} is attributed to the hydroxyl group emerging from the pores of the polymer (Adams et al. 2012). There was a shift in bands observed at 3436 cm^{-1} and 975 cm^{-1} with the addition of g- C_3N_4 nanosheets. During the electrospinning of PVDF fibers, the simultaneous poling and stretching of fibers resulted in the formation of β -phase in PVDF while, solution cast PVDF film was dominated with α -phase and there was no indication of formation of the β -phase. There was also a small contribution of DMF in enhancing the β -phase content of PVDF fibers because of the interaction between C=O dipole of DMF molecules with CH_2CF_2 group of PVDF or by hydrogen bonding (Farid Abraham 1962; Benz et al. 2001). With an addition of g- C_3N_4 , the β -phase content of PVDF further increased up to a loading of 0.75%, after which there was a slight decrease in the same (Table 6.1). With an addition of g- C_3N_4 , the hydroxyl band shifted to lower wavenumber indicating the strong hydrogen bonding interaction between the fluorine atom of PVDF with the hydroxyl group of g- C_3N_4 . Also, the dipole-dipole interaction between the oxygen atom of g- C_3N_4 and CH group of PVDF helps in the formation of the β -phase. The decrement in the β -phase content in PGN-1.0 and PGN-2.0 may be due to the overdose of g- C_3N_4 that resulted in agglomerations.

Fig. 6.4b depicts the WAXD patterns of E-PVDF and PGN-X at different loadings of g- C_3N_4 nanosheets. Peaks arising at 18.4° (0 2 0) and 20.4° (1 1 0/ 2 0 0), respectively correspond to the α and β -phase of PVDF. The crystallinity of the samples was also calculated and reported in Table. 6.1. The crystallinity of PVDF decreased with the addition of g- C_3N_4 nanosheets, indicating probably it hinders the PVDF chain movement.

6.1.3. DSC analysis and tensile properties

Fig. 6.5a shows the DSC curves of E-PVDF and PGN-X at different loadings of g- C_3N_4 for the second heating cycle. A single melting peak was observed for all the samples. The melting temperature (T_m) of E-PVDF was observed at 172.1 °C and increase with the addition of g- C_3N_4 up to a loading of 0.75 wt%, thereafter it shifted again to lower melting temperature. The degree of crystallinity (X_c) was found to decrease for PGN-X samples as a result of inhibition

effect of g-C₃N₄ on the PVDF chain mobility. These results are in good agreement with the WAXD results (Table. 6.1).

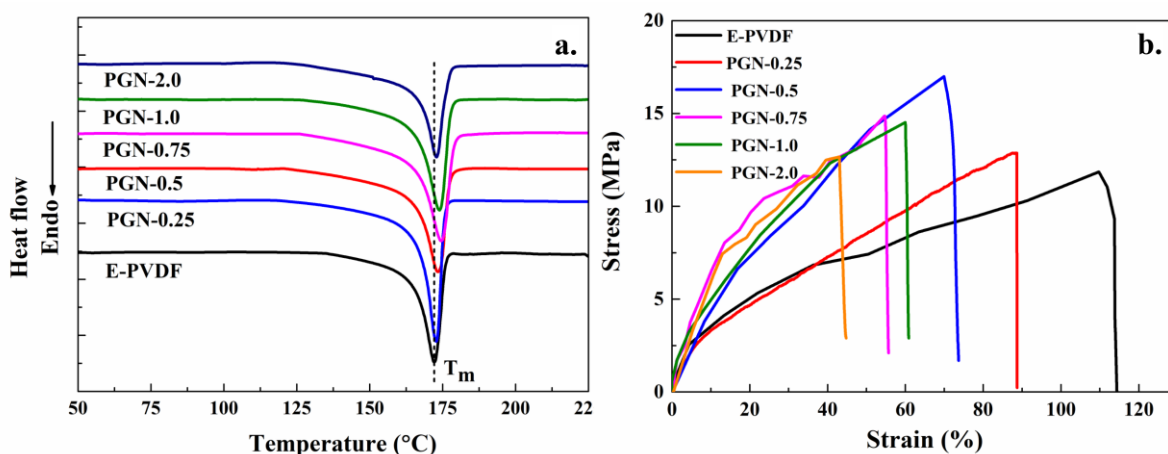


Fig. 6.5 E-PVDF and PGN-X at different loadings of g-C₃N₄ (a) DSC curves (b) Stress-strain curves.

It should be noted that, the crystallinity reduced up to 0.75 wt% and further increases for higher loading. The shift in melting temperature and change in %X_c indicates there was recrystallization occurred due to the addition of g-C₃N₄. Similar trend was observed with other nucleating agents such as carbon nanotube (Wu and Chou 2016a), montmorillonite clay (Yu et al. 2009), halloysite nano clay, graphene oxide (Fakhri et al. 2016), nano-alumina trihydrate etc. DSC analysis could be used effectively for accurate measurement of degree of crystallinity of PVDF, but the same could not be used in analyzing different phase of PVDF.

Fig. 6.5b shows the typical stress-strain curve of E-PVDF and PGN-X samples at different loadings of g-C₃N₄. For E-PVDF the tensile strength was 11.9 MPa that increases gradually with the addition of g-C₃N₄. Tensile strength decreased when the samples were loaded with g-C₃N₄ above 0.5 wt%. The maximum tensile strength of 17 MPa was observed for PGN-0.5. For all the loadings of PGN-X, the tensile strength was higher than that of E-PVDF (11.9 MPa). It must be noted that the increase in g-C₃N₄ loading gradually decreased the % elongation of the sample. Young's modulus was found to increase with the addition of g-C₃N₄ (E-PVDF: 26.4 MPa; PGN-0.25: 38.9 MPa; PGN-0.5: 45.8 MPa; PGN-0.75: 48.5 MPa; PGN-2.0: 52.4 MPa). The increase in tensile strength of nanocomposites is attributed to the presence of g-C₃N₄ nanosheets, which have tremendously high surface area and intrinsic mechanical properties. Also, the compatibility and high degree of dispersion of g-C₃N₄ provides good interfacial stress transfer efficiency.

Table 6.1. Melting temperatures, crystallization temperature and crystallinity of E-PVDF and PGN-X at different loadings of g-C₃N₄.

Sample	% β -phase	Second heating		Crystallinity (%)	
		FTIR	T _m (°C)	ΔH_m	DSC
E-PVDF	39.5	172.1	41.7	39.9	41.2
PGN-0.25	46.7	172.7	41.1	39.4	40.4
PGN-0.5	50.7	173.4	38.8	37.1	38.9
PGN-0.75	78.6	174.6	36.7	35.1	36.2
PGN-1.0	60.0	173.8	38.6	37.0	36.8
PGN-2.0	57.7	172.8	39.8	38.1	39.2

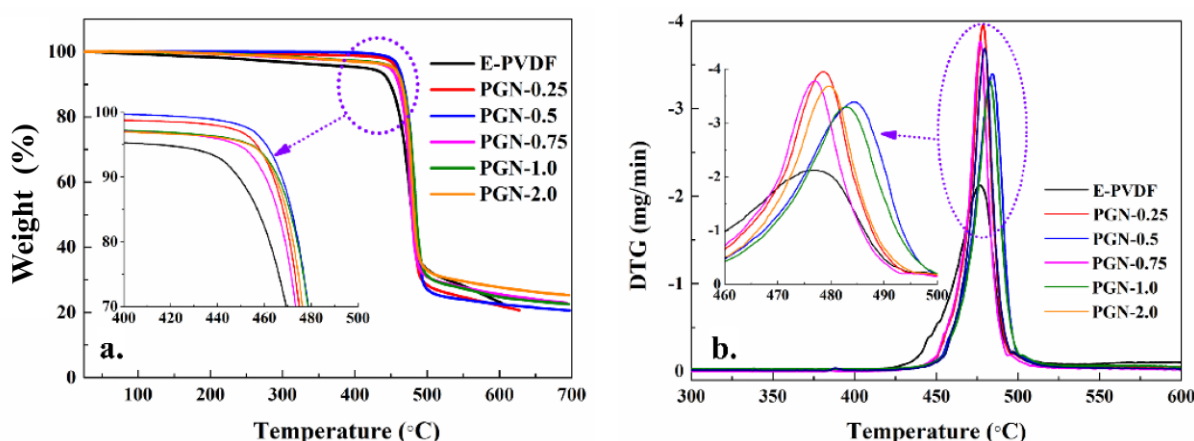


Fig. 6.6 (a) TGA curves of of E-PVDF and PGN-X for different loadings of g-C₃N₄ (b) DTG curves of E-PVDF and PGN-X for different loadings of g-C₃N₄.

6.1.4. TGA and DTG analysis

TGA and derivative thermograms (DTG) curves of E-PVDF and PGN-X samples at different loadings of g-C₃N₄ is shown in Fig.6.6a & 6.6b. For all the samples, one step degradation was observed. E-PVDF was stable up to 400 °C with 5% weight loss and major loss was observed at 440 °C and continued up to 600 °C. For PGN-X the onset temperature shifted to higher temperature compared with E-PVDF. Highest onset temperature of ~490 °C was observed for PGN-1.0. The increase in the stability is due to the presence of g-C₃N₄ in PVDF that acts as an insulating barrier to the expansion of heat and prevents the scissoring of PVDF chains. However, for PGN-2.0, the thermal decomposition temperature decreases, which may be due

to the presence of aggregates in g-C₃N₄ nanosheets at higher loading. Also, with an increase in g-C₃N₄ content, the % char formation was increased.

6.1.5. Piezoelectric performance of PGN-X

Fig. 6.7a shows the output voltage generated upon one finger tapping on E-PVDF and PGN-0.75 based nanogenerator. For E-PVDF maximum voltage output was 0.6 V while, for PGN-0.75 it was 2.6 V. Also, the piezoelectric voltage output improved with an increase in g-C₃N₄ content. It is important to note that the voltage output increased up to 0.75 wt% of g-C₃N₄ loading, thereafter a decline was observed in the output (Fig. 6.7b). This may be attributed to the presence of β -phase content and finer diameter of fibers. Fig. 6.8a shows the voltage output generated upon two-finger imparting for PGN-X. Upon imparting, the voltage output up to 3.8V was observed. Interestingly, the voltage output was found to be uniform compared to one finger tapping. This may be due to the uniform application of pressure throughout the surface of nanogenerator.

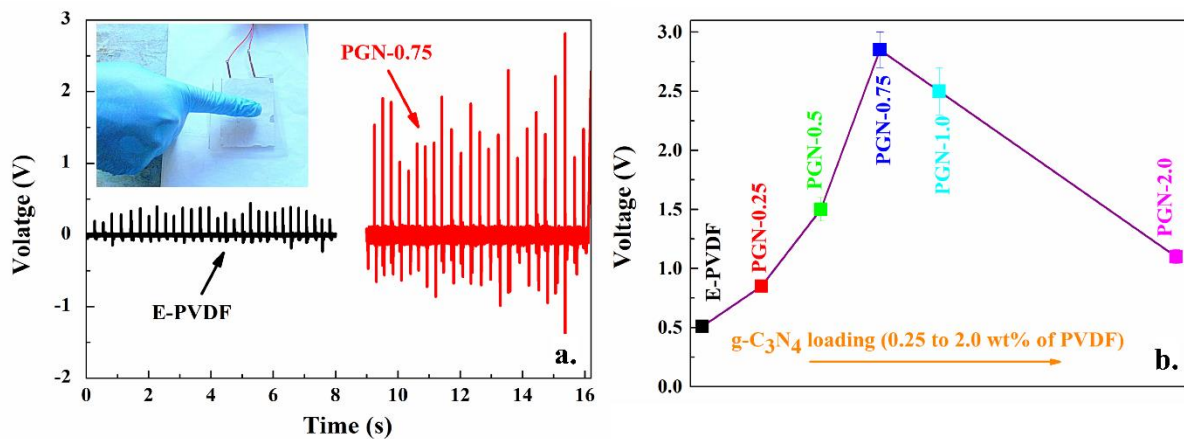


Fig. 6.7 (a) & (b) Piezoelectric performance of E-PVDF and PGN-X for different loadings of g-C₃N₄ under one finger tapping mode.

Fig. 6.8b shows the voltage output generated for E-PVDF and PGN-X for different loadings of g-C₃N₄. A similar trend was observed as in one finger tapping. The maximum voltage output was observed for PGN-0.75 based nanogenerator, which is ~4 times higher than that of E-PVDF. From the above observations it is clear that the β -phase content and morphology of the nanocomposite fiber influence the piezoelectric response of the nanogenerator. Hereafter, PGN-0.75 nanogenerator was considered for further study because of its high piezoelectric voltage output compared to the other systems developed in this study. The nanogenerator also showed superior touch sensitivity, which is very essential in energy harvesting application. Fig. 6.9a & b shows the voltage output produced due to imparting of a human thumb (pressing

and releasing) and palm (impact), respectively. The nanogenerator generated a maximum voltage output of $\sim 0.7V$ and $\sim 7.5V$ upon the application of pressure by thumb and palm imparting, respectively.

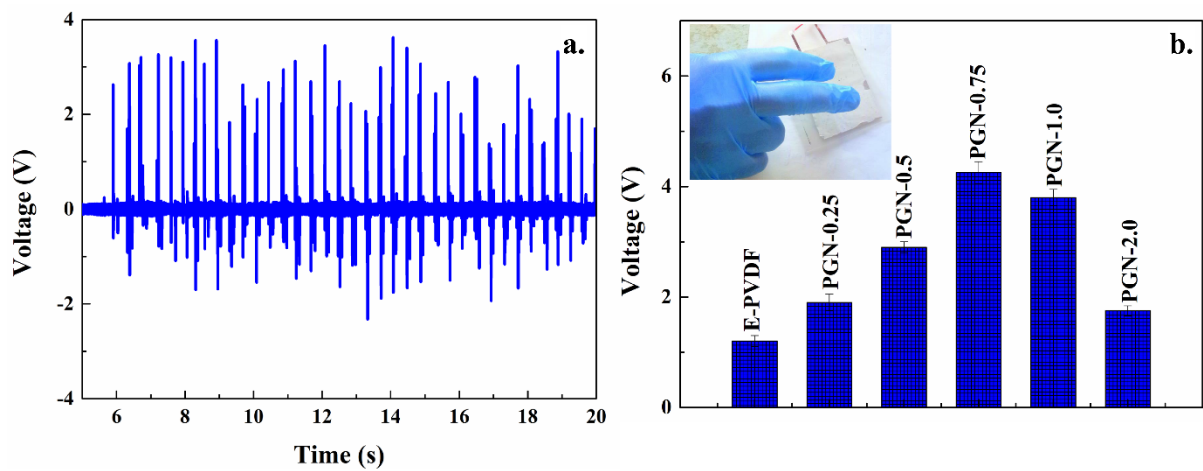


Fig. 6.8 (a) & (b) Piezoelectric performance of E-PVDF and PGN-X for different loadings of $g-C_3N_4$ under two finger tapping mode.

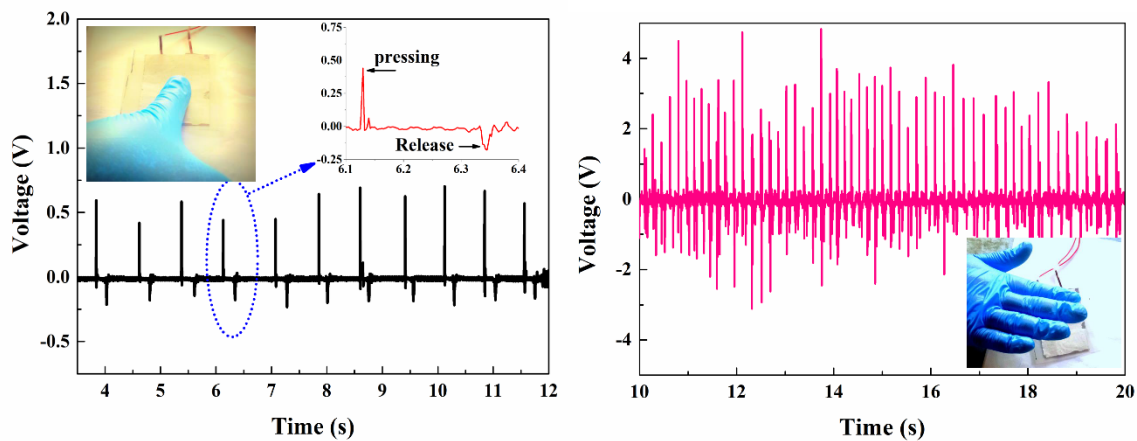


Fig. 6.9 Piezoelectric performance of PGN-0.75 under (a) thumb imparting b) palm (slapping) and releasing).

To verify that the voltage output is solely due to the piezoelectric effect, the switching polarity test was carried out (Fig. 6.10a & b). Upon finger imparting, the nanogenerator showed consistent voltage output in forward and reverse condition. The nanogenerator produced same voltage output in both the directions indicating that the voltage output produced was solely due to the piezoelectric effect and there is no interference of artificial charge generation or triboelectric effect. Also, these observations indicate the dipole reversibility due to the high level of ordering of CH_2 and CF_2 group of PVDF (Tamang et al. 2015). Also, the nanogenerator was tested for repeated bending test (Fig. 6.11a). Under the bending stress the nanogenerator generated piezoelectric voltage output. Upon bending the nanogenerator showed a voltage

output of $\sim 2\text{V}$ while, it was $\sim 1.5\text{V}$ when it was released. The current output of E-PVDF and PGN-X were evaluated under two finger tapping mode using picoammeter (DMC-111, SES instruments, India). The highest current output of $0.23\ \mu\text{A}$ was generated for PGN-0.75 nanogenerator (Fig. 6.12). In addition, the power density and voltage output generated with varying load resistance were investigated for PGN-0.75. The highest power density of $0.21\ \mu\text{W}/\text{cm}^2$ was obtained at a load resistance of $6\ \text{M}\Omega$ (Fig. 6.11b).

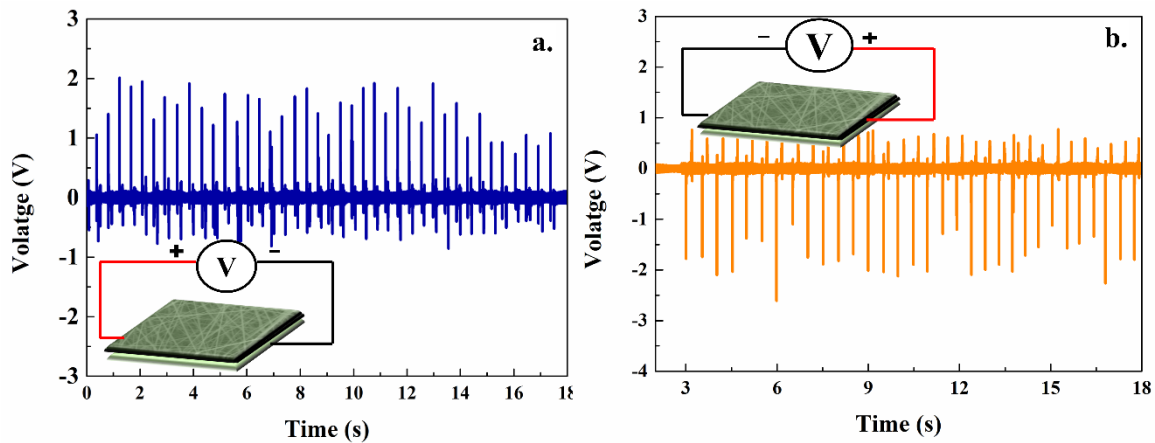


Fig. 6.10 Voltage output response of PGN-0.75 under (a) forward bias connection (b) reverse bias connection.

The nanogenerator responded to these stresses with maximum voltage output of $\sim 0.7\text{V}$ and $\sim 4\text{V}$ was generated for imparting of human thumb and palm, respectively.

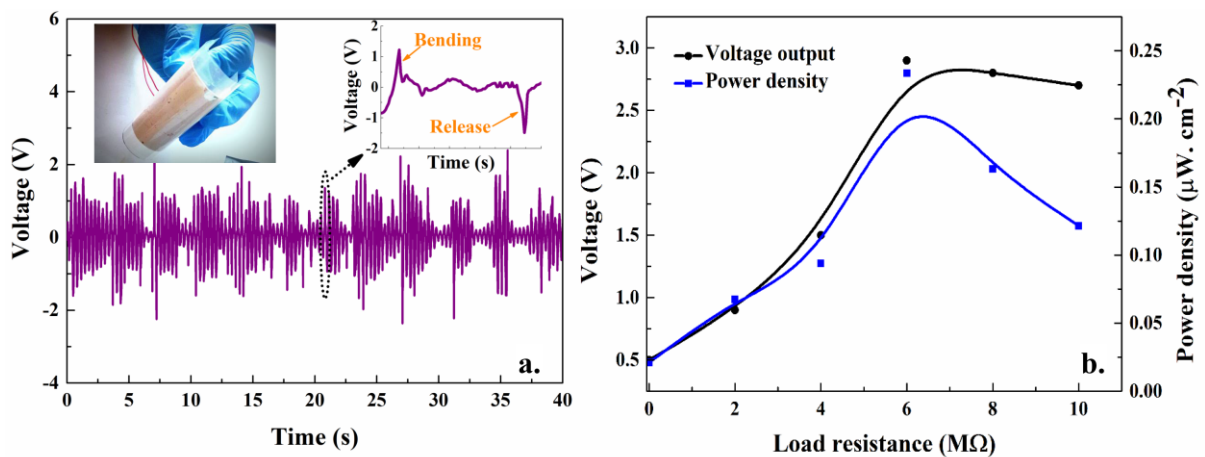


Fig. 6.11 (a) Voltage output of PGN-0.75 nanogenerator under bending mode (b) Power density of PGN-0.75 nanogenerator with respect to the load resistance under two fingers tapping.

The PGN-0.75 nanogenerator was tested for its reproducibility and stability. The nanogenerator displayed excellent stability without any loss in piezoelectric performance even after 18 weeks. To confirm its durability and stability, PGN nanogenerator was tested for 10000 cycles over a

period of 30 days. Interestingly, the nanogenerator showed consistent voltage output even after repeated cycles. The morphology of sample remained stable and there was no breakage of fibers observed even after 10000 cycles (Fig. 6.13a). Also, it is noteworthy that the electroactive phase of PVDF (β -phase: 76.1%) did not decay even after repeated cycles and time (Fig. 6.13b).

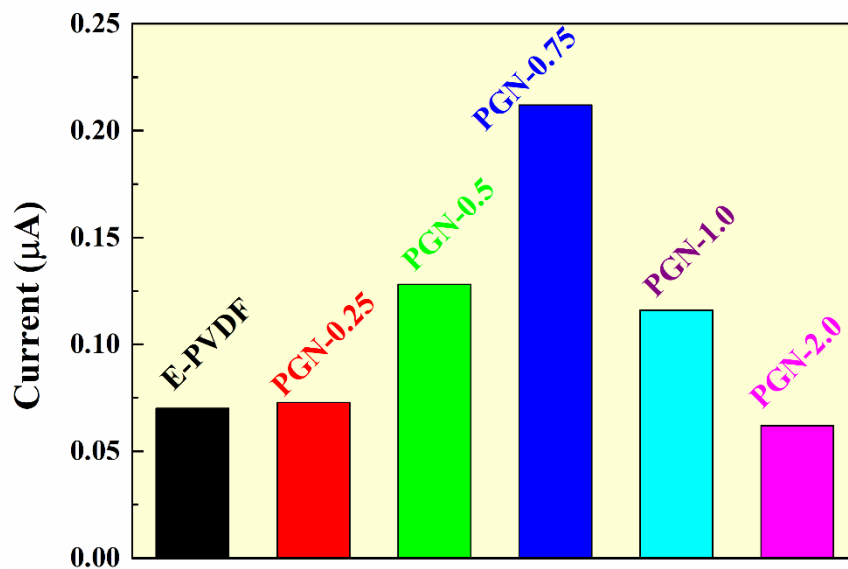


Fig.6.12 Current output of E-PVDF and PGN-X (X = 0.25, 0.5, 0.75, 1.0 & 2.0).

The voltage output of E-PVDF and PGN-0.75 at different loads (0.19-0.98N) is shown in Fig. 6.14. With an increase in the load on the nanogenerator, the voltage output of E-PVDF and PGN-0.75 increased. The highest voltage output of 5.1 V was generated for PGN-0.75 at 0.98 N.

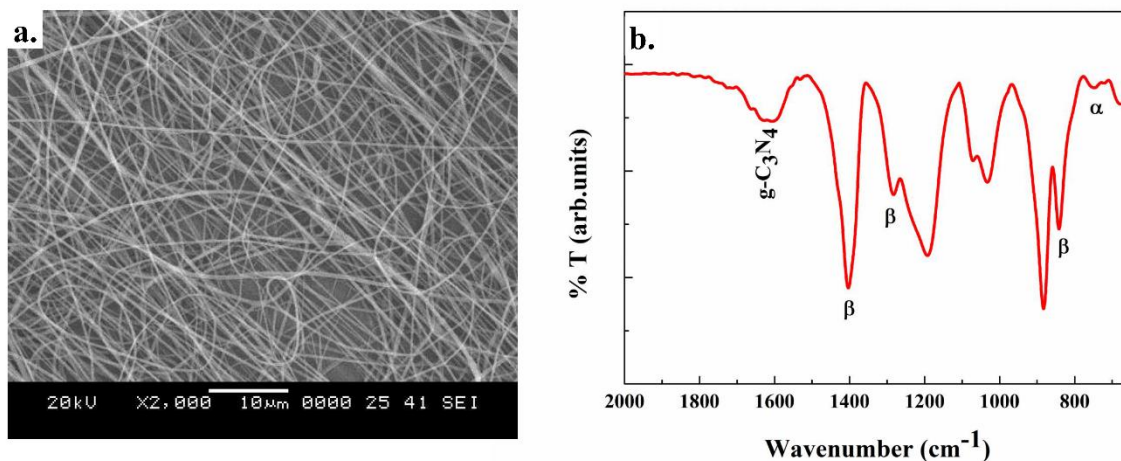


Fig. 6.13 (a) SEM micrograph of PGN-0.75 after 10000 cycles (b) FTIR spectrum of PGN-0.75 after 10000 cycles and 30 days.

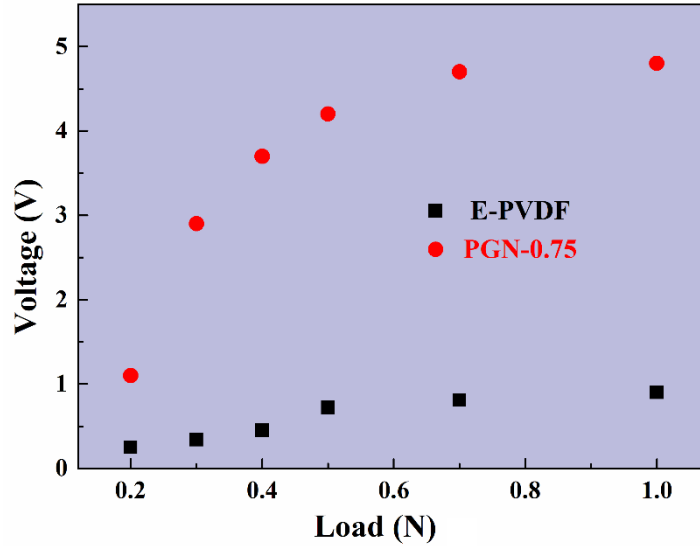


Fig. 6.14 Voltage output of E-PVDF and PGN-0.75 at different loads.

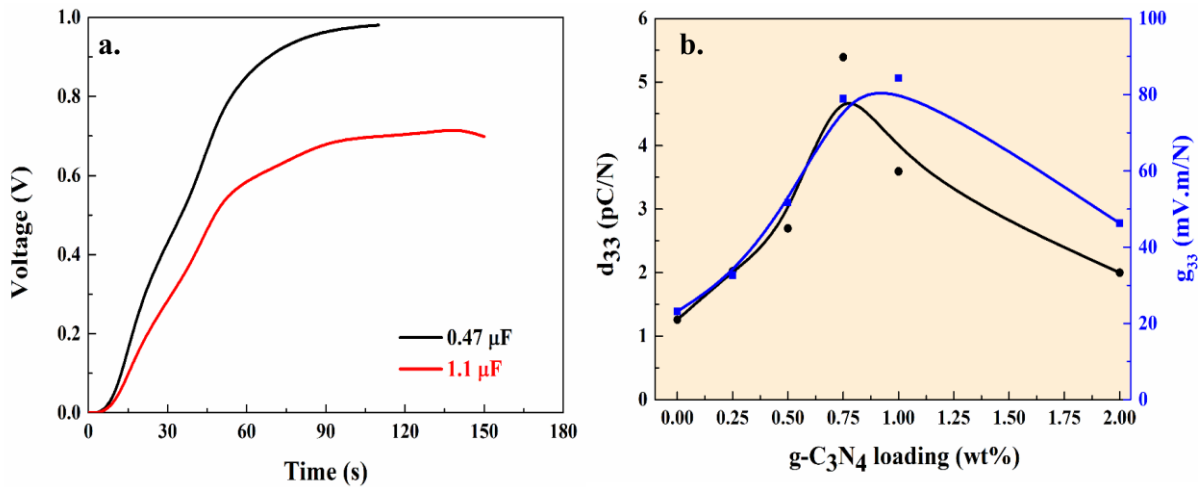


Fig. 6.15 (a) Charging voltage across a capacitor in PGN-0.75 nanogenerator (b) Dependence of g-C₃N₄ nanosheet loading on the piezoelectric coefficient and piezoelectric voltage coefficient.

Fig. 6.15a shows the charging voltage of PGN nanogenerator across a capacitor (0.47 μF and 1.1 μF). The nanogenerator was able to fully charge within 140 s under repeated imparting of pressure. Initially, the nanogenerator did not show any response for ~10s, which later increased steeply to a maximum charging voltage of 0.98 V. The maximum energy stored (E_s) [$E_s = 0.5 \times C \times V^2$] where, C is the capacitance and V is the voltage output] was 0.4 μJ across 1.1 μF capacitor. The use of electrospinning and g-C₃N₄ nanosheets not only improved the β-phase content, but also the piezoelectric coefficient (d_{33}) and voltage coefficient (g_{33}) of PVDF

(Fig.6.15b). The governing equations used for the determination of d_{33} and g_{33} are described elsewhere (Vatansever et al. 2011; Abbasipour et al. 2017) (Section I.5). The superior flexibility, stability, reproducibility and sensitivity of this nanogenerator makes it a promising material for wearable energy harvesting devices.

6.2.CONCLUSIONS

We have demonstrated a flexible piezoelectric PVDF/g-C₃N₄ nanocomposite fibers (PGN-X) based nanogenerator for energy harvesting application from human hand movements. Addition of g-C₃N₄, improved the spinnability and β -phase content of PVDF. The tensile and thermal properties improved for PGN samples while, the crystallinity of PVDF decreased with the addition of g-C₃N₄. The highest piezoelectric voltage of ~7.5 V and a current output of 0.23 μ A was generated for PGN-0.75 nanogenerator. The observed stability and improved piezoelectric performance of PGN based nanogenerators have prospective to be used for flexible and self-powered devices.

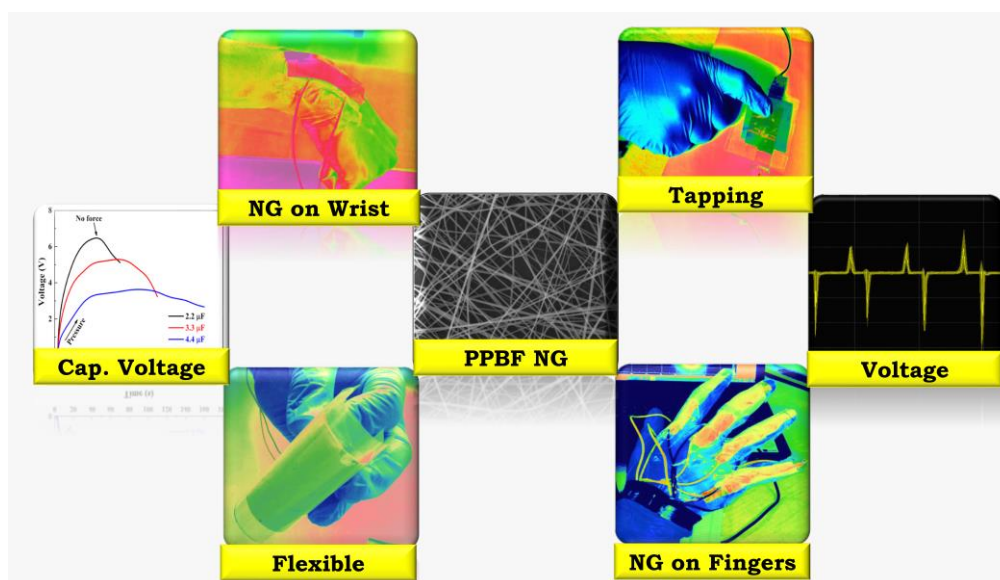
CHAPTER 7

EFFECTUAL AUGMENTATION OF PIEZOELECTRIC ENERGY CONVERSION OF ELECTROSPUN POLY(VINYLDENE FLUORIDE)/POLYANILINE/GRAPHITIC-CARBON NITRIDE BLEND NANOCOMPOSITES

The results of this chapter have been submitted to ACS applied nanomaterials (Revised version under review).

CHAPTER 7

EFFECTUAL AUGMENTATION OF PIEZOELECTRIC ENERGY CONVERSION OF ELECTROSPUN POLY(VINYLDENE FLUORIDE)/POLYANILINE/GRAPHITIC-CARBON NITRIDE BLEND NANOCOMPOSITES



A flexible, sensitive, durable, eco-friendly and cost-effective electrospun poly(vinylidene fluoride) (PVDF)/polyaniline (PANi)/graphitic-carbon nitride ($g\text{-C}_3\text{N}_4$) blend nanocomposite (PPBF-X) was fabricated using electrospinning technique for energy harvesting from human locomotion. Incorporation of $g\text{-C}_3\text{N}_4$ /PANi nanocomposite (GPC) into PVDF nanofibers led to significant increment in the β -phase of PVDF ($\sim 96\%$). The PPBF-7.5 nanogenerator showed outstanding improvement in the voltage and current output compared to electrospun PVDF (600%). The maximum voltage output of 28 V was generated with a current output of $3.7\ \mu\text{A}$. The PPBF nanogenerator was subjected to various motions (tapping, bending, heel pressing, blowing, impact, etc.) to demonstrate the flexibility, durability, sensitivity and stability. The PPBF nanogenerator exhibited very high-power density and conversion efficiency. The nanogenerator was able to fully light up 30 LED lights. The nanogenerator was able to achieve charging voltage of 6.2 V within 50 s across $2.2\ \mu\text{F}$ capacitor. The high performance of PPBF nanogenerator could be a potential material in smart, self-powered wearable devices.

7.1. RESULTS AND DISCUSSION

7.1.1. Morphological studies of g-C₃N₄/PANi nanocomposites (GPC-X)

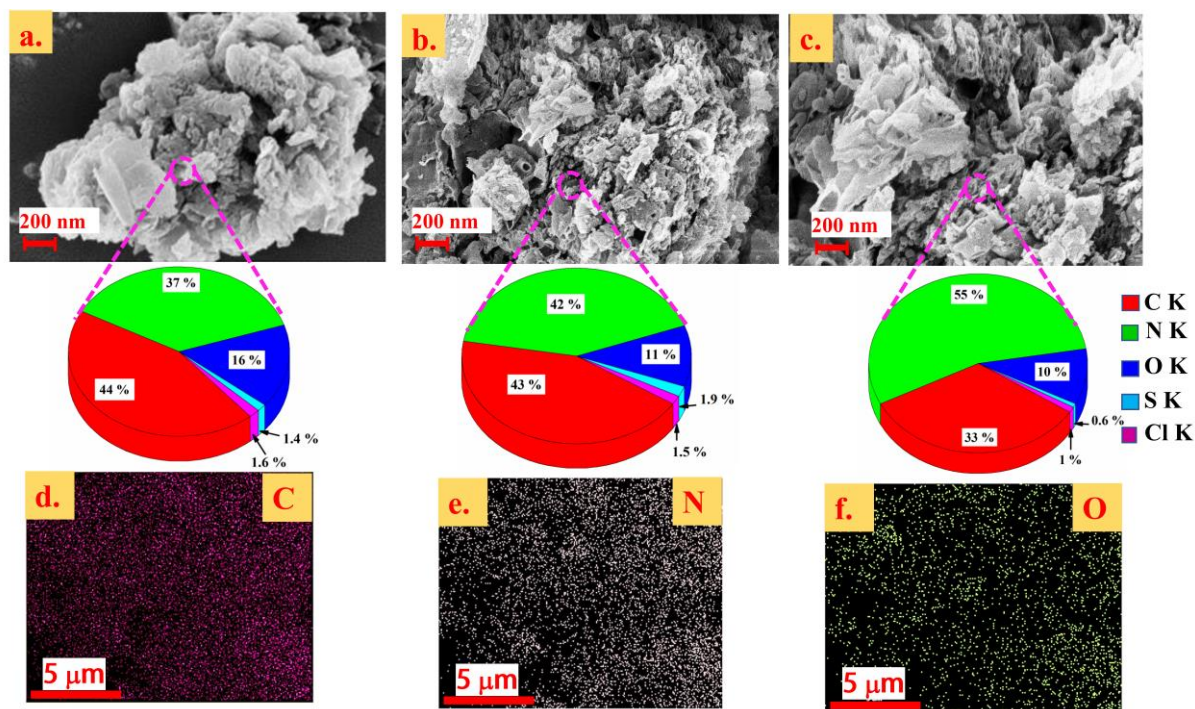


Fig. 7.1 HRSEM image of a) GPC-5.0 b) GPC-7.5 c) GPC-10 with chemical composition (d-f). Elemental mapping of major elements in GPC-7.5 sample.

Fig. 7.1 (a-c) shows the HRSEM images of GPC-X samples at different loading of g-C₃N₄. Two distinct morphologies were observed in all the compositions corresponding to g-C₃N₄ and PANi. Moreover, PANi nanorods were seen to be scattered on the surface of g-C₃N₄. Interestingly, the morphology of PANi nanorods and g-C₃N₄ were seen to be unchanged upon the addition of GPC. However, the size of PANi nanorods reduced with the increase in g-C₃N₄. In addition, PANi nanorods were deposited evenly on the surface of g-C₃N₄ without agglomeration (Section I.3).

The elemental composition of the GPC specifies the presence of moieties of both the entities, confirming the compatibility between PANi nanorods and g-C₃N₄. The nitrogen weight percent increased with g-C₃N₄ loading. Also, the presence of sulphur and chlorine is attributed to traces of APS and HCl, respectively. Fig. 7.1(d-f) shows the elemental maps of GPC-7.5. The homogenous distribution of carbon, nitrogen and oxygen indicates that PANi nanorods and g-C₃N₄ interacted with each other without much agglomeration. The synthesis method used here is a relatively simple and productive one. The formation of nanorod like morphology of PANi is dependent on the relative amounts of aniline, dopant and oxidant and temperature during the

synthesis. The initially formed linear PANi chains serve as the template for the growth of nanorod like morphology on the surface of g-C₃N₄ (Wang et al. 2014).

7.1.2. FTIR analysis of GPC

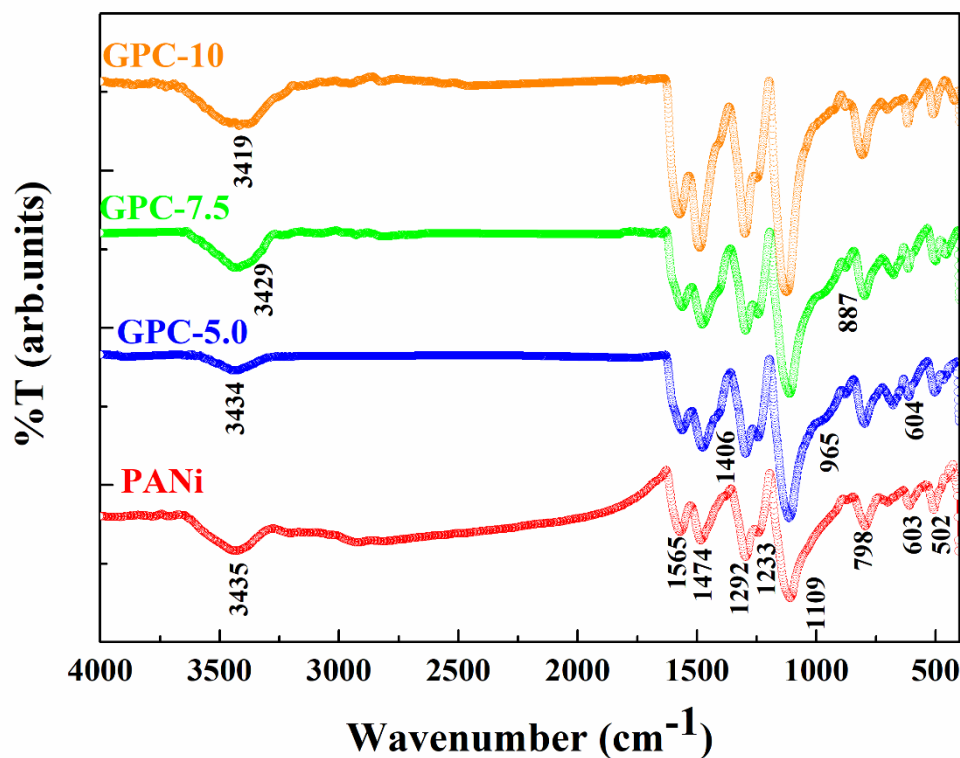


Fig. 7.2 FTIR spectra of PANi nanorods and GPC for different loadings.

The structure of PANi nanorods and GPC for different loadings of g-C₃N₄ were further investigated by FTIR spectroscopy (Fig. 7.2). For PANi nanorods, a broad band at 3435 cm⁻¹ is attributed to the NH₂ stretching vibrations of aromatic amines. The band arising at ~2950 cm⁻¹ is ascribed to the aromatic C-H stretching mode. The band at 1565 cm⁻¹ is the characteristic band of quinoid ring structure, while band at 1474 cm⁻¹ is the characteristic of benzene ring structure. Bands arising at 1292 cm⁻¹ and 1233 cm⁻¹, respectively correspond to the C-N stretching mode of the secondary aromatic amine and C-N stretching mode related to the characteristic band of conducting protonated form. The band at 1109 cm⁻¹ is attributed to the C=N stretching vibration (-N=quinoid=N-). Band at 798 cm⁻¹ is attributed to the C-H out of plane bending vibration. Bands arising at 603 cm⁻¹ and 502 cm⁻¹ are ascribed to the ortho substitution and meta substitution of PANi chains, respectively. Similar bands were observed for GPC with marginal shifts. The bands at 502 cm⁻¹ and 603 cm⁻¹ were shifted to the lower and higher wavenumber, respectively. The characteristic band ascribed to quinoid ring structure was shifted to lower wave number. The band at 3435 cm⁻¹ was shifted to lower

wavenumber, which could be attributed to the hydrogen bonding interaction between N-H group of PANi and oxygen atom of g-C₃N₄. Also, new bands were observed at 1406 cm⁻¹ and 887 cm⁻¹ that correspond to g-C₃N₄ (Mostafaei and Zolriasatein 2012a; Ibrahim 2017; Zhao et al. 2017). The shift in the characteristic bands of PANi nanorods and g-C₃N₄ indicates strong interaction and compatibility between them. The intensity ratio of the characteristic peaks of quinoid to the benzenoid moieties of PANi nanorods (deconvoluted) signifies its electrical conductivity. The intensity ratio of bands for pristine PANi nanorods was 0.88, while it decreased to 0.87, 0.86 and 0.84 for GPC-5, GPC-7.5 and GPC-10, respectively. An intensity ratio equal to 1 indicates higher electrical conductivity and a ratio less than 1 suggests that there are more benzene rings than quinoid rings in PANi chains (Abdiryim et al. 2005; Banerjee and Kumar 2011).

The electrical conductivities of PANi nanorods and GPC at different loadings of g-C₃N₄ were measured using four probe conductivity meter (Asico, India). The GPC samples were pelletized (pellet press, Kimaya Engineers, Mumbai, India). The electrical conductivity of PANi nanorods was 3.81 ± 0.2 S.cm⁻¹, while it decreased to 3.77 ± 0.3 , 3.62 ± 0.15 , 3.62 ± 0.1 S.cm⁻¹ for GPC-5.0, GPC-7.5 and GPC-10, respectively.

7.1.3. SEM micrographs of electrospun PVDF nanocomposites

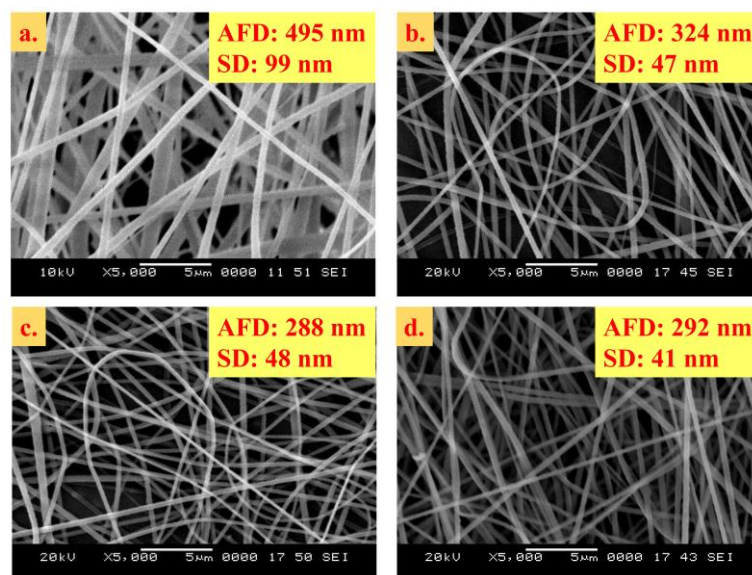


Fig. 7.3 SEM micrographs of a) E-PVDF b) PPBF-5.0 c) PPBF-7.5 d) PPBF-10.

The morphology of E-PVDF and PPBF-X at different loadings of g-C₃N₄ is shown in Fig. 7.3. For the preparation of electrospun mats, the electrospinning conditions, polymer concentration (13.5 wt/v%) and filler loading (20 wt%) were kept constant (optimized conditions). Loading

of GPC above 20 wt% leads to significant agglomerations and formation of lumps, which further blocked the syringe needle and prevented the formation of the Taylor cone. Also, the percolation threshold of PANi nanorods in PVDF was observed at ~20 wt% loading of GPC. Hence, the GPC loading of 20 wt% was preferred throughout the study (Ico et al. 2016a). For all the samples, the fibers produced were long, continuous and defect free. The absence of beads in PVDF fibers is attributed to the complete evaporation of solvent and sufficient voltage potential used during the electrospinning process (Motamedi et al. 2017). E-PVDF fibers were seen to be defect free, but the diameter of fibers was not uniform and the fibers were randomly arranged.

Fig. 7.3 (b-d) highlights the significant impact of inclusion of GPC on the morphology and diameter of PPBF-X nanofibers. It is evident that the inclusion of GPC not only reduced the fiber diameter, but also improved the uniformity of fibers. The decrease in AFD is attributed to the negative and positively charged surface of $g\text{-C}_3\text{N}_4$ and PANi nanorods, respectively (Li and Xia 2004).

7.1.4. Polymorphism and Crystallinity analysis

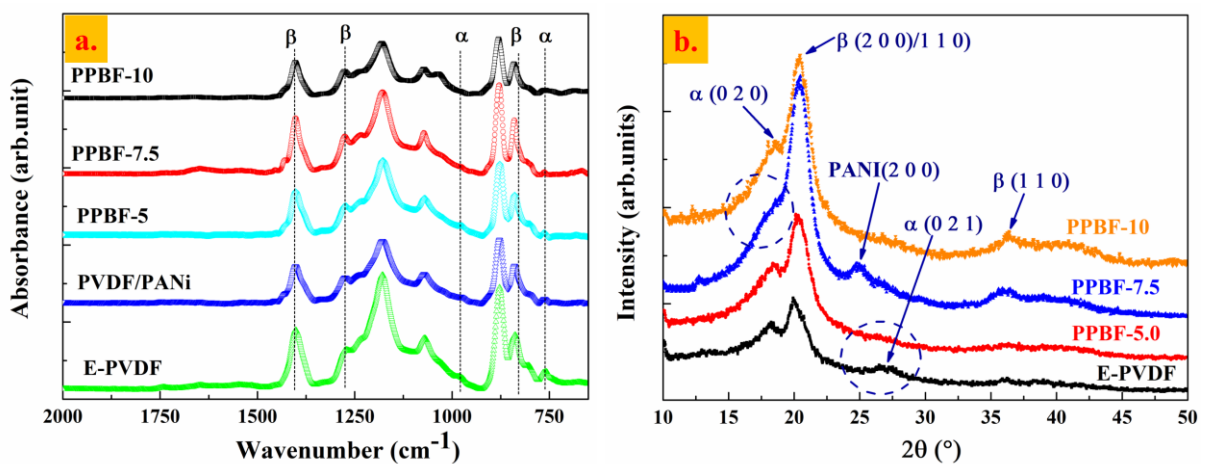


Fig.7.4 E-PVDF, PVDF/PANi blend and PPBF-X at different loadings of GPC **a)** FTIR spectra **b)** WAXD patterns of E-PVDF and PPBF-X at different loadings of GPC.

Fig. 7.4a shows the absorbance spectra of E-PVDF, PVDF/PANi blend and PPBF-X at different loadings of GPC. It is well known fact that the electrospinning induces the formation electroactive phases of PVDF. For E-PVDF, bands arising at 765, 798, 975 cm^{-1} assigned to the α -phase (TGTG') of PVDF while, band arising at 840, 1071, 1234, 1278 and 1401 cm^{-1} attributed to the β -phase (TTT) of PVDF (Kobayashi et al. 1975; Salimi and Yousefi 2003b; Peng and Wu 2004; El Achaby et al. 2012; Cai et al. 2017). In the spectrum of E-PVDF, the

bands arising at 765, 798, 975 cm^{-1} are assigned to the α -phase (TGTG') of PVDF, while those arising at 840, 1071, 1234, 1278 and 1401 cm^{-1} are attributed to the β -phase (TTT) of PVDF (Farid Abraham 1962; Benz et al. 2001; Cozza et al. 2013). Probably, when DMF dissolves PVDF chains, it disturbs the dipolar and van der Waal's interactions in PVDF, thereby providing more space for the mobility of polymer chains. However, this happens only to a limited extent when the solution is prepared at room temperature. The amount of the α -phase of PVDF was reduced significantly with the addition of GPC in PVDF. Also, new bands were observed at 1470, 1292 and 798 cm^{-1} that correspond to the PANi nanorods. In E-PVDF, the β -phase content of PVDF was $42 \pm 2\%$, while it increased to 62% with the addition of PANi nanorods. The β -phase content of PVDF was increased to $84.2 \pm 1.5\%$, $96.9 \pm 1\%$ and $91.2 \pm 2\%$ for PPBF-5.0, PPBF-7.5 and PPBF-10, respectively. The significant increase in the β -phase content of PVDF upon the addition of PPBF-X is ascribed to various factors. First, the improved solution conductivity of electrospinning mixture upon the addition of GPC results in increased stretching of the solution jet (Yu and Cebe 2009b; Ong et al. 2015; Najim and Salim 2017; Yang et al. 2018a). Second, formation of finer and defect-free fibers further facilitates the formation of the β -phase (Ico et al. 2016b). Third, the superior dispersion of GPC in PVDF enables better interactions between the matrix and the dispersed phase. The hydrogen bonding between the hydroxyl groups of g- C_3N_4 with the fluorine atoms of PVDF helps in the formation of the β -phase. In addition, the dipole-dipole interaction between the oxygen atoms of g- C_3N_4 with CH_2 groups of PVDF further enhances the β -phase of PVDF. Also, the $-\text{CF}_2$ group of PVDF and $(=\text{N}-\text{H})^+$ group of PANi nanorods stimulates the dipole-dipole interaction (Saidi et al. 2013a) (Fig.7.5). For PPBF-10 the β -phase content slightly decreased, which may be attributed to the higher content of g- C_3N_4 in GPC that might have caused agglomerations within the PVDF nanofiber. The effect of GPC on the β -phase of solution cast PVDF film is discussed in section I.4.

Fig. 7.4b shows the WAXD patterns of E-PVDF and PPBF-X samples. Peak arising at 18.5° is characteristic of the α -phase of PVDF that corresponds to the (0 2 0) crystal plane. The peak arising at 20.4° is characteristic of the β -phase of PVDF that corresponds to (2 0 0) / (1 1 0) crystal planes. A broad peak at $\sim 26^\circ$ is attributed to the α -phase of PVDF and ascribed to the (0 2 1) crystal plane in particular. For PPBF-X, the peak corresponding to the α -phase diminished, while that corresponding to the β -phase became intense, indicating the induction of the β -phase upon the addition of GPC. For PPBF-7.5, the peak at 20.4° became intense and

new peaks were observed at $\sim 24^\circ$ and 36.1° , respectively that correspond to the PANi nanorods and the β -phase of PVDF. The presence of peak relating to the PANi nanorods confirmed their presence in PVDF nanofibers. Interestingly, the α -phase peaks arising at 18.5° and 26.2° were completely diminished in PPBF-7.5, indicating the complete transformation of the non-polar phase into the electroactive one. However, the α -phase peak was observed for PPBF-10 and the intensity of the β -phase peak declined slightly.

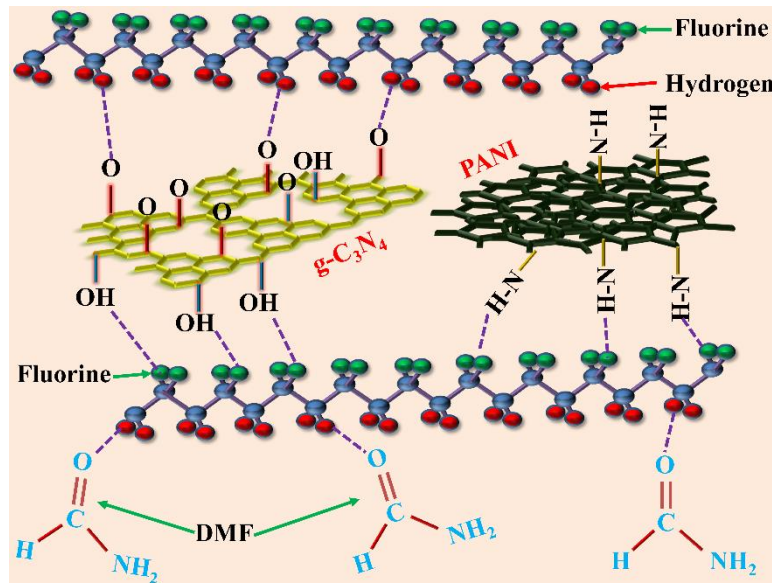


Fig. 7.5 Plausible interaction mechanism between g-C₃N₄ nanosheets, PANi nanorods, DMF and PVDF chains for the formation of TTT conformation.

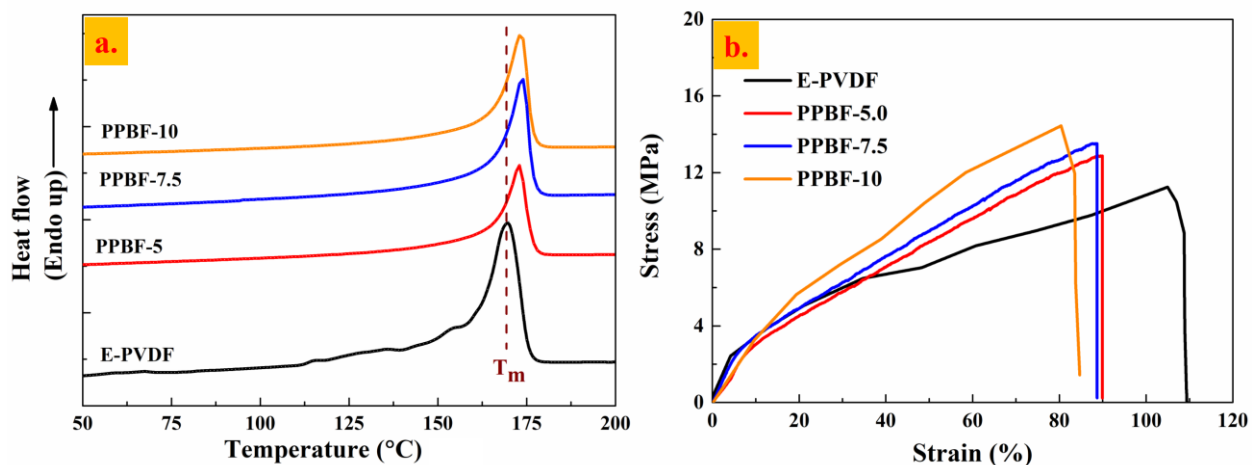


Fig. 7.6 E-PVDF and PPBF-X at different loadings of g-C₃N₄ loading a) DSC curves b) Stress-strain curves.

The above observations indicate strong interactions between GPC and PVDF nanofibers that could significantly improve the piezoelectric performance of the nanocomposite fibers. Electrospinning and GPC affect the degree of crystallinity of PVDF nanofibers. The degree of

crystallinity (X_c) of E-PVDF was 43.1%, while it decreased upon the addition of GPC (**Table. 7.1**).

Fig. 7.6a shows the DSC curves of E-PVDF and PPBF-X at different loading of g-C₃N₄. For E-PVDF, the melting peak (T_m) was observed at 169.6 °C; while it increased to 172.7 °C, 173.6 °C and 173.3 °C for PPBF-5.0, PPBF-7.5 and PPBF-10, respectively, which could be attributed to the rearrangement of PVDF chains upon the addition of GPC. In addition, the peaks were broadened and became less intense for PPBF-X samples. There was noticeable decrease in X_c of PVDF upon the addition of GPC (Table.7.1). The decrease in X_c indicates that GPC not only helps in the induction of the β -phase, but also hinders the free movement of PVDF chains. These results are in-line with the WAXD results. The difference in WAXD and DSC results is due to the unavoidable error that occurs during the baseline correction and smoothing of curves.

Table. 7.1. % β -phase, Melting temperature, degree of crystallinity and Tensile strength of E-PVDF and PPBF -X samples.

Sample	% β -phase	Melting temperature (°C)	% crystallinity		Tensile strength (MPa)
			DSC	WAXD	
E-PVDF	42 ± 2	169.5	42.5	43.1	11.2 ± 0.3
PVDF/PANi	62 ± 3.5	-	-	-	-
PPBF-5.0	84.2 ± 1.5	172.7	37.5	39.8	14.2 ± 0.5
PPBF-7.5	96.9 ± 1	173.6	35.9	36.1	14.6 ± 0.2
PPBF-10	91.2 ± 2	173.3	35.8	37.3	15.4 ± 1.0

*The results of electrospun PVDF/PANi blends were shown only to demonstrate the benefit of g-C₃N₄ nanosheet addition to PVDF nanofibers, hence the results were restricted to FTIR spectroscopy.

7.1.5. Mechanical properties

The nanogenerator should exhibit good mechanical properties, which would enhance its scope in practical applications. Also, the nanogenerator undergoes stretching, bending-releasing motions during energy conversion. Hence, it is essential to evaluate the tensile strength and ultimate elongation of PVDF nanofibers, especially in nanocomposite fibers as the fillers may significantly affect the elongation of nanofibers. Fig. 7.6b shows the stress-strain curves of E-PVDF and PPBF-X at different loadings of g-C₃N₄. The tensile strength and elongation of E-PVDF were 11.3 MPa and 109 %, respectively. The tensile strength increased

to 13.1, 13.6 and 14.7 MPa for PPBF-5.0, PPBF-7.5 and PPBF-10, respectively. However, there was a slight decrease in elongation for PPBF-X. Interestingly, the elastic regions of PVDF broadened upon the addition of GPC. The reduction in elongation suggest that the PVDF chain mobility was hindered by the of GPC. Improvement in tensile strength is attributed to the higher stiffness associated with PANi backbone and intrinsic mechanical properties of g-C₃N₄(Wang et al. 2018a). Use of higher dopant (HCl) concentration during the synthesis of GPC makes it more brittle and crystalline, leading to the reduction in the ultimate elongation of PPBF-X (Malmonge et al. 2010).

7.1.6. Piezoelectric evaluation of PPBF

The piezoelectric performance of E-PVDF and PPBF-X based nanogenerator for energy harvesting application from human locomotion was investigated in various modes. Capability of these nanogenerators was evaluated to harvest energy from human activity, which would be useful in wearable electronics.

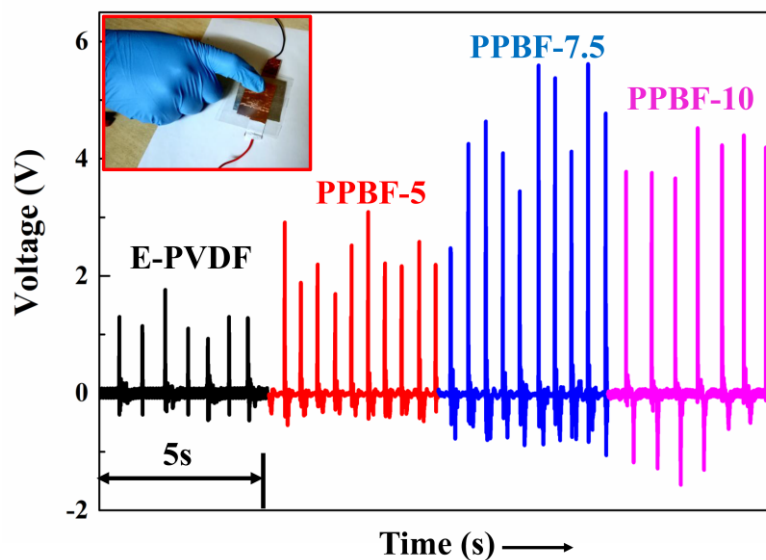


Fig. 7.7 Piezoelectric evaluation of E-PVDF and PPBF-X nanogenerators under periodic human finger (one) tapping mode.

Fig.7.7 shows the voltage output generated from E-PVDF and PPBG-X under one-finger tapping mode. For E-PVDF nanogenerator, the maximum voltage output was 0.9 V, which increased significantly for PPBF-X nanogenerators. The maximum voltage outputs were 3.0, 5.5 and 4.3 V for PPBF-5.0, PPBF-7.5 and PPBF-10, respectively. The increase in the voltage output of the nanogenerators can be directly related to their β -phase content. The repeated tapping on the nanogenerator results in the generation of piezoelectric potential within the fibers, which in turn gives rise to a momentary free flow of electrons that are collected by

the electrodes and supplied to the external loads. When the load is released, the piezoelectric potential weakens and the electrons are released. The to and fro motion of electrons due to the application of periodic imparting results in alternating voltage output. The voltage outputs of solution cast pristine PVDF and PVDF/GPC nanocomposite film were obtained under one-finger tapping mode to demonstrate the advantages of using electrospinning for boosting the piezoelectricity of PVDF.

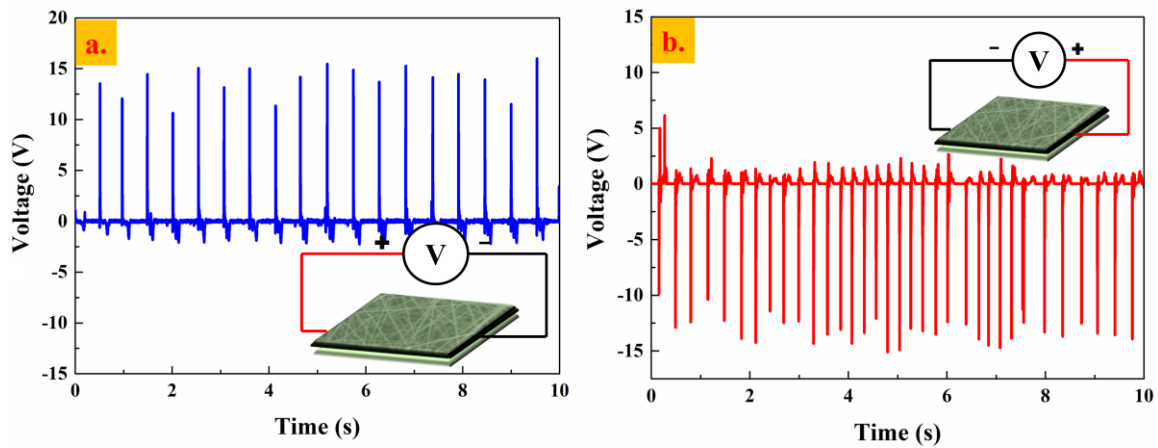


Fig. 7.8 Piezoelectric performance of PPBF-7.5 nanogenerator **a)** Forward connection **b)** Reverse connection.

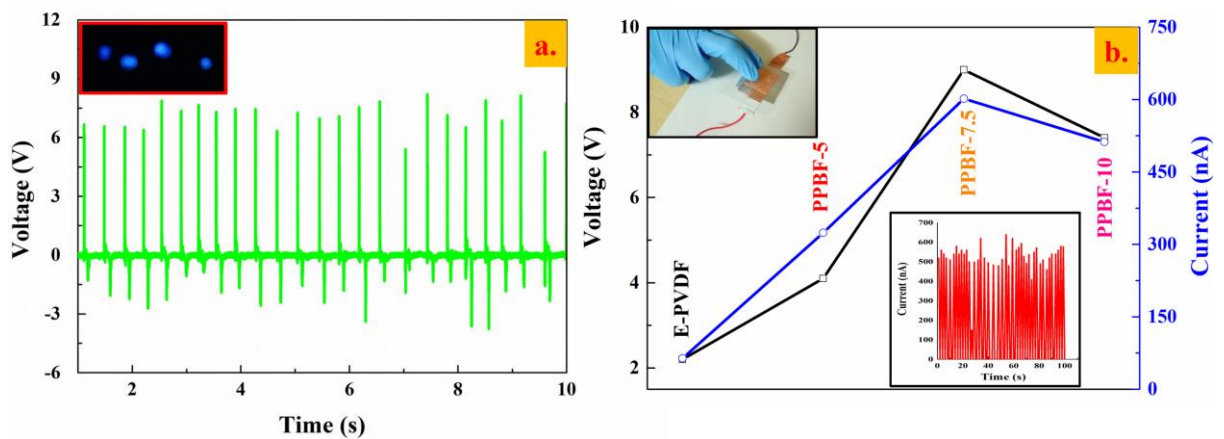


Fig. 7.9 Piezoelectric voltage output of PPBF-7.5 nanogenerator under two finger tapping mode **a)** PPBF-7.5 (Inset: light up of LED lights) **b)** Voltage and current output of E-PVDF and PPBF-X nanogenerators.

To verify that the voltage output generated is solely due to the piezoelectric effect of the nanogenerator, the switching polarity test was carried out. The measurement was carried out in forward and reverse connections for the nanogenerator (Fig.7.8a & 7.8b). In both forward and reverse connections, the nanogenerator displayed almost the same level of voltage output under constant application of pressure (impact) in an open loop system. The polarity test

confirmed that the voltage generated is entirely due to piezoelectricity and ruled out the intervention of pseudo charge or triboelectric generation.

The piezoelectric performance of E-PVDF, PPBF-5.0, PPBF-7.5 and PPBF-10 nanogenerators under periodic two-finger tapping mode was demonstrated (Fig. 7.9a & 7.9b). The trend in the voltage output is similar to that of the one finger tapping mode. The highest voltage output of 8.5 V was from PPBF-7.5, which is seven times higher than that produced by E-PVDF.

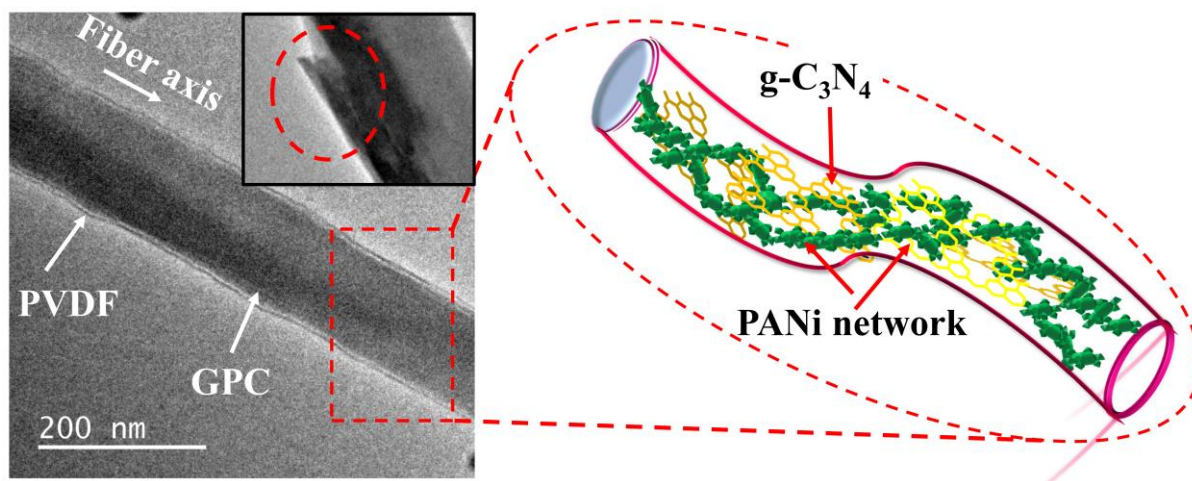


Fig. 7.10 TEM micrograph of PPBF-7.5 with schematic showing the formation of PANi nanorod network within PVDF fiber.

The inset of Fig. 7.9a shows the lighting up of LEDs under two-finger tapping on the PPBF-7.5 nanogenerator. Current outputs of 34 nA, 324 nA, 602 nA and 512 nA were generated by E-PVDF, PPBF-5.0 PPBF-7.5 and PPBF-10 nanogenerators, respectively. There are several factors that affect the piezoelectricity of PPBF nanogenerator. First, the uniformity and fineness of the fibers are believed to be beneficial for the piezoelectricity of PVDF. Secondly, the densely interconnected structure aids in electric charge mobility thereby providing an efficient energy conversion. Third, the addition of GPC facilitated high β -phase content in PVDF that boosted the piezoelectric performance.

Electrospun nanofibers were synthesized under extreme stretching conditions; therefore, the orientation of PANi nanorods inside the PVDF nanofibers increases electrical percolation by allowing the formation of electrically conductive network. A schematic diagram (Fig. 7.10) depicts the formation of a conductive network of GPC in PVDF nanofiber. In addition, the GPC was seen close to the crust of the PVDF nanofiber and in a few places the network protruded out of the PVDF nanofibers. This type of morphology not only results in the formation of a conductive network along the fiber axis, but also ensures the formation of a

network in the transverse direction. Further, the efficient distribution of GPC in PVDF matrix is ascribed to the lower interfacial energy between PANi nanorods and PVDF. Similar morphology was observed in electrospun poly(styrene-*co*-acrylonitrile)/PANi blend nanofibers (Reddy and Anandhan 2016b).

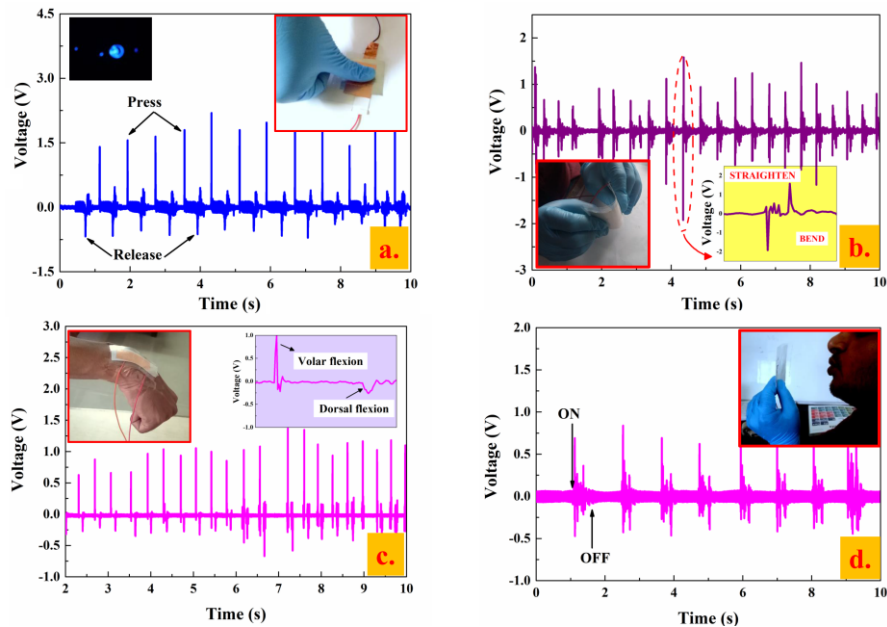


Fig. 7.11 Piezoelectric performance of PPBF-7.5 nanogenerator **a)** Thumb imparting **b)** Bending **c)** Wrist movement **d)** Blowing (mouth).

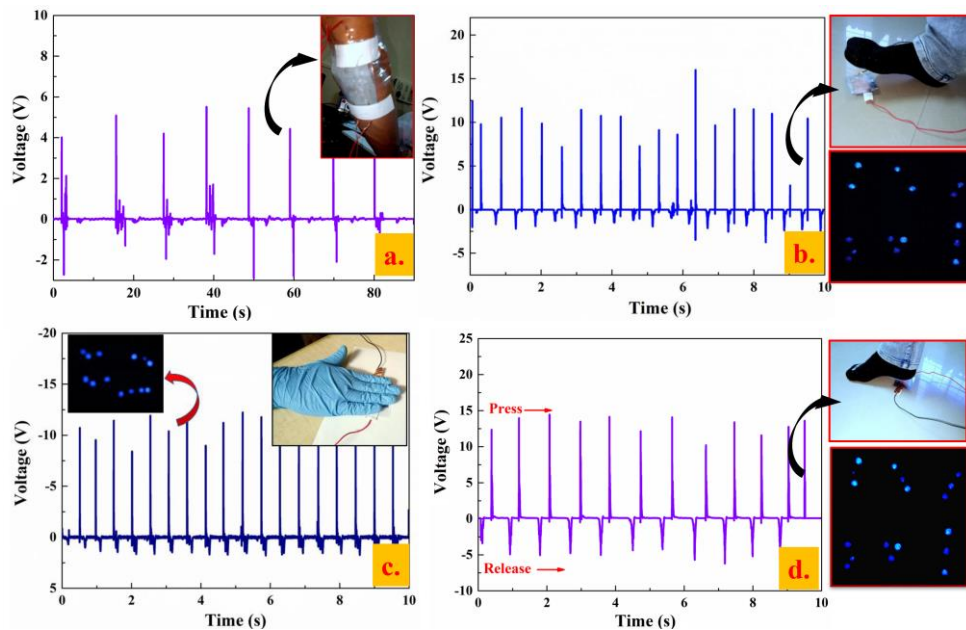


Fig. 7.12 Piezoelectric voltage output of PPBF-7.5 nanogenerator **a)** Human arm motion **b)** Toe imparting (Inset: Lighting-up of LED lights (15 nos)) **c)** Palm (impact) mode (Inset: Lighting-up of LED lights (15 nos)) **d)** Toe imparting

Lighting-up of LED lights (14 Nos) **d**) Heel pressing (Inset: Lighting -up of LED lights (18 Nos)).

To demonstrate the suitability of PPBF nanogenerator for wearable electronic devices by harvesting energy by human body locomotion, the nanogenerator was tested under various modes of stresses. Hereafter, the investigation of piezoelectric performance is restricted to PPBF-7.5 nanogenerator because of its highest β -phase content and piezoelectric performance under tapping mode. Fig. 7.11a shows the voltage output from the PPBF-7.5 nanogenerator under repeated thumb pressing. The nanogenerator was able to produce an output of 1.5 V (positive) and a negative voltage of 0.75 V when released. In addition, the nanogenerator was able to light up four LEDs. The nanogenerator was tested for its piezoelectric performance in periodic bending and releasing condition (Fig.7.11b). Further, the nanogenerator patch was attached to the wrist of a human hand (Inset of Fig.7.11c). To prevent the nanogenerator from contacting skin, it was first covered with insulating tape and the voltage output was recorded against volar flexion and dorsal flexion movement of the wrist. The nanogenerator was able to produce a voltage of ~ 1 V with repetitive movement of the wrist (Fig. 7.11c). The sensitivity was demonstrated by holding the nanogenerator in front of blowing air (mouth blowing). The nanogenerator was sensitive to the periodic blowing and able to produce a voltage output of ~ 0.75 V (Fig.7.11d).

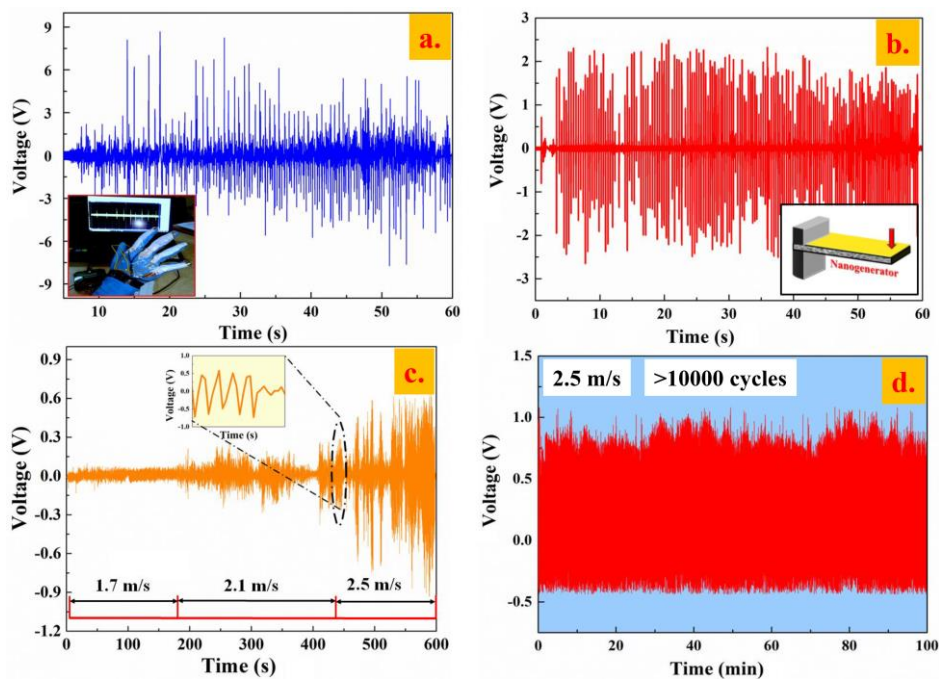


Fig. 7.13 Piezoelectric voltage output of PPBF-7.5 under a) Bending and straightening of fingers b) Cantilever free vibration c) Blowing with hair dryer at different velocity d) Durability of nanogenerator under blowing condition (>10000 cycles).

The nanogenerator was attached to a human arm and the bending and straightening of arm produced a voltage output of ~4 V (Fig. 7.12a). The nanogenerator was tested for more than 500 times under bending/releasing mode to demonstrate its flexibility and durability. The PPBF-7.5 nanogenerator was able to exhibit stable voltage and current without any loss in the output, suggesting that the PPBF nanogenerator can be used over a longer period of time. It is noteworthy that the nanogenerator is flexible, light, non-toxic with utmost comfort. In addition, the nanogenerator was able to produce a voltage of ~11 V, ~13 V and ~14.5 V under imparting of pressure under palm, toe and heel pressing mode, respectively (Fig 7.12 b-d). In these modes, the nanogenerator exhibited a current output of 1.75 μ A, 2.1 μ A and 2.7 μ A, respectively, which is higher than most of the PVDF nanofiber based nanogenerators reported hitherto (Section I.6). On the other hand, the nanogenerator was able to light up 13, 63 and 70 LEDs under palm, toe and heel imparting mode, respectively. It is noteworthy that the PPBF nanogenerator was able to generate an electric output at higher loads, which was not possible in our previous study on electrospun PVDF/PANi/HNT blend nanocomposite, attributing to the better electron transport characteristics of g-C₃N₄. This may be attributed to the presence of g-C₃N₄ nanosheets that provides better stress transfer.

The PPBF-7.5 nanogenerator patches (3 cm \times 1 cm \times 0.0025 cm) were attached to human fingers resembling wearable electronics on robot hand (Inset of Fig.14a). The multiple patches were connected in series to evaluate the voltage output. Interestingly, the nanogenerator exhibited an output voltage of ~8.5 V (Fig. 7.13a). However, the voltage output was not consistent because of the difficulty in bending the fingers simultaneously. It is important to note that the nanogenerator was subjected to simultaneous bending and stretching movement when attached to human fingers, signifying that the PPBF-7.5 nanogenerator can withstand large deformations without breakage. Here, the PPBF-7.5 not only produced a higher voltage output, but also attested its flexibility and applicability that could be seen as a potential material for robot arm for self-power generation.

The PPBF-7.5 nanogenerator was subjected to the cantilever free vibrations (Inset of Fig.7.13b). The vibrations were generated by tapping the nanogenerator at the free end. Once tapped, the nanogenerator was able to produce alternating voltage output of 6 V (peak to peak) for 7-10 sec (Fig.7.13b). The nanogenerator showed consistent voltage output even after 500 times of to and fro movement. Further, the nanogenerator was tested against the air blowing using a commercial hair dryer at a velocity of 1.7 m/s, 2.1 m/s and 2.5 m/s (Fig.7.13c). The blower was kept at a distance of 10 cm and held opposite to the length of the nanogenerator.

At 1.7 m/s the response of the generator was quite low and generated a voltage less than 150 mV. At a velocity of 2.5 m/s, the nanogenerator produced a maximum peak to peak voltage of 1.8 V. Further, the nanogenerator was subjected to the repeated blowing of air at 2.5 m/s for > 30,000 cycles (not shown in Fig. 7.13). Fig. 7.13d shows the response of the nanogenerator for the first 100 mins for better readability. During this process, the nanogenerator had undergone more than 30,000 cycles without any loss in voltage output. The generation of consistent voltage output even after 30,000 cycles affirms the flexibility, durability and stability of PPBF-7.5 nanogenerator. It is important to point out the fact that the same nanogenerator (PPBF-7.5) was used for the evaluation of piezoelectric performance under various modes such as tapping, bending, free vibration, impact loading, toe and heel imparting mode, which will further add up to the total number of cycles the nanogenerator experienced (~50,000-60,000 cycles). The above results revealed the sensitivity, stability, durability and reproducibility of PPBF-7.5 nanogenerator.

The morphology of the nanogenerator remained stable and there was no breakage of fibers observed even after 50000 cycles. Also, it is noteworthy that the electroactive phase of PVDF did not decay even after repeated cycles and time (Section I.6).

We also evaluated the voltage output of PPBF nanogenerator when imparting pressure on it through punching (Fig. 7.14a). Interestingly, a voltage of ~30 V and a current of 3.7 μ A were generated in an open loop system, which is better than most of the electrospun PVDF based nanogenerators (Table I.7). We have also demonstrated electrical energy generation capacity of the nanogenerator by lighting up LEDs (30 Nos) (Inset of Fig. 7.14a). Fig. 7.14b shows the charging behavior of the PPBF-7.5 nanogenerator across different capacitors (2.2, 3.3 and 4.7 μ F). A rectified bridge circuit was built to evaluate the charging voltage of the nanogenerator (inset of Fig. 7.14b). The energy harvested by the PPBF-7.5 nanogenerator could be stored in capacitors under repetitive imparting of pressure. Initially, the charging voltage did not show any response for ~5 s, later the voltage across the capacitors increased steeply. The 2.2 μ F capacitor was charged quickly within 54 s to 6.3 V due to repeated imparting of pressure. For 3.3 μ F and 4.4 μ F it took 77 s and 109 s, respectively (Fig. 7.14b). In addition, the charging voltage dropped to 5.3 V and 3.3 V for 3.3 μ F and 4.4 μ F capacitor, respectively. The maximum energy stored [$E_s = \frac{1}{2} \times C \times V_s^2$] where, C is the capacitance, V_s is the saturation voltage] was $49.6 \pm 0.7 \mu$ J by the PPBF-7.5 nanogenerator across 3.3 μ F capacitor (Shi et al. 2018).

shows the voltage and current output signals of PPBF nanogenerator across different load resistance (R_L). The results were obtained by measuring the voltage output across different load resistance ranging from 0.1 to 14 M Ω by imparting pressure under punching mode and the corresponding circuit used is shown as Inset of Fig. 7.14c. The voltage output of the nanogenerator increased steeply and the current output decreased gradually with the increase in load resistance. At higher resistance values, a slight decrease in voltage output was observed. The instantaneous power density (P_d) of PPBF nanogenerator was evaluated using the equation $P_d = V^2/(A \times R_L)$, where V is the voltage output and A is the effective area of the PPBF nanogenerator. The PPBF nanogenerator showed a maximum power density of $\sim 14.7 \mu\text{W}/\text{cm}^2$ at 8 M Ω (Fig. 7.14d). The instantaneous piezoelectric conversion efficiency (η_e) was estimated as the ratio of energy stored in a capacitor in one cycle ($E_o = \int \frac{V \cdot t^2}{R} dt$) to the input energy ($E_i = F \cdot \Delta L$), where, F is the force applied, V is the voltage output, ΔL is the total deformation of the nanogenerator. The input energy was calculated as described elsewhere (Sinha et al. 2016). The conversion efficiency of PPBF-7.5 nanogenerator at 8 M Ω was estimated to be 19.7 %.

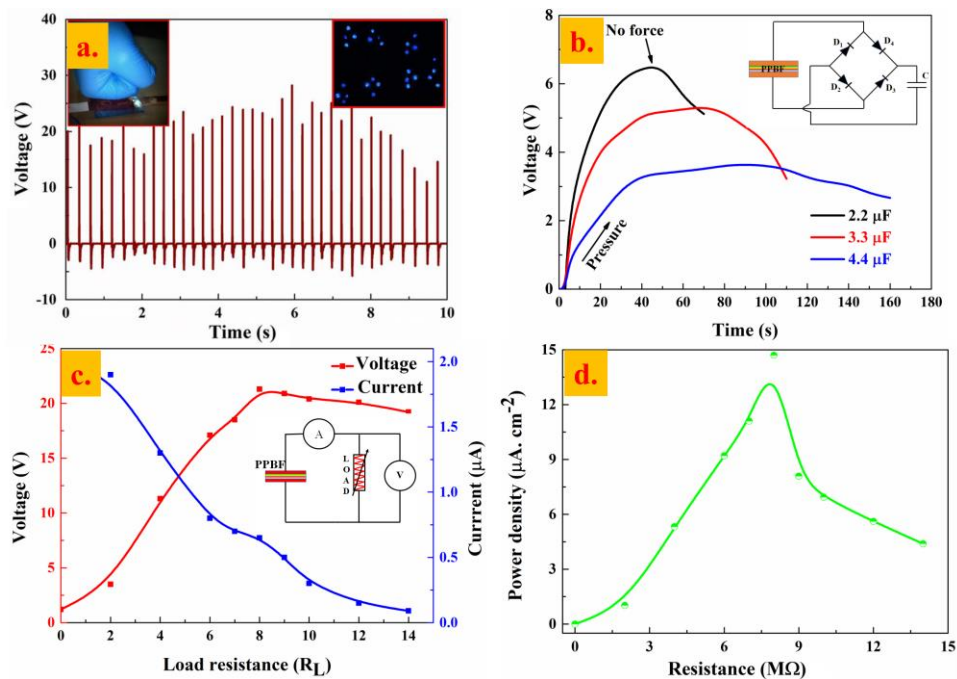


Fig. 7.14 a) Piezoelectric voltage output of PPBF-7.5 under punching mode b) capacitor charging performance of PPBF-7.5 nanogenerator (Inset: schematic of the circuit used for the evaluation) c) Voltage and current output as a function of load resistance (Inset: schematic circuit used for the evaluation) d) Power density of PPBF-7.5 nanogenerator as a function of load resistance.

At a maximum power density of PPBF-7.5 nanogenerator, the current output was $\sim 0.65 \mu\text{A}$ which is $\sim 61\%$ of the theoretical current value ($I_t = \sqrt{\frac{P_{d \max}}{R_L}}$). The difference in the value with respect to the theoretical current value is attributed to the internal resistance and current leakage.

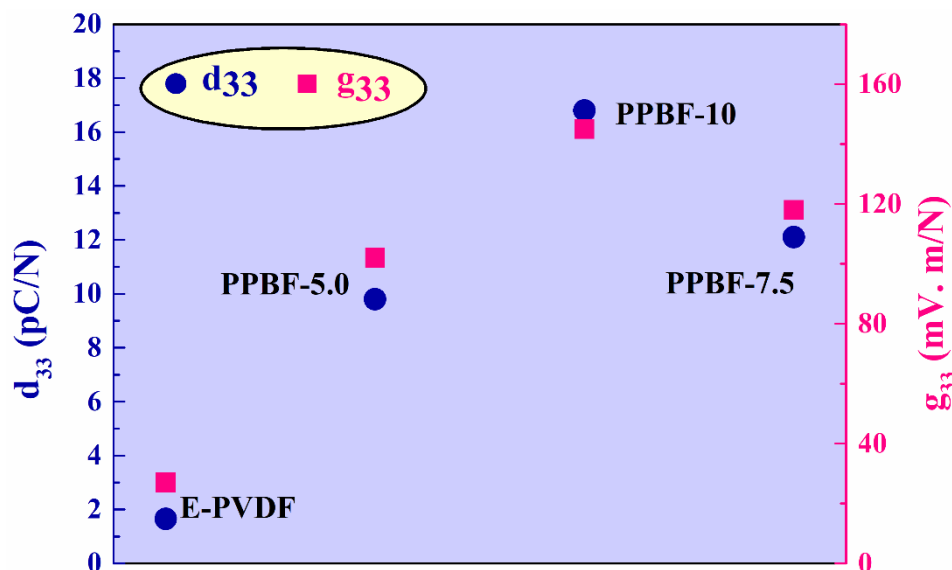


Fig. 7.15 Piezoelectric coefficient and voltage coefficient of E-PVDF and PPBF-X nanogenerators.

The piezoelectric coefficient and piezoelectric voltage coefficient increased significantly for PPBF-X nanogenerator piezoelectric co-efficient and piezoelectric voltage coefficient increased significantly for PPBF-X nanogenerator (Fig.7.15).

The stability of the PPBF-7.5 nanogenerator was evaluated over a period of 15 consecutive weeks by imparting the pressure under finger tapping mode (Fig. 7.16). Interestingly, the nanogenerator showed high stability and reproducibility even after 15 weeks. This clearly displays the excellent characteristics and reliability of PPBF nanogenerator for energy harvesting application.

There are several advantages of PPBF nanogenerator, which makes it a potential material for energy harvesting application. Firstly, the nanogenerator provides excellent flexibility and durability, which makes it suitable for its usage in harsh environments. PPBF nanofibers are clean, non-toxic, chemically inert, eco-friendly and exhibit high thermal stability and mechanical strength, which are considered to be most vital characteristics that are needed for sustainable energy harvesting applications. Further, the superior sensitivity of the PPBF nanogenerator boosts its response to even small input signals. The generation of high voltage

(~30 V) and current (~3.7 μ A) from human locomotion could make this a potential material for smart, self-powered and wearable devices. The PPBF nanogenerator can easily be attached to any complex shapes because of its flexibility, which is due to the characteristics of electrospinning process. Also, the excellent stability and durability of the PPBF nanogenerator could run devices for a long duration. Finally, the most important aspect of this energy harvester is the use electrospinning process for the preparation, which is widely recognised as one of the most versatile and industrially scalable techniques.

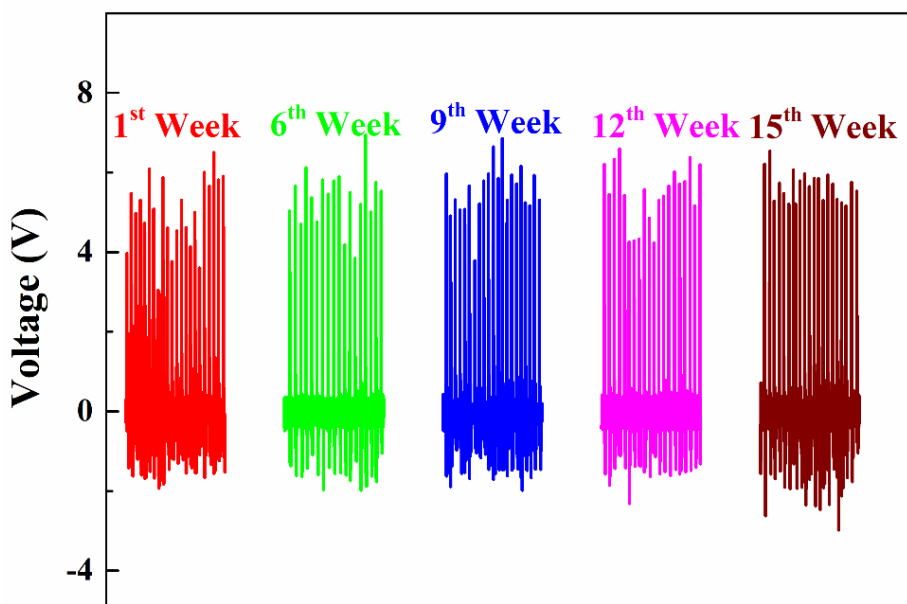


Fig. 7.16 Response of the PPBF-7.5 nanogenerator tested over 15 weeks under finger tapping mode.

7.2. CONCLUSIONS

A highly flexible electrospun PVDF/PANi/g-C₃N₄ blend nanocomposite (PPBF) nanogenerator for piezoelectric energy harvesting was successfully developed and demonstrated. The synergistic effect of electrospinning and PANi/g-C₃N₄ nanocomposite (GPC) improved the β -phase content and tensile strength of PVDF. The PPBF nanogenerator generated a maximum voltage and current output of ~30 V and 3.7 μ A, respectively. The PPBF nanogenerator underwent more than ~50,000 cycles of stressing and destressing and remained stable even after 15 weeks, which demonstrates its durability and stability. Also, the PPBF nanogenerator exhibited a maximum power density and conversion efficiency of 14.7 μ W/cm² and ~20 %, respectively. The PPBF nanogenerator not only exhibits high performance, but also provides robustness, eco-friendliness, flexibility, low cost and scalability to mass production, making it a highly promising piezoelectric material for energy harvesting applications.

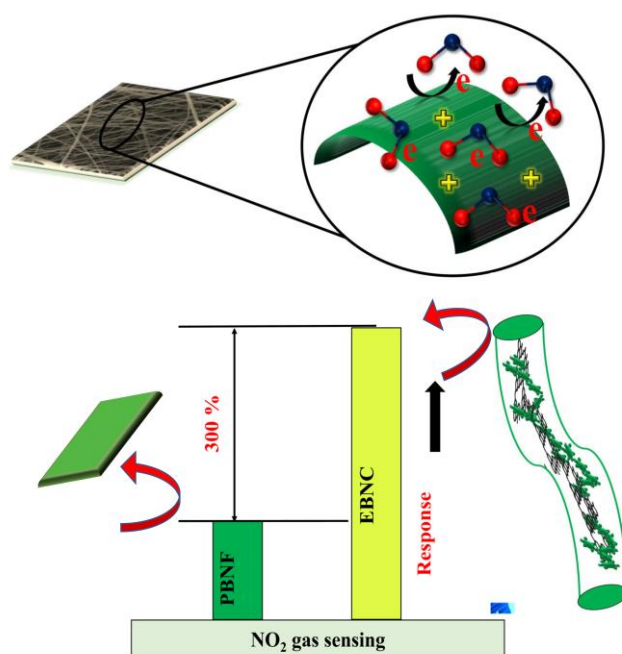
CHAPTER 8

**DURABLE, SENSITIVE AND FLEXIBLE ELECTROSPUN
POLY(VINYLDENE FLUORIDE)/POLYANILINE/GRAPHITIC
CARBON NITRIDE NANOCOMPOSITE-BASED NO₂ GAS SENSOR**

The results of this chapter have been submitted to Sensors and Actuators-B (Under revision).

CHAPTER 8

DURABLE, SENSITIVE AND FLEXIBLE ELECTROSPUN POLY(VINYLIDENE FLUORIDE)/POLYANILINE/GRAPHITIC CARBON NITRIDE NANOCOMPOSITE-BASED GAS SENSOR FOR NO₂ SENSING



In this chapter, a novel and flexible electrospun PVDF/PANi/g-C₃N₄ nanocomposite (PPBF) based gas sensor was developed to detect NO₂ gas at room temperature. Electrospinning conditions were optimized to produce uniform and defect free fibers. g-C₃N₄/PANi nanocomposite (GPC) was synthesized by in-situ polymerization technique. SEM, FTIR, TEM and WAXD analysis was carried out to study the morphological and polymorphism of samples. An indigenous setup was prepared to study the performance of the gas sensor. On the other hand, for the comparison study thin film of PVDF/GPC nanocomposite (SCNF) was fabricated using the doctor blade technique. NO₂ gas was purged into the test chamber at different concentration and the response of the sensor was noted. The response, sensitivity, selectivity, durability, stability was also investigated.

8.1.RESULTS AND DISCUSSION

8.1.1. UV-Vis spectroscopy

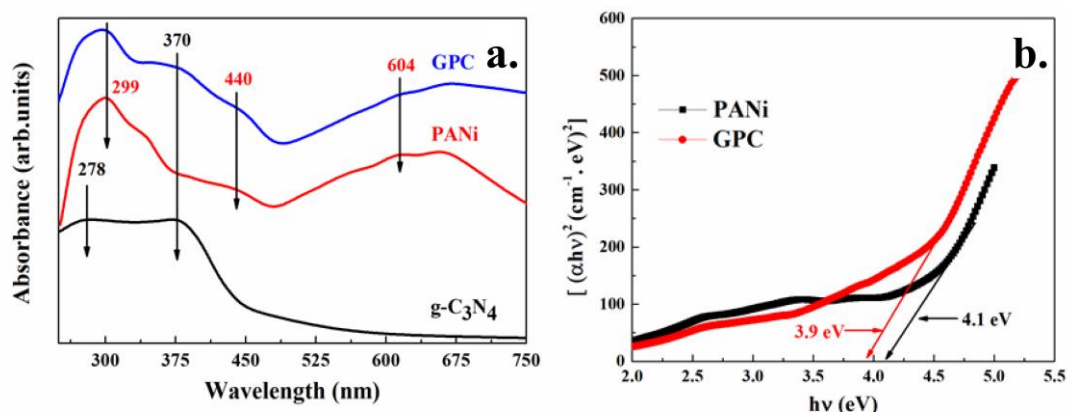


Fig. 8.1 a) UV–Visible spectra of g-C₃N₄, PANi and GPC b) Band gap of PANi and GPC.

The optical properties were studied in order to understand the influence of g-C₃N₄ nanosheets in GPC. Use of dopant and oxidant during the synthesis protonate/deprotonate the PANi base sites. Hence, there will be transition in the oxidation states of PANi nanorods and are interlinked with the optical properties. UV-Vis NIR spectra of g-C₃N₄ nanosheets, PANi nanorods and GPC are shown in Fig. 8.1a. For g-C₃N₄ nanosheets, peak arising in the range of 250-400 nm attributes to the typical semiconductor behavior of g-C₃N₄ nanosheets. For PANi nanorods, the peak arising at 299 nm correspond to the π - π^* benzenoid band interaction. Broad peaks arising ~440 nm and ~604 nm, respectively correspond to the polaron/bipolaron transition and polaron- π^* band transition (Babu et al. 2013; Abd El-Ghaffar et al. 2016). For GPC samples, peaks were similar to PANi nanorods, but there was slight shift in the peak positions. Peak at 299 nm blue shifted to 295 nm. Also, the peak at 604 nm corresponding to polaron- π^* band transition redshifted. In addition to this, peak at 370 nm was observed that correspond to the presence of g-C₃N₄ nanosheets. The shift in peak positions suggest that there is a strong interaction between PANi nanorods and g-C₃N₄ nanosheets (Patil 2012; Nimkar et al. 2015).

The use of dopant helps to generate the charge carriers. The size of the band gap is influenced by the conjugation and delocalization, which determines the conducting behavior of PANi. Fig. 8.1b shows the band gap energy of PANi and GPC samples. The band gap of PANi nanorods for the absorptions of 299 nm and 604 nm was found to be 4.1 eV and 2.3 eV, respectively, while for GPC it was 3.9 eV and 2.1 eV. The shift in the band gap energies in GPC is attributed to the presence of g-C₃N₄ nanosheets, which lead to disorder and structural defects in the PANi chains. When the band gap is small (0.1- 3 eV), the energy of electrons is

increased and tend to detach from their atoms by hopping to a higher energy levels in the conduction band, thereby conducting the electricity. In addition, the holes that are created in the valence band will also contribute to the electrical conductivity (Banerjee and Kumar 2011).

8.1.2. SEM Micrographs

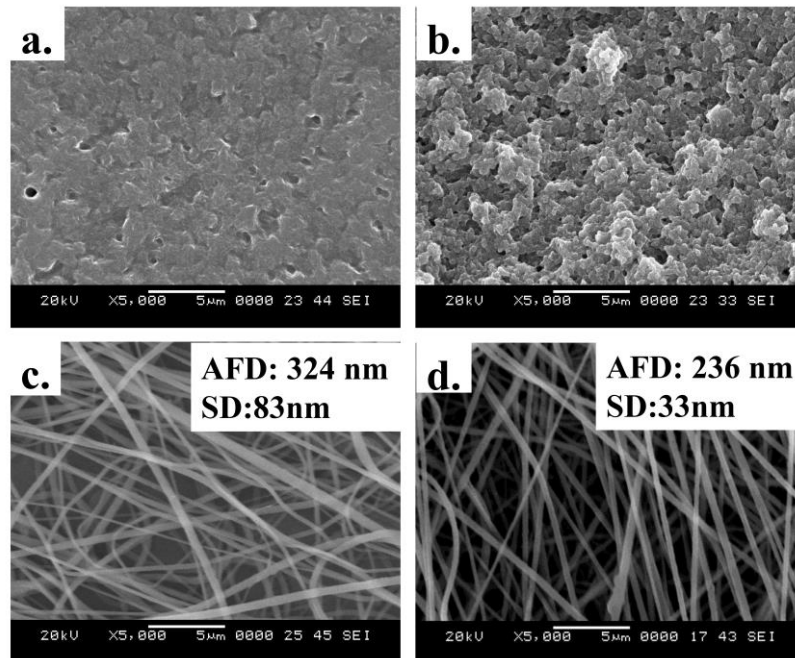


Fig.8.2 a) SEM micrograph of SPF b) SEM micrograph of SCNF c) SEM micrograph of E-PVDF d) SEM micrograph of PPBF.

The morphology of SPF and SCNF is shown in Fig. 8.2a & 8.2b. The morphology of SPF consists of spherulites, which are usually observed in PVDF when crystallized from the solution or melt. In SPF, the surface of the film was found to be less porous with an average size of spherulites of $\sim 5 \mu\text{m}$. The formation of large spherulites is ascribed to the chain mobility that favors the growth of spherulites during the evaporation of the solvent. In addition, the use of acetone along with DMF increased the evaporation rate that resulted in an increase of the spherulite size. On the other hand, SCNF showed distinct morphology compared with the SPF. In SCNF, the spherulite size decreased and the morphology was seen to be porous, which may be attributed to the presence of PANi and $g\text{-C}_3\text{N}_4$. The decrease in spherulite size is attributed to the presence of GPC that destroyed the grain boundaries of the spherulites. Also, the concentration of PVDF and GPC in DMF hindered the growth of spherulites (Gregorio et al. 2010; Bracciale et al. 2017; Fortunato et al. 2018).

SEM images of E-PVDF and PPBF are shown in Fig. 8.2c & 8.2d. Electrospun E-PVDF and PPBF nanofibers were found to be continuous and bead free. It is essential to fabricate defect free nanofibers as defects tends to suppress the electrical properties and gas sensing response of the latter (Doshi and Reneker 1993). The PPBF fibers were uniform and the most of the nanofibers was oriented in one direction, while non- uniformity and random arrangement was observed in E-PVDF. The AFD of E-PVDF was 324 ± 81 nm, whereas for PPBF it was 236 ± 33 nm. Finer and defect free nanofibers provide high surface area, aspect ratio and porosity that are essential for the efficient transport of molecules, fast response and quick recovery (Low et al. 2014).

8.1.3. FTIR and WAXD analysis

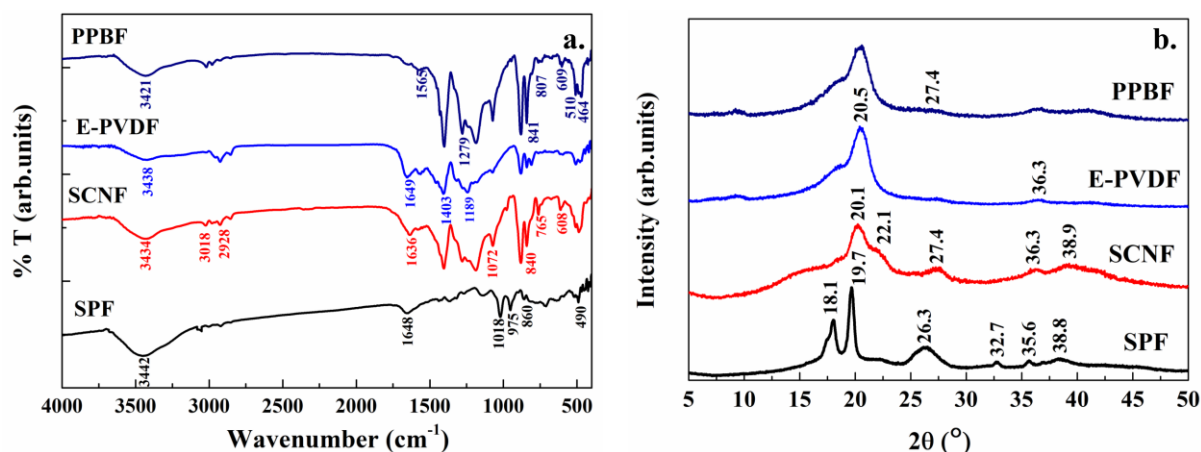


Fig. 8.3 a) FTIR spectra of SPF, SCNF, E-PVDF and PPBF b) WAXD patterns of SPF, SCNF, E-PVDF and PPBF.

FTIR spectra of SPF, SCNF, E-PVDF and PPBF are shown in Fig. 8.3a. For SPF, bands arising at 490, 532, 860, 975 and 1648 cm⁻¹ correspond to the α -phase of PVDF, which are generally observed in unstretched and unpoled PVDF films. Also, the bands at 2924 and 3024 cm⁻¹, respectively correspond to the symmetric and asymmetric stretching vibrations of CH₂ groups of PVDF. For SCNF, new bands were observed at 840, 1279 and 1402 cm⁻¹ corresponding to the β -phase of PVDF alongside α -phase, which is attributed to the nucleation activity of GPC. In E-PVDF, α & β -phase bands were observed, while α -phase bands were completely diminished in PPBF, signifying the complete transformation of α -phase to β -phase of PVDF. The characteristic bands of GPC were also observed at 1565, 807 and 609 cm⁻¹. Also, the band at 3438 cm⁻¹ corresponding to the hydroxyl group shifted to a lower wavenumber, indicating the strong hydrogen bonding interaction between the fluorine atoms

of PVDF and OH group of GPC (Bormashenko et al. 2004; Martins et al. 2012; Saïdi et al. 2013b; Cai et al. 2017).

8.1.4. Gas sensing evaluation

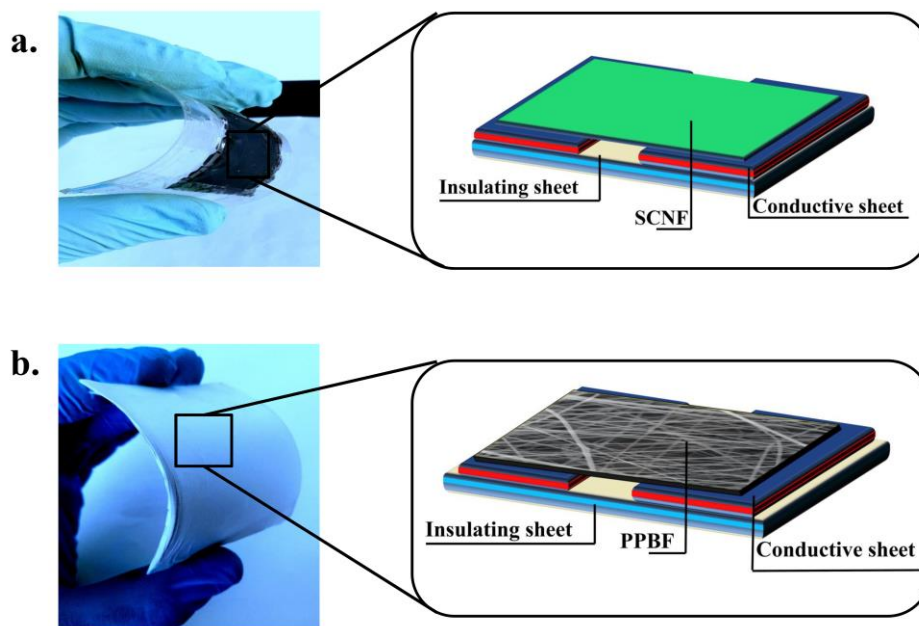


Fig. 8.4 Digital photograph and schematic of gas sensor used in this study **a)** SCNF-based gas sensor **b)** PPBF-based gas sensor.

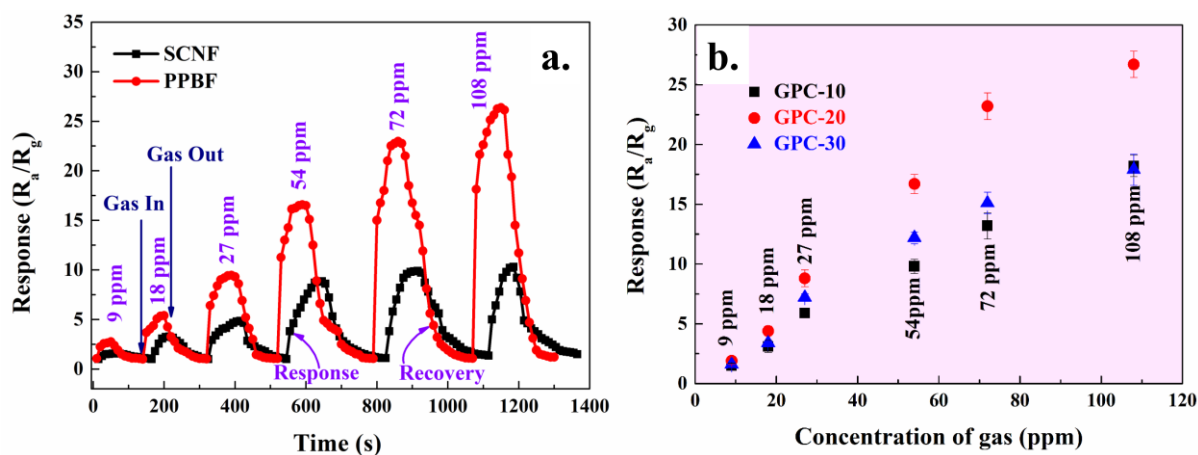


Fig. 8.5 a). Response and recovery curves of SCNF and PPBF against NO_2 gas at a different concentration **b).** Effect of $\text{g-C}_3\text{N}_4$ nanosheet loading on the response of PPBF sensor against NO_2 gas at different concentrations.

Fig. 8.3b shows the WAXD patterns of SPF, SCNF, E-PVDF and PPBF. In the WAXD patterns of SPF, peaks arising at 18.1° , 19.7° , 26.3° , 32.7° , 35.6° and 38.8° correspond to the α -phase of PVDF, while these peaks become weak; and new peaks were observed for SCNF. The peaks at 20.1° and 36.3° correspond to the β -phase of PVDF, while peaks at 22.1° and 27.4°

correspond to the PANi and g-C₃N₄ nanosheets, respectively. In addition, peaks at 19.1° and 38.9° was observed, which is attributed to the presence of α -phase of PVDF (Martins et al. 2014; Zhu et al. 2015). For PPBF, α -phase had diminished completely, which is in-line with the FTIR results.

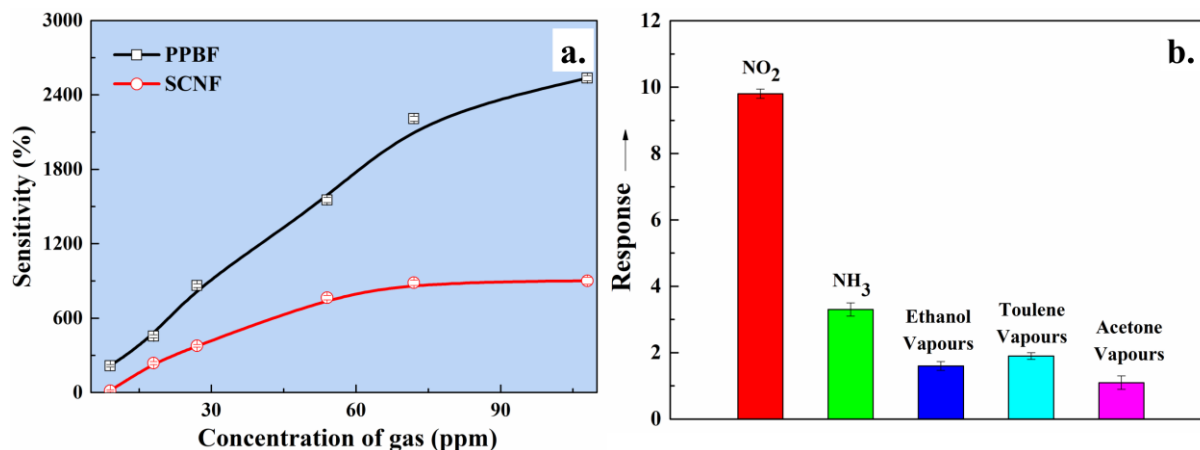


Fig. 8.6 a) Sensitivity of SCNF and PPBF against NO₂ gas at a different concentration of gas
b) selectivity (with error bar) of PPBF-based gas sensor.

The gas sensing performance of SCNF and PPBF based gas sensor against NO₂ molecules at different concentration was investigated. Fig. 8.4(a-d) shows the digital photograph and schematic illustration of SCNF and PPBF-based gas sensor used in this study. The response and recovery curves of SCNF and PPBF against NO₂ molecules at different concentrations are shown in Fig. 8.5a. The electrical resistance decreased when NO₂ molecules interacted with the sensor suggesting the p-type behavior. NO₂ being electron acceptor induces an increase in electrical conductivity of the sensor. Usually, p-type sensors exhibit good response to NO₂ molecules compared with other electron accepting gases. The response of the sensor increased with an increase in the gas concentration. PPBF showed high response compared to SCNF at all concentration of NO₂ considered in this study. Also, the PPBF showed quick response and complete recovery, while SCNF took more time to respond and struggled to recover completely at higher concentrations. Fig. 8.5b shows the effect of g-C₃N₄ loading in GPC on the response of the PPBF sensor at different concentrations of NO₂ gas molecules. The response of the gas sensor is a function of its g-C₃N₄ loading. The highest response was noted for PPBF sensor loaded with GPC-20, while the same decreased for GPC-30. The presence of g-C₃N₄ provide excellent adsorption characteristics, which enhances the interaction of the sensor surface with the NO₂ molecule.

The sensitivity of the gas sensor is considered to be the most critical factor in considering it for practical application. The sensitivity of SCNF and PPBF based gas sensor is shown in Fig. 8.6a. The sensitivity of the gas sensor increased with increase in NO₂ concentration. The highest sensitivity of ~2600 % and ~895% were achieved for PPBF and SCNF based gas sensor, respectively.

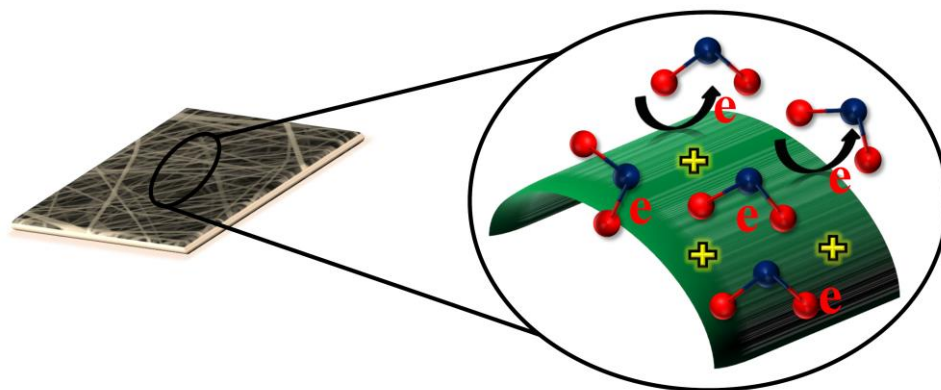


Fig. 8.7 Plausible sensing mechanism of PPBF-based gas sensor for NO₂ sensing.

It is also essential to address the selectivity of the PPBF gas sensor. The selectivity of the PPBF-based gas sensor was examined against NO₂, NH₃, ethanol, toluene and acetone vapors at 18ppm. Since the sensor did not respond to acetone and toluene vapors at lower gas concentrations, 27 ppm was chosen in this selectivity studies. The response of the sensor for NO₂ gas was at least 300% higher than that for the other gases considered (Fig. 8.6b). The high selectivity of PPBF gas sensor provides a valuable additive and is considered ideal for designing a high-performance gas sensor.

Improved response and recovery with an excellent sensitivity of PPBF based gas sensor is attributed to the synergistic effect of electrospinning and GPC. Electrospun fibers provide excellent flexibility, porosity and high surface area compared to thin films (Mahant et al. 2015a; Wang et al. 2016). High surface area and porosity of the electrospun nanofibers of the sensor facilitates its interaction with NO₂ molecules. Further, g-C₃N₄ nanosheets have triazine structure and provide superior catalytic properties (Mortazavi et al. 2015). The layered structure of g-C₃N₄ nanosheets provides active sites to interact with the gas molecules. In addition, it has excellent adsorption and desorption characteristics, which makes the sensor to recover completely (Zhu et al. 2014; Zou et al. 2015; Hang et al. 2017). Also, PANi nanorods have superior charge carrier mobility, which provides a pathway in the sensing process.

The sensing mechanism of SCNF and PPBF based gas sensors is shown in Fig. 8.7. When the NO₂ molecule comes in contact with the surface of the gas sensor, it diffuses into the blend nanofibers and subsequently leaves behind a hole in the g-C₃N₄ nanosheets. The hole is

then transported by PANi nanorods, which increases the electrical conductivity of the sensor. In addition, when the gas molecules come in direct contact with PANi nanorods, electrons are transferred to NO₂ that results in a decrease in the electrical resistance of the sensor. During recovery of the sensor, when the sensor is exposed to open air, O₂ molecules deposits on the surface of the sensor to form anions by capturing electrons from the conduction band and hence the electrical resistance (increased) comes back to its initial value (Reddy and Anandhan 2016a; Zhang et al. 2016b, 2017; Hang et al. 2017).

Fig.8.8a and 8.8b show the repeatability and stability of the sensors (PPBF and SCNF), respectively. The sensor was exposed to NO₂ at 18 ppm over a period of 30 days. On the other hand, the sensor was exposed to NO₂ at 18 ppm for 100 cycles. Interestingly, both the sensors showed excellent repeatability characteristics and there was no loss in the response of the sensors even after 30 days. The sensors also showed excellent stability when repeatedly exposed to the NO₂ for 100cycles. However, there was a small decrement in the response of PBNF based gas sensor after repeated exposure of gas molecules and the sensor struggled to recover after few cycles.

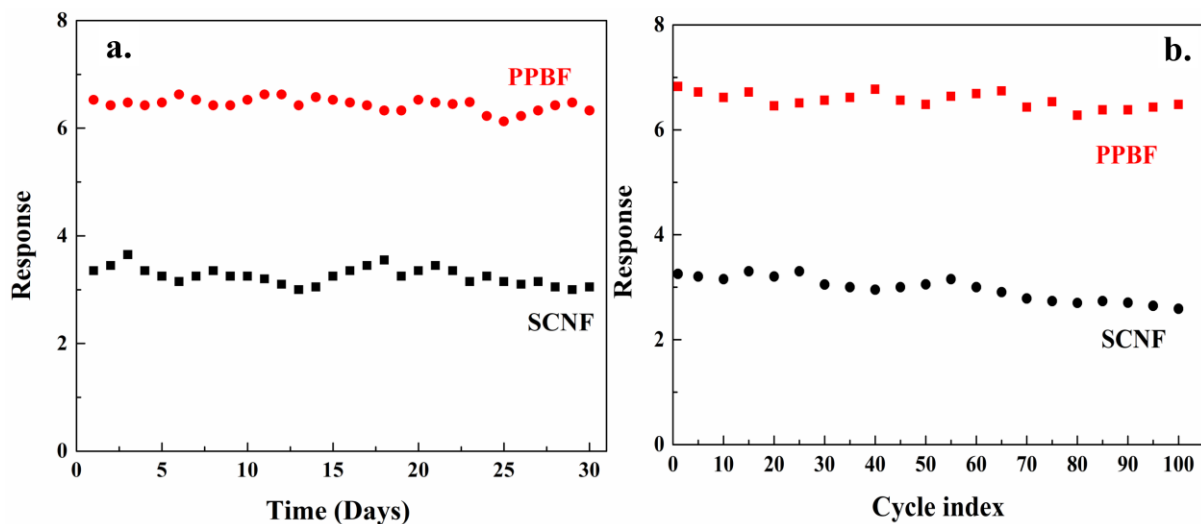


Fig. 8.8 (a). The response of SCNF and PPBF-based gas sensor exposed to NO₂ gas for over 100 cycle (b). Long-term stability of SCNF and PPBF-based gas sensor.

To summarize, the synergistic effect of electrospinning and GPC improves the performance of PPBF based gas sensor. Also, the presence of PANi provide a pathway network for the change in electrical conductivity. g-C₃N₄ nanosheets have excellent catalytic and adsorption characteristics, which provide a faster response of the sensor. PVDF fibers provide high surface area and porosity, which improve the interaction of the gas molecules with the surface of the sensor. The PPBF sensor provides excellent response and recovery, high sensitivity, stability

and exceptional sensitivity. Also, electrospinning being a low cost and scalable technique with simplicity in design and fabrication of gas sensor makes it a promising material for gas sensing application. Sensors made of electrospinning process have superior sensitivity and flexibility compared to solution cast thin films because of their higher surface area, higher porosity, better adsorption and diffusion characteristics. Therefore, PPBF sensor appear to have high potential in NO₂ gas sensing.

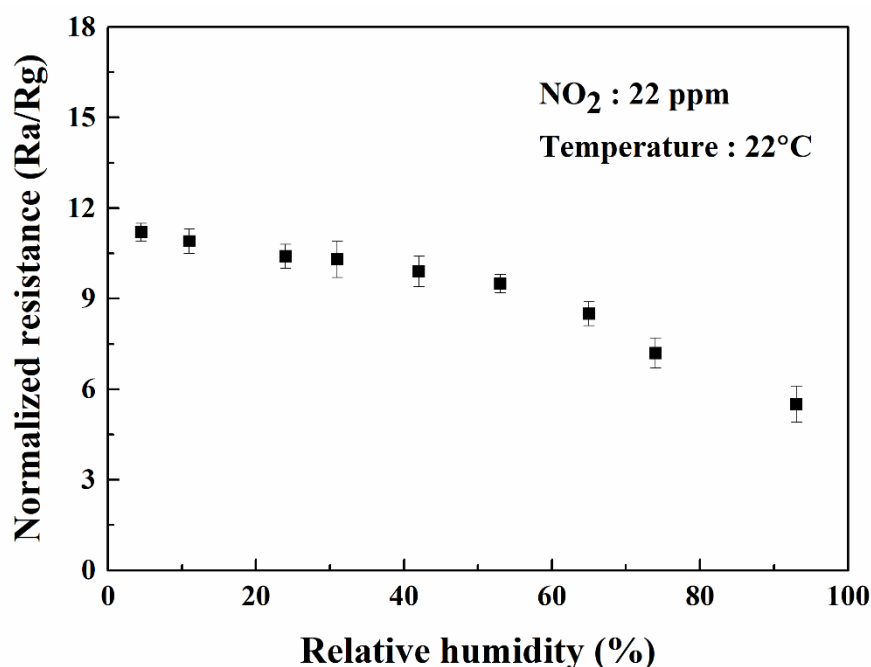


Fig. 8.9 PPBF sensor response against NO₂ at different humidity conditions.

Also, the response of the sensor was evaluated against NO₂ at 22 ppm and 24°C at different relative humidity conditions (**Fig. 8.9**). The response of the sensor insignificantly decreased with an increase in relative humidity (< 60%). However, the response deteriorated at higher relative humidity values (> 60%). The decrease in the response is attributed to the fact that the sensing environment contains more water molecules, which occupy the active sites available on the sensor surface and hence the sites available for to interact with the NO₂ molecules drops significantly leading to a decrease in response of the sensor.

8.2.CONCLUSIONS

A flexible PVDF/PANi-g-C₃N₄ (GPC) nanocomposite (PPBF) based gas sensor was designed for NO₂ gas sensing by a simple, cost-effective and scalable electrospinning technique. PPBF based gas sensor was exposed to NO₂ gas molecules at different gas concentrations (9-108 ppm). The sensor showed high response and recovered completely. Electrospinning not only

provides high surface area and flexibility, but also helps to interact with the gas molecules. The sensor showed high sensitivity (~96 %) and selectivity with excellent repeatability. PPBF sensor showed stable response over 30 days and 100 cycles and can be used multiple times without affecting its efficiency.

CHAPTER 9

SUMMARY AND CONCLUSIONS

CHAPTER 9

SUMMARY AND CONCLUSIONS

Long, continuous and bead free PVDF nanofibers can be produced by electrospinning process. Several trials were carried out to optimize the electrospinning conditions of PVDF for obtaining bead-less and defect-free nanofibers. The average fiber diameter (AFD) of PVDF nanofibers decreased upon the addition of nanofillers. Nanofillers containing the surface charges improved the electrical conductivity of the electrospinning solution that resulted in the formation finer fibers. The crystallinity of PVDF decreased upon the addition of nanofillers, while the β -phase content increased simultaneously. The properties of PVDF were found to be affected with the loading of nanofillers. In the case of PVDF/HNT nanocomposite, the highest β -phase content was observed in PHNF-10 and the HNTs were oriented along the axis of the fiber because of the strong interaction between HNTs and PVDF. On the other hand, short PANi networks were observed in BNCNF, which may be ascribed to the high stretching of fibers during the electrospinning process. HNT and $g\text{-C}_3\text{N}_4$ nucleated the β -phase of PVDF while, PANi improved the electrical conductivity of nanofibers.

The highest β -phase content of $\sim 97\%$ was observed in electrospun PVDF nanofibers containing $g\text{-C}_3\text{N}_4$ and PANi. The interplay between the effects brought about by the nanofillers and electrospinning could be used to engineer the crystallinity, polymorphism and piezoelectric behavior of PVDF. Addition of HNT and PANi showed a detrimental effect in thermal stability while, $g\text{-C}_3\text{N}_4$ increased the onset temperature of thermal degradation. Also, the nanocomposites exhibited high tensile strength, tensile modulus and flexibility. The piezoelectric properties of PVDF enhanced appreciably due to the synergism of electrospinning and nanofillers. An indigenous setup was prepared to measure the piezoelectric performance of electrospun PVDF nanocomposites. The piezoelectric performance of electrospun PVDF nanocomposites under real-life situation was evaluated under various human movement such as tapping, bending, arm movement, pressing etc. Maximum piezoelectric voltage of 0.95 V, 7.2 V, 7.5 V and 30 V were generated for PHNF, BNCNF, PGN and PPBF based nanogenerator, respectively. The maximum current outputs 34 nA, 0.75 μA , 0.25 μA and 3.75 μA was generated for PHNF, BNCNF, PGN and PPBF nanogenerator, respectively. The nanogenerators exhibited excellent stability, durability and reproducibility that are beneficial in adopting the nanogenerators for practical applications. The power density of PVDF was

found to increase upon the addition of nanofillers. Overall, the simplicity and scalability of fabrication of these nanogenerators combined with their high performance could make them a suitable candidate for flexible self-powered devices and sensors.

Due to the flexibility, lower crystallinity and high tensile properties, PHNF was explored in lithium ion battery as gel polymer electrolyte (GPE). Fine, uniform and interconnected porous structure of PHNF resulted in high electrolyte uptake. Electrochemical stability and ionic transference of PHNF separator increased compared with that of the commercial and E-PVDF separator. PHNF separator exhibited low-ionic resistance, superior tensile strength, and thermal stability. The separator showed high resistance to puncture compared with E-PVDF separator. PHNF-based separator not only addresses the issue of ionic conductivity and high-energy density, but is also safe and cost effective. The performance of PHNF separator at different current densities was remarkably better than those of Celgard[®]2400 and E-PVDF separators. Most importantly, the separator performed exceptionally well when subjected to repeated charge–discharge cycles. Therefore, the PHNF separator could be a promising material to be used as a thermally stable, cost-effective and active separator for lithium ion batteries.

A flexible, wearable and cost-effective PPBF based chemi-resistive gas sensor was designed and deployed to detect the NO₂ gas at different concentrations (9-108 ppm). Addition of PANi/g-C₃N₄ nanocomposite in PVDF nanofibers provided a new insight in enhancing the electrical properties of the PVDF nanofibers. The presence of g-C₃N₄ nanosheets provided excellent adsorption and desorption characteristics, which resulted in quick response and recovery of the sensor. The sensor exhibited high response, sensitivity and selectivity against NO₂ gas along with high stability and reproducibility.

Overall, the electrospun PVDF nanocomposites proved to be flexible and their fabrication process is relatively simpler and economical. The PVDF nanocomposites showed better physical characteristics than pure PVDF nanofibers. Finally, preparation of nanofibers by electrospinning is a potential and scalable technique to tailor the properties of PVDF depending on the desired application.

An ephemeral summary on the properties of nanocomposites of the present work is described in the following scheme.

CHAPTER-3	CHAPTER-4	CHAPTER-5
Electrospun PVDF/HNT nanocomposite	Electrospun PVDF/HNT nanocomposite	Electrospun PVDF/HNT /PANi Blend Nanocomposite
<p>Solvent: DMSO Concentration of PVDF: 18 w/v% HNT loading: 2.5, 5.0, 7.5, 10.0, 15.0 & 20.0 wt%.</p>	<p>Solvent: DMSO Concentration of PVDF: 18 w/v% HNT loading: 10wt% Coin Cell: Li/PHNF/LiCoCO₂ Separator thickness: 25.6 μm</p>	<p>Solvent: DMF: Acetone (85:15) Concentration of PVDF: 13 w/v% HNT loading: 10 wt% PANi loading: 17.5 wt% Thickness: 50 μm Nanogenerator size: 2 cm × 2 cm</p>
Piezoelectric force sensor	Gel polymer electrolyte in Lithium ion battery	Pressure Sensor
<p>AFD:202 nm Crystallinity: ~36% (reduced). HNT oriented along the fiber axis. Strong interaction between HNT & PVDF. Max. %β-phase: 80% Max. Voltage: 0.95 V at 100 g Max. Current: 34 nA</p>	<p>Tensile Strength : 32 MPa No shrinkage at 130 °C Electrolyte uptake: 456% Ionic conductivity:1.77 mS.cm⁻² Ionic transference: 0.57 Initial capacity: 138.1 mAhg⁻¹ (96% of theoretical efficiency). (Outperformed Celgard®2400)</p>	<p>PANi nanorod size: 65 nm AFD: 205 nm Max. %β-phase: 84% Crystallinity: 30.4% (reduced) Max. Voltage: 7.2 V. Max. Current: 0.75 μA. Power density: 0.25 μW.cm⁻² Good stability & reproducibility</p>

CHAPTER-6	CHAPTER-7	CHAPTER-8
Electrospun PVDF/g-C ₃ N ₄ nanocomposite	Electrospun PVDF/g-C ₃ N ₄ /PANi Blend Nanocomposite	Electrospun PVDF/g-C ₃ N ₄ /PANi Blend Nanocomposite
<p>Solvent: DMF Concentration of PVDF: 12.5 w/v% g-C₃N₄ loading: 0.25, 0.5, 0.75, 1.0 & 2.0 wt%. (g-C₃N₄ was synthesized by thermal decomposition process)</p>	<p>Solvent: DMF Concentration of PVDF: 13.5w/v% g-C₃N₄/PANi nanocomposite (GPC) synthesized by in-situ polymerization. GPC loading: 20 wt%. Nanogenerator size: 3 cm × 3cm × 0.005cm (Flexible).</p>	<p>Solvent: DMF Concentration of PVDF: 10 w/v% GPC loading: 25 wt%. Solution cast film prepared for comparison. Sensor size: 3 cm × 2 cm × 0.0025 cm</p>
Piezoelectric nanogenerator (Energy harvesting from human locomotion)	Piezoelectric nanogenerator (Energy harvesting from human locomotion) (Tapping, bending, impact, vibrations, twisting, pressing etc)	Gas sensor (NO ₂ gas sensing) Concentration: 9-108 ppm P-type gas sensor
<p>AFD:218 nm. %β-phase: 79.8%. Tensile strength: 17 MPa. Improved thermal stability. Max. Voltage: 7.5 V Max. Current: 0.75 μA Power density: 0.23 μW.cm⁻² Energy stored : 0.49 μJ at 1.1μF. Good stability & reproducibility (18weeks & 10⁴cycles).</p>	<p>AFD: 288 nm. Tensile Strength : ~15 MPa. Crystallinity: 35.9% (reduced). Max. Voltage: ~30 V. Max. Current: 3.75 μA. Energy stored : 49.5 μJ at 3.3 μF. Piezoelectric conversion efficiency : ~20%. Power density: 14.7 μW.cm⁻² Excellent stability & reproducibility (15weeks & 5×10⁴ cycles).</p>	<p>AFD: 236 nm. Highly flexible and non toxic. PANi network formed within the fibers. Response: 3 times better than film. Max. Sensitivity: ~2600%. Selectivity: Highly selective towards NO₂ gas. Stability & reproducibility: 100 cycles & 30 days.</p>

*The results mentioned for the optimized conditions or maximum outputs.

SCOPE FOR FURTHER WORK

1. Preparation of electrospun PVDF nanofibers using conductive fillers for the fabrication of flexible and efficient energy harvesting system.
2. PVDF nanocomposites can be explored in sodium ion batteries, fuel cells, supercapacitors and filtration membranes.
3. A theoretical model can be developed to investigate the effects of electrospinning parameters and nanofillers on the properties of PVDF.
4. Piezoelectric coefficients, ferroelectric and dielectric properties of PVDF nanocomposites can be explored.

APPENDIX -I

I.1. Optimization of electrospinning conditions

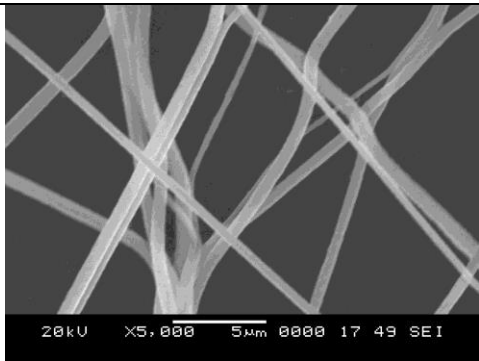
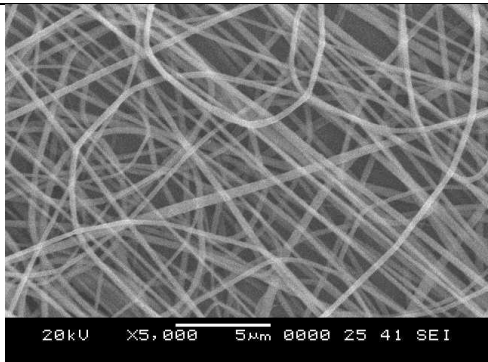
Several experiments were performed to optimize the electrospinning process for producing PVDF nanofibers. Various parameters such as solvent, tip to collector distance (TCD), and flow rate to get bead-free, smooth and uniform fibers with smaller average fiber diameter (AFD). In general, N,N-dimethylformamide (DMF), dimethyl sulfoxide (DMSO) and triethylphosphate (TEP) are considered as good solvents for PVDF as they have high dielectric constants to match with that of PVDF. DMSO plays a vital role in increasing the electrical properties and dielectric constant in PVDF compared to DMF and TEP (Gonçalves et al. 2013).

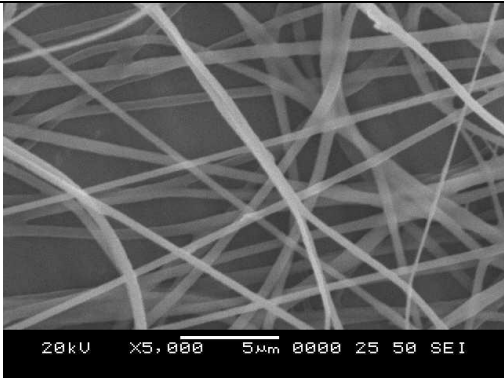
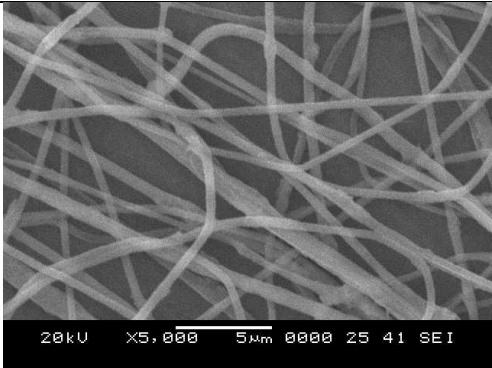
TCD, flow rate and type of solvents has played a vital role in obtaining the desired nanofiber morphology. The fibers produced from DMF solution were brittle and difficult to handle. However, fibers produced using DMSO were ductile with improved morphology and higher production rate (Table I.1). This may be attributed to the high boiling point and high dielectric constant of DMSO (Janakiraman et al. 2016). The critical entanglement concentration for PVDF in DMSO was found to be around 18 wt./v%. Increase in flow rate resulted in increased AFD. At a TCD of 15 cm fibers were randomly oriented and partially wet. However, at a TCD of 20 cm fibers were smooth, uniform and bead-free with improved orientation. A further increase in TCD leads to decrease in collection of fibers with bead formation.

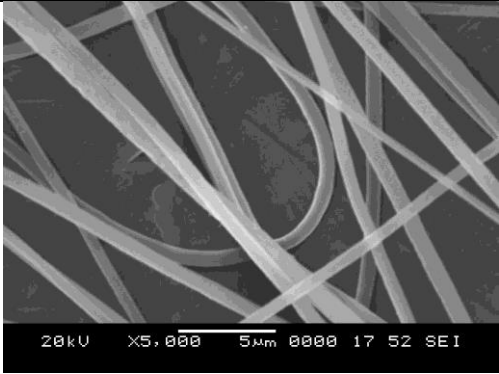
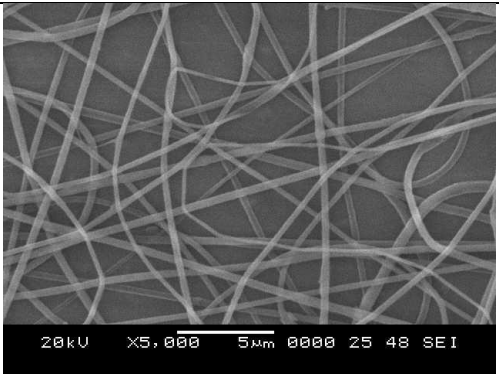
I.2. Synthesis and characterization of PVDF film

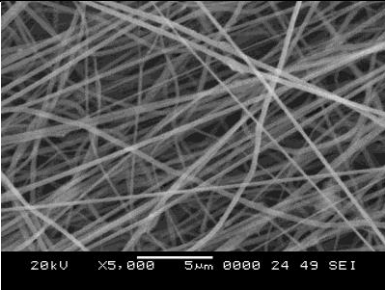
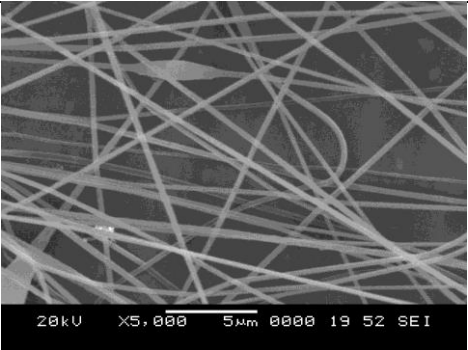
13 w/v% PVDF in powder form was dissolved in DMF and cast on the glass substrate for the preparation of film. Films were dried at 50 °C for 4 h. Once the solvent evaporated completely, PVDF film was detached from the substrate.

Table. I.1 SEM micrographs of E-PVDF at different electrospinning conditions

Parameters	Solvent	SEM Micrographs	Remarks
Flow rate :0.5 mL/hr Tip to collector Distance (TCD) : 20 cm Concentration : 18 wt./v% Applied Voltage : 20 kV	DMF		Fibers were smooth and bead free. Fibers were brittle and the AFD was 790 nm. Production rate of fibers was low.
AFD ± SD (nm)		790 ± 143	
Flow rate :0.5 mL/hr Tip to collector Distance (TCD) : 20 cm Concentration : 18 wt./v% Applied Voltage : 20 kV	DMSO		Smooth, uniform and bead free fibers. Fibers were collected at larger rate compared to DMF solvent.
AFD ± SD (nm)		302±85	

Parameters	Flow rate (mL/hr)	SEM micrographs	Remarks
Solvent : DMSO Tip to collector Distance (TCD) : 20 cm Concentration : 18 wt./v% Applied Voltage : 20 kV	0.5		<ul style="list-style-type: none"> Smooth, Uniform and bead free fibers were produced.
AFD ± SD (nm)		302 ± 85	
Solvent : DMSO Tip to collector Distance (TCD) : 20 cm Concentration : 18 wt./v% Applied Voltage : 20 kV	0.8		<ul style="list-style-type: none"> Fibers were randomly oriented and also fibers were not uniformly distributed.
AFD ± SD (nm)		464 ± 92	

Solvent : DMSO Tip to collector Distance (TCD) : 20 cm Concentration : 18 wt./v% Applied Voltage : 20 kV	1.0		<ul style="list-style-type: none"> Fiber diameter increased drastically. Fibers had a ribbon-like morphology.
AFD ± SD (nm)		632 ± 93	
Parameters	TCD, cm	SEM micrographs	Remarks
Solvent : DMSO Flow rate :0.5 mL/hr Concentration : 18 wt./v% Applied Voltage : 20 KV	15		<ul style="list-style-type: none"> Fibers were randomly oriented. Partially dried.
AFD ± SD (nm)		358 ± 87	

<p>Solvent : DMSO Flow rate :0.5 mL/hr Concentration : 18 wt./v% Applied Voltage : 20 KV</p>	20		<ul style="list-style-type: none"> • Nanofibers produced were smooth, uniform and bead free. • Proper drying and collection of fibers.
AFD ± SD (nm)		302 ± 85	
<p>Solvent : DMSO Flow rate :0.5 mL/hr Concentration : 18 wt./v% Applied Voltage : 20 KV</p>	25		<ul style="list-style-type: none"> • AFD of fibers decreased. • Beads were observed. • Collection of fibers was too low.
AFD ± SD (nm)		289 ± 53	

I.3. TEM micrographs of GPC

For TEM micrograph, the homogenous dispersion consisting of 5 mg of GPC in 10 mL of ethanol was ultrasonicated for 4 hours at 20 ± 3 °C. The ethanolic dispersion was coated onto a carbon-coated copper grid (200 mesh) (Sigma Aldrich, India) and dried in a vacuum oven at 40 °C for 24 h.

Fig. I.1 shows the TEM micrograph of GPC-10 with schematic representing the conductive network. It clearly reveals that the PANi nanorods were deposited uniformly on the surface of g-C₃N₄ confirming that the entities are compatible with each other and forms good interaction between them.

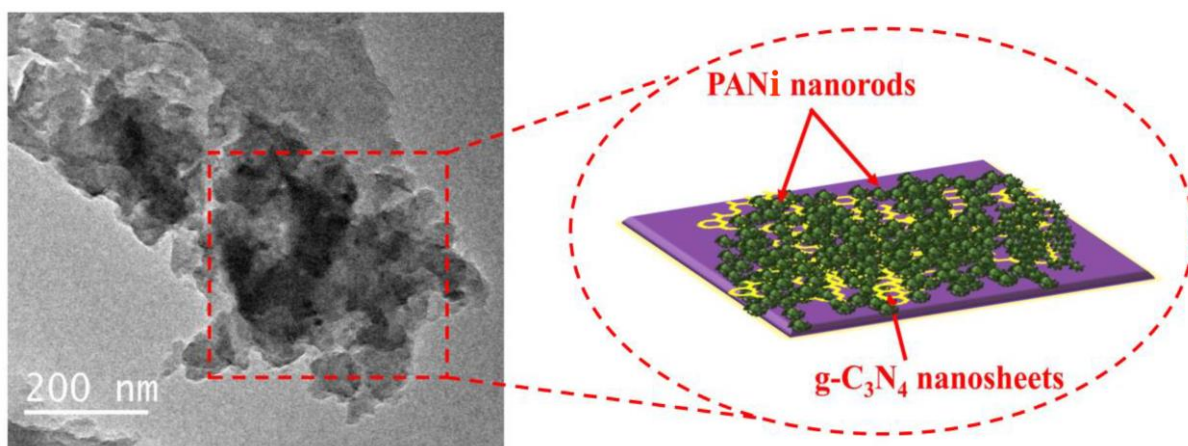


Fig. I.1 TEM image of GPC-10.

I.4. FTIR analysis of PVDF and PVDF/GPC films

Fig. I.2 shows the solution cast pure PVDF and PVDF/GPC nanocomposite film. In the spectrum of pure PVDF film, bands were dominated with the α -phase of PVDF and there were no any bands corresponding to the β -phase of PVDF. For, PVDF/GPC film, β -phase bands were observed along with the α -phase. However, α -phase was seen to be dominated in the solution cast film. The β -phase content of 38% was observed in PVDF/GPC film, which is much lower than E-PVDF (41%) and PPBF-7.5 (~97%). Post processing such as uniaxial stretching, poling or annealing is necessary to obtain higher β -phase content in solution cast PVDF films, while electrospun PVDF mat do not require any post processing because of the involvement of localized poling and stretching during the synthesis of fibers.

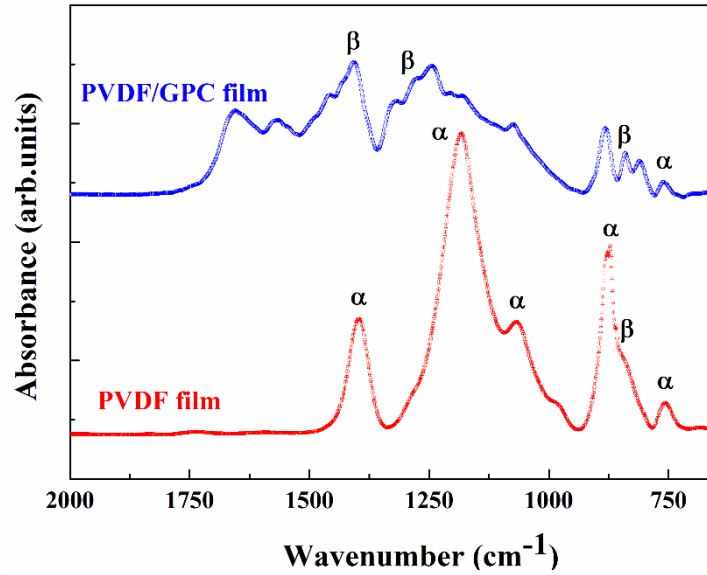


Fig. I.2 FTIR spectra of PVDF and PVDF/GPC film.

I.5. Piezoelectric coefficient and voltage coefficient

The following governing equations have been used to determine the piezoelectric coefficient (d_{33}) and piezoelectric coefficient (g_{33}) of E-PVDF and PGN-X as reported elsewhere [8 & 9]. The g_{33} of PVDF and PGN-X was calculated using Eqn. S1.

$$g_{33} = \frac{V \times 2 \times b \times t}{3 \times F \times l} \quad (\text{I.1})$$

Where, V is the voltage output; b , t & l are the width, thickness and length, respectively of the nanogenerator; F is the applied load (0.49N).

Further, d_{33} was calculated using the following Eqn. S2:

$$d_{33} = \frac{C \times V_c}{F} \quad (\text{I.2})$$

Where, C is the capacitance (0.47 μF); V_c is the voltage output generated across the capacitor.

I.6. Piezoelectric performance of PPBF nanogenerator

Fig.I.4. shows the piezoelectric voltage output of PVDF film, PVDF/GPC nanocomposite film, E-PVDF and PPBF-7.5 under one-finger tapping mode. The voltage output of 0.5 mV, 0.85 V, 0.9 V and 5.4 V was generated for PVDF film, PVDF/GPC nanocomposite film, E-PVDF and PPBF-7.5, respectively. These results confirm the benefits of electrospinning of PVDF in piezoelectric performance.

β -phase content of PVDF seems to be remain unchanged even after the PPBF nanogenerator undergone multiple cycles (>30,000) and time (Fig. I.5a). On the other hand, we also studied

the morphology of fibers after using the nanogenerator numerous times. The morphology of fibers seen to be stable, homogenous and continuous, resembling the morphology of unused PPBF sample (Fig. I.5b).

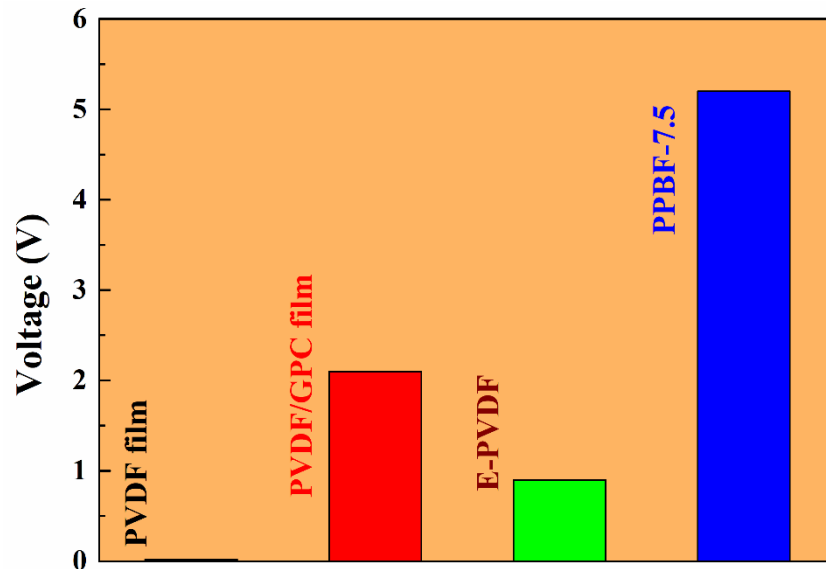


Fig. I.3. Piezoelectric voltage output of PVDF film, PVDF/GPC film, E-PVDF and PPBF-7.5 under one-finger tapping mode.

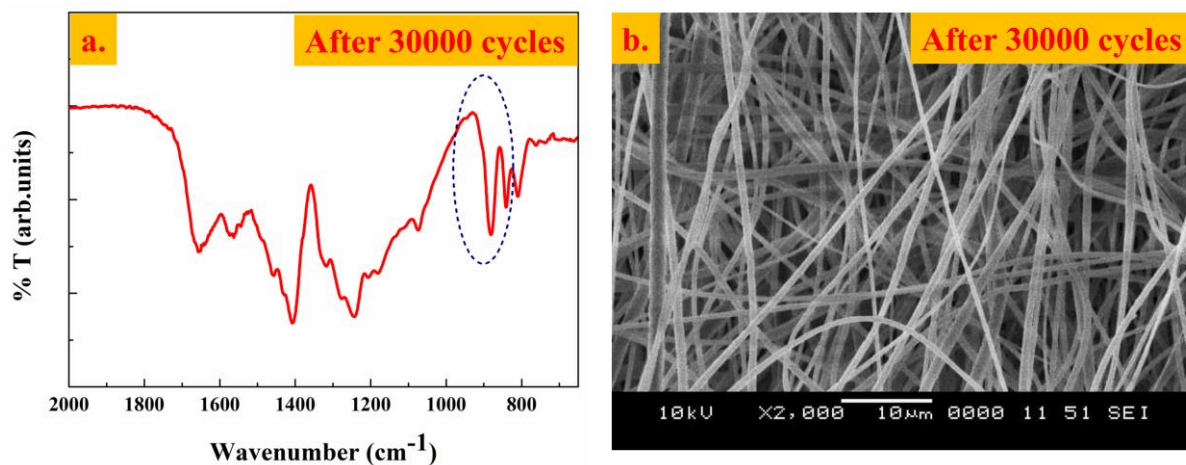


Fig. I.4. PPBF-7.5 nanogenerator after undergoing more than 30000 cycles (a) FTIR spectrum (b) SEM image.

The sensitivity of PPBF-7.5 nanogenerator was also demonstrated by placing the nanogenerator in front of 6 W speaker. The nanogenerator was able to respond against small vibration and generated a piezoelectric voltage output of ~40 mV (Fig. I. 6). Further the current output of PPBF-7.5 nanogenerator was also evaluated under various modes (Fig. I.7) The

nanogenerator generated a maximum current output of $3.7 \mu\text{A}$ when the pressure imparted by punching.

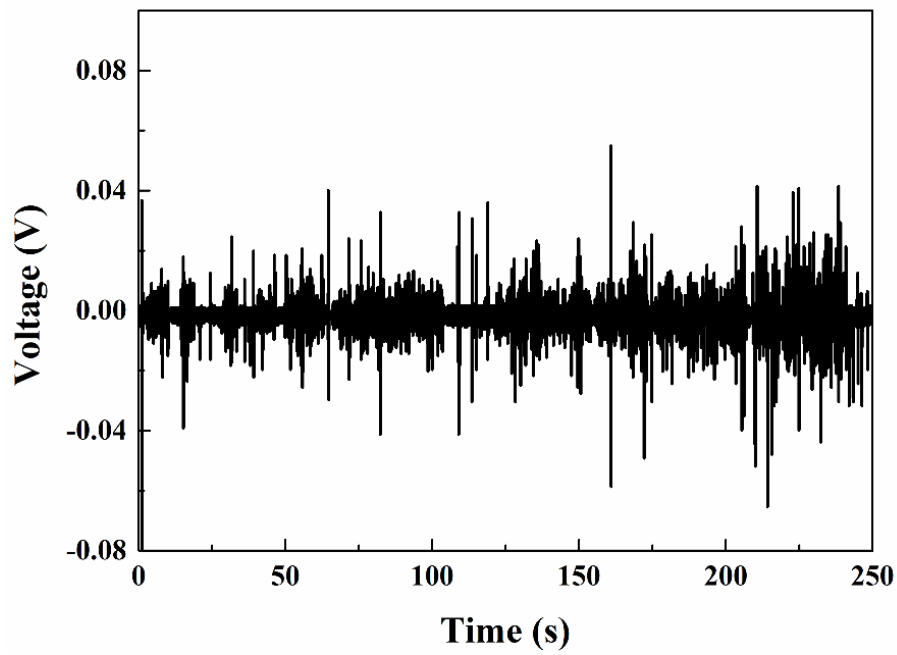


Fig. I.5. Piezoelectric response of PPBF-7.5 nanogenerator kept in front of speaker.

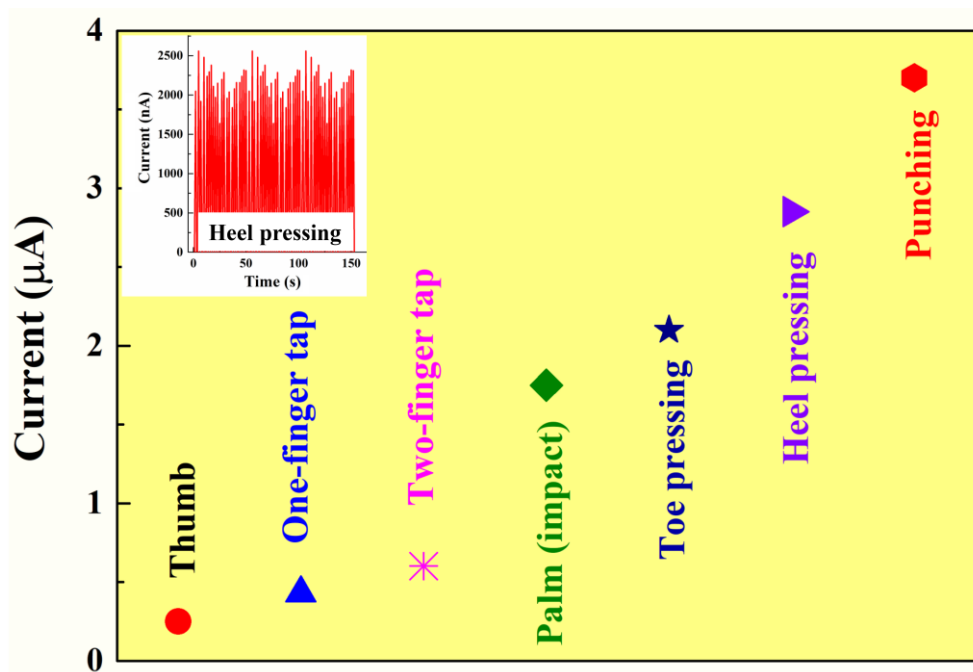


Fig. I.6. Current output of PPBF-7.5 nanogenerator under various modes.

Table I.2. Piezoelectric performance of various electrospun based PVDF nanocomposite nanogenerators.

Nanofillers	Polymer	Max. Voltage output (V)	Current output (μA)	Power density ($\mu\text{W}/\text{cm}^2$)	Ref.
TiO ₂	PVDF	0.72	0.6×10^{-3}		(Dong et al. 2017)
Graphene	PVDF	0.064	0.1		(Abbasipour et al. 2017)
Graphene oxide	PVDF	0.08	0.07		(Abbasipour et al. 2017)
Halloysite nanotube	PVDF	0.1	0.1		(Abbasipour et al. 2017)
Carbon nanotube	PVDF	0.845			(Mokhtari et al. 2017b)
(Na _{0.5} K _{0.5})NbO ₃	PVDF-TrFE	0.98	0.78×10^{-3}		(Kang et al. 2015)
Lithium chloride	PVDF	8			(Mokhtari et al. 2017a)
Zinc oxide	PVDF	1.1			(Sorayani Bafqi et al. 2015)
BaTiO ₃	PVDF	0.48			(Lee et al. 2016)
poly(γ -methyl L- glutamate)	PVDF	0.2	1.8		(Pan et al. 2015a)

cellulose nanocrystal	PVDF	6.3	2.1		(Fashandi et al. 2016)
Graphene/BaTiO ₃	PVDF	8	1.5	5.8*	(Yaqoob et al. 2017)
	PVDF	1.5	4×10 ⁻³		(Z Liu, S Zhang, Y M Jin, H Ouyang, Y Zou, X X Wang 2017)
	PVDF	3	4		(Hwang et al. 2011b)
	PVDF	.085			(Chang et al. 2009a)
	PVDF-HFP	1.6			(Najjar et al. 2017)
	PVDF	4.1			(Bera and Sarkar 2017)
	PVDF	0.4			(Sengupta et al. 2017a)
Ytterbium	PVDF	10		1	(Ghosh et al. 2016)
	P(VDF- TrFE)	1.2	3 × 10 ⁻⁸		(Persano et al. 2013b)

	P(VDF-TrFE)	2.3	3×10^{-8}		(Zaccaria et al. 2016)
	P(VDF-TrFE)	2.5	3×10^{-8}		(Whiter et al. 2014)
TiO ₂	PVDF	20		1.6	(Alam et al. 2018)
Microbead based electrodes	P(VDF-TrFE)	10.4	2.3		(Kim et al. 2018)
	PVDF	0.025	3.9×10^{-8}	5.7×10^{-14}	(Liu et al. 2014)
Polypeptide	PVDF	0.185			(Pan et al. 2015b)
	PVDF	2.3	2.4		(Shao et al. 2015b)
Nanoclay	PVDF	2.2			(Xin et al. 2016)
BaTiO ₃ /polyurethane	P(VDF-TrFE)	9	0.2	1.7	(Siddiqui et al. 2018)
hectorite clay	PVDF	12			(Rahman et al. 2018)
Tri-p-tolylamine (TTA) and 2-(4-tert-butylphenyl)-5-(4-biphenyl)-	PVDF	3.1	3.4		(Shao et al. 2017)

1,3,4-oxadiazole (Butyl-PBD)					
Graphene/ BaTiO ₃	PVDF	11	1.3	4.1*	(Shi et al. 2018)
BaTiO ₃	PVDF	8	0.05		(Lu et al. 2017)
BaTiO ₃	P(VDF TrFE)	0.6	0.6	0.28*	(Nunes-Pereira et al. 2015)
NaNbO ₃	PVDF	3.4	4.4		(Zeng et al. 2013)
Silver nanoparticles	P(VDF TrFE)	3.1			(Mandal et al. 2014)
MWCNT	PVDF	6		0.081	(Yu et al. 2013)
Graphene	PVDF	7.9			(Abolhasani et al. 2017)
	PVDF	0.28	3×10^{-8}		(Pan et al. 2017)
Silver particles	PVDF	2			(Issa et al. 2017)
g-C ₃ N ₄	PVDF	7.2	0.23	0.25	[40]
PANi/g-C₃N₄	PVDF	28	3.7	14.7	Present work

*Power

I.3. Gas sensing measurements

To confirm the performance of PPBF gas sensor, we have synthesized PVDF/PANi film by doctor blade technique and electrospun PVDF/PANi nanocomposite (PPNF). **Fig. S4** shows the sensitivity of PVDF/PANi film, PPNF, PPBF and SCNF at 27 ppm of NO₂ gas. Among all the gas sensors considered, PPBF sensor showed high sensitivity, which confirm the synergistic effect GPC and electrospinning enhances the performance of gas sensor.

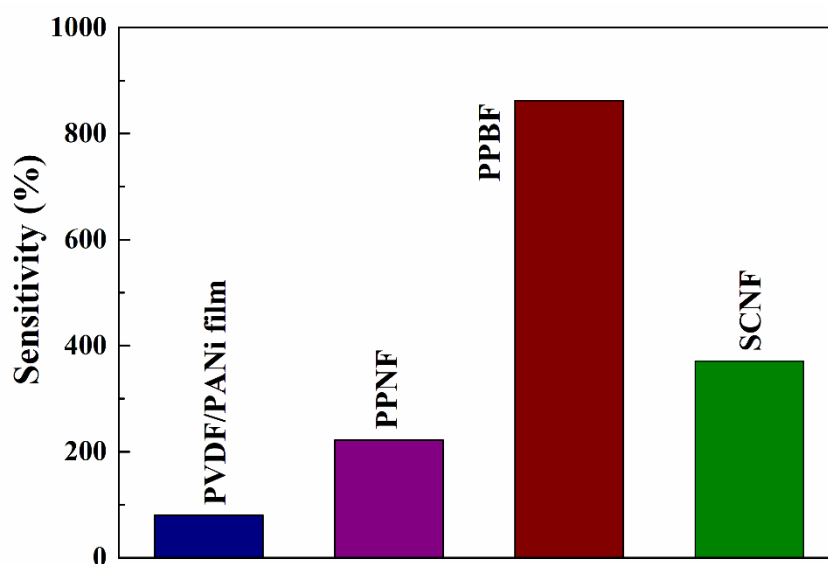


Fig. I.6 Sensitivity of PVDF/PANi film, PPNF, PPBF and SCNF at 27ppm of NO₂ gas.

REFERENCES

- Abbasipour, M., Khajavi, R., Yousefi, A.A., Yazdanshenas, M.E., and Razaghian, F. (2017). "The Piezoelectric Response of Electrospun PVDF Nanofibers with Graphene Oxide, Graphene, and Halloysite Nanofillers: A Comparative Study." *J. Mater. Sci. Mater. Electron.* 28, 15942–15952.
- Abd El-Ghaffar, M.A., Shaffei, K.A., Fouad Zikry, A.A., Mohamed, M.B., and Marzouq, K.A.G. (2016). "Novel Conductive Nano-Composite Ink Based on Poly Aniline, Silver Nanoparticles and Nitrocellulose." *Egypt. J. Chem.* 59, 429–443.
- Abdiryim, T., Xiao-Gang, Z., and Jamal, R. (2005). "Comparative Studies of Solid-State Synthesized Polyaniline Doped with Inorganic Acids." *Mater. Chem. Phys.* 90, 367–372.
- Abolhasani, M.M., Shirvanimoghaddam, K., and Naebe, M. (2017). "PVDF/Graphene Composite Nanofibers with Enhanced Piezoelectric Performance for Development of Robust Nanogenerators." *Compos. Sci. Technol.* 138, 49–56.
- Achaby, M. El, Arrakhiz, F.Z., Vaudreuil, S., Essassi, E.M., and Qaiss, A. (2012). "Piezoelectric β -Polymorph Formation and Properties Enhancement in Graphene Oxide – PVDF Nanocomposite Films." *Appl. Surf. Sci.* 258, 7668–7677.
- Adams, F. V., Nxumalo, E.N., Krause, R.W.M., Hoek, E.M.V., and Mamba, B.B. (2012). "Preparation and Characterization of Polysulfone/ β -Cyclodextrin Polyurethane Composite/Nanofiltration Membranes." *J. Memb. Sci.* 405, 291–299.
- Aggarwal, S., Sreeja, K.S., Chakrabarti, S., Palkar, V.R., and Bhattacharyya, A.R. (2016). "Fabrication and Characterization of Flexible Films of Poly(Vinylidene Fluoride)/Pb(Fe_{0.5}Ti_{0.5})O₃-multi-Ferroic Nano-Composite." *RSC Adv.* 6, 42892–42898.
- Ahn, Y., Lim, J.Y., Hong, S.M., Lee, J., Ha, J., Choi, H.J., et al. (2013a). "Enhanced Piezoelectric Properties of Electrospun Poly(vinylidene fluoride)/Multiwalled Carbon Nanotube Composites." *J. Phys. Chem. C* 117, 11791–11799.
- Alam, M., Sultana, A., and Mandal, D. (2018). "Biomechanical and Acoustic Energy Harvesting from TiO₂ Nanoparticle Modulated PVDF Nanofiber Made High Performance Nanogenerator." *Applied Energy Mater.* 1, 3103–3112.
- Alamusi, Xue, J., Wu, L., Hu, N., Qiu, J., Chang, C., et al. (2012). "Evaluation of Piezoelectric

Property of Reduced Graphene Oxide (RGO)–Poly(Vinylidene Fluoride) Nanocomposites." *Nanoscale* 4, 7250–7255.

Arafat, M.M., Dinan, B., Akbar, S.A., and Haseeb, A.S.M.A. (2012). "Gas Sensors Based on One Dimensional Nanostructured Metal-Oxides: A Review." *Sensors (Switzerland)* 12, 7207–7258.

Arlt, K., and Wegener, M. (2010). "Piezoelectric PZT/PVDF-Copolymer 0-3 Composites: Aspects on Film Preparation and Electrical Poling." *IEEE Trans. Dielectr. Electr. Insul.* 17, 1178–1184.

Babu, V.J., Vempati, S., and Ramakrishna, S. (2013). "Conducting Polyaniline-Electrical Charge Transportation." *Mater. Sci. Appl.* 04, 1–10.

Bai, H., Wang, X., Zhou, Y., and Zhang, L. (2012). "Preparation and Characterization of Poly(Vinylidene Fluoride) Composite Membranes Blended with Nano-Crystalline Cellulose." *Prog. Nat. Sci. Mater. Int.* 22, 250–257.

Banerjee, S., and Kumar, A. (2011). "Swift Heavy Ion Irradiation Induced Modifications in the Optical Band Gap and Urbach's Tail in Polyaniline Nanofibers." *Nucl. Instruments Methods Phys. Res. Sect. B Beam Interact. with Mater. Atoms* 269, 2798–2806.

Bartenev, G.M., Remizova, A.A., Kuleshov, I. V, Martynov, M.A., and Sarminskaya, T.N. (1975). "The Effect of Crystalline Modifications on the Melting of Polyvinylidene Fluoride." *Polym. Sci. U.S.S.R.* 17, 2381–2388.

Beachley, V., and Wen, X. (2009). "Effect of Electrospinning Parameters on the Nanofiber Diameter and Length." *Mater. Sci. Eng. C* 29, 663–668.

Benz, M., Euler, W.B., and Gregory, O.J. (2001). "The Influence of Preparation Conditions on the Surface Morphology of Poly(Vinylidene Fluoride) Films." *Langmuir* 17, 239–243.

Bera, B., and Sarkar, M. Das (2017). "PVDF Based Piezoelectric Nanogenerator as a New Kind of Device for Generating Power from Renewable Resources." *IOSR J. Polym. Text. Eng.* 04, 01–05.

Bhute, M. V, Mahant, Y.P., and Kondawar, S.B. (2017). "Titanium Dioxide/Poly (Vinylidene Fluoride) Hybrid Polymer Composite Nanofibers as Potential Separator for Lithium Ion Battery." 4, 6–12.

- Bodkhe, S., Turcot, G., Gosselin, F.P., Therriault, D., and Accepted, J. (2017). "One-Step Solvent Evaporation- Assisted 3D Printing of Piezoelectric." 1–33.
- Bormashenko, Y., Pogreb, R., Stanevsky, O., and Bormashenko, E. (2004). "Vibrational Spectrum of PVDF and Its Interpretation." *Polym. Test.* 23, 791–796.
- Bracciale, M.P., Santarelli, M.L., and Sarto, M.S. (2017). Piezo-resistive Properties of Graphene Based PVDF Composite Films for Strain Sensing. In IEEE International Conference on Nanotechnology, pp 411–415.
- Bruce, P.G., Evans, J., and Vincent, C.A. (1988). "Conductivity and Transference Number Measurements on Polymer Electrolytes." *Solid State Ionics* 28–30, 918–922.
- Cai, X., Lei, T., Sun, D., and Lin, L. (2017). "A Critical Analysis of the α , β and γ Phases in Poly(Vinylidene Fluoride) Using FTIR." *RSC Adv.* 7, 15382–15389.
- Cardoso, V.F., Correia, D.M., Ribeiro, C., Fernandes, M.M., and Lanceros-Méndez, S. (2018). "Fluorinated Polymers as Smart Materials for Advanced Biomedical Applications." *Polymers (Basel)*. 10, 1–26.
- Chang, C., Fuh, Y.-K., and Lin, L. (2009a). A direct-write piezoelectric PVDF nanogenerator. In Solid-State Sensors, Actuators and Microsystems Conference, 2009. TRANSDUCERS 2009. International, (IEEE), pp 1485–1488.
- Chang, C., Tran, V.H., Wang, J., Fuh, Y.K., and Lin, L. (2010). "Direct-Write Piezoelectric Polymeric Nanogenerator with High Energy Conversion Efficiency." *Nano Lett.* 10, 726–731.
- Chang, J., Dommer, M., Chang, C., and Lin, L. (2012). "Piezoelectric Nanofibers for Energy Scavenging Applications." *Nano Energy* 1, 356–371.
- Chiang, C.Y., Shen, Y.J., Reddy, M.J., and Chu, P.P. (2003). "Complexation of Poly(Vinylidene Fluoride):LiPF₆ solid Polymer Electrolyte with Enhanced Ion Conduction in 'wet' Form." *J. Power Sources* 123, 222–229.
- Choi, S.-S., Lee, Y.S., Joo, C.W., Lee, S.G., Park, J.K., and Han, K.-S. (2004). "Electrospun PVDF Nanofiber Web as Polymer Electrolyte or Separator." *Electrochim. Acta* 50, 339–343.
- Choi, S.W., Jo, S.M., Lee, W.S., and Kim, Y.R. (2003). "An Electrospun Poly(vinylidene fluoride) Nanofibrous Membrane and Its Battery Applications." *Adv. Mater.* 15, 2027–2032.

- Choi, S.W., Kim, J.R., Ahn, Y.R., Jo, S.M., and Cairns, E.J. (2007). "Characterization of Electrospun PVdF Fiber-Based Polymer Electrolytes." *Chem. Mater.* 19, 104–115.
- Choudhury, S., Mangal, R., Agrawal, A., and Archer, L.A. (2015). "A Highly Reversible Room-Temperature Lithium Metal Battery Based on Crosslinked Hairy Nanoparticles." *Nat. Commun.* 6, 1–9.
- Costa, C.M., Nunes-Pereira, J., Sencadas, V., Silva, M.M., and Lanceros-Mendez, S. (2013a). "Effect of Fiber Orientation in Gelled Poly(Vinylidene Fluoride) Electrospun Membranes for Li-Ion Battery Applications." *J. Mater. Sci.* 48, 6833–6840.
- Costa, C.M., Silva, M.M., and Lanceros-Méndez, S. (2013b). "Battery Separators Based on Vinylidene Fluoride (VDF) Polymers and Copolymers for Lithium Ion Battery Applications." *RSC Adv.* 3, 11404-11420.
- Cozza, E.S., Monticelli, O., Marsano, E., and Cebé, P. (2013). "On the Electrospinning of PVDF: Influence of the Experimental Conditions on the Nanofiber Properties." *Polym. Int.* 62, 41–48.
- CreCORIO, R., and Cestari, M. (1994). "Effect of Crystallization Temperature on the Crystalline Phase Content and Morphology of Poly (Vinylidene Fluoride)." *J. Polym. Sci. Part B Polym. Phys.* Vol. 32, 859–870.
- Croy, J.R., Abouimrane, A., and Zhang, Z. (2014). "Next-Generation Lithium-Ion Batteries: The Promise of near-Term Advancements." *MRS Bull.* 39, 407–415.
- Deka, M., and Kumar, A. (2011). "Electrical and Electrochemical Studies of Poly(Vinylidene Fluoride)–Clay Nanocomposite Gel Polymer Electrolytes for Li-Ion Batteries." *J. Power Sources* 196, 1358–1364.
- Delnavaz, A., and Voix, J. (2014). "Flexible Piezoelectric Energy Harvesting from Jaw Movements." *Smart Mater. Struct.* 23, 105020-105028.
- Deng, D. (2015). "Li-Ion Batteries: Basics, Progress, and Challenges." *Energy Sci. Eng.* 3, 385–418.
- Dhakras, D., Gawli, Y., Chhatre, S., Wadgaonkar, P., and Ogale, S. (2014). "A High Performance All-Organic Flexural Piezo-FET and Nanogenerator via Nanoscale Soft-Interface Strain Modulation." *Phys. Chem. Chem. Phys.* 16, 22874–22881.

- Ding, B., Wang, M., Wang, X., Yu, J., and Sun, G. (2010). "Electrospun Nanomaterials for Ultrasensitive Sensors." *Mater. Today* 13, 16–27.
- Ding, B., Wang, M., Yu, J., and Sun, G. (2009a). "Gas Sensors Based on Electrospun Nanofibers." *Sensors* 9, 1609–1624.
- Ding, R., Zhang, X., Chen, G., Wang, H., Kishor, R., Xiao, J., et al. (2017). "High-Performance Piezoelectric Nanogenerators Composed of Formamidinium Lead Halide Perovskite Nanoparticles and Poly(Vinylidene Fluoride)." *Nano Energy* 37, 126–135.
- Ding, Y., Zhang, P., Long, Z., Jiang, Y., Xu, F., and Di, W. (2008). "Preparation of PVdF-Based Electrospun Membranes and Their Application as Separators." *Sci. Technol. Adv. Mater.* 9, 15005- 15009.
- Ding, Y., Zhang, P., Long, Z., Jiang, Y., Xu, F., and Di, W. (2009b). "The Ionic Conductivity and Mechanical Property of Electrospun P(VdF-HFP)/PMMA Membranes for Lithium Ion Batteries." *J. Memb. Sci.* 329, 56–59.
- Dipankar Mandal, B.B.K.S.K.K. (2015). "Self-Powered Flexible Fe-Doped RGO/PVDF Nanocomposite: An Excellent Material for a Piezoelectric Energy Harvester." *Nanoscale* 7, 10655–10666.
- Doll, W.W., and Lando, J.B. (1968). "The Polymorphism of Poly(Vinylidene Fluoride). II. The Effect of Hydrostatic Pressure." *J. Macromol. Sci. Part B* 2, 219–233.
- Donarelli, M., Ottaviano, L., Giancaterini, L., Fioravanti, G., Perrozzi, F., and Cantalini, C. (2016). "Exfoliated Black Phosphorus Gas Sensing Properties at Room Temperature." *2D Mater.* 3, 25002-25008.
- Dong, C., Fu, Y., Zang, W., He, H., Xing, L., and Xue, X. (2017). "Self-Powering/Self-Cleaning Electronic-Skin Basing on PVDF/TiO₂ nanofibers for Actively Detecting Body Motion and Degrading Organic Pollutants." *Appl. Surf. Sci.* 416, 424–431.
- Dong, Y., Marshall, J., Haroosh, H.J., Mohammadzadehmoghadam, S., Liu, D., Qi, X., et al. (2015). "Polylactic Acid (PLA)/Halloysite Nanotube (HNT) Composite Mats: Influence of HNT Content and Modification." *Compos. Part A Appl. Sci. Manuf.* 76, 28–36.
- Doshi, J., and Reneker, D.H. (1993). "Electrospinning Process and Applications of Electrospun Fibers." *Conf. Rec. 1993 IEEE Ind. Appl. Conf. Twenty-Eighth IAS Annu. Meet.* 35, 151–160.

- Edmondson, D.L. (2013). "Electrospinning Scaffold Fabrication of Polymer Nanofibers and Sensors for Tissue Engineering Applications." *ProQuest Diss. Theses* 178.
- Endah, R., Dyartanti, E.R., Widiassa, I.N., Purwanto, A., and Susanto, H. (2018). "Nanocomposite Polymer Electrolytes in PVDF/ZnO Membranes Modified with PVP for LiFePO₄ Batteries Nanocomposite Polymer Electrolytes in PVDF/ZnO Membranes Modified with PVP for Use in LiFePO₄ Batteries." 5, 19–25.
- Evans, J., Vincent, C.A., and Bruce, P.G. (1987). "Electrochemical Measurement of Transference Numbers in Polymer Electrolytes." *Polymer (Guildf)*. 28, 2324–2328.
- Fakhri, P., Mahmood, H., Jaleh, B., and Pegoretti, A. (2016). "Improved Electroactive Phase Content and Dielectric Properties of Flexible PVDF Nanocomposite Films Filled with Au- and Cu-Doped Graphene Oxide Hybrid Nanofiller." *Synth. Met.* 220, 653–660.
- Fang, J., Wang, X., and Lin, T. (2011). "Electrical Power Generator from Randomly Oriented Electrospun Poly(Vinylidene Fluoride) Nanofibre Membranes." *J. Mater. Chem.* 21, 11088.
- Farid Abraham (1962). "Orientation Order of Dipole Molecules in the Surface of Embryonic Droplets." *Science (80-)*. 168, 833–835.
- Fashandi, H., Abolhasani, M.M., Sandoghdar, P., Zohdi, N., Li, Q., and Naebe, M. (2016). "Morphological Changes towards Enhancing Piezoelectric Properties of PVDF Electrical Generators Using Cellulose Nanocrystals." *Cellulose* 23, 3625–3637.
- Formhals, A. (1934). "Process and Apparatus for Preparing Artificial Threads." *U.S Pat.* 1975504.
- Fortunato, M., Bidsorkhi, H.C., Bellis, G. De, Sarto, F., and Sarto, M.S. (2017). "Piezoelectric Response of Graphene-Filled PVDF Nanocomposites through Piezoresponse Force Microscopy (PFM)." *2017 IEEE 17th Int. Conf. Nanotechnology, NANO 2017* 125–129.
- Fortunato, M., Bidsorkhi, H.C., Chandraiahgari, C.R., Bellis, G. De, Sarto, F., and Sarto, M.S. (2018). "PFM Characterization of PVDF Nanocomposite Films With Enhanced Piezoelectric Response." *IEEE Trans. Nanotechnol.* 17, 955–961.
- Fuh, Y.-K., Lien, L.-C., and Jang, J.S.C. (2012). "Comparative Study of Polyvinylidene Fluoride Nanofibrous Membranes Prepared by Continuous Near-Field and Conventional Electrospinning Processes." *Micro Nano Lett.* 7, 376.

- Fukada, E., and Furukawa, T. (1981). "Piezoelectricity and Ferroelectricity in Polyvinylidene Fluoride." *Ultrasonics* 19, 31–39.
- Fukada, E., and Sakurai, T. (1970). "Piezoelectricity in Polarized Poly(Vinylidene Fluoride) Films." *Polym. J.* 2, 656–662.
- Gaabour, L.H. (2015). " Thermal Spectroscopy and Kinetic Studies of PEO/PVDF Loaded by Carbon Nanotubes." *J. Mater. J. Mater.* 2015, 824859- 824866.
- Gao, K., Hu, X., Dai, C., and Yi, T. (2006). "Crystal Structures of Electrospun PVDF Membranes and Its Separator Application for Rechargeable Lithium Metal Cells." *Mater. Sci. Eng. B Solid-State Mater. Adv. Technol.* 131, 100–105.
- Gee, S., Johnson, B., and Smith, A.L. (2018). "Optimizing Electrospinning Parameters for Piezoelectric PVDF Nanofiber Membranes." *J. Memb. Sci.* 563, 804–812.
- George, G., Selvakumar, M., Mahendran, A., and Anandhan, S. (2017). "Structure–Property Relationship of Halloysite Nanotubes/Ethylene–Vinyl Acetate–Carbon Monoxide Terpolymer Nanocomposites." *J. Thermoplast. Compos. Mater.* 30, 121–140.
- Ghosh, S.K., Biswas, A., Sen, S., Das, C., Henkel, K., Schmeisser, D., et al. (2016). "Yb₃₊-assisted Self-Polarized PVDF Based Ferroelectric Nanogenerator: A Facile Strategy of Highly Efficient Mechanical Energy Harvester Fabrication." *Nano Energy* 30, 621–629.
- Gonçalves, R., Lopes, A.C., Botelho, G., Neves, I.C., and Lanceros-Mendez, S. (2013). "Influence of Solvent Properties on the Electrical Response of Poly(Vinylidene Fluoride)/NaY Composites." *J. Polym. Res.* 20, 143-150.
- Gopalan, A.I., Santhosh, P., Manesh, K.M., Nho, J.H., Kim, S.H., Hwang, C.G., et al. (2008). "Development of Electrospun PVdF-PAN Membrane-Based Polymer Electrolytes for Lithium Batteries." *J. Memb. Sci.* 325, 683–690.
- Gregorio, R., Borges, D.S., and Lu, R.W. (2008). " Effect of crystallization rate on the formation of the polymorphs of solution cast poly(vinylidene fluoride)." *Polym.*, 2008, 4009-4016.
- Gupta, P., and Wilkes, G.L. (2003). "Some Investigations on the Fiber Formation by Utilizing a Side-by-Side Bicomponent Electrospinning Approach." 44, 6353–6359.

- Haghi, A.K. (2009). *Electrospun nanofibers research : recent developments* (Newyork).
- Hang, N.T., Zhang, S., and Yang, W. (2017). "Efficient Exfoliation of g-C₃N₄ and NO₂ sensing Behavior of Graphene/g-C₃N₄nanocomposite." *Sensors Actuators, B Chem.* 248, 940–948.
- Hao, J., Xiao, Q., Lei, G., Li, Z., and Wu, L. (2014). "A Novel Polyvinylidene Fluoride/Microfiber Composite Gel Polymer Electrolyte with an Interpenetrating Network Structure for Lithium Ion Battery." *Electrochim. Acta* 125, 450–456.
- He, F., Fan, J., and Chan, L.H. (2014). "Preparation and Characterization of Electrospun Poly(Vinylidene Fluoride)/Poly(Methyl Methacrylate) Membrane." *High Perform. Polym.* 26, 817–825.
- He, G., Zhang, F., Yu, H., Li, J., and Guo, S. (2016). "Puncture Characterization of Multilayered Polypropylene Homopolymer/Ethylene 1-Octene Copolymer Sheets." *Rsc Adv.* 6, 12744–12752.
- Hemeda, O.M., Tawfik, A., El-Shahawy, M.M., and Darwish, K.A. (2017). "Enhancement of Piezoelectric Properties for [Poly(Vinylidene Fluoride)/Barium Zirconate Titanate] Nanocomposites." *Eur. Phys. J. Plus* 132, 333-344.
- Hooker, W. (1998). *Properties Ceramics of PZT-Based Piezoelectric and 250 °C*.
- Hu, J., and Tan, L. (2017). *Polyurethane Composites and Nanocomposites for Biomedical Applications* (Elsevier Inc.).
- Hu, X., Liu, S., Zhou, G., Huang, Y., Xie, Z., and Jing, X. (2014). "Electrospinning of Polymeric Nanofibers for Drug Delivery Applications." *J. Control. Release* 185, 12–21.
- Huang, X. (2011a). "Separator Technologies for Lithium-Ion Batteries." *J. Solid State Electrochem.* 15, 649–662.
- Huang, X., and Hitt, J. (2013). "Lithium Ion Battery Separators : Development and Performance Characterization of a Composite Membrane." *J. Memb. Sci.* 425, 163–168.
- Hwang, K., Kwon, B., and Byun, H. (2011a). "Preparation of PVdF Nanofiber Membranes by Electrospinning and Their Use as Secondary Battery Separators." *J. Memb. Sci.* 378, 111–116.
- Ibrahim, K.A. (2017). "Synthesis and Characterization of Polyaniline and Poly(Aniline-co-o-Nitroaniline) Using Vibrational Spectroscopy." *Arab. J. Chem.* 10, S2668–S2674.

- Ico, G., Showalter, A., Bosze, W., Gott, S.C., Kim, B.S., Rao, M.P., et al. (2016a). "Size-Dependent Piezoelectric and Mechanical Properties of Electrospun P(VDF-TrFE) Nanofibers for Enhanced Energy Harvesting." *J. Mater. Chem. A* 4, 2293–2304.
- Issa, A., Al-Maadeed, M., Luyt, A., Ponnamma, D., and Hassan, M. (2017). "Physico-Mechanical, Dielectric, and Piezoelectric Properties of PVDF Electrospun Mats Containing Silver Nanoparticles." 3, 30–45.
- Jain, A., Prashanth, K.J., Sharma, A.K., Jain, A., and P.n, R. (2015). "Dielectric and Piezoelectric Properties of PVDF/PZT Composites: A Review." *Polym. Eng. Sci.* 55, 1589–1616.
- Janakiraman, S., Surendran, A., Ghosh, S., Anandhan, S., and Venimadhav, A. (2016). "Electroactive Poly(Vinylidene Fluoride) Separator for Sodium Ion Battery with High Coulombic Efficiency." *Solid State Ionics* 292, 130–135.
- Jang, S., Kim, H., Kim, Y., Kang, B.J., and Oh, J.H. (2016). "Honeycomb-like Nanofiber Based Triboelectric Nanogenerator Using Self-Assembled Electrospun Poly(Vinylidene Fluoride-Co-Trifluoroethylene) Nanofibers." *Appl. Phys. Lett.* 108, 143901-143906.
- Ji, S., Li, Y., and Yang, M. (2008). "Gas Sensing Properties of a Composite Composed of Electrospun Poly(Methyl Methacrylate) Nanofibers and in Situ Polymerized Polyaniline." *Sensors Actuators, B Chem.* 133, 644–649.
- Jia, X., Tang, C., Yan, X., Yu, G., Li, J., Zhang, H., et al. (2016). "Flexible Polyaniline/Poly(Methyl Methacrylate) Composite Fibers via Electrospinning and In Situ Polymerization for Ammonia Gas Sensing and Strain Sensing." *J. Nanomater.* 2016, 9102828-9102836.
- Jiang, J., and Zhang, C. (2015). Fundamentals and applications of lithium-ion batteries in electric drive vehicles.
- Jiyong, H., Yuanyuan, G., Hele, Z., Yinda, Z., and Xudong, Y. (2018). "Effect of Electrospinning Parameters on Piezoelectric Properties of Electrospun PVDF Nanofibrous Mats under Cyclic Compression." *J. Text. Inst.* 109, 843–850.
- Kakimoto, K., Fukata, K., and Ogawa, H. (2013). "Fabrication of Fibrous BaTiO₃-Reinforced PVDF Composite Sheet for Transducer Application." *Sensors Actuators A Phys.* 200, 21–25.
- Kang, H.B., Han, C.S., Pyun, J.C., Ryu, W.H., Kang, C.Y., and Cho, Y.S. (2015).

"(Na,K)NbO₃ Nanoparticle-Embedded Piezoelectric Nanofiber Composites for Flexible Nanogenerators." *Compos. Sci. Technol.* 111, 1–8.

Kao, K.C. (2004). "Ferroelectrics, Piezoelectrics, and Pyroelectrics." *Dielectr. Phenom. Solids - With Emphas. Phys. Concepts Electron. Process.* 213–282.

Kaur, S., Kumar, A., Sharma, A.L., and Singh, D.P. (2017). "Influence of Annealing on Dielectric and Polarization Behavior of PVDF Thick Films." *J. Mater. Sci. Mater. Electron.* 28, 8391–8396.

Kawai, H. (1969). "Piezoelectricity of Poly (Vinylidene Fluoride)." *Japan J. Appl. Phys.* 975.

Kepler, G. (1995). Ferroelectric, Pyroelectric, and Piezoelectric Properties of Poly(vinylidene Fluoride), 183-232.

Khurana, R., Schaefer, J., Archer, L.A., Coates, G.W., Schaefer, J.L., and Coates, G.W. (2014). "Suppression of Lithium Dendrite Growth Using Cross- Linked Polyethylene / Polyethylene Oxide Electrolytes : A New Approach for Practical Lithium-Metal Polymer Batteries Suppression of Lithium Dendrite Growth Using Cross-Linked Polyethylene/ Polyethylene." *J. Am. Chem. Soc.* 136, 7395–7402.

Kim, J.R., Choi, S.W., Jo, S.M., Lee, W.S., and Kim, B.C. (2004). "Electrospun PVdF-Based Fibrous Polymer Electrolytes for Lithium Ion Polymer Batteries." *Electrochim. Acta* 50, 69–75.

Kim, Y.-J., Ahn, C.H., Lee, M.B., and Choi, M.-S. (2011). "Characteristics of Electrospun PVDF/SiO₂ Composite Nanofiber Membranes as Polymer Electrolyte." *Mater. Chem. Phys.* 127, 137–142.

Kim, Y.W., Lee, H.B., Yeon, S.M., Park, J., Lee, H.J., Yoon, J., et al. (2018). "Enhanced Piezoelectricity in a Robust and Harmonious Multilayer Assembly of Electrospun Nanofiber Mats and Microbead-Based Electrodes." *ACS Appl. Mater. Interfaces* 10, 5723–5730.

Kizildag, N., Ucar, N., Karacan, I., Onen, A., and Demirsoy, N. (2016). "The Effect of the Dissolution Process and the Polyaniline Content on the Properties of Polyacrylonitrile– Polyaniline Composite Nanoweb." *J. Ind. Text.* 45, 1548–1570.

Kobayashi, M., Tashiro, K., and Tadokoro, H. (1975). "Molecular Vibrations of Three Crystal Forms of Poly(Vinylidene Fluoride)." *Macromolecules* 8, 158–171.

- Kong, L., Liu, B., Ding, J., Yan, X., Tian, G., Qi, S., et al. (2018a). "Robust Polyetherimide Fibrous Membrane with Crosslinked Topographies Fabricated via In-Situ Micro-Melting and Its Application as Superior Lithium-Ion Battery Separator with Shutdown Function." *J. Memb. Sci.* 549, 244–250.
- Kong, L., Yan, Y., Qiu, Z., Zhou, Z., and Hu, J. (2018b). "Robust Fluorinated Polyimide Nanofibers Membrane for High-Performance Lithium-Ion Batteries." *J. Memb. Sci.* 549, 321–331.
- Kumar, a, and Dek, M. (2010). Nanofiber Reinforced Composite Polymer Electrolyte Membranes, 438-467.
- Lee, C., Wood, D., Edmondson, D., Yao, D., Erickson, A.E., Tsao, C.T., et al. (2016). "Electrospun Uniaxially-Aligned Composite Nanofibers as Highly-Efficient Piezoelectric Material." *Ceram. Int.* 42, 2734–2740.
- Lee, M., Chen, C.Y., Wang, S., Cha, S.N., Park, Y.J., Kim, J.M., et al. (2012). "A Hybrid Piezoelectric Structure for Wearable Nanogenerators." *Adv. Mater.* 24, 1759–1764.
- Lee Min, Y., Kim, J.W., Choi, N.S., Lee An, J., Seol, W.H., and Park, J.K. (2005). "Novel Porous Separator Based on PVdF and PE Non-Woven Matrix for Rechargeable Lithium Batteries." *J. Power Sources* 139, 235–241.
- Lee, Y.Y., and Liu, Y.L. (2017). "Crosslinked Electrospun Poly(Vinylidene fluoride) Fiber Mat as a Matrix of Gel Polymer Electrolyte for Fast-Charging Lithium-Ion Battery." *Electrochim. Acta* 258, 1329–1335.
- Leporatti, S. (2017). "Halloysite Clay Nanotubes as Nano-Bazookas for Drug Delivery S." *Polym. Int.* 66, 1111–1118.
- Li, B., Xu, C., Zheng, J., and Xu, C. (2014). "Sensitivity of Pressure Sensors Enhanced by Doping Silver Nanowires." *Sensors (Switzerland)* 14, 9889–9899.
- Li, D., and Xia, Y. (2004). "Electrospinning of Nanofibers: Reinventing the Wheel?." *Adv. Mater.* 16, 1151–1170.
- Li, H., Chen, Y.-M., Ma, X.-T., Shi, J.-L., Zhu, B.-K., and Zhu, L.-P. (2011). "Gel Polymer Electrolytes Based on Active PVDF Separator for Lithium Ion Battery. : Preparation and Property of PVDF/Poly(Dimethylsiloxane) Blending Membrane." *J. Memb. Sci.* 379, 397–402.

- Li, W., Xing, Y., Wu, Y., Wang, J., Chen, L., Yang, G., et al. (2015). "Study the Effect of Ion-Complex on the Properties of Composite Gel Polymer Electrolyte Based on Electrospun PVdF Nanofibrous Membrane." *Electrochim. Acta* 151, 289–296.
- Li, X., Tao, J., Zhu, J., Pan, C., Li, X., Tao, J., et al. (2017). "A Nanowire Based Triboelectric Nanogenerator for Harvesting Water Wave Energy and Its Applications A Nanowire Based Triboelectric Nanogenerator for Harvesting Water Wave Energy and Its Applications." *APL Mater.* 5, 74104–74110.
- Li, Z., and Wang, C. (2013). "One-Dimensional Nanostructures." 15–29.
- Liu, Y., and Luo, Y. (2006). "Effects of Heat-Treatment on the Gas Response of PVDF/CB Conductive Composite Sensing Films." *Mater. Res. Innov.* 10, 215-230.
- Liu, Y., Peng, X., Cao, Q., Jing, B., Wang, X., and Deng, Y. (2017). "Gel Polymer Electrolyte Based on Poly(Vinylidene Fluoride)/Thermoplastic Polyurethane/Polyacrylonitrile by the Electrospinning Technique." *J. Phys. Chem. C* 121, 19140–19146.
- Liu, Z.H., Pan, C.T., Lin, L.W., Huang, J.C., and Ou, Z.Y. (2014). "Direct-Write PVDF Nonwoven Fiber Fabric Energy Harvesters via the Hollow Cylindrical near-Field Electrospinning Process." *Smart Mater. Struct.* 23, 25003–25014.
- Liu, Z.H., Pan, C.T., Yen, C.K., Lin, L.W., Huang, J.C., and Ke, C.A. (2015). "Crystallization and Mechanical Behavior of the Ferroelectric Polymer Nonwoven Fiber Fabrics for Highly Durable Wearable Sensor Applications." *Appl. Surf. Sci.* 346, 291–301.
- Long, L., Wang, S., Xiao, M., and Meng, Y. (2016). "Polymer Electrolytes for Lithium Polymer Batteries." *J. Mater. Chem. A* 4, 10038–10069.
- Lopes, A.C., Costa, C.M., Tavares, C.J., Neves, I.C., and Lanceros-Mendez, S. (2011). "Nucleation of the Electroactive γ -Phase and Enhancement of the Optical Transparency in Low Filler Content Poly(Vinylidene)/Clay Nanocomposites." *J. Phys. Chem. C* 115, 18076–18082.
- Lovinger, J., Davis, D.D., Cais, R.E., Kometani, J.M., Laboratories, T.B., and Hill, M. (1987). "The Role of Molecular Defects on the Structure and Phase Transitions of Poly (Vinylidene Fluoride)." *Polymer (Guildf)*. 28, 617–626.
- Low, K., Chartuprayoon, N., Echeverria, C., Li, C., Bosze, W., Myung, N. V., et al. (2014). "Polyaniline/Poly(ϵ -Caprolactone) Composite Electrospun Nanofiber-Based Gas Sensors:

Optimization of Sensing Properties by Dopants and Doping Concentration." *Nanotechnology* 25, 115501-115512.

Lu, X., Qu, H., and Skorobogatiy, M. (2017). "Piezoelectric Microstructured Fibers via Drawing of Multimaterial Preforms." *Sci. Rep.* 7, 1–12.

Ma, L., Fan, H., Fu, K., Lei, S., Hu, Q., Huang, H., et al. (2017). "Protonation of Graphitic Carbon Nitride (g-C₃N₄) for an Electrostatically Self-Assembling Carbon@g-C₃N₄ Core–Shell Nanostructure toward High Hydrogen Evolution." *ACS Sustain. Chem. Eng.* 5, 7093–7103.

Ma, W., Zhang, J., and Wang, X. (2008). "Effect of Initial Polymer Concentration on the Crystallization of Poly (Vinylidene Fluoride)/Poly (Methyl Methacrylate) Blend from Solution Casting." *J. Macromol. Sci. Part B Phys.* 47, 139–149.

Ma, Y., Li, L.B., Gao, G.X., Yang, X.Y., and You, Y. (2016). "Effect of Montmorillonite on the Ionic Conductivity and Electrochemical Properties of a Composite Solid Polymer Electrolyte Based on Polyvinylidenedifluoride/Polyvinyl Alcohol Matrix for Lithium Ion Batteries." *Electrochim. Acta* 187, 535–542.

Mago, G., Kalyon, D.M., and Fisher, F.T. (2008). "Membranes of Polyvinylidene Fluoride and PVDF Nanocomposites with Carbon Nanotubes via Immersion Precipitation." *J. Nanomater.* 2008, 759825-759833.

Mahant, Y.P., Kondawar, S.B., Bhute, M., and Nandanwar, D. V (2015a). "Electrospun Poly (Vinylidene Fluoride)/Poly (Methyl Methacrylate) Composite Nanofibers Polymer Electrolyte for Batteries." *Procedia Mater. Sci.* 10, 595–602.

Mahant, Y.P., Kondawar, S.B., Nandanwar, D. V., and Koinkar, P. (2018). "Poly(Methyl Methacrylate) Reinforced Poly(Vinylidene Fluoride) Composites Electrospun Nanofibrous Polymer Electrolytes as Potential Separator for Lithium Ion Batteries." *Mater. Renew. Sustain. Energy* 7, 1–9.

Malmonge, L.F., Langiano, S. do C., Cordeiro, J.M.M., Mattoso, L.H.C., and Malmonge, J.A. (2010). "Thermal and Mechanical Properties of PVDF/PANI Blends." *Mater. Res.* 13, 465–470.

Mandal, D., Henkel, K., and Schmeißer, D. (2014). "Improved Performance of a Polymer Nanogenerator Based on Silver Nanoparticles Doped Electrospun P(VDF-HFP) Nanofibers."

Phys. Chem. Chem. Phys. 16, 10403–10407.

Martins, J.N., Kersch, M., Altstädt, V., and Oliveira, R.V.B. (2013). "Poly(Vinylidene Fluoride)/Polyaniline/Carbon Nanotubes Nanocomposites: Influence of Preparation Method and Oscillatory Shear on Morphology and Electrical Conductivity." *Polym. Test.* 32, 1511–1521.

Martins, P., Caparros, C., Gonçalves, R., Martins, P.M., Benelmekki, M., Botelho, G., et al. (2012). "Role of Nanoparticle Surface Charge on the Nucleation of the Electroactive β -Poly(Vinylidene Fluoride) Nanocomposites for Sensor and Actuator Applications." *J. Phys. Chem. C* 116, 15790–15794.

Martins, P., Lopes, A.C., and Lanceros-Mendez, S. (2014). "Electroactive Phases of Poly(Vinylidene Fluoride): Determination, Processing and Applications." *Prog. Polym. Sci.* 39, 683–706.

Mateu, L., and Moll, F. (2005). "<Title>Review of Energy Harvesting Techniques and Applications for Microelectronics (Keynote Address)</Title>." *SPIE Digit. Libr.* 5837, 359–373.

Maulana, R., Samsudin, A.M., and Susanto, H. (2016). "Preparation and Characterization of Fly Ash/PVdF-PAN Composite Polymer Electrolyte Membranes and Their Potential Use for Li-Ion Batteries." *Int. J. ChemTech Res.* 9, 831–844.

Melilli, D, G., A, G., O, O., E, B., O, D., et al. (2018). "Enhanced Piezoelectric Response in Nanostructured Ni/PVDF Films." *J. Mater. Sci. Eng.* 07, 1000444-1000449.

Minazara, E., Vasic, D., and Costa, F. (2008). "Piezoelectric Generator Harvesting Bike Vibrations Energy to Supply Portable Devices." *Renew. Energy Power Qual. J.* 1, 508–513.

Mirjalili, M., and Zohoori, S. (2016). "Review for Application of Electrospinning and Electrospun Nanofibers Technology in Textile Industry." *J. Nanostructure Chem.* 6, 207–213.

Mishra, M., Roy, A., Dash, S., and Mukherjee, S. (2018). "Flexible Nano-GFO/PVDF Piezoelectric-Polymer Nano-Composite Films for Mechanical Energy Harvesting." *IOP Conf. Ser. Mater. Sci. Eng.* 338, 012026-012032.

Mokhtari, F., Latifi, M., Shamshirsaz, M., Khelghatdoost, M., and Rahmani, S. (2017a). "Modeling of Electrospun PVDF/LiCl Nanogenerator by the Energy Approach Method:

Determining Piezoelectric Constant." *J. Text. Inst.* 108, 1917–1925.

Mokhtari, F., Shamsirsaz, M., Latifi, M., and Asadi, S. (2017b). "Comparative Evaluation of Piezoelectric Response of Electrospun PVDF (Polyvinylidene Fluoride) Nanofiber with Various Additives for Energy Scavenging Application." *J. Text. Inst.* 108, 906–914.

Monaca, A. La, Giorgio, F. De, Focarete, M.L., Fabiani, D., Zaccaria, M., and Arbizzani, C. (2017). "Polyvinylidene Difluoride–Polyethyleneoxide Blends for Electrospun Separators in Li-Ion Batteries." *J. Electrochem. Soc.* 164, 6431–6439.

Monroe, C., and Newman, J. (2003). "Dendrite Growth in Lithium Polymer Systems." *J. Electrochem. Soc.* 150, 1377–1384.

Mortazavi, B., Cuniberti, G., and Rabczuk, T. (2015). "Mechanical Properties and Thermal Conductivity of Graphitic Carbon Nitride: A Molecular Dynamics Study." *Comput. Mater. Sci.* 99, 285–289.

Mostafaei, A., and Zolriasatein, A. (2012a). "Progress in Natural Science : Materials International Synthesis and Characterization of Conducting Polyaniline Nanocomposites Containing ZnO Nanorods." *Prog. Nat. Sci. Mater. Int.* 22, 273–280.

Mostafaei, A., and Zolriasatein, A. (2012b). "Synthesis and Characterization of Conducting Polyaniline Nanocomposites Containing ZnO Nanorods." *Prog. Nat. Sci. Mater. Int.* 22, 273–280.

Motamedi, A.S., Mirzadeh, H., Hajiesmaeilbaigi, F., Bagheri-Khoulenjani, S., and Shokrgozar, M. (2017). "Effect of Electrospinning Parameters on Morphological Properties of PVDF Nanofibrous Scaffolds." *Prog. Biomater.* 6, 113–123.

Murayama, N., Nakamura, K., Obara, H., and Segawa, M. (1976). "The Strong Piezoelectricity in Polyvinylidene Fluoroide (PVDF)." *Ultrasonics* 14, 15–23.

Murayama, N., and Obara, H. (1983). "Piezoelectric Polymers and Their Applications." *Jpn. J. Appl. Phys.* 22, 3–6.

Najim, T.S., and Salim, A.J. (2017). "Polyaniline Nanofibers and Nanocomposites: Preparation, Characterization, and Application for Cr(VI) and Phosphate Ions Removal from Aqueous Solution." *Arab. J. Chem.* 10, 3459–3467.

- Najjar, R., Luo, Y., Jao, D., Brennan, D., Xue, Y., Beachley, V., et al. (2017). "Biocompatible Silk/Polymer Energy Harvesters Using Stretched Poly (Vinylidene Fluoride-Cohexafluoropropylene) (PVDF-HFP) Nanofibers." *Polymers (Basel)*. 9, 479-494.
- Nakamura, K., Sawai, D., Watanabe, Y., Taguchi, D., Takahashi, Y., Furukawa, T., et al. (2003). "Effect of Annealing on the Structure and Properties of Poly(Vinylidene Fluoride) β -Form Films." *J. Polym. Sci. Part B Polym. Phys.* 41, 1701–1712.
- Neppalli, R., Wanjale, S., Birajdar, M., and Causin, V. (2013). "The Effect of Clay and of Electrospinning on the Polymorphism, Structure and Morphology of Poly(Vinylidene Fluoride)." *Eur. Polym. J.* 49, 90–99.
- Nimkar, S.H., Kondawar, S.B., and More, P.S. (2015). "Polyaniline/TiO₂ Nanocomposite Thin Film Based Carbon Dioxide Gas Sensor." 12–18.
- Novikov, S., Lebedeva, N., Satrapinski, A., Walden, J., Davydov, V., and Lebedev, A. (2016). "Graphene Based Sensor for Environmental Monitoring of NO₂." *Sensors Actuators, B Chem.* 236, 1054–1060.
- Nunes-Pereira, J., Sencadas, V., Correia, V., Cardoso, V.F., Han, W., Rocha, J.G., et al. (2015). "Energy Harvesting Performance of BaTiO₃/Poly(Vinylidene Fluoride-Trifluoroethylene) Spin Coated Nanocomposites." *Compos. Part B Eng.* 72, 130–136.
- Nunes-Pereira, J., Sencadas, V., Correia, V., Rocha, J.G., and Lanceros-Méndez, S. (2013). "Energy Harvesting Performance of Piezoelectric Electrospun Polymer Fibers and Polymer/Ceramic Composites." *Sensors Actuators, A Phys.* 196, 55–62.
- Nurwaha, D., Han, W., and Wang, X. (2013). "Effects of Processing Parameters on Electrospun Fiber Morphology." *J. Text. Inst.* 104, 419–425.
- Ohigashi, H. (1985). "Piezoelectric Polymers – Materials and Manufacture." *Jap. J. Appl. Phys.* 24, 23–27.
- Okutan, N., Terzi, P., and Altay, F. (2014). "Affecting Parameters on Electrospinning Process and Characterization of Electrospun Gelatin Nanofibers." *Food Hydrocoll.* 39, 19–26.
- Olmos, D., González-Gaitano, G., Kholkin, A.L., and González-Benito, J. (2013). "Flexible PVDF-BaTiO₃ Nanocomposites as Potential Materials for Pressure Sensors." *Ferroelectrics* 447, 9–18.

Ong, W.J., Tan, L.L., Chai, S.P., Yong, S.T., and Mohamed, A.R. (2015). "Surface Charge Modification via Protonation of Graphitic Carbon Nitride (g-C₃N₄) for Electrostatic Self-Assembly Construction of 2D/2D Reduced Graphene Oxide (RGO)/g-C₃N₄ Nanostructures toward Enhanced Photocatalytic Reduction of Car." *Nano Energy* 13, 757–770.

Oshiki, M., and Fukada, E. (1975). "Inverse Piezoelectric Effect and Electrostrictive Effect in Polarized Poly(Vinylidene Fluoride) Films." *J. Mater. Sci.* 10, 1–6.

Osone, S., Brinkman, K., Shimojo, Y., and Iijima, T. (2008). "Ferroelectric and Piezoelectric Properties of Pb(Zr_xTi_{1-x})O₃ Thick Films Prepared by Chemical Solution Deposition Process." *Thin Solid Films* 516, 4325–4329.

Ou, J.Z., Ge, W., Carey, B., Daeneke, T., Rotbart, A., Shan, W., et al. (2015). "Physisorption-Based Charge Transfer in Two-Dimensional SnS₂ for Selective and Reversible NO₂ Gas Sensing." *ACS Nano* 9, 10313–10323.

Ouyang, Z.-W., Chen, E.-C., and Wu, T.-M. (2015). "Enhanced Piezoelectric and Mechanical Properties of Electroactive Polyvinylidene Fluoride/Iron Oxide Composites." *Mater. Chem. Phys.* 149–150, 172–178.

Pan, C.-T., Yen, C.-K., Wu, H.-C., Lin, L., Lu, Y.-S., Huang, J.C.-C., et al. (2015a). "Significant Piezoelectric and Energy Harvesting Enhancement of Poly(Vinylidene Fluoride)/Polypeptide Fiber Composites Prepared through near-Field Electrospinning." *J. Mater. Chem. A* 3, 6835–6843.

Pan, C., Tsai, K., Wang, S., Yen, C., Sun, Y., and Tsao, C. (2017). "Development of Piezoelectric Fibers in Smart Patch by Near-Field Electrospinning Method with Closed-Loop Motor Control." *Sensors Mater.* 29, 497.

Pan, C.T., Yen, C.K., Wu, H.C., Lin, L., Lu, Y.S., Huang, J.C.C., et al. (2015b). "Significant Piezoelectric and Energy Harvesting Enhancement of Poly(Vinylidene Fluoride)/Polypeptide Fiber Composites Prepared through near-Field Electrospinning." *J. Mater. Chem. A* 3, 6835–6843.

Parangusan, H., Ponnamma, D., and Ali Almaadeed, M. Al (2017). "Flexible Tri-Layer Piezoelectric Nanogenerator Based on PVDF-HFP/Ni-Doped ZnO Nanocomposites." *RSC Adv.* 7, 50156–50165.

Park, S., Kim, Y., Jung, H., Park, J.-Y., Lee, N., and Seo, Y. (2017). "Energy Harvesting Efficiency of Piezoelectric Polymer Film with Graphene and Metal Electrodes." *Sci. Rep.* 7, 17290-17297.

Park, S., Son, C.W., Lee, S., Kim, D.Y., Park, C., Eom, K.S., et al. (2016). "Multicore-Shell Nanofiber Architecture of Polyimide/Polyvinylidene Fluoride Blend for Thermal and Long-Term Stability of Lithium Ion Battery Separator." *Sci. Rep.* 6, 1–8.

Patil, R., Ashwin, A., and Radhakrishnan, S. (2007). "Novel Polyaniline/PVDF/BaTiO₃ Hybrid Composites with High Piezo-Sensitivity." *Sensors Actuators, A Phys.* 138, 361–365.

Patil, S.L. (2012). "Effect of Camphor Sulfonic Acid Doping on Structural, Morphological, Optical and Electrical Transport Properties on Polyaniline-ZnO Nanocomposites." *Soft Nanosci. Lett.* 02, 46–53.

Paul, P. (2005). An introduction to electrospinning process.

Peng, Y., and Wu, P. (2004). "A Two Dimensional Infrared Correlation Spectroscopic Study on the Structure Changes of PVDF during the Melting Process." *Polymer (Guildf).* 45, 5295–5299.

Persano, L., Camposeo, A., Tekmen, C., and Pisignano, D. (2013a). "Industrial Upscaling of Electrospinning and Applications of Polymer Nanofibers: A Review." *Macromol. Mater. Eng.* 298, 504–520.

Persano, L., Dagdeviren, C., Su, Y., Zhang, Y., Girardo, S., Pisignano, D., et al. (2013b). "High Performance Piezoelectric Devices Based on Aligned Arrays of Nanofibers of Poly(Vinylidene fluoride-Co-Trifluoroethylene)." *Nat. Commun.* 4, 1610–1633.

Pillay, V., Dott, C., Choonara, Y.E., Tyagi, C., Tomar, L., Kumar, P., et al. (2013). "A Review of the Effect of Processing Variables on the Fabrication of Electrospun Nanofibers for Drug Delivery Applications." *J. Nanomater.* 2013, 789289–789311.

Prasad, G., Sathiyathan, P., Prabu, A.A., and Kim, K.J. (2017). "Piezoelectric Characteristics of Electrospun PVDF as a Function of Phase-Separation Temperature and Metal Salt Content." *Macromol. Res.* 25, 981–988.

Prashantha, K. (2011). "Processing and Characterization of Halloysite Nanotubes Filled Polypropylene Nanocomposites Based on a Masterbatch Route: Effect of Halloysites

Treatment on Structural and Mechanical Properties." *Express Polym. Lett.* 5, 295–307.

Price, A.D., Kao, V.C., Zhang, J.X., and Naguib, H.E. (2010). "Fabrication and Percolation Behaviour of Novel Porous Conductive Polyblends of Polyaniline and Poly(Methyl Methacrylate)." *Synth. Met.* 160, 1832–1837.

Qureshi, A., Altindal, A., and Mergen, A. (2009). "Electrical and Gas Sensing Properties of Li and Ti Codoped NiO/PVDF Thin Film." *Sensors Actuators, B Chem.* 138, 71–75.

Raghavan, P., Zhao, X., Shin, C., Baek, D.H., Choi, J.W., Manuel, J., et al. (2010). "Preparation and Electrochemical Characterization of Polymer Electrolytes Based on Electrospun Poly(Vinylidene Fluoride-Co-Hexafluoropropylene)/Polyacrylonitrile Blend/Composite Membranes for Lithium Batteries." *J. Power Sources* 195, 6088–6094.

Rahman, W., Ghosh, S.K., and Mandal, D. (2017). "Highly Durable Piezo-Electric Energy Harvester by a Super Toughened and Flexible Nanocomposite : Effect of Laponite Nano-Clay in Poly (Vinylidene Fluoride) Highly Durable Piezo-Electric Energy Harvester by a Super Toughened and Flexible Nanocomposite :." *Mater. Res. Bull.* 4, 095305–095314.

Rahman, W., Ghosh, S.K., and Mandal, D. (2018). Enhanced mechanical energy harvesting ability of electrospun poly(vinylidene fluoride)/ hectorite clay nanocomposites. Solid State Physics Symposium, pp 050081–050084.

Rajendran, S., Babu, R. shanker, and Sivakumar, P. (2008). "Investigations on PVC/PAN Composite Polymer Electrolytes." *J. Memb. Sci.* 315, 67–73.

Ramasundaram, S., Yoon, S., Kim, K.J., Lee, J.S., and Park, C. (2009). "Crystalline Structure and Ferroelectric Response of Poly(Vinylidene Fluoride)/ Organically Modified Silicate Thin Films Prepared by Heat Controlled Spin Coating." *Macromol. Chem. Phys.* 210, 951–960.

Ramasundaram, S., Yoon, S., Kim, K.J., and Park, C. (2008). "Preferential Formation of Electroactive Crystalline Phases in Poly(Vinylidene Fluoride)/Organically Modified Silicate Nanocomposites." *J. Polym. Sci. Part B Polym. Phys.* 46, 2173–2187.

Reddy, N.R., and Anandhan, S. (2016b). "Polyaniline/Poly(Styrene-co-Acrylonitrile) Blend Nanofibers Exhibit Enhanced Ammonia and Nitrogen Dioxide Sensing Characteristics." *J. Mater. Sci. Mater. Electron.* 27, 13329–13337.

Richardson, P.D. (1989). "Piezoelectric Polymers." *IEEE Eng. Med. Biol. Mag.* 8, 14–16.

- Rozemarie, M.L., Andrei, B., Liliana, H., Cramariuc, R., and Cramariuc, O. (2017). "Electrospun Based Polyaniline Sensors - A Review." *IOP Conf. Ser. Mater. Sci. Eng.* 209, 012063-012072.
- Saïdi, S., Bouzitoun, M., Mannaî, A., Gmati, F., Derouiche, H., and Mohamed, A.B. (2013a). "Effect of PANI Rate Percentage on Morphology, Structure and Charge Transport Mechanism in PANI-PVDF Composites above Percolation Threshold." *J. Phys. D. Appl. Phys.* 46, 355101–355112.
- Sajjad, M., and Feng, P. (2014). "Study the Gas Sensing Properties of Boron Nitride Nanosheets." *Mater. Res. Bull.* 49, 35–38.
- Salimi, A., and Yousefi, A.A. (2003a). "Analysis Method: FTIR Studies of β -Phase Crystal Formation in Stretched PVDF Films." *Polym. Test.* 22, 699–704.
- Satapathy, S., Pawar, S., Gupta, P.K., and RVarma, K.B. (2011). "Effect of Annealing on Phase Transition in Poly(Vinylidene Fluoride) Films Prepared Using Polar Solvent." *Bull. Mater. Sci.* 34, 727–733.
- Sengupta, D., Kottapalli, A.G.P., Chen, S.H., Miao, J.M., Kwok, C.Y., Triantafyllou, M.S., et al. (2017a). "Characterization of Single Polyvinylidene Fluoride (PVDF) Nanofiber for Flow Sensing Applications". *AIP advances*, 7, 105205-10212.
- Senthil, T., and Anandhan, S. (2014). "Structure-Property Relationship of Sol-Gel Electrospun ZnO Nanofibers Developed for Ammonia Gas Sensing." *J. Colloid Interface Sci.* 432, 285–296.
- Seoul, C., Kim, Y.-T., and Baek, C.-K. (2003). "Electrospinning of Poly(Vinylidene Fluoride)/Dimethylformamide Solutions with Carbon Nanotubes." *J. Polym. Sci. Part B Polym. Phys.* 41, 1572–1577.
- Shao, H., Fang, J., Wang, H., Lang, C., and Lin, T. (2015a). "Robust Mechanical-to-Electrical Energy Conversion from Short-Distance Electrospun Poly(Vinylidene Fluoride) Fiber Webs." *ACS Appl. Mater. Interfaces* 7, 22551–22557.
- Shao, H., Fang, J., Wang, H., Lang, C., Yan, G., and Lin, T. (2017). "Mechanical Energy-to-Electricity Conversion of Electron/Hole-Transfer Agent-Doped Poly(Vinylidene Fluoride) Nanofiber Webs." *Macromol. Mater. Eng.* 302, 1–6.

- Shao, H., Fang, J., Wang, H., and Lin, T. (2015b). "Effect of Electrospinning Parameters and Polymer Concentrations on Mechanical-to-Electrical Energy Conversion of Randomly-Oriented Electrospun Poly(Vinylidene Fluoride) Nanofiber Mats." *RSC Adv.* 5, 14345–14350.
- Shi, K., Sun, B., Huang, X., and Jiang, P. (2018). "Synergistic Effect of Graphene Nanosheet and BaTiO₃nanoparticles on Performance Enhancement of Electrospun PVDF Nanofiber Mat for Flexible Piezoelectric Nanogenerators." *Nano Energy* 52, 153–162.
- Shi, X., Zhou, W., Ma, D., Ma, Q., Bridges, D., Ma, Y., et al. (2015). "Electrospinning of Nanofibers and Their Applications for Energy Devices." *J. Nanomater.* 2015, 140716-140736.
- Shokri, A., and Salami, N. (2016). "Gas Sensor Based on MoS₂ Monolayer." *Sensors Actuators, B Chem.* 236, 378–385.
- Siddiqui, S., Lee, H.B., Kim, D. II, Duy, L.T., Hanif, A., and Lee, N.E. (2018). "An Omnidirectionally Stretchable Piezoelectric Nanogenerator Based on Hybrid Nanofibers and Carbon Electrodes for Multimodal Straining and Human Kinematics Energy Harvesting." *Adv. Energy Mater.* 8, 1–11.
- Singh, H.H., Singh, S., and Khare, N. (2018). "Enhanced β -Phase in PVDF Polymer Nanocomposite and Its Application for Nanogenerator." *Polym. Adv. Technol.* 29, 143–150.
- Sinha, T.K., Ghosh, S.K., Maiti, R., Jana, S., Adhikari, B., Mandal, D., et al. (2016). "Graphene-Silver-Induced Self-Polarized PVDF-Based Flexible Plasmonic Nanogenerator Toward the Realization for New Class of Self Powered Optical Sensor." *ACS Appl. Mater. Interfaces* 8, 14986–14993.
- Sivakumar, M., Subadevi, R., Rajendran, S., Wu, H.C., and Wu, N.L. (2007). "Compositional Effect of PVdF-PEMA Blend Gel Polymer Electrolytes for Lithium Polymer Batteries." *Eur. Polym. J.* 43, 4466–4473.
- Sorayani Bafqi, M.S., Bagherzadeh, R., and Latifi, M. (2015). "Fabrication of Composite PVDF-ZnO Nanofiber Mats by Electrospinning for Energy Scavenging Application with Enhanced Efficiency." *J. Polym. Res.* 22, 130–138.
- Stephan, A.M. (2006). "Review on Gel Polymer Electrolytes for Lithium Batteries." *Eur. Polym. J.* 42, 21–42.
- Subbiah, T., Bhat, G.S., Tock, R.W., Parameswaran, S., and Ramkumar, S.S. (2005).

"Electrospinning of Nanofibers." *J. Appl. Polym. Sci.* 96, 557–569.

Sun, G., Sun, L., Xie, H., and Liu, J. (2016). "Electrospinning of Nanofibers for Energy Applications." *Nanomaterials* 6, 129-159.

Supaphol, P., Mit-Uppatham, C., and Nithitanakul, M. (2005). "Ultrafine Electrospun Polyamide-6 Fibers: Effect of Emitting Electrode Polarity on Morphology and Average Fiber Diameter." *J. Polym. Sci. Part B Polym. Phys.* 43, 3699–3712.

Tamang, A., Ghosh, S.K., Garain, S., Alam, M., and Haeberle, J. (2015). "DNA-Assisted β - Phase Nucleation and Alignment of Molecular Dipoles in PVDF Film: A Realization of Self-Poled Bioinspired Flexible Polymer Nanogenerator for Portable Electronic Devices." *ACS Appl. Mater. Interfaces* 7, 16143–16147.

Tang, Q.C., and Li, X. (2013). A wide-band piezoelectric energy-harvester for high-efficiency power generation at low frequencies. In 2013 Transducers and Eurosensors XXVII: The 17th International Conference on Solid-State Sensors, Actuators and Microsystems, TRANSDUCERS and EUROSENSORS 2013, 697–700.

Tang, X., Cao, Q., Wang, X., Peng, X., and Zeng, J. (2015). "Study of the Effect of a Novel High-Performance Gel Polymer Electrolyte Based on Thermoplastic Polyurethane/Poly(Vinylidene Fluoride)/Polystyrene and Formed Using an Electrospinning Technique." *RSC Adv.* 5, 58655–58662.

Tao, M., Liu, F., Ma, B., and Xue, L. (2013). "Effect of Solvent Power on PVDF Membrane Polymorphism during Phase Inversion." *Desalination* 316, 137–145.

Thakur, P., Kool, A., Hoque, N.A., Bagchi, B., Khatun, F., Biswas, P., et al. (2017). "Superior Performances of In Situ Synthesized ZnO/PVDF Thin Film Based Self-Poled Piezoelectric Nanogenerator and Self-Charged Photo-Power Bank with High Durability." *Nano Energy*, 44, 456-467.

Thenmozhi, S., Dharmaraj, N., Kadirvelu, K., and Kim, H.Y. (2017). "Electrospun Nanofibers: New Generation Materials for Advanced Applications." *Mater. Sci. Eng. B Solid-State Mater. Adv. Technol.* 217, 36–48.

Thompson, C.J., Chase, G.G., Yarin, A.L., and Reneker, D.H. (2007). "Effects of Parameters on Nanofiber Diameter Determined from Electrospinning Model." *Polymer (Guildf)*. 48, 6913–

6922.

Toprak, A., and Tigli, O. (2018). "Micron Scale Energy Harvesters Using Multiple Piezoelectric Polymer Layers." *Sensors Actuators, A Phys.* 269, 412–418.

Touny, A.H., Lawrence, J.G., Jones, A.D., and Bhaduri, S.B. (2010). "Effect of Electrospinning Parameters on the Characterization of PLA/HNT Nanocomposite Fibers." *J. Mater. Res.* 25, 857–865.

Ulrich, R., Schaper, L., Nelms, D., and Leftwich, M. (2000). "Comparison of Paraelectric and Ferroelectric Materials for Applications as Dielectrics in Thin Film Integrated Capacitors." *Int. J. Microcircuits Electron. Packag.* 23, 172–181.

Vacche, S.D., Oliveira, F., Leterrier, Y., Michaud, V., Damjanovic, D., and Månson, J.-A.E. (2012). "The Effect of Processing Conditions on the Morphology, Thermomechanical, Dielectric, and Piezoelectric Properties of P(VDF-TrFE)/BaTiO₃ Composites." *J. Mater. Sci.* 47, 4763–4774.

Varghese, S., Varghese, S., Swaminathan, S., Singh, K., and Mittal, V. (2015). "Two-Dimensional Materials for Sensing: Graphene and Beyond." *Electronics* 4, 651–687.

Vatansver, D., Hadimani, R.L., Shah, T., and Siores, E. (2011). "An Investigation of Energy Harvesting from Renewable Sources with PVDF and PZT." *Smart Mater. Struct.* 20, 55019.

Vonch, J., Yarin, a, and Megaridis, C.M. (2007). "Electrospinning : A Study in the Formation of Nanofibers." *J. Undergrad. Res.* 1, 1-6.

Wan, C., and Bowen, C.R. (2017). "Multiscale-Structuring of Polyvinylidene Fluoride for Energy Harvesting: The Impact of Molecular-, Micro- and Macro-Structure." *J. Mater. Chem. A* 5, 3091–3128.

Wang, B., and Huang, H.-X. (2014a). "Incorporation of Halloysite Nanotubes into PVDF Matrix: Nucleation of Electroactive Phase Accompany with Significant Reinforcement and Dimensional Stability Improvement." *Compos. Part A Appl. Sci. Manuf.* 66, 16–24.

Wang, H., and Gao, H. (2016). "A Sandwich-like Composite Nonwoven Separator for Li-Ion Batteries." *Electrochim. Acta* 215, 525–534.

Wang, H., Gong, R., and Qian, X. (2018a). "Preparation and Characterization of TiO₂/g-

C₃N₄/PVDF Composite Membrane with Enhanced Physical Properties." *Membranes (Basel)* 8, 14–23.

Wang, L., Lu, X., Lei, S., and Song, Y. (2014). "Graphene-Based Polyaniline Nanocomposites: Preparation, Properties and Applications." *J. Mater. Chem. A* 2, 4491–4509.

Wang, S.G., Zhang, Q., Yang, D.J., Sellin, P.J., and Zhong, G.F. (2004). "Multi-Walled Carbon Nanotube-Based Gas Sensors for NH₃ Detection." *Diam. Relat. Mater.* 13, 1327–1332.

Wang, X., Yu, J., Sun, G., and Ding, B. (2016). "Electrospun Nanofibrous Materials: A Versatile Medium for Effective Oil/Water Separation." *Mater. Today* 19, 403–414.

Wang, Y., Jia, W., Strout, T., Ding, Y., and Lei, Y. (2009). "Preparation, Characterization and Sensitive Gas Sensing of Conductive Core-Sheath TiO₂-PEDOT Nanocables." *Sensors* 9, 6752–6763.

Wang, Z., Guo, F., Chen, C., Shi, L., Yuan, S., Sun, L., et al. (2015). "Self-Assembly of PEI/SiO₂ on Polyethylene Separators for Li-Ion Batteries with Enhanced Rate Capability." *ACS Appl. Mater. Interfaces* 7, 3314–3322.

Wang, Z., Xiang, H., Wang, L., Xia, R., Nie, S., Chen, C., et al. (2018b). "A Paper-Supported Inorganic Composite Separator for High-Safety Lithium-Ion Batteries." *J. Memb. Sci.* 553, 10–16.

Whiter, R.A., Narayan, V., and Kar-Narayan, S. (2014). "A Scalable Nanogenerator Based on Self-Poled Piezoelectric Polymer Nanowires with High Energy Conversion Efficiency." *Adv. Energy Mater.* 4, 1–7.

Wootthikanokkhan, J., Phiriyawirut, M., and Pongchumpon, O. (2015). "Effects of Electrospinning Parameters and Nanofiller Content on Morphology and Gel Electrolyte Properties of Composite Nanofibers Based on La₂O₃-Filled PVDF-HFP." *Int. J. Polym. Mater. Polym. Biomater.* 64, 416–426.

Wu, C.M., and Chou, M.H. (2016a). "Polymorphism, Piezoelectricity and Sound Absorption of Electrospun PVDF Membranes with and without Carbon Nanotubes." *Compos. Sci. Technol.* 127, 127–133.

Wu, D., Deng, L., Sun, Y., Teh, K.S., Shi, C., Tan, Q., et al. (2017). "A High-Safety PVDF/Al₂O₃ composite Separator for Li-Ion Batteries via Tip-Induced Electrospinning and

Dip-Coating." *RSC Adv.* 7, 24410–24416.

Wu, D., Huang, S., Xu, Z., Xiao, Z., Shi, C., Zhao, J., et al. (2015a). "Polyethylene Terephthalate/Poly(Vinylidene Fluoride) Composite Separator for Li-Ion Battery." *J. Phys. D: Appl. Phys.* 48, 285305-285312

Wu, Q.Y., Liang, H.Q., Gu, L., Yu, Y., Huang, Y.Q., and Xu, Z.K. (2016). "PVDF/PAN Blend Separators via Thermally Induced Phase Separation for Lithium Ion Batteries." *Polym. (United Kingdom)* 107, 54–60.

Wu, Y., Yuan, X., Zhano, S., and Ree, T. V. (2015b). *Lithium-Ion Batteries Fundamentals and Applications*, 1-568.

Xin, Y., Qi, X., Tian, H., Guo, C., Li, X., Lin, J., et al. (2016). "Full-Fiber Piezoelectric Sensor by Straight PVDF/Nanoclay Nanofibers." *Mater. Lett.* 164, 136–139.

Xu, R., Huang, X., Lin, X., Cao, J., Yang, J., and Lei, C. (2017). "The Functional Aqueous Slurry Coated Separator Using Polyvinylidene Fluoride Powder Particles for Lithium-Ion Batteries." *J. Electroanal. Chem.* 786, 77–85.

Xue, Z., He, D., and Xie, X. (2015). "Poly(Ethylene Oxide)-Based Electrolytes for Lithium-Ion Batteries." *J. Mater. Chem. A* 3, 19218–19253.

Yang, C.-S., Mahmood, A., Kim, B., Shin, K., Jeon, D.H., Han, J.K., et al. (2016a). "Enhancing Gas Sensing Properties of Graphene by Using a Nanoporous Substrate." *2D Mater.* 3, 011007-011014.

Yang, C.L., Li, Z.H., Li, W.J., Liu, H.Y., Xiao, Q.Z., Lei, G.T., et al. (2015). "Batwing-like Polymer Membrane Consisting of PMMA-Grafted Electrospun PVdF-SiO₂ Nanocomposite Fibers for Lithium-Ion Batteries." *J. Memb. Sci.* 495, 341–350.

Yang, D.C., and Thomas, E.L. (1984). "On the $\alpha \rightarrow \beta$ Transition by Deformation of Highly Oriented Poly(Vinylidene Fluoride)." *J. Mater. Sci. Lett.* 3, 929–936.

Yang, F.L., Xia, F.F., Hu, J., Zheng, C.Z., Sun, J.H., and Yi, H.B. (2018a). "The Improvement of Photocatalytic Activity of Monolayer g-C₃N₄ via Surface Charge Transfer Doping." *RSC Adv.* 8, 1899–1904.

Yang, J., Wang, J., Zhang, Q., Chen, F., Deng, H., Wang, K., et al. (2011). "Cooperative Effect

of Shear and Nanoclay on the Formation of Polar Phase in Poly(Vinylidene Fluoride) and the Resultant Properties." *Polymer (Guildf)*. 52, 4970–4978.

Yang, L., Cheng, M., Lyu, W., Shen, M., Qiu, J., Ji, H., et al. (2018b). "Tunable Piezoelectric Performance of Flexible PVDF Based Nanocomposites from MWCNTs/Graphene/MnO₂ three-Dimensional Architectures under Low Poling Electric Fields." *Compos. Part A Appl. Sci. Manuf.* 107, 536–544.

Yang, W., Gan, L., Li, H., and Zhai, T. (2016b). "Two-Dimensional Layered Nanomaterials for Gas-Sensing Applications." *Inorg. Chem. Front.* 3, 433–451.

Yang, Y., Jia, Z., Li, Q., and Guan, Z. (2006). "Experimental Investigation of the Governing Parameters in the Electrospinning of Polyethylene Oxide Solution." *IEEE Trans. Dielectr. Electr. Insul.* 13, 580–584.

Yanilmaz, M., Chen, C., and Zhang, X. (2013). "Fabrication and Characterization of SiO₂/PVDF Composite Nanofiber-Coated PP Nonwoven Separators for Lithium-Ion Batteries." *J. Polym. Sci. Part B Polym. Phys.* 51, 1719–1726.

Yanilmaz, M., Lu, Y., Dirican, M., Fu, K., and Zhang, X. (2014). "Nanoparticle-on-Nanofiber Hybrid Membrane Separators for Lithium-Ion Batteries via Combining Electrospraying and Electrospinning Techniques." *J. Memb. Sci.* 456, 57–65.

Yaqoob, U., Uddin, A.S.M.I., and Chung, G. (2017). "Applied Surface Science A Novel Tri-Layer Flexible Piezoelectric Nanogenerator Based on Surface-Modified Graphene and PVDF-BaTiO₃ Nanocomposites." *Appl. Sci.* 405, 420–426.

Yee, W.A., Kotaki, M., Liu, Y., and Lu, X. (2007). "Morphology, Polymorphism Behavior and Molecular Orientation of Electrospun Poly(Vinylidene Fluoride) Fibers." *Polymer (Guildf)*. 48, 512–521.

Yong Lei, Qinglin Wu, Craig M. Clemons, Fei Yao, Y.X. (2007). "Influence of Nanoclay on Properties of HDPE/Wood Composites." *J. Appl. Polym. Sci.* 106, 3958–3966.

Yoon, K., and Kellarakis, A. (2014). "Nanoclay-Directed Structure and Morphology in PVDF Electrospun Membranes." *J. Nanomater.* 2014, 367671.

You, A., Be, M.A.Y., and In, I. (2017). "BaTiO₃-Based Piezoelectrics : Fundamentals , Current Status , and Perspectives." 041305,.

- Yousefi, A.A. (2011). "Hybrid Polyvinylidene Fluoride/Nanoclay/MWCNT Nanocomposites: PVDF Crystalline Transformation." *Iran Polym J* 20, 725–733.
- Yu, B., Mao, M., Yu, H., Huang, T., Zuo, W., Wang, H., et al. (2017). "Enhanced Piezoelectric Performance of Electrospun Polyvinylidene Fluoride Doped with Inorganic Salts." *Macromol. Mater. Eng.* 302, 1–8.
- Yu, G.-F., Yan, X., Yu, M., Jia, M.-Y., Pan, W., He, X.-X., et al. (2016). "Patterned, Highly Stretchable and Conductive Nanofibrous PANI/PVDF Strain Sensors Based on Electrospinning and in Situ Polymerization." *Nanoscale* 8, 2944–2950.
- Yu, H., Huang, T., Lu, M., Mao, M., Zhang, Q., and Wang, H. (2013). "Enhanced Power Output of an Electrospun PVDF/MWCNTs-Based Nanogenerator by Tuning Its Conductivity." *Nanotechnology* 24, 405401–405410.
- Yu, L., and Cebe, P. (2009a). "Crystal Polymorphism in Electrospun Composite Nanofibers of Poly(Vinylidene Fluoride) with Nanoclay." *Polymer (Guildf)*. 50, 2133–2141.
- Yu, W., Zhao, Z., Zheng, W., Long, B., Jiang, Q., Li, G., et al. (2009). "Crystallization Behavior of Poly(Vinylidene Fluoride)/Montmorillonite Nanocomposite." *Polym. Eng. Sci.* 49, 491–498.
- Yuan, P., Tan, D., and Annabi-Bergaya, F. (2015). "Properties and Applications of Halloysite Nanotubes: Recent Research Advances and Future Prospects." *Appl. Clay Sci.* 112–113, 75–93.
- Z Liu, S Zhang, Y M Jin, H Ouyang, Y Zou, X X Wang, L.X.X.Z.L. (2017). "Flexible Piezoelectric Nanogenerator for Wearable Self-Powered Respiration Active Sensor and Healthcare Monitoring." *Semicond. Sci. Technol.* 32, 64004–64010.
- Zaccaria, M., Fabiani, D., and Zucchelli, A. (2016). "Vibration Energy Harvesting Using Electrospun Nanofibrous PVdF-TrFE." 1, 4–7.
- Zampetti, E., Bearzotti, A., and Macagnano, A. (2014). "Flexible Piezoelectric Transducer Based on Electrospun PVDF Nanofibers for Sensing Applications." *Procedia Eng.* 87, 1509–1512.
- Zeng, W., Tao, X.-M., Chen, S., Shang, S., Chan, H.L.W., and Choy, S.H. (2013). "Highly Durable All-Fiber Nanogenerator for Mechanical Energy Harvesting." *Energy Environ. Sci.* 6,

2631–2638.

Zhai, Y., Wang, N., Mao, X., Si, Y., Yu, J., Al-Deyab, S.S., et al. (2014). "Sandwich-Structured PVdF/PMIA/PVdF Nanofibrous Separators with Robust Mechanical Strength and Thermal Stability for Lithium Ion Batteries." *J. Mater. Chem.* 2, 14511.

Zhang, F., Ma, X., Cao, C., Li, J., and Zhu, Y. (2014). "Poly(Vinylidene Fluoride)/SiO₂ Composite Membranes Prepared by Electrospinning and Their Excellent Properties for Nonwoven Separators for Lithium-Ion Batteries." *J. Power Sources* 251, 423–431.

Zhang, H., Zhang, Y., Yao, Z., John, A.E., Li, Y., Li, W., et al. (2016a). "Novel Configuration of Polyimide Matrix-Enhanced Cross-Linked Gel Separator for High Performance Lithium Ion Batteries." *Electrochim. Acta* 204, 176–182.

Zhang, S., Hang, N., Zhang, Z., Yue, H., and Yang, W. (2017). "Preparation of g-C₃N₄/Graphene Composite for Detecting NO₂ at Room Temperature." *Nanomaterials* 7, 12–22.

Zhang, S.S. (2007). "A Review on the Separators of Liquid Electrolyte Li-Ion Batteries." *J. Power Sources* 164, 351–364.

Zhang, Y., Zhang, D., Guo, W., and Chen, S. (2016b). "The α -Fe₂O₃/g-C₃N₄ Heterostructural Nanocomposites with Enhanced Ethanol Gas Sensing Performance." *J. Alloys Compd.* 685, 84–90.

Zhao, Y., Ma, J., Chen, K., Zhang, C., Yao, C., Zuo, S., et al. (2017). "One-Pot Preparation of Graphene-Based Polyaniline Conductive Nanocomposites for Anticorrosion Coatings." *Nano* 12, 1750056-1750065.

Zhao, Z., Li, J., Yuan, X., Li, X., Zhang, Y., and Sheng, J. (2005). "Preparation and Properties of Electrospun Poly(Vinylidene Fluoride) Membranes." *J. Appl. Polym. Sci.* 97, 466–474.

Zhong, Z., Cao, Q., Jing, B., Wang, X., Li, X., and Deng, H. (2012). "Electrospun PVdF-PVC Nanofibrous Polymer Electrolytes for Polymer Lithium-Ion Batteries." *Mater. Sci. Eng. B Solid-State Mater. Adv. Technol.* 177, 86–91.

Zhu, G., Zhao, L.Y., Zhu, L.T., Deng, X.Y., and Chen, W.L. (2017). "Effect of Experimental Parameters on Nanofiber Diameter from Electrospinning with Wire Electrodes." *IOP Conf. Ser. Mater. Sci. Eng.* 230, 012043-012055.

Zhu, J., Xiao, P., Li, H., and Carabineiro, S.A.C. (2014). "Graphitic Carbon Nitride: Synthesis, Properties, and Applications in Catalysis." *ACS Appl. Mater. Interfaces* 6, 16449–16465.

Zhu, L., Wang, Y., Hu, F., and Song, H. (2015). "Structural and Friction Characteristics of G-C₃N₄/PVDF Composites." *Appl. Surf. Sci.* 345, 349–354.

Zhu, M., Lan, J., Tan, C., Sui, G., and Yang, X. (2016). "Degradable Cellulose Acetate/Poly-L-Lactic Acid/Halloysite Nanotube Composite Nanofiber Membranes with Outstanding Performance for Gel Polymer Electrolytes." *J. Mater. Chem. A* 4, 12136–12143.

Zhu, Y., Wang, F., Liu, L., Xiao, S., Yang, Y., and Wu, Y. (2013). "Cheap Glass Fiber Mats as a Matrix of Gel Polymer Electrolytes for Lithium Ion Batteries." *Sci. Rep.* 3, 3187.

Zou, H., Yan, X., Ren, J., Wu, X., Dai, Y., Sha, D., et al. (2015). "Photocatalytic Activity Enhancement of Modified g-C₃N₄ by Ionothermal Copolymerization." *J. Mater.* 1, 340–347.

BIO-DATA

Mohammed Khalifa

Permanent address:

Sector No: 15, Plot No: 21/D

Navanagar, Bagalkot.

Karnataka:587103

India.



Contact details:

Email: mohammed.khalifa89@gmail.com

Phone: +91 9611758785 / +43 67763117123

Academic qualifications:

- Master's degree in Machine design Engineering (2012-2014) from Visveswaraya Technological university, Belgaum, Karnataka.
- Bachelor's degree in Mechanical Engineering (2009-2012) from Visveswaraya Technological university, Belgaum, Karnataka.
- Diploma in Mechanical Engineering (2006-2009) from board of technical education, Bengaluru, Karnataka.

Research publications:

Articles in international journals: 08

Articles in conference proceedings: 07

List of publications in international journals (Peer reviewed)

1. Khalifa, M., Mahendran, A., and Anandhan, S. (2016). "Probing the Synergism of Halloysite Nanotubes and Electrospinning on Crystallinity, Polymorphism and Piezoelectric Performance of Poly(Vinylidene Fluoride)." *RSC Adv.* 6, 114052–114060.
2. Khalifa, M., Janakiraman, S., Ghosh, S., Venimadhav, A., and Anandhan, S. (2019). "PVDF/Halloysite Nanocomposite-Based Non-Wovens as Gel Polymer Electrolyte for High Safety Lithium Ion Battery." *Polym. Compos.* 40, 2320–2334.
3. Khalifa, M., Mahendran, A., and Anandhan, S. (2018). "Durable, Efficient, and Flexible Piezoelectric Nanogenerator from Electrospun PANi/HNT/PVDF Blend Nanocomposite." *Polym. Compos.* 40, 1663–1675.
4. Khalifa, M., and Anandhan, S. (2019). "Synergism of Graphitic-Carbon Nitride and Electrospinning on the Physico-Chemical Characteristics and Piezoelectric Properties of Flexible Poly(Vinylidene Fluoride) Based Nanogenerator." *J. Polym. Res.* 26, 1–13.

List of paper in international conferences (Abstract reviewed)

1. Khalifa, M., Mahendran, A., and Anandhan, S., Development of Electrospun Halloysite/Poly(vinylidene fluoride) Nanocomposite Nanofibers for Force Sensor Applications, International Conference on Material Science and Technology (2016).
2. Khalifa, M., Mahendran, A., and Anandhan, S., Probing the synergism of halloysite nanotubes and electrospinning on crystallinity, polymorphism and piezoelectric performance of poly(vinylidene fluoride), *International conference on Advancements in polymeric materials* (2017).
3. Khalifa, M., Janakiraman, S., Ghosh, S., Venimadhav, A., and Anandhan, S., Development of Halloysite nanotubes/Poly(vinylidene fluoride) Nanocomposite Nanofiber Separator for Lithium Ion Battery, *Second International Conference on Advanced Polymeric Materials* (2017).
4. Khalifa, M., Janakiraman, S., Ghosh, S., Venimadhav, A., and Anandhan, S., New Gel Polymer Electrolyte from Electrospun PVDF/Halloysite Nanocomposite-based Non-woven Fabric for Lithium Ion Battery, International Conference on Nanotechnology: Ideas, Innovations and Initiatives (2017).
5. Khalifa, M., Mahendran, A., and Anandhan, S., Physico-chemical characteristics of electrospun PVDF/PANI blend nanofibers for piezoelectric energy harvesting application, *International conference on advanced ceramics and nanomaterials for sustainable development* (2018).